Dissertation zur Erlangung des Doktorgrades
der Fakultät für Chemie und Pharmazie
der Ludwig – Maximilians – Universität München

Development of an automated micromixer for the controlled formulation of multi-component polyplexes

Dominik Manuel Loy (geb. Wendel)
aus Zorneding, Deutschland

2021

Erklärung

Diese Dissertation wurde im Sinne von § 7 der Promotionsordnung vom 28. November 2011 von Herrn Prof. Dr. Ernst Wagner betreut.

Eidesstattliche Versicherung

Diese Dissertation wurde eigenständig und ohne unerlaubte Hilfe erarbeitet.

München, 28. Januar 2021

……

Dominik Loy

Dissertation eingereicht am 01.02.2021

1. Gutachter: Prof. Dr. Ernst Wagner

2. Gutachter: Prof. Dr. Joachim Rädler

Mündliche Prüfung am 24.03.2021

Meiner Familie

“I'd take the awe of understanding over the awe of ignorance any day.”

― Douglas Adams, The Salmon of Doubt

Table of Contents

1. Introduction

1.1. Prospects of nanotechnology

Nanotechnology has the capability to exert a more significant influence on our way of life than the industrial revolution. In his seminal talk at the annual American Physical Society meeting in December 1959, Nobel laureate Richard Feynman made a series of educated guesses about the future of engineering and, in particular, about nanotechnology. He based his predictions on the limits of natural laws and stated that "[t]he principles of physics, as far as I can see, do not speak against the possibility of maneuvering things atom by atom." (Feynman, 1959).

If this technology were already available, the consequences would be enormous. MIT engineer K. Drexler has written an influential book about the implications of Feynman's ideas (Drexler, 2007). In particular, this technology would enable the precise manufacturing of materials at the nanoscale with absolute control over the exact placement of every atom of a given device. This technique would also include precise gene manipulations in living systems.

Possibilities of such power are overwhelming. Fiction has readily accepted the advent of nanotechnology and has explored various aspects of its application in our world, albeit usually as a tool to wreak havoc on humankind. The author M. Crichton, for example, makes the threats of nanobots equipped with artificial intelligence and the power to reproduce indefinitely a subject of his novel (Crichton, 2008). The science fiction writer D. Koontz introduces injectable nanotechnology that assembles in the victims` brains and gives complete power over them (Koontz, 2017). Koontz also writes about the ambiguity of bioengineering by introducing two creatures with enhanced intelligence – a golden retriever and a predator - into our world, literally as metaphors for the promises and threats of this technology (Koontz, 2003). Both are enormous.

In reality, the promises of nanotechnology have already led to extensive research in many different fields. In medicine, for example, the term 'nanomedicine' is defined by the European Technology Platform on Nanomedicine as "[…] the application of nanotechnology to health. It exploits the improved and often novel physical, chemical, and biological properties of materials at the nanometric scale."(Boisseau et al., 2005). That means therapeutics ranging in size from 1 – 1000 nm are considered to be nanomedicines. The development of nanomedicines presumably has the potential to increase the specificity of medical interventions. Instead of flooding the body with active substances that inhibit or stimulate a limited number of pathways, nanomedicines could go in and specifically replace or repair damaged molecules like a

mechanic would repair a car. In a discussion with Mr. Feynman, his student Albert A. Hibbs said, “it would be interesting in surgery if you could swallow the surgeon” (Feynman, 1959). As he pointed out, currently it is a “very wild idea” (Feynman, 1959), but if we look at the advances in gene therapeutics and nanomedicines, for example our ability to change DNA in living systems with the CrispRCas system, it seems not too far-fetched that one day we will be able to have much greater precision in our medical interventions.

1.2. First clinical trials

Nevertheless, what has research on nanomedicine achieved so far? The last decades have brought many promising results as well as setbacks as a chronological overview of the development of nanomedicines illustrates. The first clinically relevant demonstration of the promises and power of nanomedicine and gene therapy, in particular, was the transduction of tumor-infiltrating lymphocytes tagged with a gene coding for the resistance to neomycin by Rosenberg et al. in 1989 (Rosenberg et al., 1990). Target cells had been gathered from patients with metastatic melanoma, and the resistance gene was transduced into the cells by a retroviral vector. After reinfusion of the lymphocytes, the resistance gene could be detected by polymerase chain reaction (PCR) in circulating cells for three weeks up to two months. One year later, in 1990, these principles were applied to treating two patients suffering from adenosine deaminase (ADA) deficiency (Blaese et al., 1995). This congenital gene defect causes faulty B – and T – cell function, which in turn leads to severe combined immunodeficiency (SCID) (Giblett et al., 1972). Retroviral transduction of T-cells with the adenosine deaminase gene outside of the patients led to an integration of this gene into the genome of the T-cells and bestowed a survival advantage on modified T-cells in contrast to natural T-cells (Ferrari et al., 1991). Reinfused cells persisted over time, and immune responses normalized in both patients.

These groundbreaking results invigorated the gene therapy community, and the number of clinical trials increased worldwide from one trial in 1989 to 113 trials in 1999. Unfortunately, employing retroviral vectors to do gene modifications lacks the precision and control envisioned by Feynman, as discussed above. This problem emerged in a clinical trial similar to the ADA-SCID one, but with patients having the X1-linked severe combined immunodeficiency (SCID – X1). In this hereditary disease, differentiation of T – lymphocytes and natural killer cells is blocked early by mutations in the gene coding for γc cytokine receptor subunits. This gene defect causes a condition similar to patients affected by the ADA gene

defect, and it was treated the same way. Lymphocytes were obtained from the patients and transduced with a retroviral vector outside of the patients. The retroviral vector integrated the correct version of the γc cytokine receptor into the genome of the lymphocytes, and reinfusion alleviated the symptoms of the gene defect. The supposedly random gene integration, however, placed the repaired gene preferentially near the LMO2 proto-oncogene promoter, which led to the development of leukemia in three of ten patients (Hacein-Bey-Abina et al., 2003; Hacein-Bey-Abina, 2003). Two of the three patients with leukemia responded well to chemotherapy. Sadly, the third child died in October 2004. Another problem using viral vectors surfaced when Jesse Gelsinger, an 18-year-old patient suffering from a mild form of ornithine transcarbamylase deficiency, was enrolled in a phase 1 clinical trial to test the safety of an adenoviral vector against his disease. He developed a massive immune reaction to this vector with subsequent multi-organ failure and died after four days. He is considered to be the first person to have died from a gene therapy product (Lehrman, 1999). These tragic events sparked a global debate about safety and risk/benefit ratios of gene therapy and severely lowered the number of approved trials in the following years (Gansbacher, 2003).

Nevertheless, the first gene therapy product, Gendicine, was granted marketing authorization in China in 2003 (Pearson, Jia & Kandachi, 2004). Gendicine is an adenoviral vector loaded with the tumor suppressor gene p53 for the treatment of head and neck squamous cell carcinoma (HNSCC). It was not, however, approved by the FDA or by the EMA due to concerns about the quality of the data from phase II/III clinical trials in China. Additionally, the State Food and Drug Administration of China did not demand proof for Gencidine extending the life of treated patients, and the drug was approved based on tumor shrinkage only (Guo & Xin, 2006).

The path to the first approved gene therapy in Europe and North America was paved with many hard lessons and insights. In 2006, a clinical trial treating two patients with X-linked chronic granulomatous disease (X-CGD) yielded promising results at first (Ott et al., 2006). X-CGD is a primary immunodeficiency due to the mutated gene $gp91^{phox}$ causing a defect in the oxidative antimicrobial activity of phagocytes. The risk for leukemia due to the insertional mutagenesis by the retroviral vector was deemed to be very low since the corrected gp91 gene did not bestow a survival advantage on target hematopoietic stem cells and cancer genesis had not been observed in mice (Dinauer et al., 1999). This conceived advantage, however, was also the curse of this therapeutic idea. In total, twelve patients had been treated, but a slow decline of immune-competent cells was observed in nine patients, which led to the resurgence of X-CGD. Only three patients had engrafted with high levels of gene-modified cells. Unfortunately, all three

developed myelodysplastic syndrome due to clonal expansion triggered by the insertional activation of EVI1. One patient died from this condition in combination with a septic shock and multi-organ failure (Grez et al., 2011).

Utilizing the immune system of the patient to detect and destroy tumor cells is an elegant approach to tumor therapy. Autologous T-cells can be genetically modified to destroy cells featuring unique surface proteins (Sadelain, Brentjens & Rivière, 2009). Previous therapies utilizing the first generation of chimeric antigen receptor (CAR) T-cells, however, were not successful due to a disability to expand t-cell populations *in vivo*. These T-cells were modified to produce specific chimeric antigen receptors but lacked the signaling domains for T-cell expansion. The first generation receptor was a transmembrane protein which contained two subdomains: the intracellular CD3-ζ chain (Irving & Weiss, 1991; Romeo, Amiot & Seed, 1992) for induction of cell lysis signaling and an antigen recognition domain for the target surface proteins. Since prolonged anti-tumoral effects rely on T-cell expansion *in vivo*, second-generation CAR T-cells were developed. Here, the CD28 domain was integrated into the chimeric fusion protein to enable the reception of secondary signals (Maher et al., 2002). Indeed, T-cells expanded by more than two logs without losing their cell lysing potential.

Additionally, transfection vectors were changed from retroviral systems (Eshhar et al., 1996) to lentiviral vectors because of their safety profile and their higher efficiency for human T – cells (Naldini et al., 1996; Sinn, Sauter & McCray, 2005). The considerable progress in this field led to the development of CAR-T cells against chronic lymphoid leukemia, which target CD19 on B-lymphocytes and feature CD3-ζ and 4-1BB signaling domains for enhanced T-cell expansion (Kalos et al., 2011; Porter et al., 2011). These genetically modified cells were used to treat three patients with spectacular results: two patients experienced a complete remission of their tumors with stable engraftment of CAR-T cells. Serious side effects in relation to the treatment could not be observed except for a tumor lysis syndrome in all patients after ten days due to the destruction of around one kg of tumor cells. In 2017, the first patient was celebrating five years of being cancer-free (Emily Whitehead Foundation, 2017).

Promising results were also expected from a clinical trial with patients suffering from Leber's congenital amaurosis. The disease comprises a group of mostly recessively inherited, rod-cone dystrophy in the eyes due to mutations in the gene coding for retinal pigment proteins, which is associated with visual impairment. It progresses over time to complete blindness by the age of 30 (Bainbridge et al., 2008). The eye is an immuno-privileged space, which is why the application of an adenoviral vector to transfect the correct version of the gene was a plausible

approach. Indeed, no unexpected adverse events were observed, but only one of three patients had a measurable improvement in visual acuity. Nevertheless, the transfection of the gene has the potential to slow down or even avert the progression of the disease, motivating further research (Maguire et al., 2008, 2009). These hopes, however, could not be fulfilled so far. Further studies examining the long-term effects of the gene therapy concluded that improvement of visual acuity was unfortunately unreliable and modest (Bainbridge et al., 2015), while retinal degeneration was not arrested (Cideciyan et al., 2013).

Cartier and colleagues published the first clinical trial involving lentiviral vectors in 2009 (Cartier et al., 2009). These vectors are advantageous when hematopoietic cells or non-dividing cells are to be transduced (Naldini et al., 1996; Miyoshi et al., 1999). The treatment group consisted of two boys with X-linked adrenoleukodystrophy (X-ALD), which is a serious disease affecting the myelin sheath of nerve cells due to insufficient removal of fatty acids by the relevant proteins. The general procedure was comparable to gene therapies with other viral vectors. Autologous hematopoietic stem cells were obtained from the patients and transfected with the lentiviral vector carrying the correct version of the target gene (ABCD1). The vector was deliberately designed not to confer a survival advantage on modified cells, a lesson learned from the occurrence of leukemia in SCID – X1 patients. Therefore, patients needed to receive myeloablative treatment to facilitate the engraftment of modified cells in advance to the reinfusion of these cells. Treatment was tolerated well, considering the circumstances. It resulted in a sustained ALD protein expression, and the progression of cerebral demyelination was arrested 12 – 14 months after treatment. Long-term follow-up showed a stable expression of ALD protein in 18% of bone marrow cells without the emergence of a dominant clone. Although it was considered a success story, the fraction of corrected cells needs to be improved to shorten the time between therapy and arrest of cerebral demyelination.

1.3. Viral vectors

1.3.1. Approved viral vectors

In June 2012, 1843 clinical trials involving gene therapy products had been completed (Ginn et al., 2013), and the community was eagerly waiting for the first product to be granted marketing authorization by the FDA or EMA. Indeed, in November 2012, the first gene therapy product, Glybera® (alipogene tiparvovec), was approved by the EMA (EMA, 2012; Ylä-Herttuala, 2012). Glybera® is an adeno-associated vector (AAV1) that delivers a therapeutic gene to muscle cells to treat lipoprotein lipase deficiency (LPLD). It is a rare disease that affects

1-2 per million and results in a disability to catabolize triglyceride-rich lipoproteins (Gaudet et al., 2010). This hereditary condition usually manifests during childhood, induces developmental disorders, and has a high probability for acute pancreatitis, which can be lethal. In 2017, however, the marketing authorization of Glybera® was not renewed by its company uniQure. The cost-effectiveness of the drug was considered to be negative due to the enormous maintenance costs of phase IV trials and a limited patient number suffering from the ultra-rare disease (Warner, 2017).

The first genetically modified product targeting cancer was approved in October 2015 by the FDA (Amgen, 2015; Fong, 2015). Imlygic® (T-vec) is a herpes simplex virus (HSV-1) that was genetically modified to proliferate in tumor cells selectively. It is administered into advanced melanoma lesions, infecting and destroying tumor cells during the process. Released molecules increase the immunogenicity of the tumor, systemically enhancing the response of the immune system to the tumor (Harrington et al., 2015; Bommareddy et al., 2017).

Encouraging results from the ADA-SCID trials reported above warranted further clinical trials with 18 children in total. 100% survival rate, no evidence of insertional mutagenesis, and the protocol improvements summarized by Aiuti et al. (Aiuti, Roncarolo & Naldini, 2017) culminated in the approval of the first ex vivo gene therapy - Strimvelis™ - by the EMA in April 2016 (EMA, 2016; Ylä-Herttuala, 2016).

In August 2017, the same year the first patient treated with CAR T-cells celebrated five years cancer free (Emily Whitehead Foundation, 2017), the FDA granted marketing authorization to Kymriah®, the first gene therapy available in the US. (FDA, 2017a,b). Kymriah® (tisagenlecleucel) is approved for treating acute lymphoblastic leukemia, and it is marketed as a single injection of the patient's own T-cells genetically modified with a lentiviral vector to express chimeric antigen receptors (CAR) on their surfaces. These receptors specifically recognize malignant cells, initiate their destruction, and signal for the expansion of the T-cells to engraft into the immune system of the patient, providing protection over extended time periods (Maude et al., 2018). In October 2017, the FDA approved another CAR T-cell therapy targeting the CD19 antigen on B-cells: Yescarta® (axicabtagene ciloleucel) for use in adults with refractive large B-cell lymphoma (FDA, 2017c). It differs from Kymriah® in two aspects: for transducing T-cells, a retroviral vector was used in contrast to the lentiviral vector utilized for Kymriah®. Additionally, a different T-cell activation domain (CD28) was integrated into the chimeric receptor, distinguishing it from Kymriah® with its CD137 activation domain

(Neelapu et al., 2017). Effects, as well as side-effects, were comparable in both therapies (Locke et al., 2019).

Despite skepticism concerning the effectiveness of the gene therapy for Leber's congenital amaurosis, the FDA approved Luxturna® (vortigene neparvovec-rzyl) in December 2017 (FDA, 2017d). Luxturna® is an AAV2 vector that delivers a functional version of the retinal pigment epithelium gene RPE65. Since Leber's congenital amaurosis can be caused by mutations in multiple genes, Luxturna® is only effective in the sub-group suffering from a biallelic RPE65 mutation-associated retinal dystrophy. It was the first gene therapy curing or temporarily alleviating an inherited disease (Ameri, 2018). It is also the first therapy utilizing an adenoviral vector to introduce functional genes into human cells *in vivo*. The huge price tag in combination with doubts about the long-term effect of the drug on disease progression and patients' quality of life led to discussions about the value of this new therapy for the public (Johnson et al., 2019; Darrow, 2019).

In 2019, gene therapies for two inherited genetic disorders, β-thalassemia (EMA, 2019a) and spinal muscle atrophy (FDA, 2019), were granted marketing authorization. In Europe, patients suffering from the hemoglobinopathy β-thalassemia can now be treated with Zynteglo® (EMA, 2019a). Autologous $CD34^+$ cells genetically modified with a lentiviral vector to express β-globin. After myeloablative treatment, modified cells are reinfused into the patient in order to engraft into the bone marrow. This therapy enables the production of functional hemoglobin, alleviating the need for monthly blood transfusions (Malik, 2016).

While treatment with Zynteglo® aims to replace defective cells with functional ones, Zolgensma® (Onasemnogene abeparvovec), approved by the FDA (FDA, 2019), delivers a copy of the functional survival motor neuron (SMN) gene to the affected motor neuron cells in patients suffering from spinal muscle atrophy. A serotype 9 adeno-associated vector is used to enable the delivery of the gene and the subsequent expression of SMN protein. A one-time infusion of Zolgensma® resulted in extended survival, improved motor functions, and increased scores on the CHOP INTEND scale (Mendell et al., 2017).

Since both therapies are one-time infusions with potentially curative outcomes, have only limited markets due to the rarity of the diseases, and were extremely expensive to develop and manufacture, they were the most expensive therapies in 2019. The manufacturers charged $ 1.8 million for Zynteglo®, and $ 2.1 million for Zolgensma® ("Gene therapy's next installment," 2019).

1.3.2. Advantages and disadvantages

Almost all clinical trials so far have only been using five different viral vectors. These vectors have been investigated, improved, and routinely used in clinical trials over the last 30 years. They can be categorized according to their genetic material and the existence of an envelope. Retroviruses and lentiviruses both carry RNA in enveloped capsids. Herpes simplex virus 1 (HSV-1) and adenoviruses deliver dsDNA to target cells, although the HSV-1 capsid is enveloped while the adenoviruses do not feature an envelope. Adeno-associated viruses (AAV) are ssDNA viruses without an envelope (Thomas, Ehrhardt & Kay, 2003).

Utilizing viral vectors to deliver genes to target cells has certain advantages. First and foremost, nature has already developed very efficient delivery systems for various cell types that can be exploited, alleviating the efforts researchers must invest in new delivery vehicles. Moreover, genes can be integrated into the genome of a cell by retro- and lentiviruses enabling continuous expression with the expansion of the transduced cells. HSV-1, AAV, and adenoviruses, however, are episomal vectors with different favorable properties: HSV-1 has a large packaging capacity. AAV is not naturally occurring in humans, justifying its low inflammatory and immunogenic potential. Adenoviruses are extremely efficient in transducing most tissues (Kay, Glorioso & Naldini, 2001; Thomas, Ehrhardt & Kay, 2003).

Despite numerous possible positive fields of application, it should also be considered that exploiting systems aimed at increasing their gene copy number without regard for the host's survival for gene therapy can have unintended consequences. First of all, humans have been exposed to many of those viral strains for centuries, making it difficult for physicians to use viral vectors without eliciting immune responses (Bessis, GarciaCozar & Boissier, 2004). The first death associated with gene therapy, Jesse Gelsinger, was the direct result of a strong response to the infused viral particles against his partial ornithine transcarbamylase (OTC) deficiency, which resulted in high fever, unintended blood clotting and finally multi-organ failure (Lehrman, 1999).

Moreover, integrating into the genome of the host to achieve a permanent expression of the target gene is dangerous as well. On the one side, it is a useful approach, since it promises the live-long cure of a condition. On the other side, integration events are poorly understood and inherently carry the possibility to disrupt essential genes (Baum et al., 2006). The probability of interfering with the gene expression of the cells was calculated to be very low. However, the case of the X-SCID trails described above indicated a preferred integration of transduced genes

into active genes and, in this case, next to a tumor-promoting gene resulting in the development of leukemia in treated patients.

Additionally, complete control over tissue specificity of viral vectors is seldom achieved (Waehler, Russell & Curiel, 2007). Adenoviruses, for example, will mainly infect liver cells when infused systemically, while HSV-1 vectors rely on delicate interaction between surface and capsid proteins, which are difficult to exploit.

Furthermore, looking at the wild type viruses, nature has designed its vectors perfectly for their purpose: replicating indefinitely inside certain cell types. Delivering genes exceeding the allotted cargo space, however, is usually impossible. Therefore, the applicability of certain vectors is limited to their respective payload requirements, which are mostly in the range between 5 – 8 kb (Thomas, Ehrhardt & Kay, 2003).

Finally, working with inherently infectious particles poses serious threats to researchers, producers, and patients. Researchers and manufacturers have to make sure that no infectious particles contaminate either the product or the factory. At the same time, there will always be a risk for the patient to have a second viral infection that randomly transfers virulent genes back to the attenuated viral therapeutics (Bouard, Alazard-Dany & Cosset, 2009).

These risks have accompanied the utilization of viral vectors for gene therapy since the beginning and have sparked many efforts to circumvent or alleviate the problems associated with viral vectors. One solution is the abandonment of viral vectors and the investigation of non-viral vectors.

1.4. Non-viral vectors

Non-viral vectors have the potential to address most of the problems mentioned above but usually suffer from decreased transfection efficiency in comparison to viral vectors. Especially the safety profile of non-viral vectors tends to be favorable since synthetic agents tend to be less immunogenic, and patients usually do not exhibit acquired immune responses to new vehicles (Behr, 1993). Additionally, the production of these vectors is more straightforward, as they are usually accessible synthetically and do not require the deployment of viruses. Moreover, the capacity limits of the non-viral vector are less restrictive than the capacity limits of the virus. Payloads do not need to be integrated into a viral delivery vehicle with all its additional requirements to generate functional viral particles but can be easily adapted to the needs of the therapy. Even the delivery of larger proteins is possible (Yin et al., 2014).

1.4.1. Payloads

In comparison to viral vectors, non-viral vectors are much more flexible regarding possible payloads. Indeed, without the constraint to always integrate the payload into the genome of the virus, a variety of different payload classes is possible. The most common classes are nucleotides and proteins: DNA (Luo & Saltzman, 2000; Ibraheem, Elaissari & Fessi, 2014), mRNA (Yamamoto et al., 2009), microRNA, and siRNA (Peer & Lieberman, 2011) are commonly used nucleotides. In contrast, Zinc-finger proteins (ZFPs), transcription activator-like effectors (TALEs), and clustered regular interspaced short palindromic repeat (CRISPR) – systems are nucleases, a subclass of proteins (Wang, Glass & Xu, 2016). Directly delivering tumor suppressor genes (for example, p53 in Gendicine) or enzymes to damage cells or activate otherwise harmless drugs in specific cells is also feasible.

Additionally, non-viral vectors can be used to alter the pharmacokinetic profile of small-molecule drugs. Doxil®, for example, is a liposomal, polyethylene glycol (PEG) shielded formulation of the DNA intercalating agent doxorubicin with reduced dose-limiting side effects like cardiotoxicity (Duggan & Keating, 2011). In conclusion, non-viral vectors can influence the complete gene expression process due to the applicability of diverse payloads.

1.4.1.1. Proteins

Delivering gene-editing tools, like ZFPs, TALEs, or CRISPR-Cas9 enables the precise mutation of target DNA sequences *in vivo*. Applications for this technology are manifold, especially for correcting genetic mutations in hereditary diseases or for enabling the continuous expression of a newly introduced gene without the risk of insertional mutagenesis (Wang, Glass & Xu, 2016). Introducing proteins into tumor cells with the intent to damage their internal machinery sufficiently enough to induce apoptosis is another interesting strategy (Yu et al., 2016).

1.4.1.2. Nucleotides

Therapeutic oligo- or polynucleotides are usually chemically modified to increase their nuclease resistance, decrease excretion, and avoid detection by the immune system (Schiffelers, Blenke & Mastrobattista, 2019). Oligonucleotides can bind either to complementary sequences, as discussed in the next sections, or form highly specific structures to detect and interact with small molecules or larger proteins with picomolar affinity (Zimmermann et al., 2000). Single-stranded oligonucleotides with around 60 bp that fold into precisely defined structures are named according to their origin. If they occur naturally, they are called riboswitches; otherwise,

they are called aptamers. Both can be used to modulate the function of target proteins (Schiffelers, Blenke & Mastrobattista, 2019).

Therapeutic oligonucleotides that act at the level of mRNA have the advantage that they are less mutagenic because RNA molecules cannot integrate into the genome. Additionally, they exhibit reduced immunogenicity in comparison to DNA. Unmodified RNA can, however, activate specific toll-like receptors and is usually less stable than DNA. Delivering mRNA oligonucleotides directly to the cytosol can lead to the expression of the desired protein and is usually faster than delivering DNA molecules because mRNA can be translated directly into proteins (Yamamoto et al., 2009).

1.4.1.3. Mode of action

RNA oligonucleotides can serve additional purposes when successfully delivered to the cytosol. Short dsRNA molecules designed to imitate the cleavage products of the enzyme Dicer can modulate gene expression on the RNA level. Dicer is part of the RNAse III family and processes cytosolic dsRNA into 19-25 bp long fragments with a two base pair overhang at the 5' end. Exogenous short dsRNA molecules are called short interfering RNA (siRNA), while endogenous short dsRNAs are called microRNA (miRNA). miRNAs are transcribed from non-coding parts of the genome to modulate gene expression. Both RNAs are incorporated into the RNA induced silencing complex (RISC) and enable the silencing of the target mRNA complementary to its sequence with the associated catalytic argonaute component (Fire et al., 1998; Aagaard & Rossi, 2007). Splice switching oligonucleotides are another class of effective RNA oligomers for gene therapy. They exert their effect by sterically blocking splicing sites of the pre-mRNA, altering the sequence of the final product in the process. (Havens & Hastings, 2016; Kuhn et al., 2019) Therefore, delivering RNA oligonucleotides to target cells is an elegant way to influence expression patterns transiently.

There is no shortage of interesting molecules to choose from in order to influence target cells. Delivery, however, is still the major bottleneck to efficient therapies (Ibraheem, Elaissari & Fessi, 2014). Several approaches to trafficking the described payloads have been developed over the last years. Most approaches employ nanosized structures or materials to deliver their cargo safely to target cells (Allen & Cullis, 2013; Dong, Siegwart & Anderson, 2019). Encapsulating the payload does not only enable the design of favorable pharmacokinetic profiles but also offers protection of the payload (Allen, 2004). Especially oligonucleotides suffer from low stability *in vivo*, as discussed above. Endogenous nucleases, for example, degrade pDNA in around 10 minutes (Kawabata, Takakura & Hashida, 1995).

1.4.2. Classification

Non-viral vectors can broadly be divided into three groups: inorganic vectors, lipid-based vectors, and polymeric vectors (Bobo et al., 2016). Naturally, boundaries between these categories are fluent. Polymers, like polyethylene glycol (PEG), are used to shield all sorts of particles from interactions with blood and immune system components. At the same time, some vectors are assembled equally from organic and inorganic materials, for example, metal organic frameworks (MOFs) (Horcajada et al., 2010; Furukawa et al., 2013; Zhu & Xu, 2014). The main representatives of nanoparticles based on inorganic materials are calcium phosphate nanoparticles (CPN), carbon nanotubes (CNT), layered double hydroxides (LDH), mesoporous silica nanoparticles (MSN), and superparamagnetic iron oxide nanoparticles (SPION). Detailed descriptions and recent therapeutic applications can be found in the reviews from Sokolova et al. and Naz et al. (Sokolova & Epple, 2008; Naz et al., 2019).

Lipid nanoparticles were the first nanomedicine that made the translation into the clinics as delivery systems. Currently, most advanced delivery systems are based on lipid nanoparticles (Allen & Cullis, 2013). These drug delivery systems build on the experience of five decades of research. They are usually composed of various components, especially cationic lipids, anionic lipids, and helper lipids (for example, cholesterol) (Zabner, 1997). Conjugated lipids like PEG-lipids, polymer-lipids, and targeting-lipids can be added to increase performance (Li & Szoka, 2007; Kulkarni, Cullis & van der Meel, 2018).

Polymers for drug delivery are a group of materials that are used either in combination with inorganic or lipid nanoparticles or on their own (Pack et al., 2005). Nanoparticles made from polymers usually feature a polycationic backbone for oligonucleotide binding. The cations in the backbone usually carry positive charges at physiological pH, for example, primary, secondary, tertiary, or quaternary amines or amidines. Integrating additional structures to optimize the performance of the nanoparticle, biological compatibility, and pharmacokinetic profile is easily possible (Pack et al., 2005; Lächelt & Wagner, 2015). The final polymers can be categorized according to their structure in linear, branched, dendritic, or T-shaped. Utilization of solid phase supported synthesis, initially developed by R. B. Merrifield (Merrifield, 1963), has further increased the control over the placement of different functionalities to the degree that changed the material´s character from a random, polymeric structure to a defined, oligomeric structure (Schaffert et al., 2011). All advances combined enable the production of defined oligomers that feature various structures to deliver their payload to target cells efficiently.

1.4.3. Approved non-viral vectors

Several non-viral vectors from different materials have already been granted marketing authorization.

The FDA granted marketing authorization to the first gene therapy utilizing non-viral vectors in August 1998 (Roehr, 1998). One year later, the EMA followed suit (EMA, 1999). Vitravene® (fomivirsen) is a phosphorothioate oligonucleotide with 21 nucleotides for the treatment of cytomegalovirus retinitis in immunodeficient patients, especially patients affected from AIDS. It is injected into the human eye and silences the mRNA of the CMV coding for the major immediate-early region (IE2), effectively slowing down or even halting the progression of the infection (de Smet, Meenken & van den Horn, 1999). Unfortunately, approval of Vitravene® coincided with the development of the highly active antiretroviral therapy (HAART) for patients, substantially lowering the cases of CMV retinitis. Therefore, Novartis returned the marketing authorization in 2002 (EU) and 2006 (USA) (Stein & Castanotto, 2017).

In 2004, Macugen® (pegaptanib) was approved (EMA, 2006). It is a pegylated 27 nucleotide RNA aptamer developed by the systematic evolution of ligands by exponential enrichment (SELEX) process targeting vascular endothelial growth factor (VEGF) (Ruckman et al., 1998). It is used to prevent the pathological neo-angiogenesis in ocular vascular diseases, especially wet, age-related macular degeneration (AMD). Pegaptanib binds VEGF with nano- to picomolar affinity and suppresses its interaction with the receptor tyrosine kinases VEGFR1 and VEGFR2, decreasing its pro-angiogenic effects. (Ng et al., 2006). In 2018, Pfizer returned its approval for Macugen® in the European Union.

Non-viral gene vectors were also affected by the safety concerns surrounding the above discussed SCID-X1 trials. Therefore, it took nine years until the next oligonucleotide entered the market. The FDA approved Kynamro® (mipomersen) in 2013, but the EMA came to a contrary conclusion and denied market access to the EU (Hair, Cameron & McKeage, 2013). The drug is an antisense oligonucleotide against the coding region of the mRNA of the apolipoprotein B-100 (Crooke et al., 2005). It is injected subcutaneously in patients suffering from homozygous familial hypercholesterolemia (HoFH) and delivered to hepatocytes. Complementary bound mRNA is subsequently degraded by RNAse H, leading to a 25 – 37% reduction in LDL cholesterol when given once a week in 200 mg doses to patients already receiving lipid-lowering medications (Hair, Cameron & McKeage, 2013).

Duchenne muscular dystrophy (DMD) is a fatal X-linked recessive neuromuscular disorder caused by mutations in the gene coding for dystrophin. Affected children, almost exclusively boys, lose muscle functions rapidly, and death usually occurs during their second decade. Currently, no curative treatment is available, and affected children are treated palliatively only (Manzur, Kinali & Muntoni, 2008). Therefore, the approval of Exondys 51® (eteplirsen) by the FDA in 2016 was highly anticipated (FDA, 2016a). The decision of the FDA, however, was highly controversial due to the limited evidence supplied by Sarepta Therapeutics to prove the efficacy of Exondys 51®. The drug is a phosphorodiamidate morpholino oligomer (PMO) and belongs to the class of antisense oligomers. It is uncharged and binds to exon 51 from the pre-mRNA coding for dystrophin and causes it to be skipped during splicing. By skipping exon 51, a shortened but functional version of dystrophin is produced, and any mutation (for example, a premature stop codon) or deletion present on exon 51 is removed. This elegant approach, however, faces several limitations. First, Exondys 51® is only effective if a mutation or deletion in exon 51 is the cause for the disease. However, only ~ 14% of all patients suffering from DMD have this mutation. Second, Exondys 51® needs to enter muscle cells to be useful, but it is preferentially distributed to the kidney and liver. It was shown that muscle cells produce only 1% of functional dystrophin, which is deemed to be insufficient to elicit clinically relevant effects. Nevertheless, it is the only potentially curative treatment on the market so far, and some patients seem to profit from it (Lim, Maruyama & Yokota, 2017).

In 2016, a completely different drug to all other approved non-viral gene therapies discussed so far was granted marketing authorization by the FDA (FDA, 2016b). Defitelio® (defibrotide) is a mixture of phosphodiesters derived from intestinal pig mucosa. It consists of ~ 90% single-stranded oligonucleotides and ~ 10% double-stranded oligonucleotides (9-80 bp; mean 50 bp; average molecular mass 16.5 ± 2.5 kDa) (Pescador et al., 2013). Since phosphodiester nucleotides are negatively charged, defibrotide is comparable to heparin. It does not act on the genomic machinery inside a cell but reduces endothelial cell activation of endogenous effectors. It is approved to treat patients who develop veno-occlusive disease (VOD) after undergoing hematopoietic stem cell transplantation (HSCT).

The end of 2016 brought another treatment for a fatal muscle disease to the patients. In December, Spinraza® (nusinersen), an antisense oligonucleotide, was granted marketing authorization by the FDA to treat spinal muscular atrophy (SMA) (FDA, 2016c). The disease is marked by low levels of survival motor neuron (SMN) protein due to deletions or mutations in the SMN1 gene. Fortunately, humans possess a second copy of the SMN gene.

SMN2, however, produces an unstable and only partially functional version of the gene, but it can be targeted by Spinraza® to splice into the fully functional SMN mRNA 117 correctly. Treatment with Spinraza® resulted in prolonged survival, and most children reached motor milestones while side effects were comparable to children in the control group. How the drug affects disease progression in the long term, however, remains to be seen.

Transthyretin Amyloidosis is an autosomal dominant hereditary polyneuropathy caused by transthyretin monomers slowly aggregating into fibrils, damaging neurons in the process. Transthyretin (TTR), the transport protein for thyroxine and retinol, is a homotetramer that is expressed mainly in the liver but also in the retinal pigment epithelial cells and the choroid plexus epithelium. Usually, monomers form stable tetramers, except if mutations occur in one of the copies of the gene, which renders transthyretin thermodynamically unstable and promotes the buildup of fibrils from free monomers. Therapeutic options for treating this disease are liver transplantation and tetramer stabilization with tafamidis and diflunisal. Both approaches showed clinical efficacy by slowing down the progression of the disease (Buxbaum, 2018). In 2018 two new drugs extended the therapeutic options for treating hereditary transthyretin amyloidosis (hATTR): Onpattro® (patisiran) (Hoy, 2018) and Tegsedi® (inotersen) (Keam, 2018). The FDA and the EMA granted both drugs marked access. Tegsedi® is a naked single-strand oligonucleotide targeted to TTR mRNA. When binding to the mRNA transcript inside the nucleus, RNAse H induced cleavage reduces available mRNAs significantly. Onpattro® is the first approved drug containing siRNA. Integration of siRNA molecules into the RISC complex inside the cytosol, as discussed above, mediates the degradation of TTR mRNA molecules, effectively decreasing translation into transthyretin monomers. Onpattro® is marketed as suspension of lipid nanoparticles containing siRNA. Both drugs are preferentially taken up by the liver due to their formulation (Niemietz, Chandhok & Schmidt, 2015). Both therapeutic oligonucleotides significantly slowed disease progression in clinical trials.

The latest antisense oligonucleotide therapy approved in May 2019 by the EMA is Waylivra® (volanesorsen) (EMA, 2019b). It is indicated for the adjunct therapy of patients suffering from genetically confirmed familial chylomicronemia syndrome (FCS). Weekly subcutaneous injections decrease apoCIII mRNA in hepatocytes and subsequently reduce plasma levels of triglycerides. These results suggest a decreased risk of developing pancreatitis due to elevated serum triglyceride levels (Paik & Duggan, 2019).

1.5. Designing nanomedicines

1.5.1. Non-viral vectors for tumor therapy

So far, no non-viral vector for tumor therapy has been approved. On the one hand, it is surprising, since research concerning tumor therapy is a diverse field with many disciplines trying to overcome its many hurdles. This area is also well funded, and 65% of all clinical trials in 2017 have been targeting tumor therapy. However, most of them used viral vectors, while only 21% of all trials employed non-viral vectors (Ginn et al., 2018). These numbers foster high hopes for gene therapy and nanomedicine in particular.

On the other hand, the absence of non-viral tumor therapies can be explained by the difficulty of targeting cancerous cells selectively. Cancer is the umbrella term for a vast range of different tumors that can derive from every possibly human cell type, essentially making each occurrence of a tumor in a patient his or her individual chronic disease. The individuality of the disease mandates the application of treatments tailored to the patient, explaining the success story of employing the immune system of the patient (CAR T-cells, see above). Targeting tumor cells without the aid of the immune system, however, is still a significant bottleneck. Since tumor cells derive from human cells, it is often impossible to target cancerous cells selectively. Indeed, it would be advantageous if patients could "swallow the surgeon" (Feynman, 1959) to cure the disease. Unfortunately, this is still a long way off, and payload delivery to target cells specifically is still the most prominent problem in nanomedicine.

Advances in solving this problem are incremental but steady. With increased knowledge of the human body and molecular pathways influencing tumor proliferation, comes the means to assert influence on its outcome as well. Because of the heterogeneous nature of cancer, each patient needs its own, personal approach. Therefore, the development of delivery vehicles with equally sophisticated components tailored to the individual tumor of the patient is inevitable. As described above, there have been significant advances in the development of liposomal, poly-/oligomeric, and inorganic materials to efficiently deliver its payload. In our lab, we focus on the development of oligomeric, cationic materials. The following sections will discuss the process of nucleic acid complexation with polycations, the quality of educts, and the influence of formulation parameters.

1.5.2. Nucleic acid complexation

The crucial step in creating nanoparticles from DNA or RNA is the condensation of negatively charged nucleotides with cationic materials. Electrostatic repulsion from phosphates in the backbone of the oligonucleotide will prevent efficient packaging if less than ~ 90% are

neutralized (Wilson & Bloomfield, 1979). Condensation of nucleotides in aqueous solutions is a rapid and spontaneous process that is readily reversed by changes in the electrolyte or cationic ligand concentrations (Bloomfield, 1997). Various energetic factors influencing the condensation process have been identified. Positive free energy from nucleotide bending, entropy loss due to mixing, configurational changes, and an increase in coulomb energy due to an increase of charge density oppose oligonucleotide complexation (He, Arscott & Bloomfield, 2000). The counterion release from both phosphates and cations, however, results in a high entropy gain making the whole process thermodynamically favorable (Ou & Muthukumar, 2006).

The mere fact of thermodynamic favorability, however, grants neither insights about the time scale of the formation process nor the characteristics of the resulting particles. Polyelectrolyte complex formation is kinetically controlled, and charge neutralization occurs in around 50 ms (Braun et al., 2005). These physicochemical properties are the reason for the critical influence of solvent composition, mixing speeds, and – most prominently – chemical properties and concentration of the educts on the characteristics of the resulting particles (Kabanov & Kabanov, 1995). Since the formation of polyelectrolyte complexes is due to charge interactions, changes in ion concentration or ion type usually alter the stability and particle characteristics of the resulting formulation (Kabanov & Kabanov, 1995). Mixing speeds are relevant to the resulting formulation in two regards. First, slow addition of one reactant to another in solution – e.g., when added dropwise – changes the relative concentrations of both reactants to each other with each drop leading to a solution of widely different particles. Second, control over particle characteristics is most substantial when equilibration of reactants in solution is in the range of 50 ms (Braun et al., 2005). Altering particle formulation processes, however, cannot optimize particle properties that are dependent on the chemical structure of the educts. Therefore, considerable effort has gone into optimizing polycationic structures in order to improve particle characteristics and transfection efficiency *in vitro* and *in vivo*.

1.5.3. Polycations

1.5.3.1. Polymers

The first polycations that were found to improve DNA transfection were diethylaminoethyl (DEAE) dextran (McCutchan & Pagano, 1968), spermin, polylysine, polyarginine, and polyornithine polymers (Farber, Melnick & Butel, 1975). They were able to condense nucleic acids in particles called polyplexes (Felgner et al., 1997). However, it was soon discovered that these first-generation polyplexes failed to deliver most of their payload to the cytosol and the

nucleus because they were prone to accumulate in endo-/lysosomes. This hurdle could be overcome with endosomolytic agents like chloroquine, but these chemicals only have a small therapeutic window and did not solve the structural problem of these polycations (Erbacher et al., 1996). Inspired by the mode of action of chloroquine, J-P. Behr and colleagues finally succeeded in developing a new chemical structure with endosomolytic properties: polyethylenimine (PEI) (Boussif et al., 1995). PEI is synthesized by hydrolysis of poly(2-ethyl-2-oxazoline), yielding a mixture of linear polyethylenimine molecules with varying molecular weights (Tanaka et al., 1983; Hall et al., 2017). It is considered to be the gold standard for DNA transfection. PEI is a polymer built from secondary amines separated by an ethane spacer. These secondary amines serve two purposes: first, in their protonated form, they facilitate the condensation of nucleic acids. At pH 7.4, around $1/6^{th}$ of all amines are protonated (Boletta et al., 1997), leaving the majority of amines to their second task: buffering the change in the endo-/lysosomal pH. Chemical structures with this ability were termed proton sponges by J P. Beer because of their assumed ability to buffer the influx of acidic protons into the lysosome, leading to a subsequent influx of counterions and water, which eventually ruptures the swollen vesicle (Behr, 1997). This theory caused heated debates in the community (Akinc et al., 2005; Benjaminsen et al., 2013). However, it was widely accepted that structural motives featuring amines with a pKa around 6 enhance transfection efficiency, probably due to a combination of increased osmotic pressure and membrane interactions (Lächelt & Wagner, 2015).

The deepened understanding of the various steps involved in trafficking payloads into the cytosol paired with the desire to create delivery vehicles tailored to tackle specific problems led to the development of many new chemical structures based on the ethylenimine motif. PEI, for example, was optimized by altering the average molecular weight (Godbey, Wu & Mikos, 1999) of the resulting polymer product and by changing its degree of branching from (hyper-) branched PEI (BPEI) to completely linear PEI (LPEI) (Itaka et al., 2004; Neu, Fischer & Kissel, 2005; Seib, Jones & Duncan, 2007). Other work focused on the development of dendritic polymers from the polyamidoamine (PAMAM) motif (Haensler & Szoka, 1993). Unfortunately, a common disadvantage of all previously mentioned cationic polymers was their safety profile (Hall et al., 2017). Toxicity on the cellular level *in vitro* or complement activation (Plank et al., 1996) *in vivo* were serious hurdles hampering the development of clinically relevant formulations. Some of these problems were ameliorated, for example, by optimizing the degree of polymerization or molecular weight (Hall et al., 2017). Despite all improvements in polymeric materials and successful clinical trials (Scaiewicz et al., 2010), the fundamental flaw of the polymerization process remains the lack of control over the final product. The exact

placement of structural motifs is as difficult to control as the complete length and, therefore, the molecular weight of the final product.

Consequently, limited batch-to-batch reproducibility inevitably leads to variable particle properties, which in turn complicate the establishment of precise structure-function relationships, the development of improved carrier systems, and the translation of delivery platforms into the clinics. Hence, the quality of the polymer is crucial to the development of successful nucleic acid delivery systems. I will discuss ways to assure sufficiently high quality in the next section.

1.5.3.2. Sequence defined oligomers

Partly adapted from Loy et al. (Loy et al., 2019).

Poorly defined educts complicate finding structure – activity relationships. Size and shape, for example, play a significant role in deciding the uptake route into cells (Rejman et al., 2004; Sykes et al., 2014). These parameters, however, are heavily influenced by assembly conditions and educt quality. Moreover, the final formulation hast to cross several barriers before it releases its payload. Thus, for each hurdle, additional structural elements must be incorporated into the particle, but each additional component included in the formulation further complicates the preparation of defined nanoparticles.

Solid-phase supported synthesis (SPSS) (Merrifield, 1963) of sequence defined oligo(ethanamino)amides (Schaffert et al., 2011) has the potential to integrate any functional element at any place in the structure of the oligomers. The crucial parameter is the biological performance of polyplexes assembled from these oligomers. To this end, various structural motifs (Schaffert, Badgujar & Wagner, 2011), as well as topologies (e.g., T-, I, and U- shapes) (Schaffert et al., 2011; Scholz, Kos & Wagner, 2014) have been investigated. The exact placement of targeting and cell-penetrating moieties in small siRNA containing polyplexes was also demonstrated (Dohmen et al., 2012a).

The continuous investigation of the function of structural motifs and the correlation to their place in polycationic carriers led to the identification of key units in the structure of the oligomers: polycationic succinyl tetraethylene pentamine (Stp) units are used for complexing nucleic acids; tyrosines, and fatty acids are added for stabilizing the resulting nanoparticles (Fröhlich et al., 2012; Troiber et al., 2013a). Usually, additional chemical moieties, for example, for shielding the nanoparticles and targeting specific receptors (Klein et al., 2018), are integrated into the chemical sequence of the oligomer to increase biological performance.

These additional units, albeit required for efficient nucleic acid delivery, can alter polyplex formation processes (Freund et al., 2018).

However, it is also evident that sophisticated structures alone do not suffice to produce efficient delivery vehicles. The manufacturing process itself is as important as the single components themselves to the success of nanomedicine.

1.5.4. Production methods

1.5.4.1. Nanoparticles

Generally, there are two distinct approaches to standardized nanoparticle production. The top-down process, on the one side, produces particles by breaking down larger materials, for example, by using sonication (Jang & Oh, 2004), extrusion (Hu et al., 2011), high-pressure homogenization (Sun et al., 2011), hydrolysis (Chen et al., 2013), or the PRINT method developed by Rolland et al. (Rolland et al., 2005). The advantage of this approach is high control over size and shape, although particle purification can be challenging, and particles usually consist of a single component only. The bottom-up process, on the other side, produces particles from smaller building units or starting materials (e.g., mono-, oligo- or polymers), which assemble into larger objects (Chan & Kwok, 2011). Here, particle size and shape are loosely predetermined by the design of the educts, while formulation parameters control their exact properties during the assembly process. In the case of ionic polyplexes, the self-assembly process is based on electrostatic interaction between oppositely charged materials (for details cf. 1.5.2 Nucleic acid complexation). On the downside, control over size and shape is challenging, and batch-to-batch variability may be large (Valencia et al., 2012).

As discussed above, nanoparticle formation from nucleic acids and polycations happens spontaneously upon contact but requires intensive mixing in order to produce nanoparticles with an acceptable diameter.

1.5.4.2. Polyplexes

Many different production methods for polyplexes from nucleic acids and polycations have been developed since the first polyplex formulation. Polyplexes (as well as lipoplexes) are often prepared batch-wise by mixing polycations with nucleic acids either by vigorous pipetting or shaking. Although this method is convenient and fast, a lack of control over the kinetically controlled particle formation process can lead to significant differences in particle characteristics between batches, as discussed above. These circumstances hampered efficient carrier development (Anchordoquy & Koe, 2000). Therefore, researchers aimed to increase

control by automating various steps of the formulation process. Controlling the feeding rates of the educts to a T-junction to produce lipoplexes (Zelphati et al., 1998) or polyplexes (Kasper et al., 2011) improved particle properties measurably. Another approach was the utilization of coaxial electrohydrodynamic spraying (Wu et al., 2010) to achieve increased control over the formulation process of PEI / pDNA polyplexes. This method attempted to control not only the feeding rates but also the mixing process itself by continuously mixing reactants at the tip of a needle and directly separating them in discrete, fine droplets that are sprayed and recombined in a dish. This setup yielded polyplexes with improved transfection properties, as well.

With the advent of microfluidics, the degrees of freedom of a system can be minimized due to the change of dominating forces at the micrometer scale (Whitesides, 2006). At this scale, forces from interfaces greatly surpass inertial forces that dominate the macro scale (Squires & Quake, 2005). A reduced number of degrees of freedom increases control over the system, allowing for greater control over the formulation process itself. Microfluidic approaches (Liu et al., 2017) to the bottom-up production of polyplexes can be broadly divided into droplet- (Seemann et al., 2012) and hydrodynamic focusing- (Lee et al., 2016) based systems. Both methods are suitable since polyplex production is performed in aqueous systems and requires fast reaction times. Emulsion based systems have the advantage of discrete reaction chambers with picolitre volumes, but they are usually unstable and need additional surfactants and oily phases to stabilize droplets (Ho et al., 2011). Laminar flow-based systems have the advantage of producing carriers continuously while mixing of reactants is diffusion-controlled only. Mixing speeds can be manipulated by employing baffle structures (Belliveau et al., 2012), organic solvents (Krzysztoń et al., 2017), or external energy sources (Westerhausen et al., 2016; Schnitzler et al., 2019) to influence the time scale reactants need to reach their counterparts allowing for greater control over particle properties. Previous studies have shown that microfluidic-based assembly improves the physicochemical properties of produced particles (Koh et al., 2009; Belliveau et al., 2012; Grigsby et al., 2013). The unique possibilities from combining sequence defined oligomers with increased control over the formulation process with microfluidics led to the writing of this thesis.

1.6. Aims of the thesis

Feynman and his colleagues provided the groundwork and theoretical background for the advent of nanotechnology and nanomedicine. In theory, it is possible to produce nanoparticles with precision at the atomic level. In practice, we are still far away from this vision.

Nevertheless, there have been a large number of successful clinical trials, and many new therapy options were granted marketing authorization in the last three decades. With the help of viral and non-viral vectors, many hitherto incurable diseases could be treated. The price of those novel treatments, however, was often horrendous. Either because of the six-figure price tag or because of unforeseen incidents caused by the formulation itself.

New nanomedicine formulations must possess certain features to survive the clinical stage and persist in the market. Key properties are well-defined educts and controlled formulation processes that enable the reproducible and reliable formulation of drug products. Therefore, this thesis pursues three aims.

The first aim of the thesis was the development of an automated system to produce multi-component polyplexes in a controlled fashion. To this end, a microfluidic mixer was to be integrated. The designs of the microfluidic mixer were developed by Krzysztoń et al. (Krzysztoń et al., 2017). The channels of the mixer were to be fed by three syringe pumps to control the fluid flow during the experiment. A custom software was to be written in python to control each pump individually and realize sophisticated mixing protocols for up to four components in any channel to increase control over the formulation even further. The software was to be executed on a headless raspberry pi to enable the remote execution of the control program and to miniaturize the complete system. In order to truly allow automated and remote experiments, a fraction collector was to be designed and built to collect the products from the microfluidic setup. The custom software for the fraction collector was to be written in python as well and executed on the same headless raspberry pi.

The second aim of the thesis was the development of multi-component polyplexes and the investigation of structure – function relationships. To this end, core polyplexes were to be assembled from cationic core oligomers (*CO*, id: 991) developed in our lab (Klein et al., 2018), siRNA, and polyethylene glycol (PEG)-ligands with zero to 48 ethylene oxide (EO) repetitions. The PEG-ligands were to be integrated non-covalently into core polyplexes by lipid anchors containing 12 additional EO repetitions. These lipid anchors were to be developed to facilitate the adsorption of PEG-ligands to hydrophobic patches of core particles without the need for covalent bonds between core and ligand oligomers. This system was to be used to investigate the effect of the PEG-ligands on transfection efficiency and to identify the optimal length of the PEG spacer. In order to enable the investigation of structure-function relationships with minimized deviations in product characteristics due to the manufacturing process, the system described in aim one was to be utilized.

The third aim of the thesis was the complete adherence to open science practices during the data collection, data evaluation, writing, and publication process. To this end, my first author publications were to be published under the creative commons attribution license (CC BY 4.0) in open access journals. Therefore, all analyses were to be coded in R to allow the simple reproduction of target figures from the raw data. The raw data for each experiment together with the respective R code were to be published alongside each publication to ensure complete transparency and reproducibility. Additionally, all designs and software source code were to be published under the same CC BY 4.0 copyright license together with the respective publication on GitHub. All unpublished data from this thesis were to be deposited in the same public repositories, as well.

2. Materials and Methods

2.1. Materials

2.1.1. Solvents and reagents

The following tables list the solvents, reagents, materials, and software that I used during the work on my thesis. I always state the source of the materials and I give additional information (e.g., purity, or pH) were applicable.

Table 1: Solvents

Solvent	Abbr.	Purity	Source
Purified water			Ultra Clear® GP UV UF [1]
Acetone		HPLC grade	VWR [3]
Acetonitrile	ACN	HPLC grade	VWR [3]
Dichloromethane	DCM	ACS	Bernd Kraft GmbH [4]
Dimethylformamide	DMF	peptide grade	Iris [2]
Dimethyl sulfoxide	DMSO	For synthesis	Acros Organics [5]
Ethanol	EtOH	Ph. Eur.	VWR [3]
n-Hexane		puriss. p.a.	VWR [3]
Methanol	MeOH	HPLC grade	VWR [3]
Methyl-*tert*-butylether	MTBE	for synthesis	VWR [3]
N-methyl pyrrolidone	NMP	peptide grade	Iris [2]
Piperidine		peptide grade	Iris [2]
Pyridine		puriss. p.a.	Acros Organics [5]

Note: [1] Evoqua Water Technologies GmbH, Günzburg, Germany; [2] Iris Biotech GmbH, Marktredwitz, Germany, [3] VWR International GmbH, Darmstadt, Germany; [4] Duisburg, Germany; [5] Geel, Belgium.

Table 2: Reagents

Reagent	Abbr.	Purity	Source
Acetic anhydride		puriss.	Sigma [6]
Agarose		BioReagent	Sigma [6]
Ammonia solution 25%		Ph. Eur.	Carl Roth [1]
5′-ATP-K_2	ATP	≥ 92%	Sigma[6]
Benzotriazol-1-yl-oxytripyrrolidinophosphonium hexafluorophosphate	PyBOP	≥ 98%	MultiSynthech [12]
Boric acid		≥ 99.5%	Sigma [6]
Bromophenol blue		ACS	Sigma [6]
2-chlorotrityl chloride resin (200–400 mesh, 1% DVB cross-linking)			Iris [2]
5β cholanic acid	CholA	≥ 99%	Sigma [6]
Coenzyme A Li_3	CoA	≥ 93%	Sigma [6]
Dibenzocyclooctyne-PEG4-N-Hydroxysuccinimidyl ester	DBCO	≥ 95%	Sigma [6]
N,N-diisopropylethylamine	DIPEA		Iris [2]
Disodium phosphate	Na_2HPO_4	p.a.	Merck [3]

Reagent	Abbr.	Purity	Source
DL-dithiothreitol	DTT	≥ 98%	Sigma [6]
Ethylenediaminetetraacetic acid-Na_2 ×$2H_2O$	EDTA	≥ 99%	Sigma [6]
Fmoc-Glu-O-2-PhiPr		peptide grade	VWR [8]
Fmoc-L-Glu-(OtBu)-OH		peptide grade	Iris [2]
Fmoc-L-His(Trt)-OH		peptide grade	Iris [2]
Fmoc-L-Lys(Boc)-OH		peptide grade	Iris [2]
Fmoc-L-Lys(Fmoc)-OH		peptide grade	Iris [2]
Fmoc-L-Lys(ivDde)-OH		peptide grade	Iris [2]
Fmoc-L-Lys(N3)-OH		peptide grade	Iris [2]
Fmoc-N-amido-dPEG12-acid		peptide grade	Quanta Biodesign [4]
Fmoc-N-amido-dPEG24-acid		peptide grade	Quanta Biodesign [4]
D(+)glucose monohydrate		DAB	Loewe [5]
2,5-dihydroxybenzoic acid		≥ 99%	Sigma [6]
Glycerol		Ph. Eur.	Carl Roth [1]
Glycylglycine		≥ 99%	Sigma [6]
1-hydroxybenzotriazole hydrate	HOBt	≥ 97%	Sigma [6]
2-hydroxy-5-methoxybenzoic acid		≥ 98%	Sigma [6]
4-(2-hydroxyethyl)-1-Piperazineethanesulfonic acid	HEPES	ultra-pure	Biomol GmbH [9]
Magnesium chloride hexahydrate	$MgCl_2$ × $6H_2O$	p.a.	Merck [3]
Monopotassium phosphate	KH_2PO_4	p.a.	Merck [3]
N10-(tri- fluoroacetyl)pteroic acid		≥ 95%	Clauson-Kass A/S [11]
Potassium chloride	KCl	p.a.	Sigma [6]
Sodium hydroxide, 1M	NaOH	standard solution	Thermo [7]
Sodium hydroxide, pellets	NaOH	puriss.	VWR [8]
Sylgard® 184; Polydimethylsiloxane silicone elastomer base	PDMS		Dow Corning GmbH [10]
Sylgard® 184 curing agent			Dow Corning GmbH [10]
Tri-chloro(1H,1H,2H,2H-perfluorooctyl)silan		≥ 97%	Sigma [6]
Triisopropylsilane	TIS	≥ 98%	Sigma [6]
Tris(hydroxymethyl)-aminomethan	TRIS	≥ 96%	Sigma [6]
Uranyl formate		≥ 99%	VWR [8]

Note: [1] Carl Roth GmbH + Co. KG, Karlsruhe, Germany; [2] Iris Biotech GmbH, Marktredwitz, Germany; [3] Merck KGaA, Darmstadt, Germany; [4] Powell, OH, USA; [6] Sigma-Aldrich Chemie GmbH, Munich, Germany, now part of Merck KGaA, Darmstadt, Germany; [5] Loewe Biochemica GmbH, Sauerlach, Germany; [7] Thermo Fisher Scientific GmbH, Schwerte, Germany; [8] VWR International GmbH, Darmstadt, Germany; [9] Hamburg, Germany; [10] Wiesbaden, Germany; [11] Farum, Denmark;
[12] Witten, Germany.

Table 3: Dyes

Dye	Abbr.	Purity	Source
3-(4,5-dimethylthiazol-2-yl)-2,5-diphenyltetrazolium bromide	MTT	≥ 98%	Carl Roth GmbH + Co. KG [1]
DBCO-PEG4-Atto488		≥ 90%	Jena Bioscience GmbH [2]
Ethidium bromide	EtBr	BioReagent	Sigma [3]
GelRed™			VWR [4]
Ninhydrin		≥ 95%	Sigma [3]

Note: [1] Karlsruhe, Germany; [2] Jena, Germany; [3] Sigma-Aldrich Chemie GmbH, Munich, Germany, now part of Merck KGaA, Darmstadt, Germany; [4] VWR International GmbH, Darmstadt, Germany.

2.1.2. Buffers

Table 4: Buffers

Buffer	pH	Composition
EDTA 0.5 M	8.0	0.55 M Na_2EDTA
HBG, isotonic	7.4	0.20 mM Hepes, 277.5 mM glucose x $1H_2O$
HBS, isotonic	7.4	0.20 mM Hepes, 150 mM NaCl
Hepes, 20 mM	7.4	0.20 mM Hepes
LAR	8.0	20 mM glycylglycine, 1.0 mM $MgCl_2$, 0.1 mM EDTA, 3.29 mM DTT, 0.548 mM ATP, 0.0013 mM coenzyme A
Loading buffer	--	8.21 mM glycerol, 60 mM EDTA, 0.003 bromophenol blue (free acid)
Luciferin	8.0	10 mM luciferin-Na, 29.375 mM glycylglycine
PBS	7.4	16.89 mM NaCl, 2.68 mM KCl, 8.10 mM Na_2HPO_4, 1.47 mM KH_2PO_4
TBE 10x	8.0	1.49 mM TRIS base, 0.89 mM boric acid, 0.02 mM EDTA

2.1.3. Nucleic acids

Table 5: Nucleic acids

Name	Sequence	Source
siGFP	Sense: 5′-AuAucAuGGccGAcAAGcAdTsdT-3′ Antisense: 5′-UGCUUGUCGGCcAUGAuAUdTsdT-3′	Axolabs [1]
siAha1-Cy5	Sense: 5′-(Cy5-NHC6)-GGAuGAAGuGGAGAuuAGudTsdT-3′ Antisense: 5′-ACuAAUCUCcACUUcAUCCdTsdT-3′	Axolabs [1]
siCtrl	Sense: 5′-AuGuAuuGGccuGuAuuAGdTsdT-3′, Antisense: 5′-CuAAuAcAGGCcAAuAcAUdTsdT-3′	Axolabs [1]

Note: [1] Kulmbach, Germany. Small letters: 2′ methoxy; s: phosphorothioate.

2.1.4. Cell culture

Table 6: Materials used in cell culture

Material	Source
96 well plates (TPP 92096)	Faust Lab Science GmbH [2]
Benzylpenicillin sodium, 100x 10k E	Biochrom [1]
Cell culture flasks (TPP90075)	Faust Lab Science GmbH [2]
Collagen A, 0.1% in HCl, 1 mg/ml	Biochrom [1]
Fetal bovine serum, Gibco™	Thermo [6]
Heparin sodium 25k	Ratiopharm [4]
Lysis buffer, 5x	Promega [3]
RPMI 1640 (R2405- 500ML)	Sigma [5]
RPMI 1640, folate free (27016021)	Thermo [6]
Streptomycin sulfate	Biochrom [1]
Trypsin/EDTA in PBS (10x)	Biochrom [1]
VivoGlo™ D-luciferin potassium	Promega [3]

Note: [1] Berlin, Germany; [2] Klettgau, Germany; [3] Mannheim, Germany; [4] Ulm, Germany; [4] Sigma-Aldrich Chemie GmbH, Munich, Germany, now part of Merck KGaA, Darmstadt, Germany; [6] Thermo Fisher Scientific GmbH, Schwerte, Germany.

2.1.5. Equipment for solid-phase supported synthesis

Peptide synthesis was carried out either manually or automatically. The manual synthesis was performed in disposable polypropylene (PP) syringe microreactors (1, 2, 5, or 10 ml volume) with polyethylene filters purchased from Multisyntech (Witten, Germany). Reactants inside syringes were continuously mixed with an overhead shaker. Removing fluids from the syringes was done either with syringe pistons or under low pressure on a laboratory vacuum manifold (Promega Corporation, Madison, WI, USA). The automated synthesis was done on a Biotage Syro Wave synthesizer (Biotage AB, Uppsala, Sweden) with the same microreactors, albeit with polytetrafluoroethylene (PTFE) filters.

2.1.6. Control module

Table 7: Materials control module

Material	Source
Jumper wires, JKMF40, JKFF40 Makerfactory	Conrad [1]
Raspberry Pi model 3B	Almost Anything Ltd. [2]
TECHly USB serial wire (USB 2.0 - RS232)	Conrad [1]
Transcend TS16GUSDHC10E Class 10 microSDHC 16GB	Transcend Information, Inc. [4]
Universal Power Supply RPI-012	Pimoroni Ltd. [3]

Note: [1] Conrad Electronic SE, Klaus-Conrad-Str. 1, 92240 Hirschau, Germany. [2] Thornaby Cecil Avenue, Salisbury, Wiltshire, Great Britain. [3] 2 Manton Street, Sheffield, S2 4BA, United Kingdom.
[4] Flughafenstraße 52b (Airport-Center), 22335 Hamburg, Germany.

Table 8: Software control module

Software	Version
PuTTY	0.71
Python	3.7.3 (Van Rossum & Drake Jr, 2009)
Python package: pySerial	3.4 (Liechti, 2017)
Python package: RPi.GPIO	0.7.0 (Croston, 2019)
Raspbian	Raspbian GNU/Linux 9 (stretch)
WinSCP	5.15.5 (Build 9925)

2.1.7. Feeding module

Table 9: Materials feeding module

Material	Source
Needles: NDL ga27, 90 mm, pst4	Hamilton [1]
Syringe 1 ml 1001 TLL, dinner = 4.61 mm,	Hamilton [1]
Syringe 100 µl 1710 TLL-XL, dinner = 1.46 mm	Hamilton [1]
Syringe 500 µl 1750 TLL-XL, dinner = 3.26 mm	Hamilton [1]
Syringe pump LA-120	Landgraf [2]
Syringe pump LA-122	Landgraf [2]
Syringe pump LA-160	Landgraf [2]

Note: [1] Hamilton Bonaduz AG, Bonaduz, Switzerland. [2] Landgraf Laborsysteme HLL GmbH, Langenhagen, Germany.

2.1.8. Formulation module

Table 10: Equipment: Channels

Material	Source
Biopsy puncher (d_{inner} = 0.96 mm; d_{outer} = 1.26 mm)	World precision instruments [1]
Fluidmedic polyethylene tube (d_{inner} = 0.38 mm; d_{outer} = 1.09 mm, $thickness_{wall}$ = 0.35 mm)	ProLiquid [2]
Object slide 76x26x1.0 mm	Plano GmbH [3]
Object slide 76x50x1.0 mm	Plano GmbH [3]
PP-Luer connector, female	ProLiquid GmbH [2]
PP-Luer connector, male	ProLiquid GmbH [2]
PP-T-Tüllenverbinder 1.6 mm	ProLiquid GmbH [2]
VersilonTM-Inert-Schlauch SE-200, 1.6 × 3.2 mm, $thickness_{wall}$ = 0.8 mm	ProLiquid GmbH [2]

Note: [1] 175 Sarasota Center Blvd. Sarasota, FL 34240, USA; [2] Heiligenbreite 19, 88662 Überlingen, Germany; [3] Ernst-Befort-Straße 12, 35578 Wetzlar, Germany.

2.1.9. Collection module

A prototype of the collection module (fraction collector) was built according to the design published at GitHub (Loy, 2020a). All parts were cut from aluminum, except the parts noted below.

The prototype was built by the workshop of the LMU Munich.

Table 11: Materials collection module

Material	Standard / Source
Brass hexagonal bar 50 X 12	
Clamping plate for toothed belt T5	
Dowel pin Ø4 X 25	
L298N H Dual-Bridge DC stepper motor driver controller	Boboshop [2]
Linear ball bearing Ø10 X Ø17	
M2,5x10 screw DIN 963	
M3x10 screw DIN 84	
M3x10 screw DIN 963	
M3x16 screw DIN 912	
M3x8 grub screw	
M4 screw, knurled head, plastic	
M4 x10 screw, plastic	
M4x16 screw DIN 912	
M4x40 screw DIN 912	
M6 washer	
M6x20 screw DIN 912	
NEMA 14 bipolar stepper 1.8 °, 40 Ncm, 1.5 A, 4.2V 35x35x52 mm	Stepper online [3]
NEMA 14 bipolar stepper, 1.8 °, 13.7 Ncm, 1 A, 12 V, 35x35x40 mm	Phidgets Inc. [4]
PChero mechanical end switch	P&Cstore [5]
Revolt universal switching power supply, 1000 mA, 3-12 V	PEARL [6]
Rod bar, stainless steel, Ø10	
Toothed belt disk 21 T5 14/2	Sahlberg [1]
Toothed belt Type AT5, PU, 10, T5 mm, 480 mm, Optibelt alpha torque	Sahlberg [1]
Toothed belt Type AT5, PU, 10, T5 mm, 545 mm, Optibelt alpha torque	Sahlberg [1]

Note: Source indicated unless Standard Part. [1] Sahlberg GmbH, Friedrich-Schüle-Str. 20, 85622 Feldkirchen, Germany; [2] Boboshop, Zhejiang Quxiu Ecommerce Co., Limited, Quzhou Zhejiang 324000, China; [3] Stepper online, OMC corp. Ltd., #7 Zhongke Road, Jiangning District Nanjing City, 211100 China; [4] Phidgets Inc. nit 1 - 6115 4 St SE Calgary AB T2H 2H9 Canada; [5] P&Cstore Brunhuberstr.116, Wasserburg, Germany. 6 PEARL GmbH Pearl-Straße 1-3 79426 Buggingen.

2.1.10. Software

Table 12: Software

Software	Version
Adobe Illustrator CC	21.0.2
ImageJ	1.52n (Schindelin et al., 2012)
LPKF CAD/CAM software	N.A.
MikroWin (BertholdTech)	5.2 (Driver: V. 1.21)
R	3.5.1 (R Core Team, 2018)
R package: effsize	0.7.4 (Torchiano, 2018)
R package: ggplot2	3.0.0 (Wickham, 2016)
R package: ggsignif	0.4.0 (Ahlmann-Eltze, 2017)
R package: pastecs	1.3.21 (Grosjean & Ibanez, 2018)
R package: RColorBrewer	1.1-2 (Neuwirth, 2014)
R package: readxl	1.1.0 (Wickham & Bryan, 2018)
R package: sjstats	0.17.3 (Lüdecke, 2019)
R package: splitstackshape	1.4.6 (Mahto, 2018)
R package: stringr	1.3.1 (Wickham, 2018)
R package: tidyverse	1.2.1 (Wickham, 2017)
RStudio	1.1.463 (RStudio Team, 2018)
SparkControl (Tekan)	2.1
Zetasizer family software (Malvern)	7.12

2.2. Methods: Controlling nanoparticle formulation: a low-budget prototype for the automation of a microfluidic platform

Adapted from Loy et al. (Loy et al., 2021).

2.2.1. Polyplex preparation

Polyplexes were prepared with a final siRNA concentration of 0.025 mg/ml. A nitrogen to phosphate (N/P) ratio of 12 was used to determine the amount of core oligomer *CO* (991) relative to the amount of siRNA. The N/P ratio relates the number of positive charges from the primary and secondary amines in the backbone of the oligomer to the number of negative charges from the phosphates in the backbone of the siRNA. The manual method of polyplex preparation was done with pipettes and rapid mixing in a batch wise process. The solvent—if not noted differently—was HEPES buffer pH 7.4 with 5% glucose (HBG). This buffer was used because it does not rely on salts to be isotonic, since polyplex formation relies on charge interactions that could be hampered by ions.

Manual polyplex preparation: *CO* solution (0.504 mg/ml) was added quickly to a siRNA solution (0.05 mg/ml) of equal volume and mixed by rapid pipetting, achieving a final siRNA concentration of 0.025 mg/ml. Subsequently, the formulation was incubated for 45 min. Concentrations and volumes for mixing polyplexes from unequal volumes were adjusted accordingly: 5.8 µl of *CO* at 3.023 mg/ml, or 64.2 µl of *CO* at 0.275 mg/ml. 64.2 µl of siRNA at 0.027 mg/ml, or 5.8 µl of siRNA at 0.300 mg/ml.

For the manual formulation of three component polyplexes, equal volumes (27.7 µl) of *CO* solution (0.637 mg/ml) and siRNA solution (0.063 mg/ml) were used. The amount of *LPO* (1203) and *LPOE* (1223) was set to 20 mol % relative to *CO*. Concentrations were set to 0.207 mg/ml *LPO*, or 0.224 mg/ml *LPOE*; volumes were 14.6 µl. Solutions were mixed sequentially by rapid pipetting. When siRNA was used in the first step, a ten-minute break was taken after the two components were mixed to allow the polyplex to stabilize. After the addition of the third component, the formulation was incubated for 45 min before DLS was measured.

Automated polyplex preparation: The formulation module with the double meander channel (DMC) was used without any additional surface treatment (**Figure 1B**). Before each usage, the channel was washed and primed with the same solvents that were used to produce the polyplexes. Details about the washing/priming process can be found in the Appendix (6.3.4 Module: setup.py). siRNA in HBG (0.033 mg/ml) was loaded into S4 (FR = 900 µl/h) and *CO* (3.025 mg/ml) in HBG or HBG with 50% acetone to retard siRNA compaction was loaded into

S3 (FR = 100 µl/h). *LPO* or *LPOE* in HBG with 50% acetone to facilitate solvent exchange were loaded into S2. The flow rate of each syringe S2 was 50 µl/h at a total flow rate of 1,100 µl/h, resulting in a flow rate ratio of lipid anchor oligomer to core polyplex of 1:11. The final product was diluted with HBG to 0.025 mg siRNA/ml.

Stability of these formulations has been investigated previously. Troiber et al. have found particles assembled from the same class of oligomers by rapid pipetting to be stable over three weeks (Troiber et al., 2013b). In section 2.3.5.2 Stability of the core formulation over time, I have investigated the changes in size, PDI, and zeta potential of our core formulation (siRNA and *CO*) over 90 min. The core formulation was assembled in the single meander channel (SMC). I saw no changes in size and PDI. However, changes in the zeta potential of the particles up to the 40 min mark were the reason why formulations were always used after 45 min incubation.

2.2.2. DLS measurements

Please refer to section 2.3.5.1 DLS measurements. Additional solvents used are listed in **Table 13**.

Table 13: Additional solvents used for DLS measurements.

Solvent	Dispersant RI	Viscosity [cP]
HBG (4.2% [V/V] acetone)	1.340	1.119
HBG (8.3% [V/V] acetone)	1.342	1.188

Note: Refractive indices (RI) and viscosities in centipoise (cP)

2.2.3. Standardization of the System

The following steps were taken to ensure standardization of the system.

1. Microfluidic channels were always prepared from the same silica wafer template.
2. Once the optimal formulation conditions for a target formulation were established, the respective mixing program was stored on the raspberry pi.
3. Each formulation produced with this system is measured by DLS.
4. Changes made to the system are validated with a standard formulation.

2.2.4. Data analysis

Data were analyzed with R (R Core Team, 2018) and RStudio (RStudio Team, 2018). I always report means with 95% confidence intervals. R code and raw data are made available on figshare (Loy, 2020b): DOI: 10.6084/m9.figshare.13285577.

2.3. Methods: A microfluidic approach for sequential assembly of siRNA polyplexes with a defined structure-activity relationship

Adapted from Loy et al. (Loy et al., 2019).

2.3.1. Oligomer synthesis

All oligomers have been synthesized by solid-phase supported synthesis (SPSS). The synthesis of the core oligomers *CO* (id: 991) and *CON* (id: 1106) has been described in detail by Klein et al. (Klein et al., 2016, 2018), and their analytical data can be found there. The synthesis of DBCO-discrete PEG(dPEG)-folic acid oligomers (termed "PEG-ligands") has also been reported in detail by Klein et al. (Klein et al., 2018), however only for PEG-ligands with PEG24 (id: 1139) or PEG48 (id: 1140). Here, PEG-ligands without PEG (PEG0, id: 1323), with STOTDA (N″-succinyl-4,7,10-trioxa- 1,13-tridecanediamine, named "PEG3" in this thesis, id: 1324) and PEG12 (id: 1325) were synthesized analogous to the PEG-ligands with longer PEG chains. Basically, Fmoc-Glu-O-2-PhiPr was coupled to the α-amine of a Lys(ivDde)-loaded resin followed by N10-(trifluoroacetyl)pteroic acid to produce functional folic acid. The trifluoroacetyl group was deprotected with 25% aqueous ammonia solution: DMF = 1:1. After standard Dde deprotection (two vol % hydrazine in DMF), the ε-amine of the lysine was modified with the designated dPEG chain followed by a DBCO-acid. For PEG0, DBCO-acid is directly coupled to the ε-amine of the lysine. For PEG3, the succinic acid from STOTDA is coupled to the ε-amine of lysine and the DBCO-acid to the terminal amine from STOTDA after Fmoc deprotection. Special care needs to be taken when cleaving the final product from the resin, since DBCO is sensitive to high concentrations of TFA and can be converted into unreactive side-products (Wang et al., 2014b). Therefore, a cleavage cocktail with only 5% TFA was used (DCM:TFA:TIS = 92.2:5:2.5). Cleavage duration was 60 min. The synthesis and analysis of the lipid anchor oligomers *LA* (id: 1203) and *LAE* (id: 1223) is described in detail in the following paragraphs.

2.3.1.1. Resin Loading

The 2-chlorotrityl chloride resin was loaded as described before (Schaffert, Badgujar & Wagner, 2011). In brief, 0.5 g resin (1.56 mmol/g) was swollen in dry dichloromethane (DCM) for 30 min. Meanwhile, 0.45 mmol Fmoc-L-azidolysine was dissolved in 3.5 ml (1:2.33) dimethylformamide (DMF) and DCM with the addition of 1.35 mmol diisopropylethylamine (DIPEA). After removing the dry DCM from the now swollen resin, the solution containing the amino acid was added, and everything was agitated for 1 h. Since the free attachment points on the resin are in threefold excess over the amino acid, the unreacted 2-chlorotrityl units needed

to be capped with methanol (MeOH). To this end, the amino acid solution was removed and replaced by a 1:1.75 mixture DCM and MeOH with 2.74 mmol DIPEA for at least 30 min. Afterward, the resin was washed with 3x1 ml DMF, and 3x1 ml DCM before an aliquot of 70-100 mg resin was taken and dried inside an exsiccator for loading determination. Roughly 7 mg of dried resin was weighed into each of three 1.5 ml tubes, agitated for 75 min with 1 ml 20% piperidine in DMF at room temperature (RT), and diluted 1:40 with DMF. The absorption at 301 nm was measured against a DMF blank, and an extinction coefficient of 7800 was used to determine the concentration of free fmoc in solution and thereby the amount of bound amino acid per g resin in mmol/g. The fmoc protected amino acid on the main resin batch was deprotected by agitating it 4x10 min with 20% piperidine in DMF. Complete deprotection was validated by performing a Kaiser test after the resin had been washed with 3x1 ml DMF and 3x1 ml DCM. For the Kaiser test, two drops of each solution (5% ninhydrin in ethanol (w/v), 80% phenol in ethanol (w/v), 2 ml 0.001 M KCN in 98 ml pyridine) were added to a few resin beads and heated to 100 °C for 1 – 3 min. If free amines are present on the resin, the solution will turn blue. Afterward, the remaining resin was dried in an exsiccator and stored at 7 °C. Alternatively, it was directly used for the intended oligomer synthesis.

Usually, the first amino acid is loaded up to a concentration of 0.25 mmol/g resin to enable fast and near quantitative conversion of reactants by allowing the usage of a fourfold excess of target amino acid. For the synthesis of the lipid anchor oligomers here, the ratio between the concentration of resin and Fmoc-amino-PEG12-*CO*OH was almost reversed in order to save expensive PEG reagents. Specifically, a higher resin loading was chosen (~ 0.5 mmol/g) and reacted with 120 µmol amino-PEG12-*CO*OH for 12 h to achieve a final loading of resin-azidolysine-PEG12-amino-Fmoc of 0.25 mmol/g resin. This approach leaves some unreacted amines on the resin, which were inactivated with acetic anhydride. In detail, the resin with an initial loading of 0.5 mmol/g was agitated for 1 h with 2.5 mmol acetic anhydride and 5.0 mmol DIPEA in DCM. After a washing step with 3x DMF and 3x DCM, a Kaiser test confirmed the successful coupling and capping. The oligomer was deprotected as described above, and synthesis was continued as described in the next paragraph.

2.3.1.2. Lipid Anchor Oligomer Synthesis

Oligomer synthesis is carried out with a pre-loaded resin (cf. 2.2.1.1. Resin Loading) and repeated cycles of coupling and deprotection steps. The resin loaded with the first amino acid (L-azidolysine) and amino-dPEG12 is swollen in DCM for 30 min. The oligomer chain elongation consists of two crucial steps for each additional amino acid. In the first step,

4 equivalents (eq, relative to mol of free amines on the resin) of the desired amino acid is dissolved in 1 ml DCM with 8 eq. DIPEA, while the activation agents PyBOP (4 eq) and HOBt (4 eq) are dissolved in 1 ml DMF. Both solutions are introduced into a syringe microreactor containing the resin, and the mixture is agitated for 4 h. Afterward, the reaction mixture is discarded, and the resin is washed three times with DMF and three times with DCM. A Kaiser-test is performed (cf. 2.2.1.1. Resin Loading) to validate the success of the coupling step. If the test is positive, i.e., free amines are still present on the resin, the previous coupling step will be repeated. If the test is negative, the deprotection of the current terminal amino acid will be done. To this end, 1 ml 20% piperidine in DMF is added to the resin, incubated for 10 min and the solvent is discarded. This step is repeated four times. Afterward, the resin is washed with DMF and DCM, three times each. A consecutive Kaiser test must be positive to proceed with coupling the next amino acid.

2.3.1.3. Cleavage Conditions

To separate the lipid anchor oligomers from the resin, a cleavage mixture of 95:2.5:2.5 TFA:TIS:H_2O (TFA: trifluoroacetic acid, TIS: triisopropylsilane) was used. The dried resin was incubated and agitated with 1.5 ml cleavage mixture for 90 min. Afterward, the solution was added dropwise to 50 ml of a solution of 75:25 n-hexane:MTBE (tert-butylmethylether) cooled to -80 °C to precipitate the crude oligomer while the scavengers and protecting groups remain dissolved. The mixture was centrifuged, the solvent was decanted, and the precipitate was dried under nitrogen flow.

2.3.2. Oligomer purification

The crude product was dissolved in 2 ml 50% acetone in purified water and purified by size exclusion chromatography with an ÄKTA system (GE Healthcare Bio-Sciences AB, Uppsala, Sweden) and a Sephadex G10 (Sigma) column using a mixture of 7:3 acetonitrile:H_2O with 10 mM HCl as mobile phase. The fractions of the first peak exhibiting 214 nm absorbance were collected, combined and lyophilized. Mass spectrometry confirmed the identity of the oligomers.

2.3.3. Analytics

Lyophilized oligomers were dissolved in purified water with 50% acetone (5 mg/ml). Sample preparation was done the following way: first, 1 µl matrix solution (Super-DHB: 2,5-dihydroxybenzoic acid and 2-hydroxy-5-methoxybenzoic acid in purified water with 50% acetonitrile and 0.1% (v/v) TFA) was spotted on an MTP AnchorChip (Bruker Daltonics,

Bremen, Germany) and allowed to crystallize. Second, 1 µl sample solution was added to the spot with the crystallized matrix solution. Samples were analyzed using an Autoflex II mass spectrometer (Bruker Daltonics, Bremen, Germany). All spectra were recorded in positive mode and can be found in the Appendix in the analytical data section.

2.3.4. Polyplex preparation

2.3.4.1. Core

The amount of siRNA is the key parameter determining quantities of all other reagents in polyplex formation. For measurements and *in vitro* experiments, polyplexes with a final concentration of 0.025 mg/ml siRNA were produced. A nitrogen to phosphate (N/P) ratio of 12 was used to determine the amount of core oligomer *CO* (**Figure 1A**) relative to the amount of siRNA. The N/P ratio sets the number of primary and secondary amines in the structure of the oligomer in relation to the number of phosphates in the backbone of the RNA. The azide-bearing core oligomer *CON* was handled the same way as *CO* and is described when the reference system is introduced (cf. 2.2.4. Characterization of *CON* – PEG-Ligand Polyplexes).

The conventional method of polyplex preparation was done with pipettes and rapid mixing in a batch-wise process. The solvent – if not noted differently – was HEPES buffer pH 7.4 with 5% glucose (HBG). This buffer was used because it does not rely on salts to be isotonic since polyplex formation relies on charge interactions that could be hampered by ions. Here, *CO* solution (c_{CO} = 0.504 mg/ml) was added quickly to a siRNA solution (c_{siRNA} = 0.05 mg/ml) of equal volume and mixed by rapid pipetting, achieving a final siRNA concentration of 0.025 mg/ml. Subsequently, the formulation has been incubated for 45 min. For automated polyplex production at a T-junction, siRNA in HBG (c_{siRNA} = 0.05mg/ml) and *CO* in HBG (c_{CO} = 0.504 mg/ml) or HBG with 50% acetone were loaded into two separate syringes (one ml, Hamilton) that were connected with silicon tubes (SE-200; ProLiquid) to a T-junction (PP-T-Tüllenverbinder; ProLiquid).

Each syringe was driven by a separate syringe pump (*LA*-120, *LA*-160) that run at the same speed (flowrates (FR) for each pump were 0.5, 1.0, 2.0, 5.0, and 30.0 ml/h) except for experiments with a final acetone concentration of 2.5% (cs_{iRNA} = 0.027 mg/ml; FR_{siRNA} = 0.917, 1.833, 4.583, 9.167, 55.000 ml/h; c_{CO} = 3.026 mg/ml; FR_{CO} = 0.083, 0.167, 0.417, 0.833, 5.000 ml/h). The final product was collected and incubated for 45 min before use. siRNA concentration in the final formulation was 0.025 mg/ml.

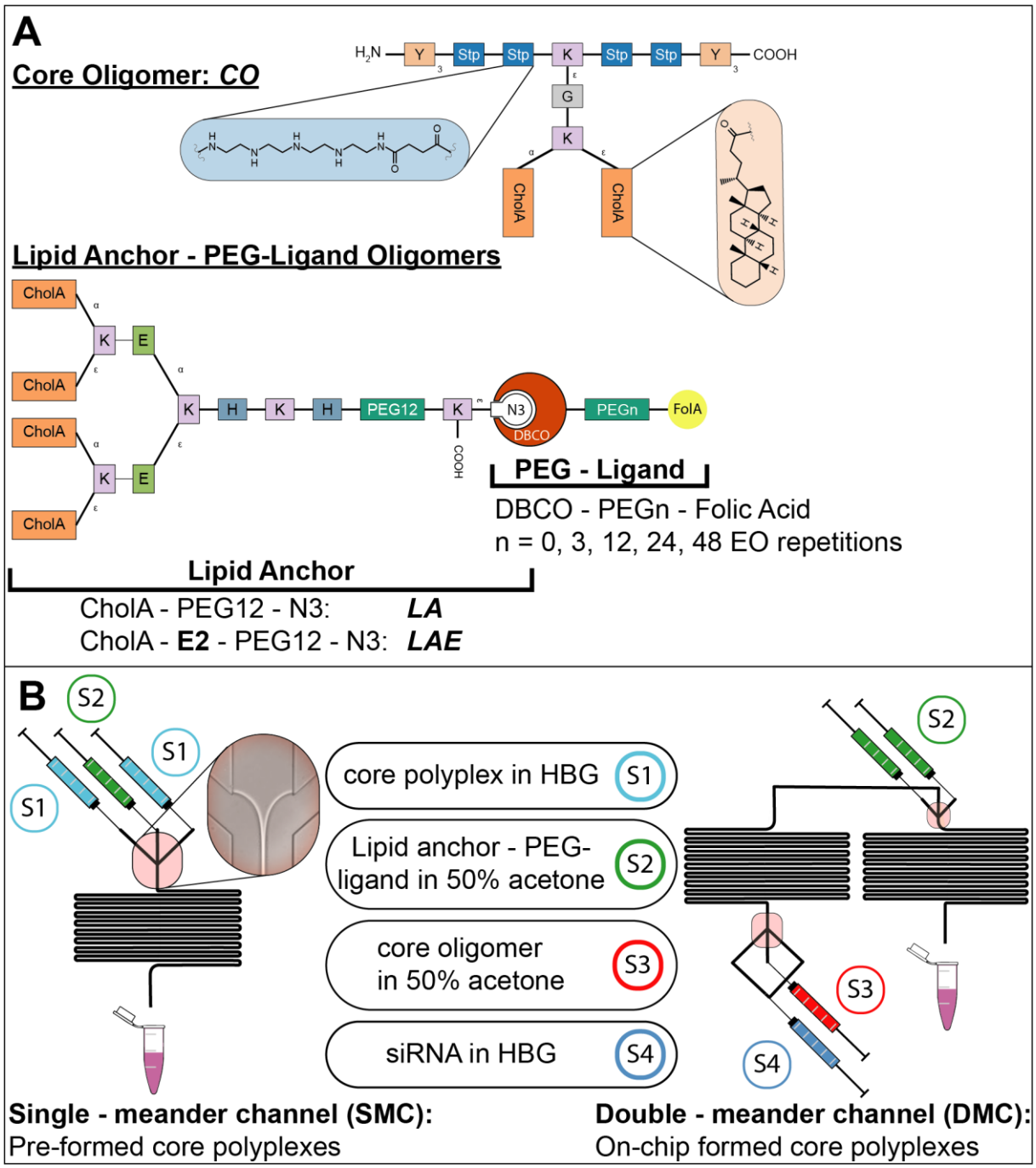

Figure 1: **Sequence-defined oligomers and their corresponding nanoparticle production method.** (A) Oligomers used in polyplex formation: Lipid anchors were coupled to PEG-ligands before polyplexes were formulated. Building blocks represent natural amino acids (E = glutamic acid, G = glycine, H = histidine, K = lysine, Y = tyrosine), synthetic building blocks (Stp = succinyl tetraethylene pentamine, PEG = polyethylene glycol), fatty acids (CholA = cholanic acid), and moieties for bio-orthogonal click chemistry (N3 = azide, DBCO = dibenzocyclooctyne). (B) Production methods for polyplexes with *CO* oligomers: Formulations used are depicted between both channels with the id of their corresponding syringe (S1-4). Two different channels were used to produce nanoparticles during the solvent exchange, a single meander channel, and a double meander channel. In the single meander channel, pre-assembled core particles were mixed with lipid anchors or lipid anchor PEG-ligand oligomers. In the double meander channel, the complete polyplex was assembled from its starting components.

For controlled core polyplex production using microfluidics, the double meander channel (DMC) in **Figure 1B** was used, albeit without the second meander and without both S2 inlets. siRNA in HBG (c_{siRNA} = 0.033 mg/ml) was loaded into S4 and *CO* in HBG or HBG with 50% acetone (c_{CO} = 3.025 mg/ml) was loaded into S3. Separate syringe pumps drove both syringes. FRs were 100 µl/h for S3 and 900 µl/h for S4, respectively. The final product was diluted with HBG to reach c_{siRNA} = 0.025 mg/ml.

2.3.4.2. Addition of lipid anchor and lipid anchor – PEG-ligand oligomers

It was determined before that 20 mol % lipid anchor oligomer (*LA* or *LAE*) or lipid anchor – PEG-ligand oligomer in relation to n_{CO} offered an optimal balance between efficacy and aggregation of the final product (data not shown).

Lipid anchor or lipid anchor – PEG-ligand oligomers were added in two different ways to core polyplexes. If the complete product is assembled in one continuous process, the DMC in **Figure 1B** will be used. siRNA in HBG (c_{siRNA} = 0.033 mg/ml) was loaded into S4 (FR = 900 µl/h) and *CO* in HBG or HBG with 50% acetone to retard siRNA compaction (c_{CO} = 3.025 mg/ml) was loaded into S3 (FR = 100 µl/h). Lipid anchor or lipid anchor – PEG-ligand oligomers in HBG with 50% acetone to facilitate solvent exchange were loaded into S2. The flow rate of each syringe S2 was 50 µl/h at a total flow rate of 1,100 µl/h, resulting in a flow rate ratio of lipid anchor oligomer to core polyplex of 1:11. The final product was diluted with HBG to c_{siRNA} = 0.025 mg/ml.

Alternatively, conventionally (i.e., with pipettes) prepared core polyplexes (c_{siRNA} = 0.032 mg/ml, c_{CO} = 0.319 mg/ml) were fed into both inlets connected to syringe S1 (single meander channel (SMC)) with the lipid anchor oligomers filled into syringe S2. In this case, flow rates were 126.5 µl/h for S2 and 600 µl/h for each S1 resulting in a flow rate ratio of 1:10.5. The final product was diluted with HBG to c_{siRNA} = 0.025 mg/ml. The difference in flow rates between the two set-ups is due to separate optimization steps. Both set-ups resulted in large volumes of core solution and only a thin stream (see **Figure 1B**) of lipid anchor solution at the junction, accelerating the solvent exchange from 50% to 4.8% acetone and facilitating the association of the hydrophobic lipid anchor with the fatty acids in the structure of the core. It is always indicated which method for producing core – lipid anchor – PEG-ligand polyplexes was used.

2.3.5. Characterization

2.3.5.1. DLS measurements

For dynamic light scattering (DLS) measurements, samples were prepared to contain 1.5 µg siRNA in 60 µl HEPES buffered glucose pH 7.4 (HBG) at 25 °C and the corresponding amount of oligomer. The refractive index and viscosity of the solution were calculated using the solvent builder integrated into the software (Zetasizer family software update v7.12). Viscosities and refractive indices (RI) are reported in **Table 14**. The RI of all particles was estimated to be 1.45. In the case of a *CO* core with N/P 12 and 20 mol % of *LA*, 16.6 and 2.8 µg were used, respectively. For size measurements, light scattering was measured at a 173° angle (backscatter) with a flexible attenuator with a Zetasizer Nano ZS ZEN 3600 (Malvern Panalytical Ltd, Malvern, UK) in DTS1070 micro cuvettes (Malvern Panalytical Ltd, Malvern, UK). Samples were measured three times with 12–15 sub runs each. The mean z-average in nm of those three runs is reported with error bars corresponding to the 95% confidence interval of the three runs. The underlying intensity distribution is depicted as violin plots in order to gain a better understanding of the size distribution of the formulation. The extension of the violin plot in x-direction corresponds to the percentage of the total intensity measured at the specific hydrodynamic diameter depicted on the y-axis.

Table 14: Solvents used for DLS measurements.

Solvent	Dispersant RI	Viscosity [cP]
HBG	1.337	1.0366
HBG (1.7% [V/V] acetone)	1.338	1.0782
HBG (3.3% [V/V] acetone)	1.339	1.1045
HBG (5.0% [V/V] acetone)	1.340	1.1324
HBG (6.7% [V/V] acetone)	1.342	1.1750

Note: Refractive indices (RI) and viscosities in centipoise (cP)

If zeta potential is measured, the sample will be taken from the cuvette after the size measurement, diluted with HBG to 800 µl and reloaded into the same cuvette. Light scattering was measured at a 90° angle with a flexible attenuator. Samples were measured three times (main runs) with enough sub runs to gather more than 10,000 total counts (usually 12–15). The mean zeta potential of those three runs is reported with error bars corresponding to the mean of the zeta deviation of each main run.

2.3.5.2. Stability of the core formulation over time

Core polyplex formulations were prepared using the SMC (**Figure 1B**) set up as described above. *CO* was diluted in HBG with 50% acetone, and siRNA was diluted in HBG only. c_{siRNA} of the final solution was 0.025 mg/ml. Size, polydispersity index (PDI), and zeta potential were

measured as described under “DLS measurements.” This protocol, however, was changed in the following way to allow for multiple measurements over time: Two samples with 60 µl each were prepared. The first sample was used to measure size and PDI. The second sample was diluted with HBG to 800 µl to enable zeta potential measurements. Both samples were measured directly after each other for 90 min.

2.3.5.3. Electrophoretic mobility assay

An 1% (w/w) suspension of agarose in Tris/Borate/EDTA (TBE) buffer (149 mM TRIS, 89 mM boric acid, two mM EDTA in demineralized water) was heated until the agarose was dissolved. After a short cooling period, 0.1% GelRed™ 10000× (Biotium Inc., Fremont, CA, USA) was added. The mixture was cast into its mold, and a comb was added to create wells. After 30 min, the solidified gel was placed in an electrophoresis chamber and completely immersed in TBE buffer. Polyplexes were prepared as described above (core polyplexes were prepared with pipettes, lipid anchors were added with the single meander channel (SMC)). Naked siRNA was used as positive control. c_{siRNA} was 0.025 mg/ml in all samples; the sample volume was 20 µl. Four µl loading buffer (8.21 mM glycerol, 60 mM EDTA, 0.003 mM bromophenol blue in purified water) was added to every sample (V_{total} = 24 µl), and each was pipetted in a well in the solidified gel. The gel was run for 60 min at 80 V.

For serum gel shifts, polyplexes were produced with higher siRNA concentration (c_{siRNA} = 0.25 mg/ml) and diluted afterwards with FBS 1:10 to reach the desired c_{siRNA} = 0.025 mg/ml. Samples containing FBS were incubated at 37 °C for up to 24 h until the loading buffer was added. Next, they were pipetted into the wells of the gel. ImageJ (v. 1.52n) (Schindelin et al., 2012) was used to conduct a densitometry analysis of the siRNA bands. To this end, ImageJ was used to extract gray values from the respective siRNA stains. The sum of gray values as a function of the extension of the gel in y (width of the stains) and x (length of the whole gel) direction was plotted with ImageJ to produce the desired analysis. The arbitrary values of the plot on the y-axis correspond to the sum of all gray values over the full width (y) at a given length position (x). The length position x is plotted on the x-axis.

2.3.5.4. FRET experiments

Polyplexes were prepared conventionally (cf. 2.2.4. Polyplex preparation), albeit with a 1:2 siRNA-Cyanine 5 (Cy5):siRNA mixture. Lipid anchors (*LA* or *LAE*) were incubated with 0.75 eq. DBCO-PEG4-Atto488 (relative to azide content) overnight at room temperature. Afterward, the modified lipid anchor solution was diluted 1:2 with unmodified lipid anchor solution,

resulting in a theoretical degree of labeling of 37.5%. The lipid anchor was added to the polyplexes using the SMC (**Figure 1B**). The final siRNA concentration was c_{siRNA} = 0.1 mg/ml. Therefore, the final Cy5 and Atto488 concentrations were 6.1 and 21.3 µmol/l, respectively. A total of 30 µl of each sample was filled into a 96 well plate and measured with a TEKAN pleat reader (Tecan Trading AG, Switzerland, Spark 10M, SparkControl V 2.1) with the following set of filters: Cy5: excitation wavelength: 625 nm, bandwidth 35 nm; emission wavelength: 680 nm, bandwidth 30 nm; Atto488: excitation wavelength: 485 nm, bandwidth 20 nm; emission wavelength: 535 nm, bandwidth 25 nm; Förster resonance energy transfer (FRET): excitation wavelength: 485 nm, bandwidth 20 nm; emission wavelength: 680 nm, bandwidth 30 nm. Measured fluorescence was divided by the value of the gain to exclude amplifier effects.

2.3.5.5. Polyplex compaction and heparin competition assay

Core polyplexes were prepared conventionally (cf. 2.2.4. Polyplex preparation). Solvents were HBG and HBG with 50% acetone for core polyplexes and lipid anchor oligomers, respectively. 20 mol % of indicated lipid anchor oligomers were attached to the polyplexes via solvent exchange inside the microchannel (**Figure 1B**, SMC). The final solvent was HBG, with 3.3% acetone. A total of 20 µl of this mixture containing siRNA (0.025 mg/ml), *CO* (0.252 mg/ml), and lipid anchor (*LA*: 0.022, *LAE*: 0.023 mg/ml) were pipetted into a 96 well plate and incubated with 10 µl heparin solution (11.0; 55.0; 110.0; 165.0 IU/ml in HBG) or HBG for 15 min. Afterward, 80 µl of a 0.5 µg/ml EtBr solution in HBG was added, and the samples were incubated for another 5 min. When EtBr intercalates into DNA or RNA, it emits a strong signal when excited. This process can be inhibited by compacting the nucleic acid with polycations. Therefore, the fluorescence of EtBr correlates with the compaction efficiency of target oligomers. The addition of heparin tests the resistance of the formulation against anionic stress. The fluorescence of all samples was measured with a TEKAN plate Reader (Spark 10M, SparkControl V 2.1; Tecan Trading AG, Männedorf, Switzerland) utilizing the following set of filters: Excitation wavelength: 535 nm, bandwidth 25 nm; emission wavelength: 590 nm, bandwidth 20 nm. The well containing only siRNA and EtBr served as positive control and was also used to choose optimal gain and Z-position settings. All readings were normalized to samples containing free siRNA and EtBr only (positive control) and are presented here in "(%) of positive control."

2.3.5.6. Transmission electron microscopy

Core polyplexes were prepared conventionally or inside the SMC (cf. 2.2.4. Polyplex preparation). Solvents were HBG and HBG with 50% acetone for core polyplexes and lipid

anchor oligomers, respectively. A total of 20 mol % of indicated lipid anchor oligomers were attached to the polyplexes using solvent exchange inside the microchannel (**Figure 1B**, SMC). The final solvent was HBG with 3.3% acetone. Carbon coated copper grids (300 mesh, 3.0 mm O. D.; Ted Pella, Inc., Redding, CA, USA) were hydrophilized with a plasma cleaner under an argon atmosphere (420 V, 1 min). The activated surface of the grid was placed face down on a 10 µl sample droplet for 3 min. Afterward, the sample was removed with a filter paper, and five µl staining solution (1.0% uranyl formate in purified water) was placed on the grid and immediately removed to wash the sample off. Staining was performed with the same staining solution for 5 s. Afterward, it was siphoned off with a filter paper, and the remaining liquid was left to evaporate for 20 min. Grids were stored at room temperature. Samples were measured with a JEOL JEM-1100 electron microscope at 80 kV acceleration voltage.

2.3.6. In vitro

2.3.6.1. Culture

I used KB cells (cervix carcinoma, derived from HeLa cells) for all *in vitro* experiments. KB wild type cells were bought from DSZM (Braunschweig, Germany), and they were subsequently modified to code for a GFP-luciferase fusion mRNA by A. Cengizeroglu (Cengizeroglu, 2012). The modified cell line is stably transcribing and translating the fusion mRNA to an eGFP-Luciferase fusion protein, which consists of two functional proteins, GFP and luciferase. The expression of the fusion protein can be silenced by any siRNA that is complementary to the GFP-luciferase fusion mRNA. Here, I used siGFP. The transfection process of the construct was described in A. Cengizeroglu's thesis (Cengizeroglu, 2012), and first use was demonstrated by Dohmen et al. (Dohmen et al., 2012b). For each experiment, cells were freshly thawed from a liquid nitrogen storage tank and passaged at least four times before experiments were conducted. Cells were subcultured when 70–90% confluency was reached. Culture conditions were 37 °C and 5% CO_2. KB cells were cultured in RPMI-1640 supplemented with 10% FBS and 1% penicillin/streptomycin (5 ml with 100 U/ml and 100 µg/ml, respectively).

2.3.6.2. Transfection

Cells were seeded into 96 well plates one day prior to transfection. All wells were pre-treated with 40 µl collagen solution per well (0.1 mg/ml, removed after 30 min, 37 °C). Afterward, cells were seeded with 4,000 cells/well in 100 µl folate free GibcoTM RPMI 1640 (Fisher Scientific, Hampton, NH, USA) supplemented with 10% FBS. The next day, the medium in all wells was replaced with 80 µl fresh medium (RMPI 1640, FolA free), and 20 µl sample solution

or HBG (negative control) was added. Samples were prepared completely inside the microfluidic channel (cf. 2.3.4 Polyplex preparation & **Figure 1B**, DMC). siRNA concentration was five µg/ml in each well. Samples were always prepared in quintuplicates. The medium was exchanged again after 4 h; total incubation time was 48 h at 37 °C, 5% CO_2.

2.3.6.3. Luciferase assay

Plates were taken from the incubator and all media was removed. A total of 100 µl/well lysis buffer (Luciferase Cell Culture Lysis 5X Reagent, Promega, diluted 1:10 with purified water) was added and incubated for another 45 min at room temperature. Plates were frozen at −80 °C until measurement. A total of 35 µl/well of the cell lysate were transferred to white, opaque 96 well plates (BertholdTech, Bad Wildbad, Germany) and measured with a Centro LB 960 luminometer (BertholdTech CENTRO, Driver V. 1.21, MikroWin, V. 5.2, 10 s integration/well). A total of 100 µl LAR buffer per well (20 mM glycylglycine, 1.0 mM MgCl2, 0.1 mM EDTA, 3.29 mM DTT, 0.548 mM ATP, 1.30 µM coenzyme A, adjusted to pH 8.5 with NaOH) were automatically added by the machine. The output of this measurement is relative light units (RLUs) per well. The raw data was handled the following way. The mean value from each sample was calculated and was set in relation to the mean value of the respective negative control. Results are depicted in “RLU (%) of HBG.” Error bars represent 95% confidence intervals of five samples.

2.3.6.4. MTT assay

Plates were taken from the incubator, 10 µl/well 3-(4,5-dimethylthiazol-2-yl)-2,5-diphenyltetrazolium bromide (MTT; Carl Roth, Karlsruhe, Germany, 5 mg/ml in PBS) were added, and everything was incubated for another 2 h at 37 °C. Afterward, the fluids were removed and the plates were frozen at −80 °C for at least 1 h. A total of 100 µl/well DMSO were added, and the plates were gently shaken at 37 °C for 20 min to dissolve the purple formazan dye. The absorbance at 590 nm of each well against the reference wavelength (630 nm) was measured with a TEKAN plate reader (Spark 10M, SparkControl V 2.1; Tecan Trading AG, Männedorf, Switzerland). The raw data was handled the following way. The mean value from each sample was calculated, and it was set in relation to the mean value of the respective negative control. Therefore, results are depicted in “(%) of HBG.” Error bars represent 95% confidence intervals of five samples.

2.3.6.5. Dose titration

Core polyplexes were prepared conventionally with pipettes as described in section 2.3.4 Polyplex preparation. siRNA concentrations were chosen to have a final amount of 100, 250, 500, 750, and 1,000 ng/well. *CO* concentrations were adjusted accordingly. To be precise, siRNA concentrations in 20 µl transfection volume were (mg/ml): 0.0050, 0.0125, 0.0250 0.0375, 0.0500. *CO* concentrations were (mg/ml): 0.0458, 0.1145, 0.2291, 0.3436, 0.5041. A total of 20 µl/well of each sample was transfected as described in section 2.3.6.2 Transfection. Samples were transfected in quintuplicates. The effect of the formulations on luciferase activity and metabolic activity was evaluated with a luciferase assay and an MTT assay as described above.

2.3.7. Preparation of microfluidic PDMS channels

2.3.7.1. Manufacturing process

The microfluidic channels design was realized on a silica wafer with soft lithographic methods. The master microstructure was designed with the LPKF CAD/CAM software (LPKF Laser and Electronics) and made using the SU8 process on a silicon wafer. The microstructure of ~72 and ~90 µm thickness for single- and double-meandering channels, respectively, was rastered using LPKF ProtoLaser LDI UV-laser (LPKF Laser and Electronics). Utilized SU-8 3000 photoresists were processed in accordance with the manufacturer's instructions. The SU-8 master was subsequently silanized in an evacuated desiccator for 12 h with tri-chloro(1H,1H,2H,2H-perfluorooctyl)silane.

The PDMS elastomer was mixed with 10% (w/w) crosslinker, degassed, poured onto the wafer, and cured (75 °C, 4 h). Subsequently, PDMS was peeled from the wafer, holes for the inlets were pierced at the designated positions with a biopsy puncher (d_{inner} = 0.96 mm; d_{outer} = 1.26 mm, World Precision Instruments, 175 Sarasota Center Blvd. Sarasota, FL 34240, USA), and it was bonded to a glass slide by oxygen plasma-induced oxidation (Diener Electronic; 10 W high-frequency generator power, 12 s, Pico Model E). The chip was left alone for 1 h to allow the reaction to complete. Afterward, polyethylene tubes (length = 110 mm, inner diameter = 0.38 mm) were fitted into the holes in the PDMS, and everything was covered with another layer of PDMS treated in the same way as mentioned above to seal the in- and outlets completely. Wang et al., 2014 investigated the tubing of PDMS channels and offer an improved protocol to prevent channel leakage (Wang et al., 2014a). Each new channel was tested before application with a standard formulation. The size and PDI measured by DLS were compared to the results from the same formulation produced with the previous channel. Solvents used in this

dissertation are classified as low-solubility solvents which are compatible with microfluidic systems fabricated in PDMS by Lee et al. Therefore, these solvents are unlikely to cause considerable changes to the channel geometry due to swelling (Lee, Park & Whitesides, 2003).

2.3.7.2. Layout

A to-scale model of the layout of both channels is shown in **Figure 2** (Single meander channel, SMC) and **Figure 3** (Double meander channel, DMC). The channels leading to the first Y - junction of the single meander channel were 50 µm, 100 µm, and 50 µm wide (left, middle, and right). They lead into the main channel, which was 100 µm wide and ~ 166 cm long. The inner and outer turn radius of the curves of the meander were 200 µm and 300 µm, respectively.

The inlets leading to the first Y - junction of the double meander channel were 100 µm, 200µm, and 100 µm wide (left, middle, and right inlet), the inlets leading to the second Y - junction had a width of 100 µm as well. The main channel was 200 µm wide and 2x ~ 166 cm long. The inner and outer turn radius of the curves of the meander were 150 µm and 350 µm, respectively.

I calculated the Reynold's number (Re), Dean's number (De), and backpressure (ΔP) for the SMC and DMC at a total flow rate of 1500 µL/h: SMC: Re ≈ 3, De ≈ 1.23, ΔP = 1249.4 mbar; DMC: Re ≈ 2.5, De ≈ 1.25, ΔP = 2498.8 mbar. Reynold's numbers of this magnitude indicate a laminar flow profile inside both channels. The Dean's numbers indicate a negligible influence of lateral flows at curvatures.

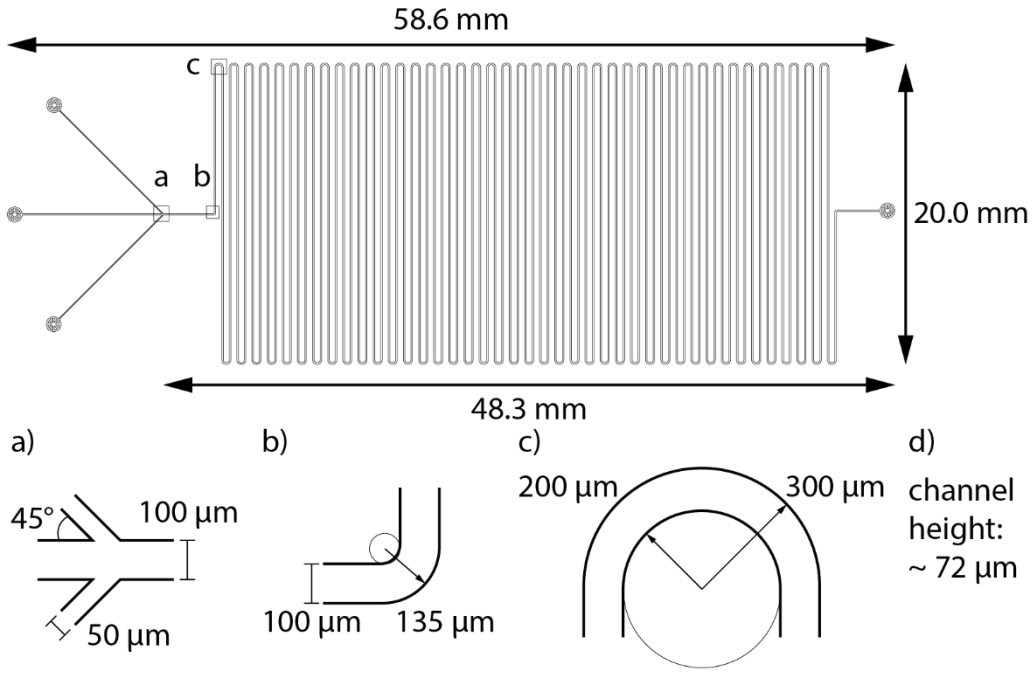

Figure 2: Single meander channel (SMC).
Circles on the left represent inlets, a circle on the right an outlet. Liquids are pumped from left to right. The inserts a, b, and c present the details of the regions marked with squares in the channel sketch.

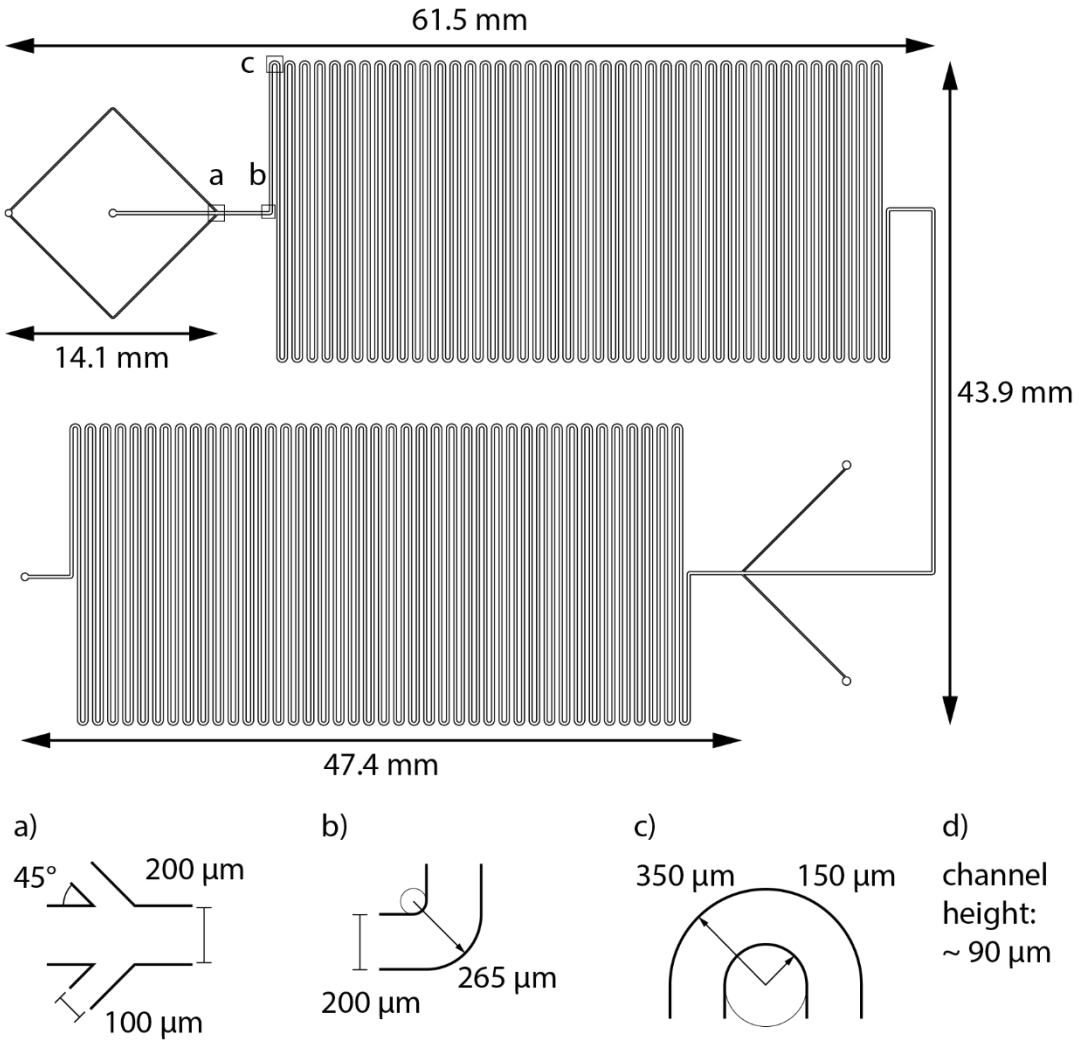

Figure 3: Double meander channel (DMC).
Circles represent inlets, except the circle on the bottom of the left side, which is an outlet. Liquids are pumped from top left to bottom left. The inserts a, b, and c present the details of the regions marked with squares in the channel sketch.

2.3.8. Data analysis

Data were analyzed with R (R Core Team, 2018) and RStudio (RStudio Team, 2018). I always report arithmetic means with 95% confidence intervals, except for zeta potential measurements. Mean zeta potential was reported ± mean of zeta deviations to allow for a better understanding of the underlying zeta distribution.

Data from cell culture experiments were normalized to its negative control, which was always on the same well plate as the respective samples.

A multifactorial two-way ANOVA was used to compare mean RLU reduction of core (*CO* + siRNA) polyplex formulations with two different lipid anchor oligomers and six different PEG-ligand oligomers.

A multifactorial two-way ANOVA was used to compare mean RLU reduction of core (*CON* + siRNA) polyplex formulations with six different PEG-ligand oligomers at four different concentrations.

After each ANOVA, post hoc two-sided student's t-tests were conducted between all samples. Test results were corrected for the family-wise error with Holm's method. Significance was set to $\alpha < 0.05$.

R code and raw data are made available in my repository on figshare (Loy, 2020b): DOI: 10.6084/m9.figshare.7971329.v1.

3. Results

3.1. Controlling nanoparticle formulation: a low-budget prototype for the automation of a microfluidic platform

Adapted from Loy et al. (Loy et al., 2021).

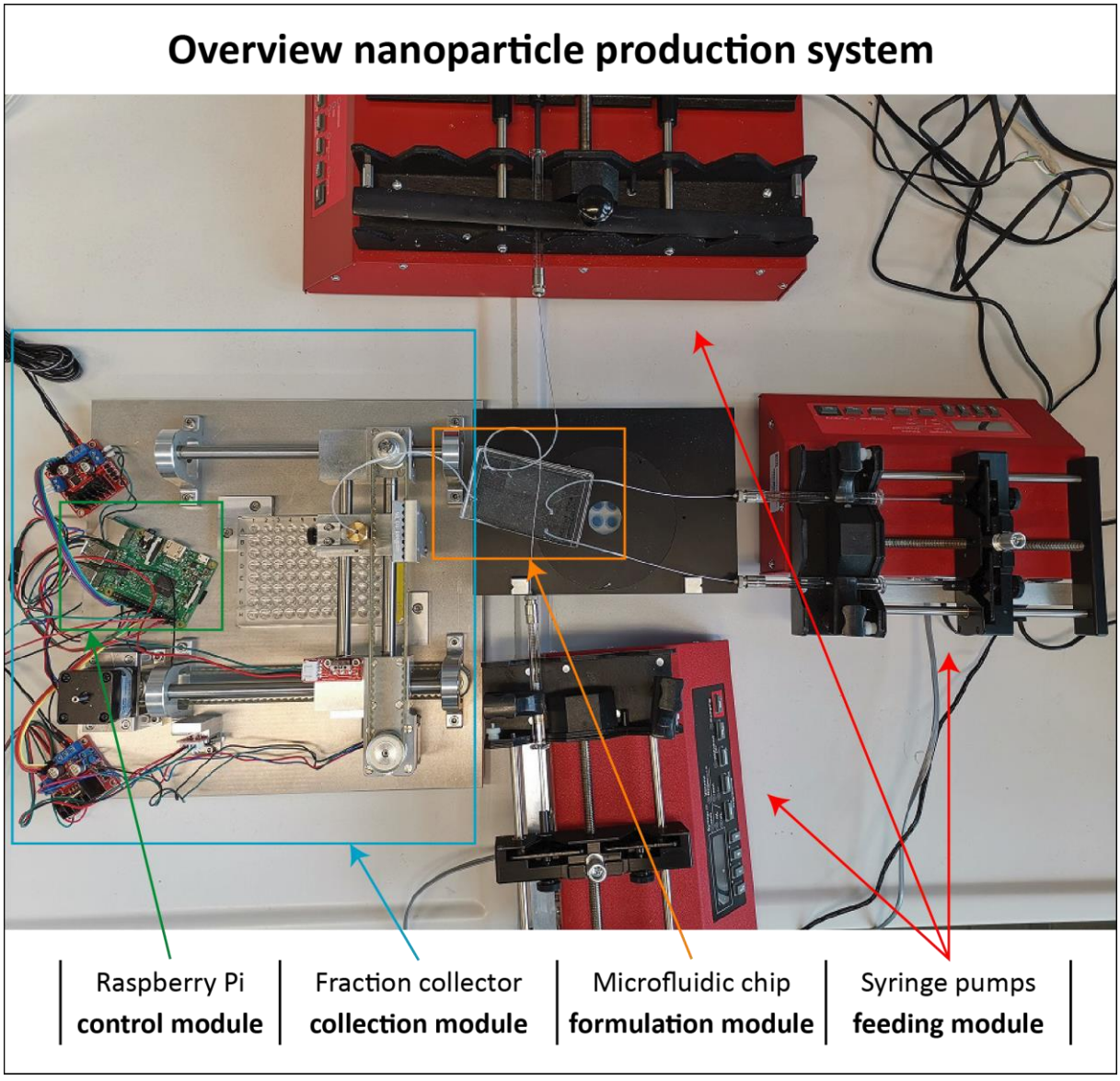

Figure 4: Overview over the nanoparticle production system.
The system consists of four modules that can be used independently. The control module (green) is a raspberry pi which controls the collection module (blue), a custom-built fraction collector, via its GPIO pins. The raspberry pi controls the feeding module (red) via the RS232 interface. It is assembled from up to three syringe pumps. The formulation module can be any macro or microfluidic chip.

The aim of this chapter is the description of our low-budget prototype for the automation of a microfluidic platform. First, the individual modules of the prototype are described.

Subsequently, the application of the system for the formulation of three component polyplexes is demonstrated.

The complete nanoparticle production system is depicted in **Figure 4**. It consists of four modules that can be used independently: the feeding module – up to three programmable syringe pumps – is responsible for supplying educts to the formulation module, which can be any macro or microfluidic chip. The collection module – a custom-built fraction collector – is responsible for collecting the final product into standardized well plates. The control module is a remotely accessible raspberry pi which controls the syringe pumps via a Recommended Standard 232 (RS232) interface and the fraction collector via the general-purpose input/output (GPIO) pins. The design of the fraction collector as well as the python program code are published together with this paper on GitHub (Loy, 2020a). This setup allows the employment of most microfluidic chips while additionally providing the ability to sample the product from the chip directly into standardized well plates. I describe all modules in detail in the following sections.

3.1.1. Feeding module

The feeding module consists of up to three syringe pumps that are daisy-chained to the raspberry pi via a R232 to USB interface. Here, I used LA120, LA122, and LA160 from Landgraf Laborsysteme HLL GmbH. LA120 and LA160 are standard syringe pumps with two and six channels, respectively. LA122 is microfluidic syringe pump with two channels which is especially suited for dispensing smaller volumes due to its higher precision.

In principle, any syringe pump can be integrated into the system if it satisfies the following prerequisites: first, the pumps must have an interface that can be connected to the control module, e.g., the RS232 serial interface. Second, the pump must be programmable. In order to reduce the risk of interferences during particle production, the complete program is written to the pumps in advance and the pumps execute the production program independently. If a pump with a different command structure is integrated into the system, however, commands sent to the pump must be adjusted. A detailed description on changing commands sent to the pumps can be found in the Appendix (6.3.3. Module: Module_pumps.py).

The control program of the feeding modules consists of six modules that are described in detail in the Appendix (6.3. Feeding module: software) together with an Unified Modeling Language (UML) class diagram to illustrate the dependencies between the classes of the modules (**Figure 37**). The main module that calls the required functions from the respective modules to execute

a certain pumping program is called ‘main.py’. I provide a library with different ‘main[…].py’ modules on GitHub (Loy, 2020a). If the module ‘main.py’ is executed, the user will be asked to input all parameters during runtime, for example, flow rates and volumes. If one of the ‘main_[…]_automated.py’ modules is executed, the parameters defined in the module will be used to run the pre-defined pumping program without requiring any user input. These modules serve as examples of how to define target variables and how to customize the main module. The code of the ‘main.py’ module is described in the Appendix (6.3.7. Modules: main[…].py).

Several features are implemented in the control program to simplify the employment of different formulation modules, to document experiments, and to save educts: first, formulation module specifications are loaded into the program during runtime from a simple text file. In order to employ a new channel, an updated text file needs to be supplied to the program. A detailed description on adding new formulation module specifications can be found in the Appendix (6.3.1. Module: channels.py). Second, a logging function was integrated into the program, which writes every event and its timestamp to a text file stored on the control module. This log can be used for documenting and for troubleshooting purposes. Third, the implementation of ramping and purging capabilities reduces the waste of educts to a minimum. When large flow rate changes occur (e.g., when a pump is started), the system needs some time to adapt to the increased pressure. This can lead to the retardation of educts due to the elasticity of the system. Bringing educts efficiently (i.e., without wasting time or educts) to the mixing zone without involuntarily changing the volume ratios is challenging especially at the beginning of a new run. The easiest solution would be to use the flow rates of the first experiment to pump all educts to the mixing zone. Applying this strategy, however, increases waste of time and educts in relation to the flow rate differences between the educts. Ramping all educts to the mixing zone without changing the mean flow rate alleviates this problem and prevents unnecessary waste.

Additionally, employing the ramping protocol can reduce the backflow from the syringe pumps. During transition from preparations to formulation, the ramping protocol ensures a smooth transition between flow rate changes and keeps the overall flow rate constant, minimizing pressured changes that can provoke backflows. Moreover, when flow rates need to be changed during the formulation of the product, the program automatically inserts an overlap volume between those two fractions to allow some time for the flow to stabilize again. The overlap volume can be adjusted according to the magnitude of the flow rate changes. If large flow rate changes take place (e.g., when flow rates between slow and fast pumping pumps are

interchanged), the modularity of the program allows another execution of the ramping protocol. Furthermore, fractions affected by backpressure instabilities can automatically be excluded using the collection module. The ramping program is described in the Appendix (6.3.5. Module: ramping_class.py). The purging functions enable the user to choose the least expensive reagent to purge the product from the channel after the experiment. A detailed description of this function can be found in the Appendix (6.3.6. Module: mixing_class.py). A flowchart describing the workflow from starting the system to collecting the final product(s) and resetting the system to its original state is shown in the Appendix (**Figure 38**).

3.1.2. Formulation module

The formulation module can be any micro- or macrofluidic chip that is connectable to syringe pumps. In our prototype, I employed two different microfluidic chips that are based on the design from Krzysztoń et. al (Krzysztoń et al., 2017). These chips are made from polydimethylsiloxane (PDMS) bonded to glass slides. Both chips exploit the advantages of solvent exchange in combination with flow-focusing inside the microchannel to produce polyplexes from siRNA and polycationic oligomers. The layout of both chips together with the utilized educts is shown in **Figure 1B**. The single meander channel (SMC) employs the design of a Y – junction followed by a long meandering channel section while the double meander channel (DMC) features two successive Y – junctions followed by their respective meandering section which allows the assembly of polyplexes in two consecutive steps. Detailed schematics of both channels are shown in section 2.3.7.2. Layout (SMC: **Figure 2**, DMC: **Figure 3**). The chips were made from polydimethylsiloxane (PDMS) bonded to glass slides. Wang et al. (Wang et al., 2014a) have made suggestions to increase durability of these chips. I used both chips in our previous publication to produce well-defined, multi-component polyplexes that allowed the establishment of structure – function relationships between PEG-ligand length and transfection efficiency due to the increased level of control over the formulation process (Loy et al., 2019). In section 3.1, I only show data produced with the DMC to highlight the potential of the device to produce sophisticated formulations. For a comparison of the core formulation (siRNA and *CO*) prepared by the SMC, at a T-junction, or by rapid pipetting see **Figure 10**.

3.1.3. Collection module

The design is based on previously published work (Andersen, 2016). It was optimized for greater robustness and user safety, especially by choosing aluminum to decrease wear, increase resistance to common solvents (except acids), and to increase the accuracy of fit of the machine. Increased user safety was realized by including stop switches into the design.

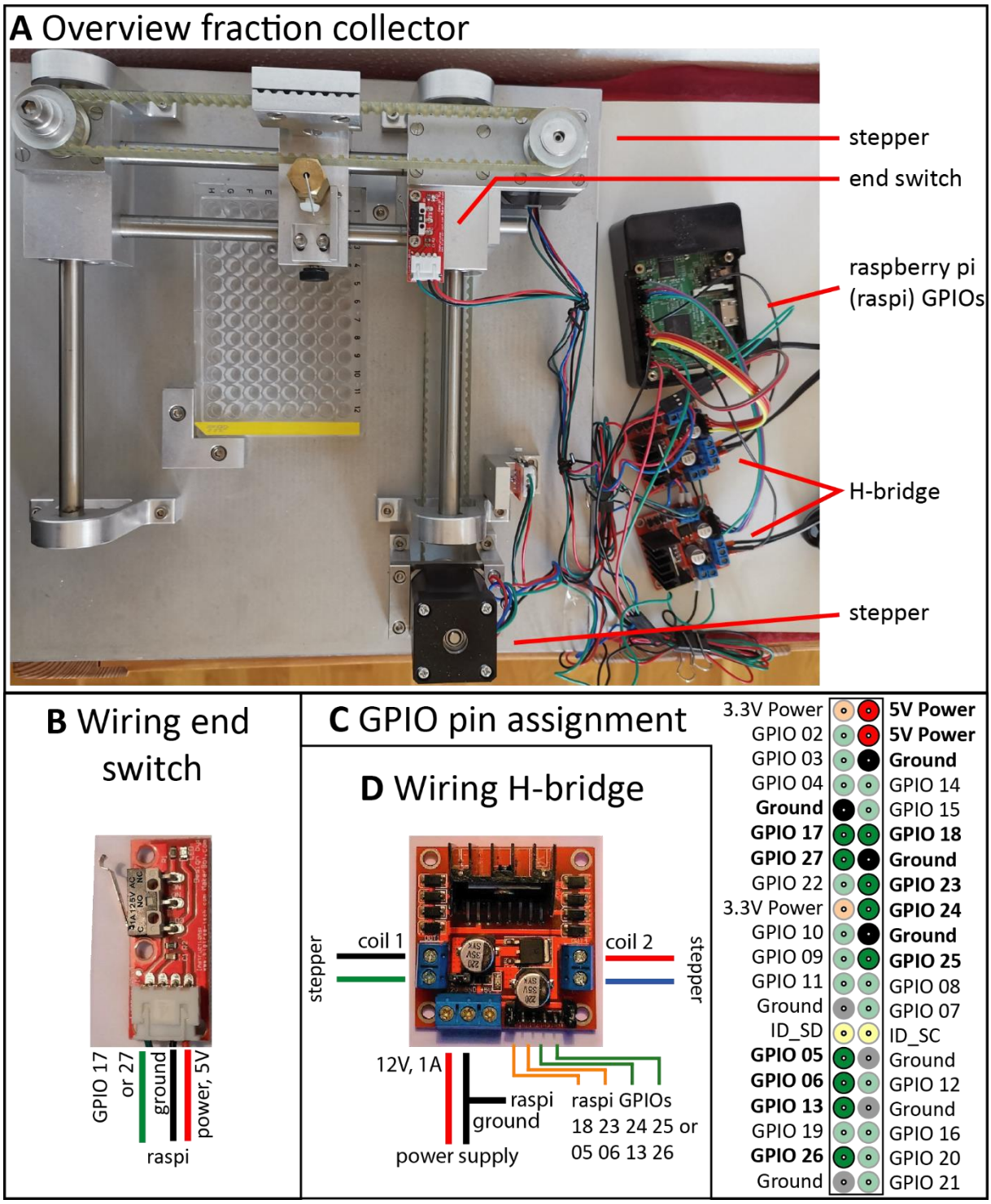

Figure 5: Overview over the fraction collector.
(A): Overview fraction collector. (B): Wiring of the end switches. The end switches are supplied with 5V power from the pins of the raspberry pi, and the signal is sent from the switches to GPIO 17 or 27 (green wire). (C): GPIO pin assignment. Schematics of the GPIO pins of the raspberry pi. Saturated colors and bold script indicate utilized pins. (D): Wiring of the H-bridge. Each H-bridge controls one stepper motor. Power is supplied by a 12 V, 1 A switching power supply and routed to each stepper motor by four output wires (coil one: black and green wires; coil two: red and blue wires). Power distribution is controlled by the GPIO pins. GPIOs 18 and 23 or 05 and 06 (orange wires) control the direction of coil one, while GPIOs 24 and 25 or 13 and 26 (light green wires) control the direction of coil two.

The fraction collector is controlled by a raspberry pi 3, model B running Raspbian GNU/Linux 9 (stretch). The raspberry pi controls the fraction collector via input/output (GPIO) pins. **Figure 5** shows an overview of the complete fraction collector (**Figure 5A**), the wiring of each component (**Figure 5B** and **5D**), and the GPIO pin assignment (**Figure 5C**).

The control program for the fraction collector is an independent piece of software. This approach allows the integration of the collector control software into the pumping program but enables usage of this device with other, non-automated processes, as well. It consists of three modules which are described in detail in the Appendix (6.4. Collection module: software). The main module is called 'main.py'. It calls the required functions from the respective modules to execute a certain collection program. The module serves as example how to define target variables and how to customize the collection program. A video documenting the execution of the 'main.py' module can be found on GitHub (Loy, 2020a). The code of the 'main.py' module is described in the Appendix (6.4.3. Module: main.py). A complete list of all classes and functions of the modules can be found on GitHub as well (Loy, 2020a). The dependencies between the classes of the program are depicted in an UML class diagram in the Appendix (**Figure 39**).

3.1.4. Application for polyplex formation

In the following, I highlight the importance of precisely defined process parameters and show the formulation of three component polyplexes with the automated nanoparticle production system.

Figure 6 demonstrates the influence of formulation parameters on polyplexes formulated from two components by rapid pipetting. By adjusting the volume ratios and the mixing order of the oligomer and siRNA solutions, significant changes in size (hydrodynamic diameter) and polydispersity index (PDI) can be achieved.

For this experiment I produced polyplexes using siRNA and a core oligomer (*CO*) (Klein et al., 2018; Loy et al., 2019). Light red dots present data obtained after the oligomer solution was pipetted into the siRNA solution, and blue squares represent the result after pipetting the siRNA into the oligomer solution. The number written on the x-axis denotes the volume parts of the two solutions in the final solution. The final volume of each solution was always 70 µl. For example, data resulting in the third light red dot (11/1 on the x-axis) were obtained from 64.2 µl oligomer solution that was pipetted to 5.8 µl siRNA solution.

Mixtures of equal volumes of educts solutions produced comparable hydrodynamic diameters (**Figure 6A**, circle: 82.5 ± 2.7 nm, square: 84.4 ± 3.1 nm) and PDIs (**Figure 6B**, circle: 0.151 ± 0.058, square: 0.136 ± 0.052) independent of the mixing order. If unequal volumes were mixed, however, the mixing order influenced particle characteristics significantly. Pipetting a smaller volume of the oligomer solution into a larger volume of the siRNA solution ('1/11' on the x-axis) produced larger polyplexes (141.0 ± 3.2 nm) with a smaller PDI (0.109 ± 0.030), while mixing siRNA solution to an oligomer solution produced smaller particles (108.0 ± 1.4 nm) with a larger PDI (0.180 ± 0.048).

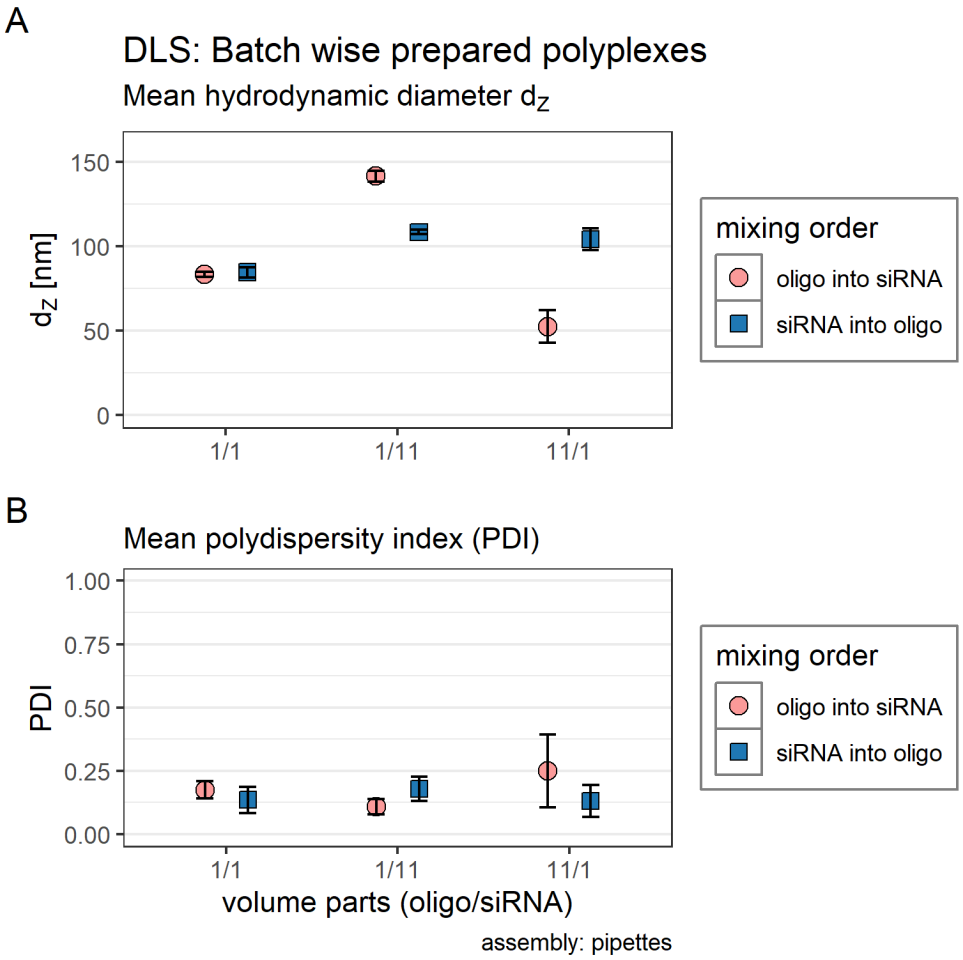

Figure 6: Influence of formulation conditions on manually prepared polyplexes (oligomer *CO* + siRNA).
Dynamic light scattering (DLS) data are represented as the mean of three measurements. Color and shape encode the mixing order. The volume parts of both educts are denoted on the x- axis. Total volume was 70 µl for each solution. That means, for example, that 64.2 µl of a diluted oligomer solution (oligo) was pipetted to 5.8 µl of a concentrated siRNA solution (light red dot, volume parts 11/1). Blue square: siRNA was pipetted into an oligomer solution. Red dot: The oligomer solution was pipetted into a siRNA solution. (A) Mean hydrodynamic diameter (z- average). (B) Mean polydispersity index (PDI). Statistics: Error bars correspond to 95% confidence intervals. N = 3.

Pipetting a larger volume of the oligomer solution to a smaller volume of the siRNA solution (‘11/1’ on the x-axis) produced very small particles (**Figure 6A**, 52.5 ± 9.7 nm) with a larger PDI (**Figure 6B**, 0.249 ± 0.144). Mixing diluted siRNA solution to concentrated oligomer solution produced slightly larger particles (104.0 ± 6.5 nm) with a comparable PDI (0.131 ± 0.063) in comparison to polyplexes from mixtures of equal volumes. The 95% confidence intervals from the z-average as well as from the PDI, however, were very large, indicating the presence of particles from different size classes.

Nanoparticles formulated from more than two components usually require increased control over the production process. **Figure 7** highlights this critical issue. The formulation (siRNA/*CO*; 1/1 on the x-axis, light red dot) described in **Figure 6** was further modified with a third oligomer that contributes shielding and targeting features to the nanoparticle. It consists of a lipid anchor for integrating into the core particle, a PEG12 chain for shielding purposes and an azide moiety that allows the simple addition of further shielding and targeting ligands via strain-promoted azide – alkyne click chemistry (Sletten & Bertozzi, 2011). Here, I utilize the two simplest versions of the lipid anchor oligomer with a free azide moiety and with (*LPOE*, id: 1223) or without (*LPO*, id: 1203) two additional glutamic acids (E). The sequences of all oligomers are depicted in the Appendix (*CO* (991): **Figure 28**, *LPO* (1203): **Figure 30, *LPOE*** (1223): **Figure 31**). Results from *in vitro* experiments with these three component polyplexes with PEG – folic acid ligands with 12 to 60 ethylene oxide repetitions can be found in section 3.2.3 Transfection of core – lipid anchor – PEG-ligand nanoparticles and in the Appendix (6.2.3 PEG-ligands). In section 3.2.5 Transfection of *CON* – PEG-ligand polyplexes, I compared the influence of the production method on the biological activity of two component polyplexes. I was able to demonstrate comparable biological activity *in vitro*.

In **Figure 7A** und **7B,** equal volumes of the three educts were mixed sequentially by rapid pipetting according to the order of appearance denoted on the x-axis. Color and shape indicate if *LPO* or *LPOE* was used. Manual production of three component polyplexes from *CO*, siRNA, and *LPO* yielded polyplexes with suboptimal hydrodynamic diameters and PDIs regardless of mixing order (*CO* + siRNA + *LPO*: d_Z = 416.2 ± 62.5 nm, PDI = 0.711 ± 0.233; *CO* + *LPO* + siRNA: d_Z = 466.7 ± 33.1 nm, PDI = 0.792 ± 0.068). When *LPO* was replaced with *LPOE*, the mean hydrodynamic diameters of the polyplexes was reduced to acceptable levels, but the mean PDI was still too large (*CO* + siRNA + *LPOE*: d_Z = 128.2 ± 22.4 nm, PDI = 0.468 ± 0.101; *CO* + *LPOE* + siRNA: d_Z = 114.5 ± 1.5 nm, PDI = 0.428 ± 0.058).

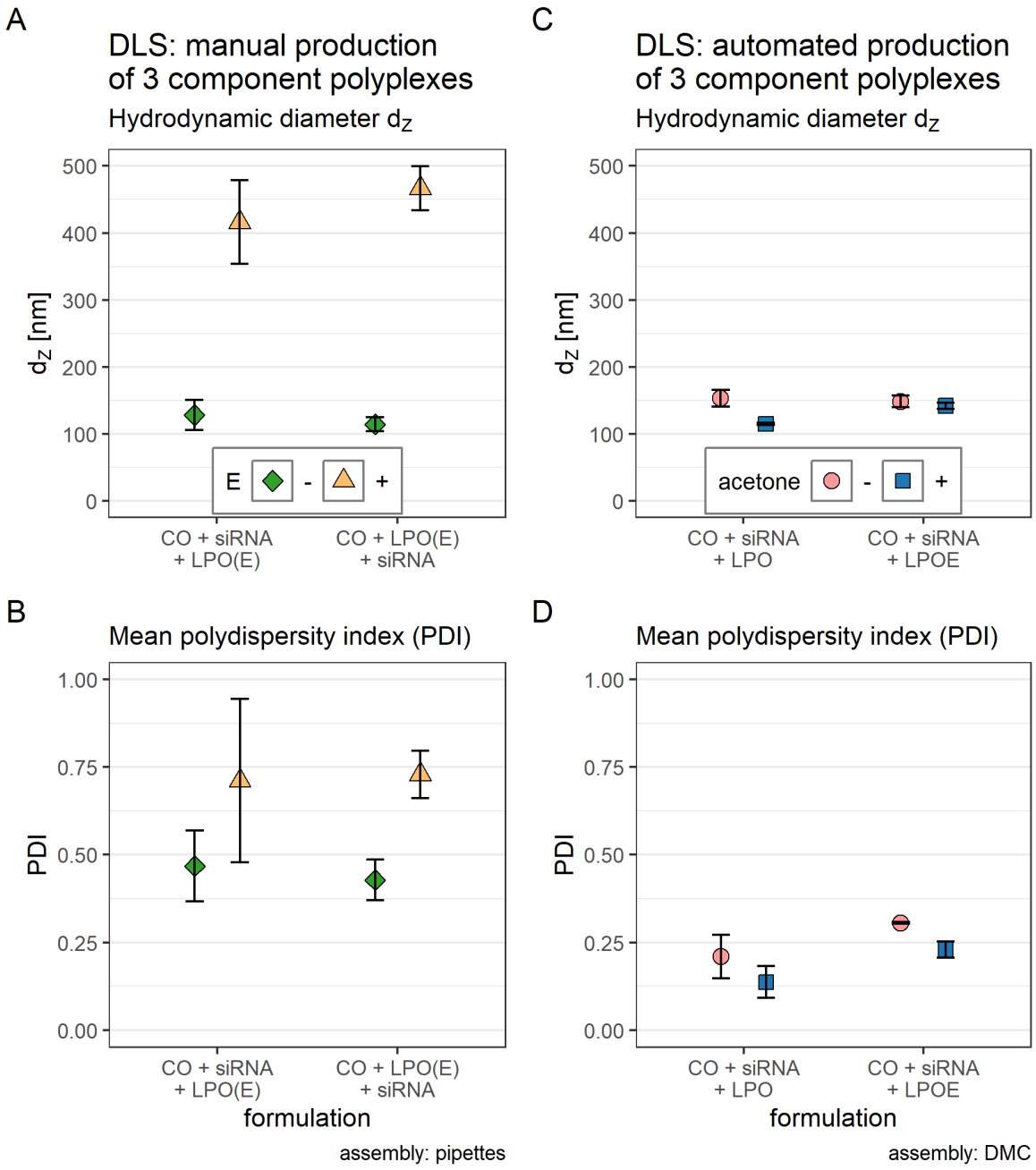

Figure 7: Manual or automated formulation of three component siRNA polyplexes.
DLS data are represented as the mean of three measurements. Color and shape encode either the difference in the sequence of lipid anchored PEG12 oligomers (*LPO*, with or without E (glutamic acid), panel A, B) or the difference in formulation conditions (oligomer *CO* dissolved in HBG with or without 50% acetone, panel C, D). (A, B): polyplexes were formulated manually by mixing all educts with pipettes. The mixing order is denoted on the x-axis. Orange triangle: the sequence of the *LPO* contains two additional glutamic acids. Green diamond: no additional glutamic acids. (C, D): polyplexes were formulated automatically inside the double meander channel (DMC, **Figure 4**) by the nanoparticle production system. Flow rates: siRNA 900 µl/h (S4), *CO* 100 µl/h (S3). *LPO*(*E*) 50 µl/h (S2, two syringes). Total flow rate: 1100 µl/h. The educts are denoted on the x-axis. Red dots: *CO* was dissolved in HBG only. Blue squares: *CO* was dissolved in HBG with 50% acetone. (A, C): mean hydrodynamic diameter (z-average). (B, D): Mean polydispersity index (PDI). Error bars correspond to 95% confidence intervals. N = 3. Raw data were selected from our previous publication (Loy et al., 2019), here presented in a new format.

In **Figure 7C** and **7D**, polyplexes from the three educts were produced automatically inside the double meander channel (DMC) by the nanoparticle production system. In the first mixing zone, *CO* and siRNA were mixed. The color and the shape of the data points indicate if *CO* was dissolved in HBG with or without 50% acetone. In the second mixing zone, *LPO* or *LPOE* was added to the mixture. Polyplexes prepared from *CO* dissolved in HBG only showed slightly higher hydrodynamic diameters d_Z and PDI (*CO* + siRNA + *LPO*: d_Z = 153.0 ± 12.7 nm, PDI = 0.210 ± 0.062; *CO* + siRNA + *LPOE*: d_Z = 148.2 ± 8.7 nm, PDI = 0.306 ± 0.003) in comparison to polyplexes prepared from *CO* dissolved in HBG with 50% acetone (*CO* + siRNA + *LPO*: d_Z = 114.7 ± 1.5 nm, PDI = 0.137 ± 0.045; *CO* + siRNA + *LPOE*: d_Z = 141.9 ± 4.7 nm, PDI = 0.230 ± 0.022).

Automated production of three component polyplexes (*CO* + siRNA + *LPO*) generated nanoparticles with smaller hydrodynamic diameters and PDIs compared to manually prepared polyplexes. Incorporating glutamic acid into the structure of the lipid anchor PEG12 oligomer facilitated the production of polyplexes with comparable mean hydrodynamic diameters regardless of production method. Nevertheless, the PDI of manually prepared polyplexes was still larger than the PDI of polyplexes prepared with the nanoparticle production system.

3.2. A microfluidic approach for sequential assembly of siRNA polyplexes with a defined structure-activity relationship

Adapted from Loy et al. (Loy et al., 2019).

The aim of this chapter is to demonstrate the precise production of multi-component polyplexes with a modular two-step microfluidic set-up. The device employs flow-focusing in combination with solvent exchange to allow for the successive assembly of multi-component nanoparticles. I show that the approach results in well-defined and reproducible polyplexes with controlled surface characteristics. It is used here to vary the surface layer in order to identify structure activity relationships between PEG-ligand length and transfection efficiency. Finally, I compare the findings with conventionally (educts are mixed manually with pipettes) prepared polyplexes.

3.2.1. Design of delivery systems

Oligomers for the formation of core polyplexes are designed to bind siRNA via electrostatic interactions and stabilize the resulting particle with its hydrophobic domains. Solid-phase supported synthesis (SPSS) is used to allow for precise control over the sequence of the oligomers (**Figure 1A**). Core oligomers (*CO*) feature four cationic Stp units that are flanked by three tyrosines (Y) on each side for aromatic and hydrophobic stabilization (Troiber et al., 2013a). Lysines (K) are used to introduce a branch in the main chain for the attachment of two cholanic acids (CholA) for further stabilization (Schaffert et al., 2011; Fröhlich et al., 2012) and to provide attachment points for lipid anchor oligomers. Glycine (G) is used as a spacer. The lipid anchor oligomers (**Figure 1A**, *LA*, *LAE*) are designed to adsorb to the core polyplexes via hydrophobic interactions between cholanic acids. In addition, they feature a histidine – lysine – histidine (H-K-H) motif to adjust solubility. The PEG12 – chain exposes the terminal azide to the surrounding solution, increasing its accessibility to alkyne-bearing entities. The two glutamic acids (E) in the sequence of *LAE* increase attachment to positively charged core polyplexes and further adjust solubility. Formulation of core – lipid anchor polyplexes requires lipid anchors to be deposited on the hydrophobic patches of the core polyplex during solvent exchange inside the microchannel. This step is crucial for controlling the hydrodynamic diameter of generated nanoparticles since manually adding lipid anchor oligomers yields a suspension of polydisperse aggregates (**Figure 8**). Functional structures of interest can be coupled to lipid anchor oligomers by azide – alkyne click chemistry. This modification is possible either before the deposition of lipid anchors on core polyplexes or afterward. Here, PEG-ligand oligomers (**Figure 1A**) were attached to lipid anchors 24 h before formulation with

core polyplexes. The PEG-ligands were used to investigate the influence of PEG length on transfection efficiency. They feature one dibenzozyclooctyne (DBCO) moiety, a PEG chain, and one molecule folic acid (FolA). The DBCO group enables the rapid and copper-free reaction with azide groups, while the folic acid moiety facilitates binding folic acid receptors. PEG chains serve two purposes in this design: firstly, to shield the positive charge of the core polyplexes, and secondly, to expose folic acid to the environment. Their influence is investigated by using PEG chains of various lengths (number of EO repetitions: 0, 3, 12, 24, or 48). Lipid anchors and PEG-ligands were coupled 24 h prior to polyplex formulation. Since lipid anchors already feature a PEG12 chain, lipid anchor – PEG-ligand oligomers have a total number of 12, 15, 24, 36, or 60 EO repetitions. Polyplexes from *CO* oligomers with siRNA and lipid anchor – PEG-ligands are named after their total number of EO repetitions, for example, "*P12-24F*" for polyplexes with lipid anchors with DBCO-PEG24-FolA modification.

3.2.2. Polyplex characterization

Multiple experiments characterizing polyplexes can only contribute viable information about a formulation if it is ensured that the starting formulation is in equilibrium at the time of each experiment. Troiber et al. (Troiber et al., 2013b) have found particles assembled from the same class of oligomers to be stable over three weeks. Here, I have investigated the changes in size, PDI, and zeta potential of our core formulation over 90 min (**Figure 9**). I saw no changes in size and PDI. I did note some changes in zeta potential up to 40 min, which is the reason why formulations were always used after 45 min incubation time.

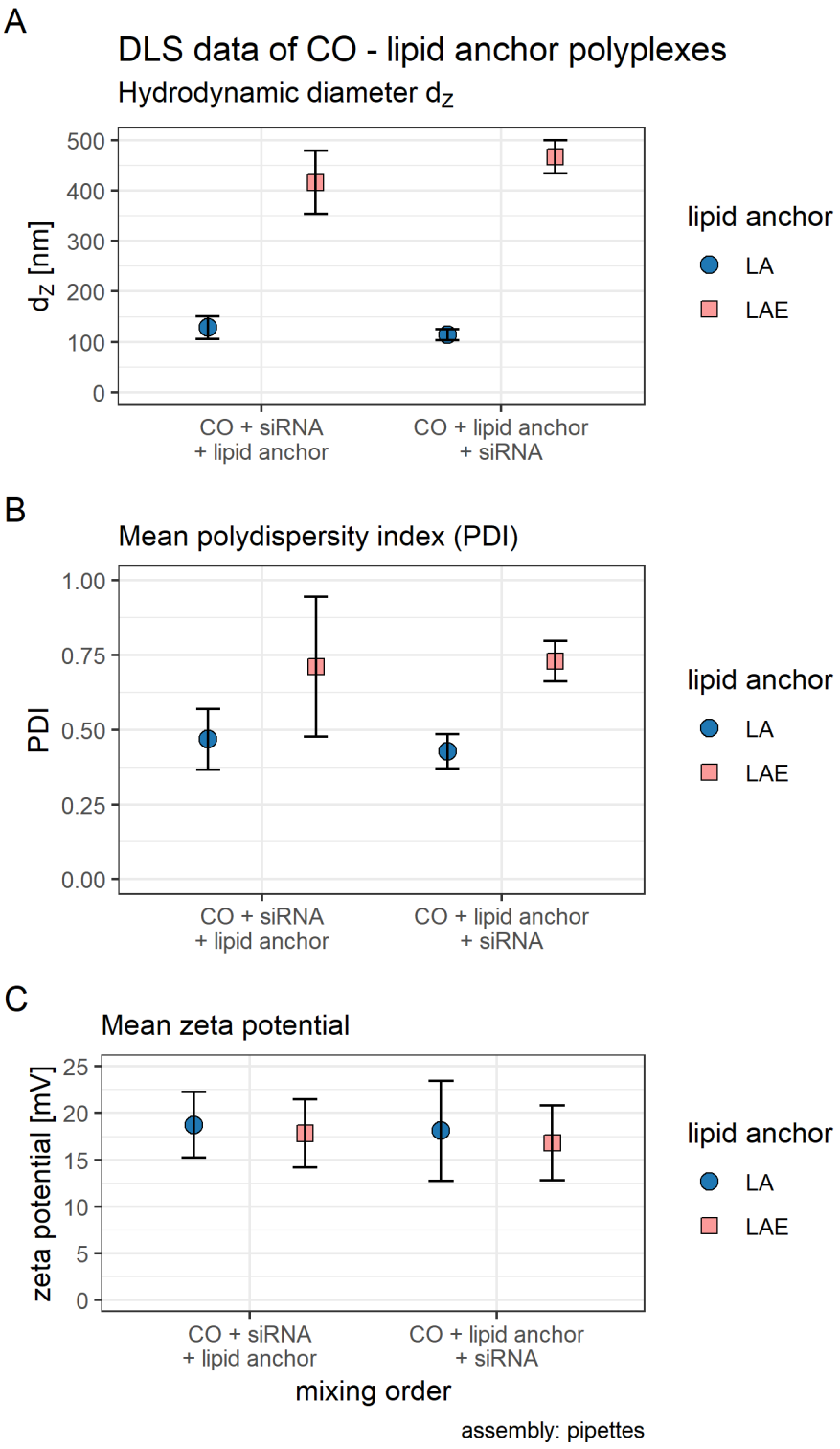

Figure 8: DLS data of core (*CO* + siRNA) – lipid anchor polyplexes produced by bulk mixing. The mixing order is denoted on the x-axis. At first, the components written in the first line were mixed. Second, the third component was added to the mixture by rapid pipetting. Whenever *CO* and siRNA were mixed, was it in the first or second step, the mixture was incubated for 45 in before the next step. Shape and color indicate which lipid anchor was used: Blue circle: *LA*, orange cube: *LAE*. (A) Mean hydrodynamic diameter (z-average). (B) Mean polydispersity index (PDI). (C) Mean zeta potential measured in HBG pH 7.4. Statistics: (A) and (B) Error bars correspond to 95% confidence intervals. (C) Error bars correspond to mean zeta deviations. N = 3.

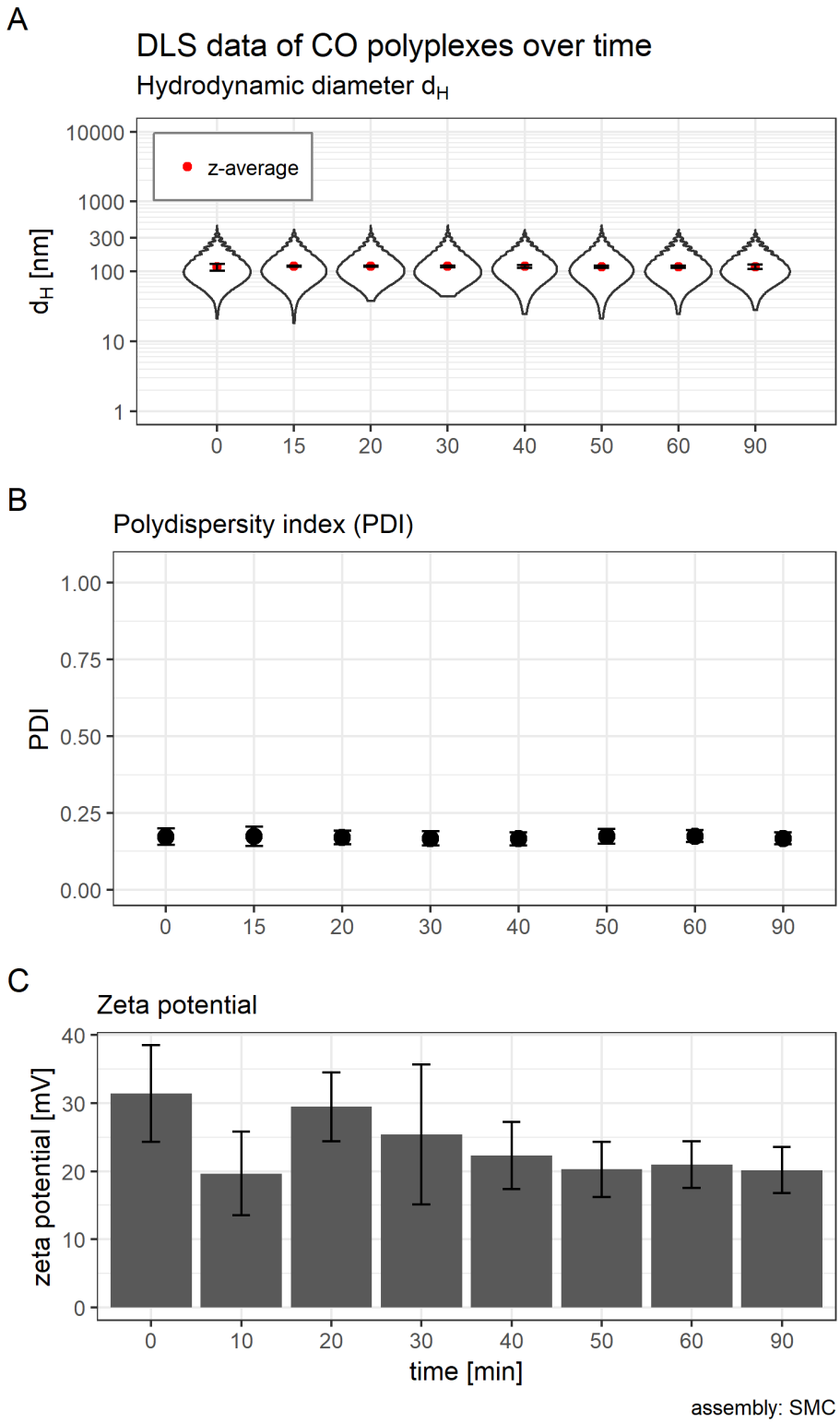

Figure 9: DLS data of core polyplexes (*CO* + siRNA) to assess stability over time.
Core polyplexes were repeatedly measured at different time points denoted at the x-axis. (A) Hydrodynamic diameter (d_H) of the polyplexes with mean z-average (red dots) and respective intensity distribution depicted as violin plot (extension in x-direction corresponds to the percentage of the total intensity measured at the specific size depicted on the y-axis). Caption states assembly method: polyplexes were prepared inside the single meander channel (SMC). (B) Polydispersity index (PDI). (C) Zeta potential measured in HBG pH 7.4. Caption states assembly method: core was prepared conventionally with pipettes. Statistics: (A) and (B) Error bars correspond to 95% confidence intervals. (C) Error bars correspond to mean zeta deviations. N = 3.

3.2.2.1. Size

Core polyplexes (*CO* + siRNA) with comparable properties were generated either by conventional bulk mixing, or at a T-junction, or with microfluidics. Integrating lipid anchor or lipid anchor PEG-ligand oligomers increased size and PDI moderately. Hydrodynamic diameter, zeta potential, and PDI of polyplexes were measured by DLS (**Figure 10** and **Figure 11**), and sizes were confirmed with transmission electron microscopy (TEM) (**Figure 12B**).

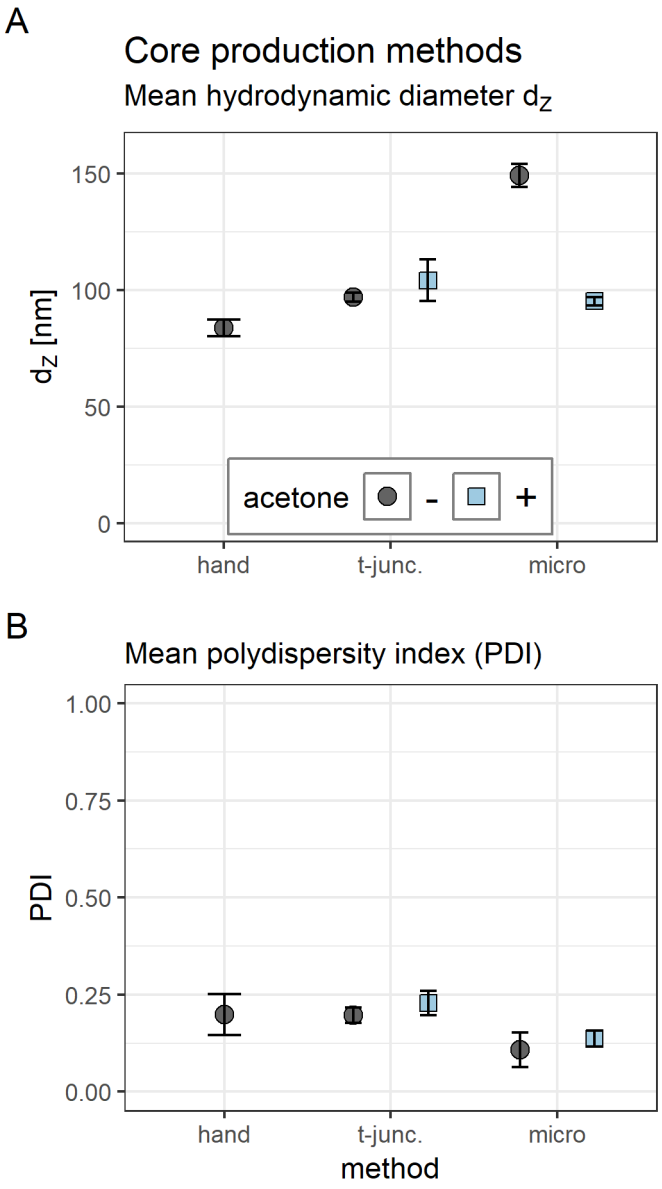

Figure 10: Comparison of core polyplex (*CO* + siRNA) production methods.
(A) Mean hydrodynamic diameter in nm. (B) Mean polydispersity index (PDI). Method key: hand: mixing equal volumes of *CO* and siRNA solution by vigorous pipetting. T-junc.: mixing equal volumes of *CO* and siRNA solution (with or without 50% acetone) at a T-junction at 60 ml/h total flow rate. Micro: mixing an 11× larger volume of *CO* with siRNA solution (with or without 50% acetone) inside the single meander channel at 1.326 ml/h total flow rate. Grey spheres: no acetone was used. Blue cubes: acetone was used. Error bars correspond to 95% confidence intervals; N =3.

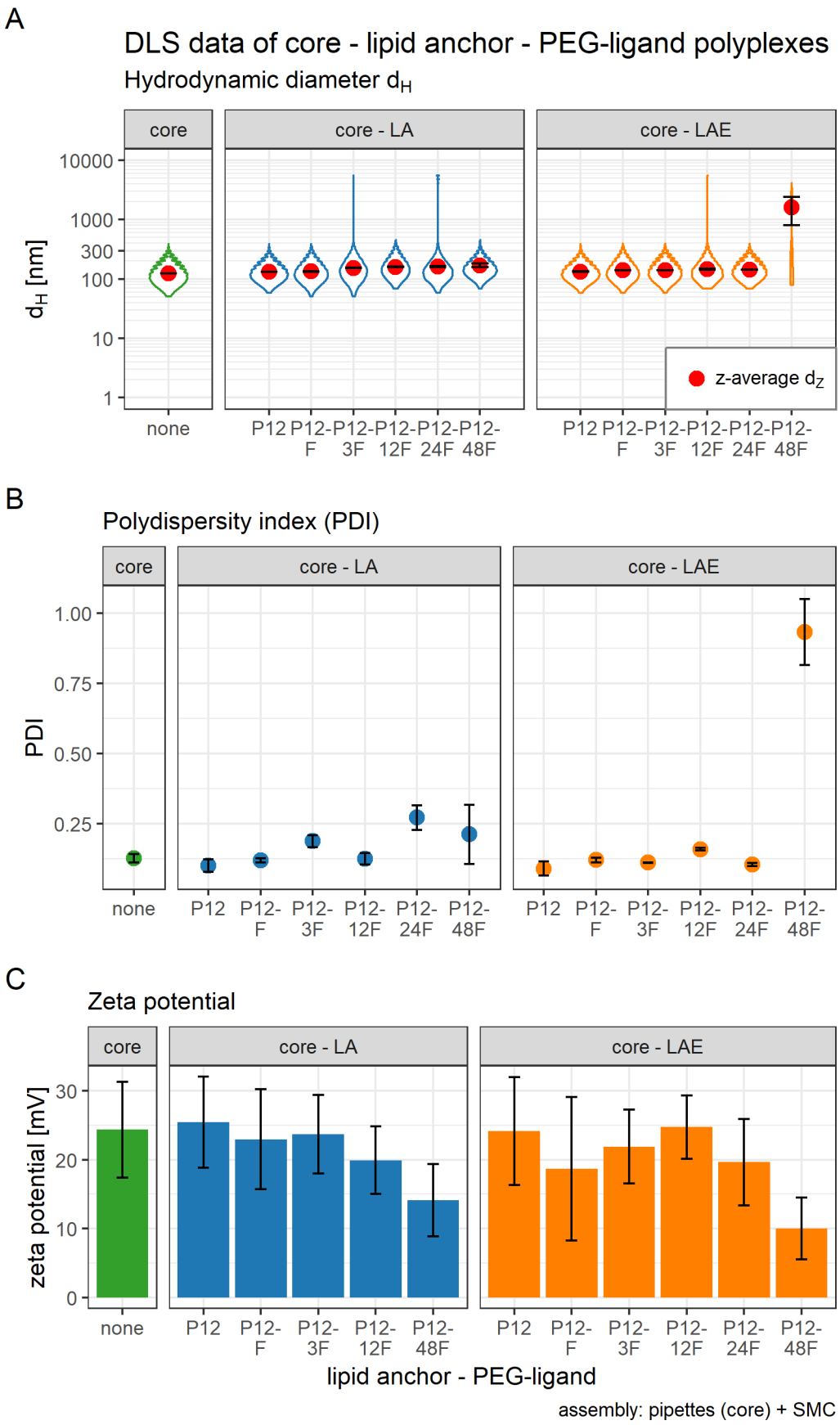

Figure 11: Hydrodynamic diameter (d_H), PDI, and zeta potential of core, core-lipid anchor, and core – lipid anchor – PEG-ligand polyplexes.

Subfigures are divided into three panels. “core” (green) depicts particle properties of the core polyplex formulation used for all subsequent modifications with 20 mol % lipid anchor and lipid anchor-PEG-ligands. “core-*LA*” (blue) and “core-*LAE*” (orange) indicate the lipid anchor oligomer used for attaching PEG-ligands to the core polyplex. Formulation key: P12-xxF: number of ethylene oxide repetitions from lipid anchors + PEG-ligands, F: Folate. Detailed PEG-ligand description in **Figure 1A**.

Compacting siRNA conventionally with core oligomers (*CO*) by rapid pipetting yields particles with a mean hydrodynamic diameter (d_Z) of 84 nm (**Figure 10A**). The PDI is very low (PDI < 0.20; **Figure 10B**). Increasing control over this process either at a T-junction or with a microfluidic device, however, needs certain additional conditions to be met in order to produce similar particles. At a T-junction, the total flow rate needs to be very high (here: 60 ml/h) to generate particles with a hydrodynamic diameter of 97 nm and a PDI < 0.20. The addition of acetone does only lead to comparable particles and PDIs when flow rates of both components are identical, and *CO* is dissolved in 50% acetone, as depicted in **Figure 10** (d_Z = 104 nm, PDI < 0.23). This approach, however, results in an acetone concentration of 25% in the final product requiring additional efforts by evaporation or dialysis to remove the organic solvent when using it *in vitro* or *in vivo*. A comparison of the influence of flow rate, acetone, and flow rate differences of 1:2 or 1:10 on polyplexes characteristics produced at a T-junction is shown in **Figure 13**.

When preparing polyplexes, it is paramount to decrease diffusion lengths or to increase the time needed for efficient siRNA compaction. Otherwise, the influence on kinetically controlled polyplex formation is decreased, and the size and polydispersity of the nanoparticles increases. Diffusion lengths inside the microchannel were minimized by flow rate differences > 1:10, and acetone was used to retard siRNA compaction. Previous experiments have shown that feeding the two outer channels with diluted siRNA solution and the middle channel with concentrated *CO* solution generates particles in an acceptable size range (data not shown). Here, a substantial difference in PDI and hydrodynamic diameter was observed when polyplexes were generated with (d_Z = 95 nm, PDI < 0.14) or without (d_Z = 149 nm, PDI < 0.11) additional acetone (**Figure 10**).

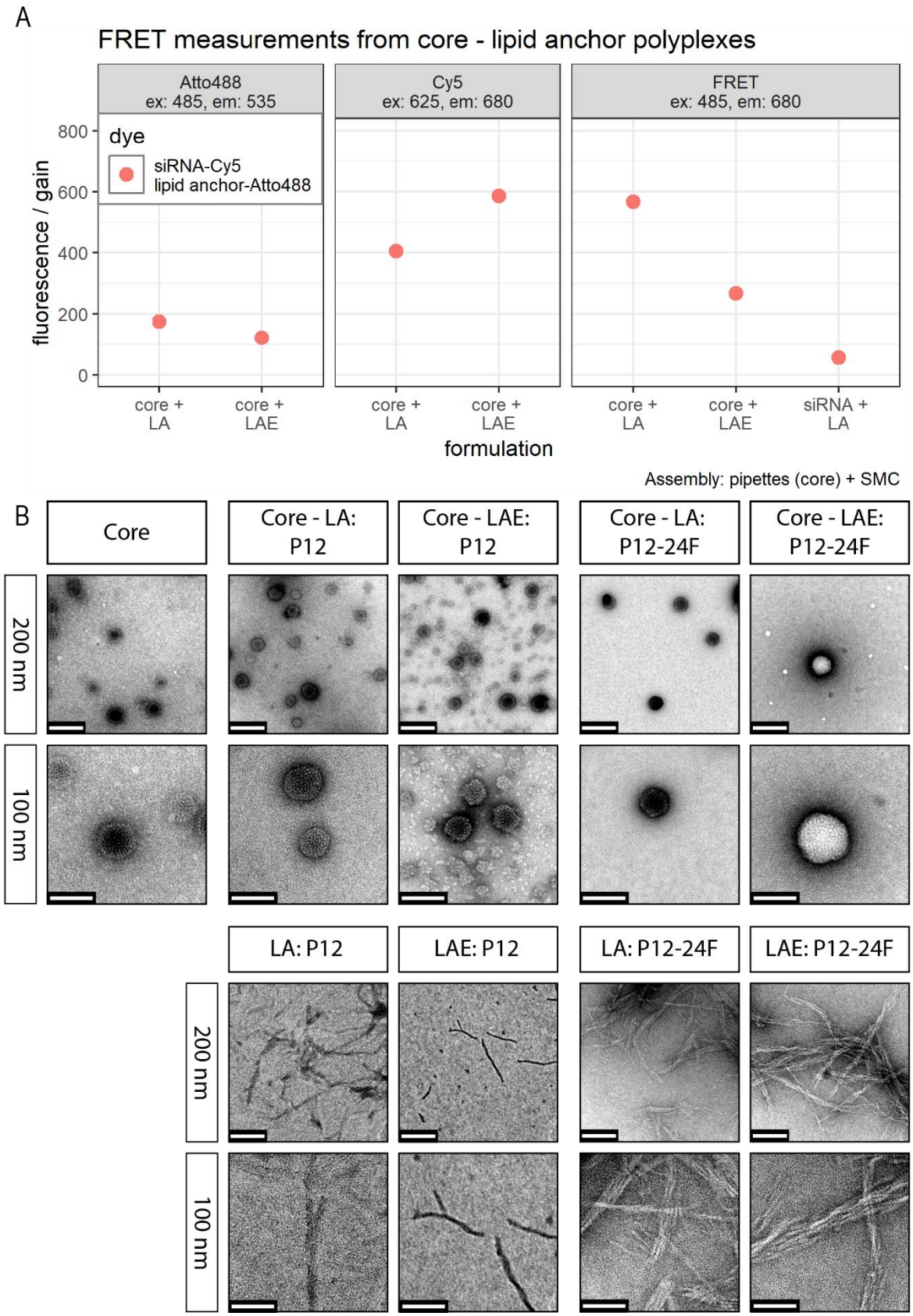

Figure 12: FRET and TEM measurements of core (*CO* + siRNA)-lipid anchor polyplexes and their components.
(A) The title of each panel indicates the dye measured. FRET: excites Atto488 (485 nm), measures Cy5 (680 nm). The color indicates dyes used in this formulation. "Sample" specifies formulation composition: "core + *LA*": core polyplex with 20 mol % *LA* oligomers. "siRNA + *LA*": control

formulation without core oligomers, that is, no particle formation. Cy5 is coupled to the sense strand of siRNA. Atto488 is coupled via azide – alkyne click chemistry to the azide of *LA* or *LAE* oligomers. Measured fluorescence is divided by the value of the gain to exclude amplifier effects. Assembly: core polyplexes were prepared with pipettes, lipid anchors were added with the single meander channel (SMC). (B) Vertical label: scale represented by the white bar of the respective row. Horizontal label: formulation visible in the respective column. "Core": core polyplex. "Core-*LA*/*LAE*: P12": core-lipid anchor polyplex. "Core + *LA*/*LAE*: *P12-24F*": core – lipid anchor – PEG-ligand polyplex. Columns without "core" depict unformulated lipid anchors or lipid anchor – PEG-ligand oligomers in solution.

The influence of lipid anchor and lipid anchor – PEG-ligand oligomers on core polyplexes was investigated. To this end, *LA* or *LAE* with or without their respective PEG-ligand oligomers (**Figure 1A**) were attached to conventionally prepared core (*CO* + siRNA) polyplexes inside the microchannel (SMC, **Figure 1B**). As described in detail in the methods section, it is essential to use concentrated lipid anchor solutions and diluted core polyplex solutions.

This setting ensured that only a thin stream of lipid anchor solution is flowing through the Y-junction, accelerating the solvent exchange from 50% to 4.8% acetone and facilitating the association of the hydrophobic lipid anchor with the fatty acids in the structure of the core. Particle size, PDI, and zeta potential of the polyplexes were measured by DLS (**Figure 11**).

In order to gain a better understanding of the intensity distribution, violin plots are provided in addition to z-average values. Therefore, z-average values can be better assessed based on the underlying distribution, be it mono- or multimodal. The expansion in x-direction represents the relative frequency the respective size has been measured. The z-average is located close to the position with the largest expansion in the x-direction for monomodal distributions (e.g., in the panel labeled "core"). When the distribution is multimodal, however, z-average's position can be quite misleading (e.g., in the panel core-*LAE*, sample *P12-48F*), and the intensity distribution needs to be considered. The effect of adding 20 mol % (relative to n_{CO}) lipid anchor or lipid anchor – PEG-ligand oligomers to core polyplexes depended on the length of the PEG-ligand on the respective lipid anchor.

The addition of *LA* containing oligomers to the core formulation (d_Z = 123 nm, PDI < 0.13) increased hydrodynamic diameters of resulting nanoparticles moderately from 131 nm (*LA* alone) to 169 nm (*LA*: *P12-48F*). Additionally, PDI decreased with the addition of *LA* (PDI < 0.11) or *LAE* (PDI < 0.10) oligomers and increased from PDI < 0.12 to PDI > 0.20 with longer PEG-ligands. The hydrodynamic diameter of *LAE* containing polyplexes was generally ~15 nm smaller than in *LA* containing formulations. Although *LAE* oligomers with longer PEG-ligands were more likely to form aggregates (*LAE*: *P12-48F*). As expected, the zeta potential of core polyplexes alone in HBG was positive with ZP = 24 mV due to the high N/P charge ratio.

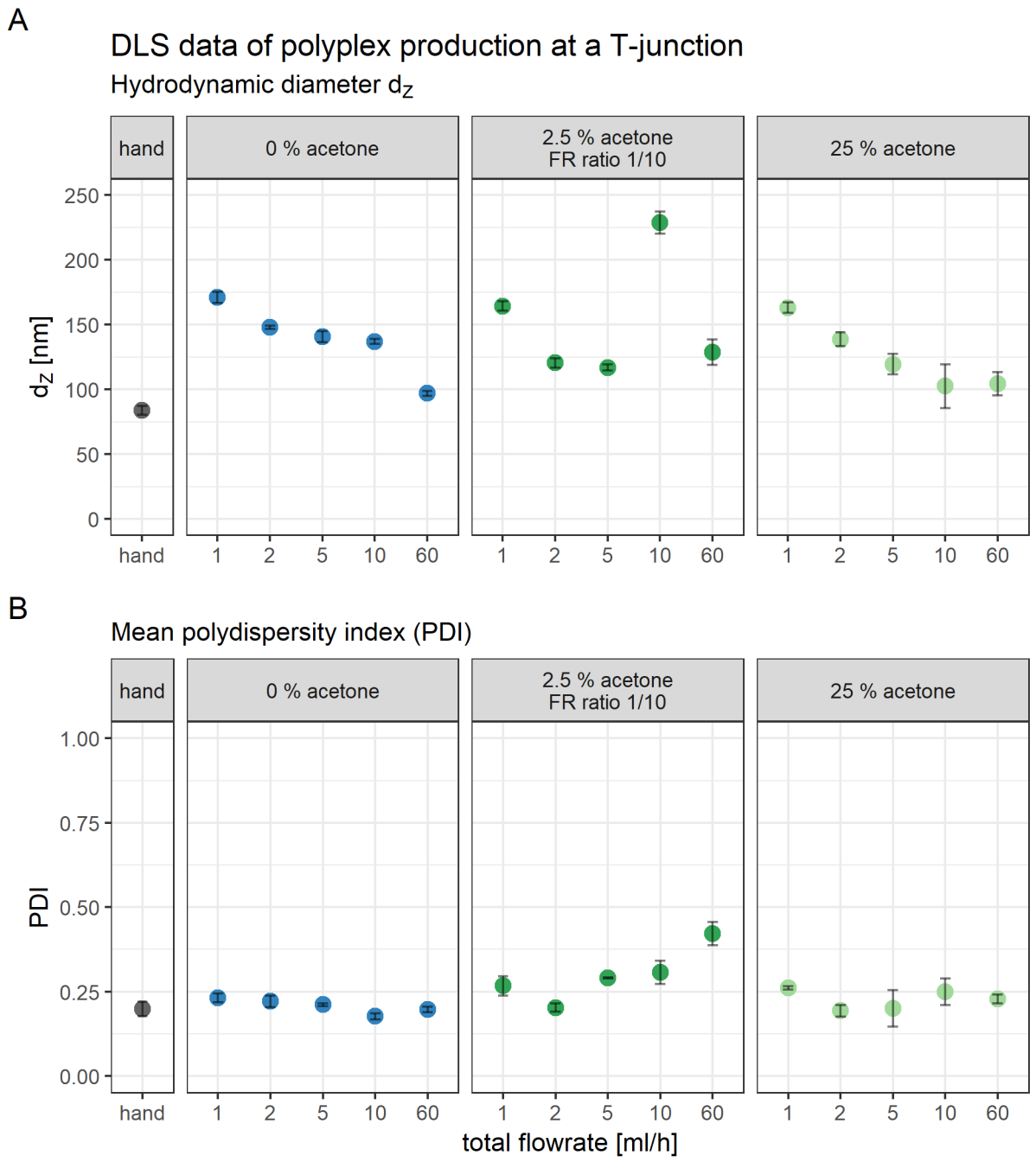

Figure 13: DLS data of core (*CO* + siRNA) polyplexes produced at a T-junction.
siRNA is dissolved in HBG pH 7.4; *CO* is dissolved either in HBG pH 7.4 (panels 1 and 2) or HBG pH 7.4 with 50% (v/v) acetone (panels 3 and 4). Subfigures are divided into four panels. Panel "hand": Bulk mixed polyplexes for comparison. Remaining panels: Depict the remaining amount of acetone in the final formulation. For panels 2 and 4, solutions were pumped at equal flow rates, while solutions depicted in panel 3 were pumped with a flow rate (FR) ratio of 1:10 (*CO*:siRNA). (A) Mean hydrodynamic diameter (z-average). (B) Mean polydispersity index (PDI). Statistics: Error bars correspond to 95% confidence intervals. N = 3.

Incorporation of 20 mol % *LA* or *LAE* with or without PEG-ligands had only a limited effect on the zeta potential of the particles, except for particles with *P12-48F* PEG-ligands

(**Figure 11C**). Incorporation of *LA*: *P12-48F* or *LAE*: *P12-48F* decreased mean zeta potential to 14 and 10 mV, respectively.

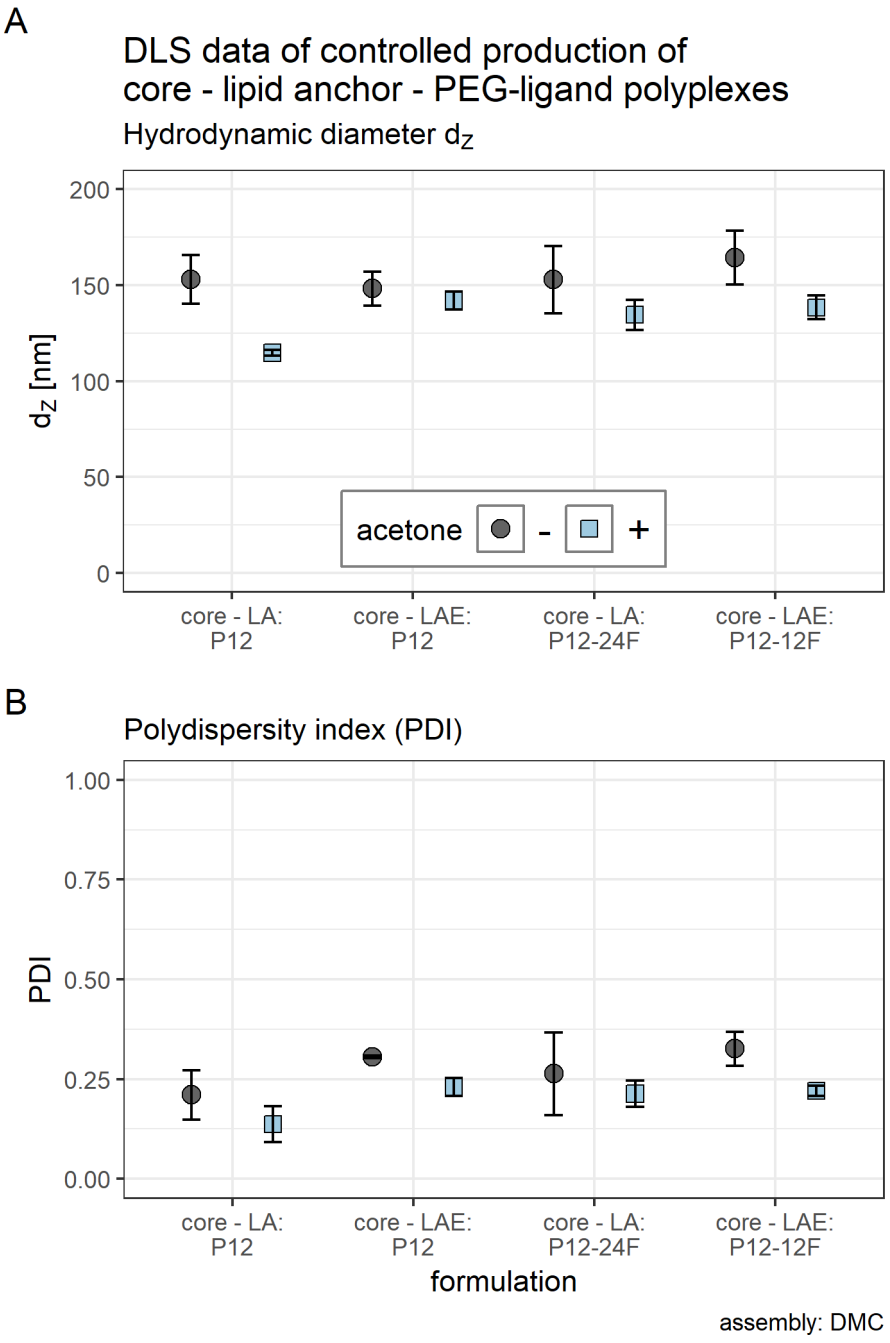

Figure 14: Automated production of core (*CO* + siRNA) – lipid anchor – PEG-ligand polyplexes. Solvents with or without acetone; assembly completely inside the double meander channel (DMC). First junction: *CO*:siRNA = 1:10, siRNA in HBG pH 7.4, *CO* in HBG pH 7.4 ± 50% acetone. 1.0 ml/h total flow rate. Second junction: core polyplex:lipid anchor oligomer (±PEG-ligand) = 1:11, lipid anchor or lipid anchor – PEG-ligand oligomer in HBG pH 7.4 ± 50% acetone, 1.1 ml/h total flow rate. Formulation key: core: core polyplex, *LA*/*LAE*: lipid anchors, Px or Px−y: ethylene oxide repetitions: x = 12 from *LA*/*LAE*; y = 12 or 24 from PEG-ligands, F: folic acid. See **Figure 1A** for detailed structures (A) Mean hydrodynamic diameter (z-average) in nm. (B) Mean polydispersity index (PDI). Grey spheres: *CO* was dissolved in HBG pH 7.4. Blue cubes: *CO* was dissolved in HBG pH 7.4 with 50% acetone. Error bars correspond to 95% confidence intervals; N = 3.

Finally, after having scrutinized all steps independently, core – lipid anchor – PEG-ligand polyplex production from its single components inside one microchannel was investigated. The DMC (**Figure 1B**) was used. Syringe S3 was filled with siRNA in HBG and S4 with *CO* in HBG with or without 50% acetone. Syringes S2 were loaded with four different oligomers in HBG with 50% acetone: *LA*, *LA*: *P12-24F*, *LAE*, or *LAE*: *P12-12F*. Eight runs were conducted, each lipid anchor or lipid anchor – PEG-ligand oligomer was mixed with core polyplexes produced with or without the aid of acetone. Sizes were comparable to the core – lipid anchor – PEG-ligand polyplexes with conventionally prepared cores when no acetone was used in the core production step. When *CO* was dissolved in 50% acetone, however, polyplexes completely prepared with microfluidics had a smaller hydrodynamic diameter and PDI (**Figure 14**).

3.2.2.2. Lipid anchor integration

LA and *LAE* integrate into core polyplexes.

Investigation of *LA* and *LAE* integration into core polyplexes was carried out by TEM and FRET measurements. TEM measurements revealed that formulations from siRNA and *CO* form spherical particles with a diameter of < 100 nm (**Figure 12B**), which is in good agreement with DLS measurements (**Figure 11A**).

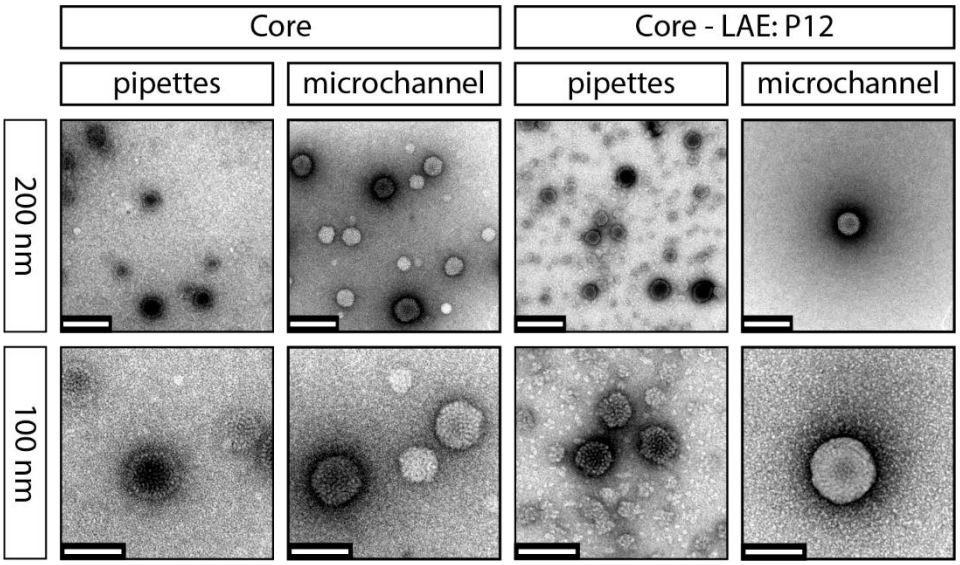

Figure 15: TEM: Comparisons of polyplexes produced with pipettes or with the double meander channel (DMC).
Vertical label: Scale represented by a white bar of the respective row. Horizontal label: Formulation visible in the respective column. "Core": Core polyplex. "Core – *LAE*: P12": Core-lipid anchor polyplex. "pipettes" and "microchannel" indicate assembly method.

There was no apparent difference when particles were produced conventionally or with microfluidics (**Figure 15**). *LA* and *LAE* with or without covalently bound PEG-ligands alone

form tubular or fibrous structures on the TEM grid that could not be found when formulated together with core polyplexes. This finding suggests that lipid anchor oligomers are indeed interacting with core polyplexes.

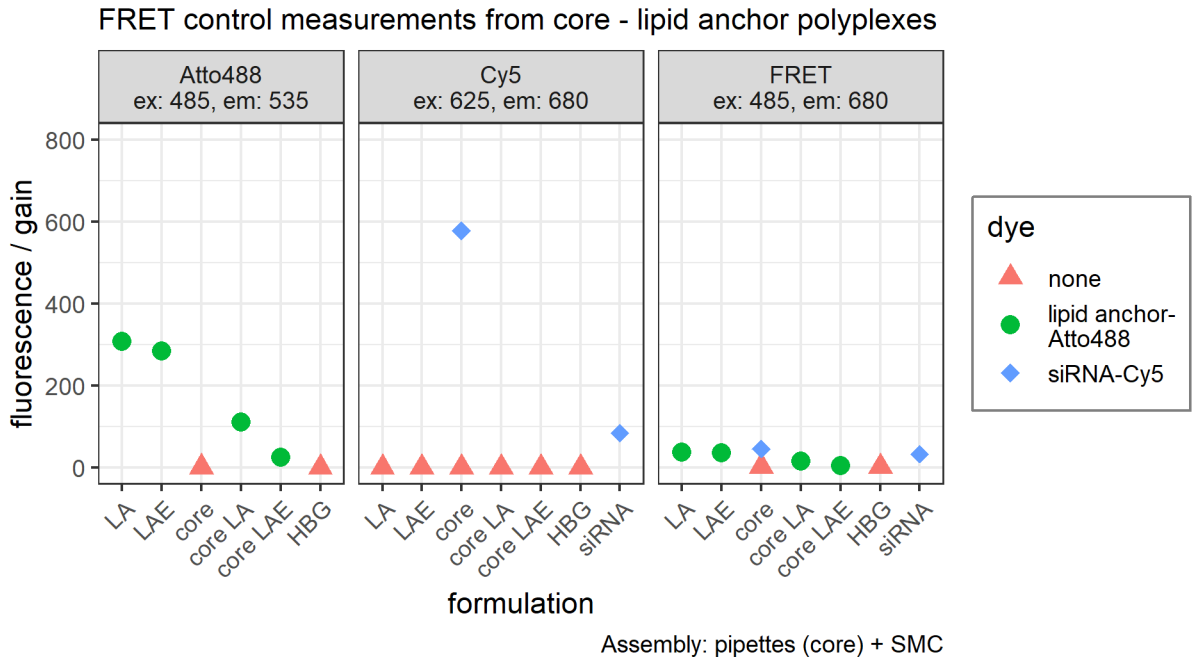

Figure 16: FRET control measurements of core (*CO* + siRNA) – lipid anchor polyplexes and their components.
The title of each panel indicates dye measured: Atto488: excites (485 nm) and measures (535 nm) Atto488 dye. Cy5: excites (625 nm) and measures (680 nm) Cy5 dye. FRET: excites Atto488 (485 nm), measures Cy5 (680 nm). Assembly: core polyplexes were prepared with pipettes, lipid anchors were added with the single meander channel (SMC). The color indicates dyes used in this formulation. "formulation" specifies formulation composition (e.g., "core + *LA*": conventionally prepared core polyplex with 20 mol % *LA* lipid anchor oligomers added inside the SMC). Cy5 is coupled to the sense strand of the siRNA. Atto488 is coupled via azide – alkyne click chemistry to the azide of *LA* or *LAE* oligomers. Measured fluorescence is divided by the value of the gain to exclude amplifier effects.

FRET measurements supported these findings obtained by TEM. Receiving measurable FRET signals implies a distance <10 nm between chromophores (Förster, 1948; Clegg, 1996). Here, 50% siRNA with one molecule Cy5 on the sense strand was used for conventional core polyplex formation. Lipid anchor oligomers were modified with 0.75 equivalents (relative to the azide of the lipid anchors) DBCO-PEG4-Atto488 and subsequently deposited on the conventionally prepared core polyplex using solvent exchange inside the micro-channel (SMC). These polyplexes emitted strong FRET signals when Atto488 dyes were excited, and fluorescence was measured from Cy5 dyes alone (**Figure 12A**). When *CO* was missing from the formulation, polyplex formation did not occur, making energy transfer between dyes a function of their dilution only (sample "siRNA + *LA*" in panel "FRET" in **Figure 12A**). All control experiments

(FRET measurements from polyplexes with only one dye and fluorescence measurements of both dyes separately) are depicted in **Figure 16**.

3.2.2.3. Stability

Lipid anchors do not influence the stability of core polyplexes.

Polyplex stability was assessed with two different methods. The general ability of polyplexes to compact and hold siRNA back under the influence of an electric field was investigated with an agarose gel shift assay and its densitometry analysis to simplify the comparison of bands. Ability to compact siRNA and resist polyanionic stress was tested with an ethidium bromide (EtBr) displacement assay with or without additional heparin. Polyplexes from *CO* and siRNA were prepared conventionally in HBG, and lipid anchors ± PEG-ligands were attached inside the microchannel (SMC). Samples were diluted 1:10 with HBG or serum (FBS). Additionally, samples containing serum were incubated at 37 °C for up to 24 h to assess stability under the influence of body temperature and serum components.

There was no visible difference between all formulations at t = 0h with or without additional FBS. (**Figure 17** and **Figure 18**). At the 4 h mark, only small differences between samples were visible, while all samples retained most of their payload. After 24 h, core – lipid anchor or core – lipid anchor – PEG-ligand formulations revealed a slight decrease in siRNA retention capability in comparison to the core formulation alone. At this time, the core – *LAE* formulation seemed to be better at retaining siRNA than the core – *LA* formulation. When lipid anchors coupled with PEG-ligands were used, however, core – *LA* – PEG-ligand formulations retained siRNA better than their *LAE* containing counterparts.

Polyplexes (*CO* + siRNA) were prepared conventionally, and lipid anchors were added inside the SMC for the EtBr displacement assay with and without heparin competition. In this assay, *LA* and *LAE* containing polyplexes showed unaltered protection against dye displacement behavior. Fluorescence without additional heparin for the core formulation, the core-*LA* formulation, and the core-*LAE* formulation was 14%, 18%, and 11% of the positive control, respectively. 1 IU/ml heparin increased fluorescence to 37%, 39%, and 22%. Total displacement was observed at heparin concentrations above five IU/ml (**Figure 19**).

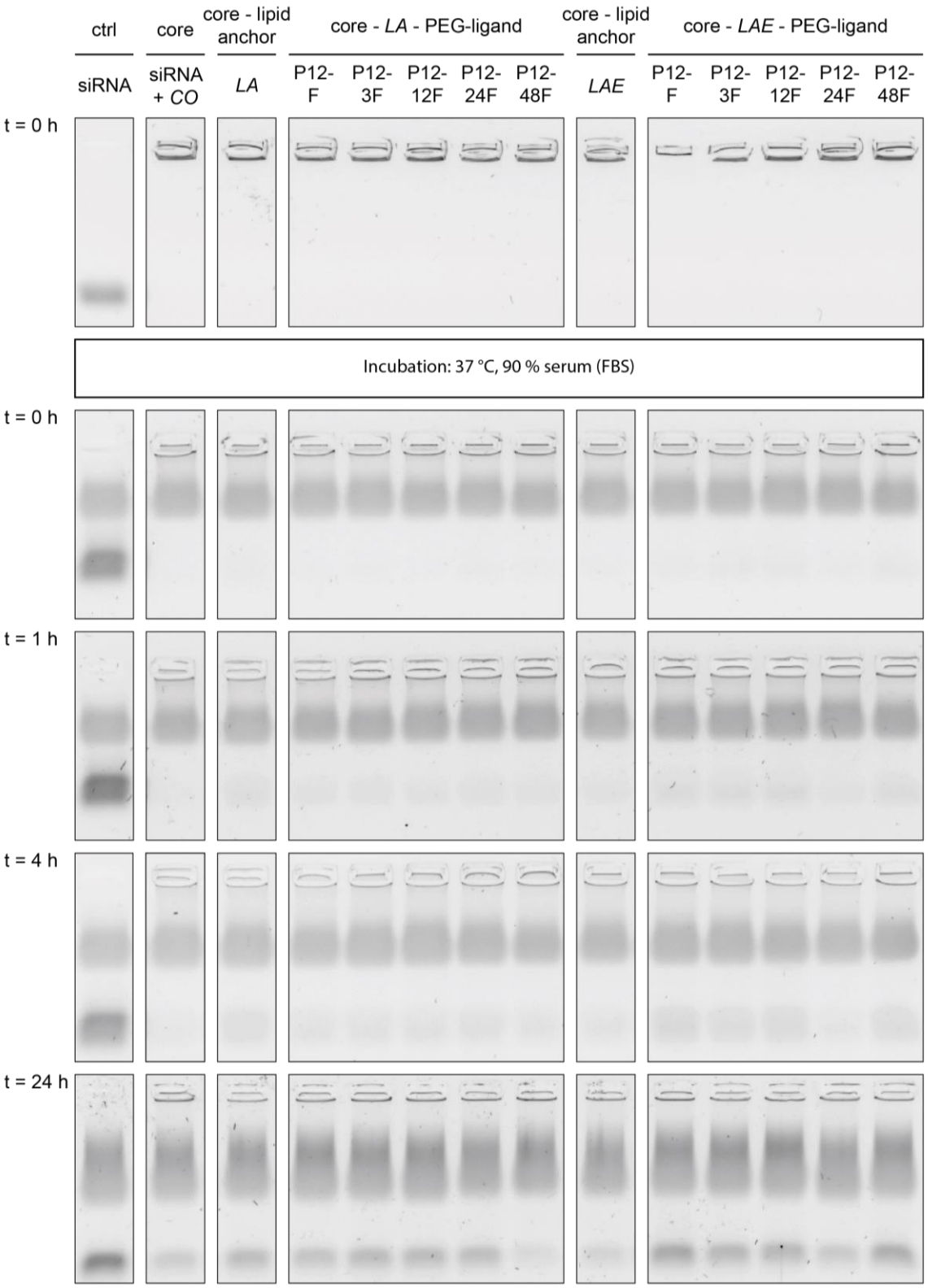

Figure 17: Agarose gel shift assay.
Core (*CO* + siRNA) – lipid anchor (*LA*/*LAE*) – PEG-ligand polyplexes. Key: P12-xxF: the total amount of ethylene oxide repetitions (*LA*/*LAE* + PEG-ligand). Assembly: core polyplexes were prepared with pipettes, lipid anchors were added with the single meander channel (SMC). Solvent: 100% HBG or HBG + 90% fetal bovine serum (FBS), up to 24 h incubation at 37 °C. Gel: 1% agarose in 1× TBE buffer with 0.1% GelRed®. A total of 17% loading buffer. Runtime: 1 h, 80 V. t: Time from formulation until measurement; t > 0: incubated at 37 °C. First row: 100% HBG pH 7.4, other rows: 10% HBG pH 7.4, 90% FBS.

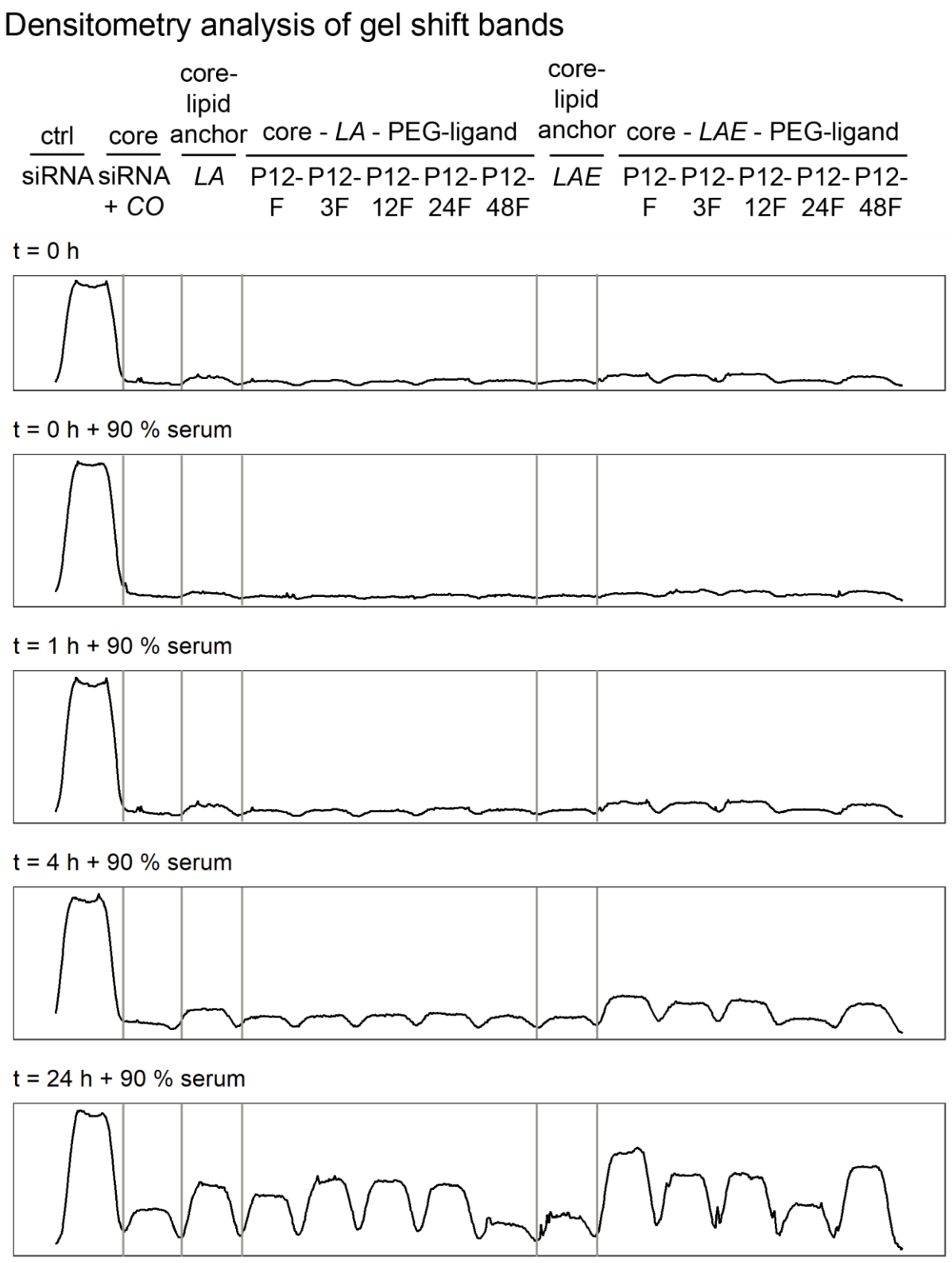

Figure 18: Densitometry Analysis.
Core (*CO* + siRNA) – lipid anchor (*LA*/*LAE*) – PEG-ligand (FolA) polyplexes. Key: P12-xxF: the total amount of ethylene oxide repetitions (*LA*/*LAE* + PEG-ligand). Assembly: core polyplexes were prepared with pipettes, lipid anchors were added with the single meander channel (SMC). Solvent: 100% HBG or HBG + 90% fetal bovine serum (FBS), up to 24 h incubation at 37 °C. Gel: 1% agarose in 1× TBE buffer with 0.1% GelRed®. A total of 17% loading buffer. Runtime: 1 h, 80 V. t: Time from formulation until measurement; t > 0: incubated at 37 °C. First row: 100% HBG pH 7.4, other rows: 10% HBG pH 7.4, 90% FBS.

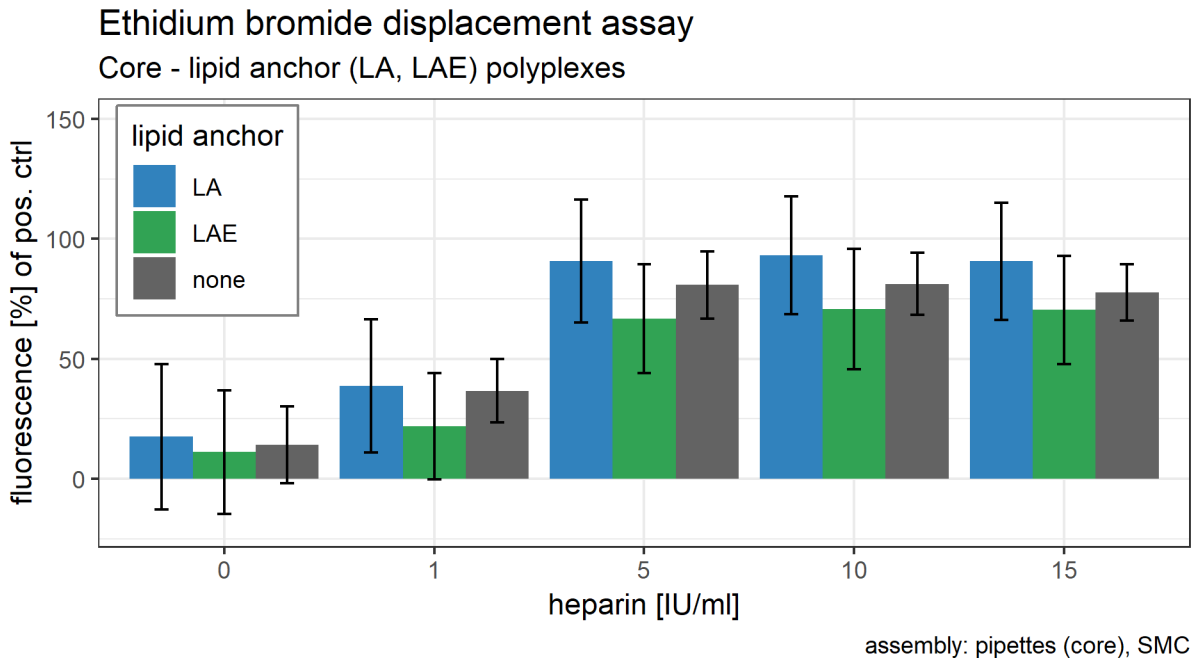

Figure 19: Ethidium bromide displacement assay ± heparin stress.
Core (*CO* + siRNA) – lipid anchor (*LA*/*LAE*) polyplexes were incubated with ethidium bromide, and the increase of fluorescence relative to siRNA with dye alone was measured. Assembly: core polyplexes were prepared with pipettes, lipid anchors were added with the single meander channel (SMC). Resistance to anionic stress was investigated with the addition of heparin. Key: *LA*: core (*CO* + siRNA) + 20 mol % *LA*; *LAE*: core (*CO* + siRNA) + 20 mol % *LAE*; none: core (*CO* + siRNA) alone. Mean fluorescence of the sample minus the mean fluorescence of the negative control (HBG alone) is reported. Error bars correspond to 95% confidence intervals; N = 3.

3.2.2.4. Toxicity

Core (*CO* + siRNA) – lipid anchor – PEG-ligand polyplexes do not alter the metabolic activity profile of KB cells in comparison to core polyplexes alone. Different fatty acids in oligo-amidoamines have been shown to induce membrane leakage in erythrocytes and to increase cell death in *in vitro* cell assays (Klein et al., 2016; Reinhard, Zhang & Wagner, 2017). The influence of target formulations completely prepared with microfluidics on the metabolic activity of KB cells was assessed by MTT assay to account for any apparent effects on cell survivability. The MTT assay correlates metabolic activity to the amount of formazan dye produced by oxidoreductase enzymes while consuming NAD(P)H. All formulations tested in this assay showed no reduction of formazan absorption relative to untreated KB cells (**Figure 20**).

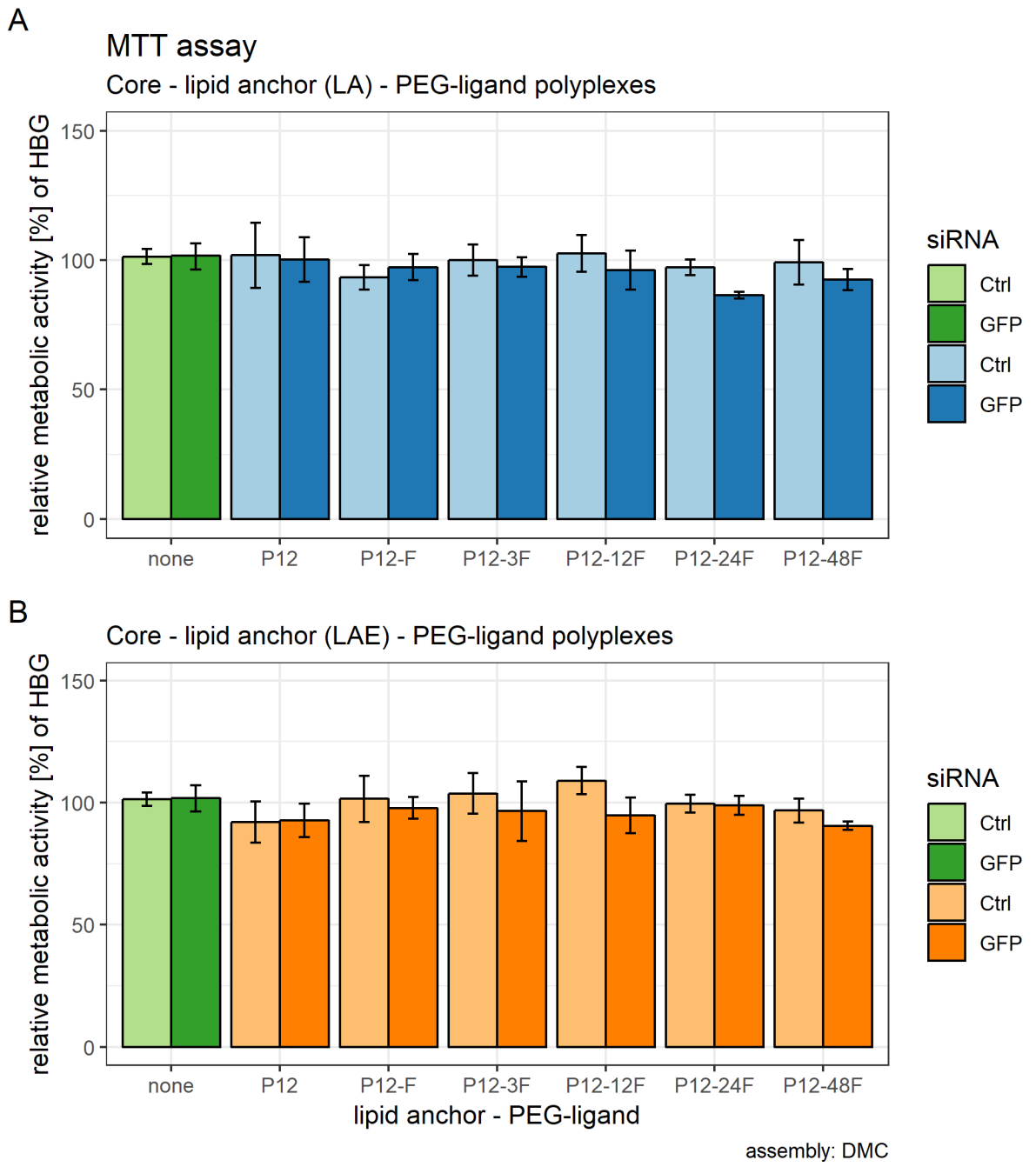

Figure 20: MTT assay of core (*CO* + siRNA) – lipid anchor (*LA*/*LAE*) – PEG-ligand polyplexes. All polyplexes were prepared using the double meander channel (DMC). Values are calculated relative to values of buffer treated cells. Colors indicate the type of siRNA used: Light color: control siRNA, saturated color: siGFP siRNA. "core polyplex" (green bars): core polyplex formulation used for all subsequent modifications with 20 mol % lipid anchors and lipid anchor-PEG-ligands. Formulation key: P12: core polyplex with unmodified lipid anchor. P12-xxF: the total amount of ethylene oxide repetitions (*LA*/*LAE* + PEG-ligand). F: Folate. Detailed PEG-ligand description in **Figure 1A**. (A) Polyplexes with *LA* lipid anchor (blue bars). (B) Polyplexes with *LAE* lipid anchor (orange bars). Statistics: Error bars correspond to 95% confidence intervals. N = 5.

3.2.3. Transfection of core – lipid anchor – PEG-ligand nanoparticles

Core (*CO* + siRNA) – lipid anchor – PEG-ligand nanoparticles with *LA*: *P12-24F* or *LAE*: *P12-12F* showed the largest effect on luciferase reporter gene silencing activity in KB cells.

KB cells possessing an eGFP-luciferase fusion gene controlled by a constitutively active promoter were used in all cell experiments. Gene expression can be modulated by RNA interference: if a siRNA (here: siGFP) that is complementary to any part of the target mRNA (here: eGFP-luciferase fusion mRNA) reaches the cytosol and is incorporated into the RISC complex, the corresponding mRNA will be degraded selectively. In this case, the eGFP-luciferase fusion protein expression is reduced, which in turn leads to a decrease in GFP and luciferase enzymatic activity. Using an *in vitro* bioluminescence assay, gene silencing efficacy of the siRNA formulation can be correlated to the reduction of, in our case, luciferase activity as measured in relative light units (RLUs). Non-siRNA dependent effects on luciferase activity were monitored with cells treated with identical polyplexes containing control siRNA only. Polyplexes were prepared from their starting materials using microfluidics (**Figure 1B**, DMC). The amount of siRNA/well was optimized and set to 500 ng/well (**Figure 21**).

The effects of lipid anchor and PEG-ligands on luciferase activity (**Figure 22**) were estimated using a multifactorial two-way ANOVA. All calculated effects were statistically significant. Main effect of lipid anchors: $F(1, 48) = 8.91$, $p = 0.032$, $\omega^2 = .02$, main effect of PEG-ligands: $F(5, 48) = 14.78$, $p < 0.001$, $\omega^2 = 0.43$, and the interaction effect between PEG-ligands and lipid anchors: $F(5, 48) = 17.02$, $p < 0.001$, $\omega^2 = 0.32$. After it was established that including lipid anchors and PEG-ligands influenced luciferase enzyme activity, post hoc student's t-tests (HOLM corrected) were conducted to identify the statistical significance of each comparison (**Table 15**). Samples with *LA* are shown in **Figure 22A**, samples with *LAE* in **Figure 22B**. **Figure 23** compares siGFP containing samples from **Figure 22A** and **22B** against each other to gauge the influence of the lipid anchor on the polyplexes gene silencing efficacy. Both sets showed an effect on eGFP-luciferase gene silencing activity that is dependent on the length of the PEG-ligand. For *LA* containing formulations, RLUs decreased with increasing PEG length, reached their base with *P12-24F*, and rose again with *P12-48F*. The same pattern was observed with *LAE* containing formulations, except that the base was already reached with *P12-12F*. The influence of polyplexes with *P12-48F* on luciferase activity was comparable to the siCtrl containing particles.

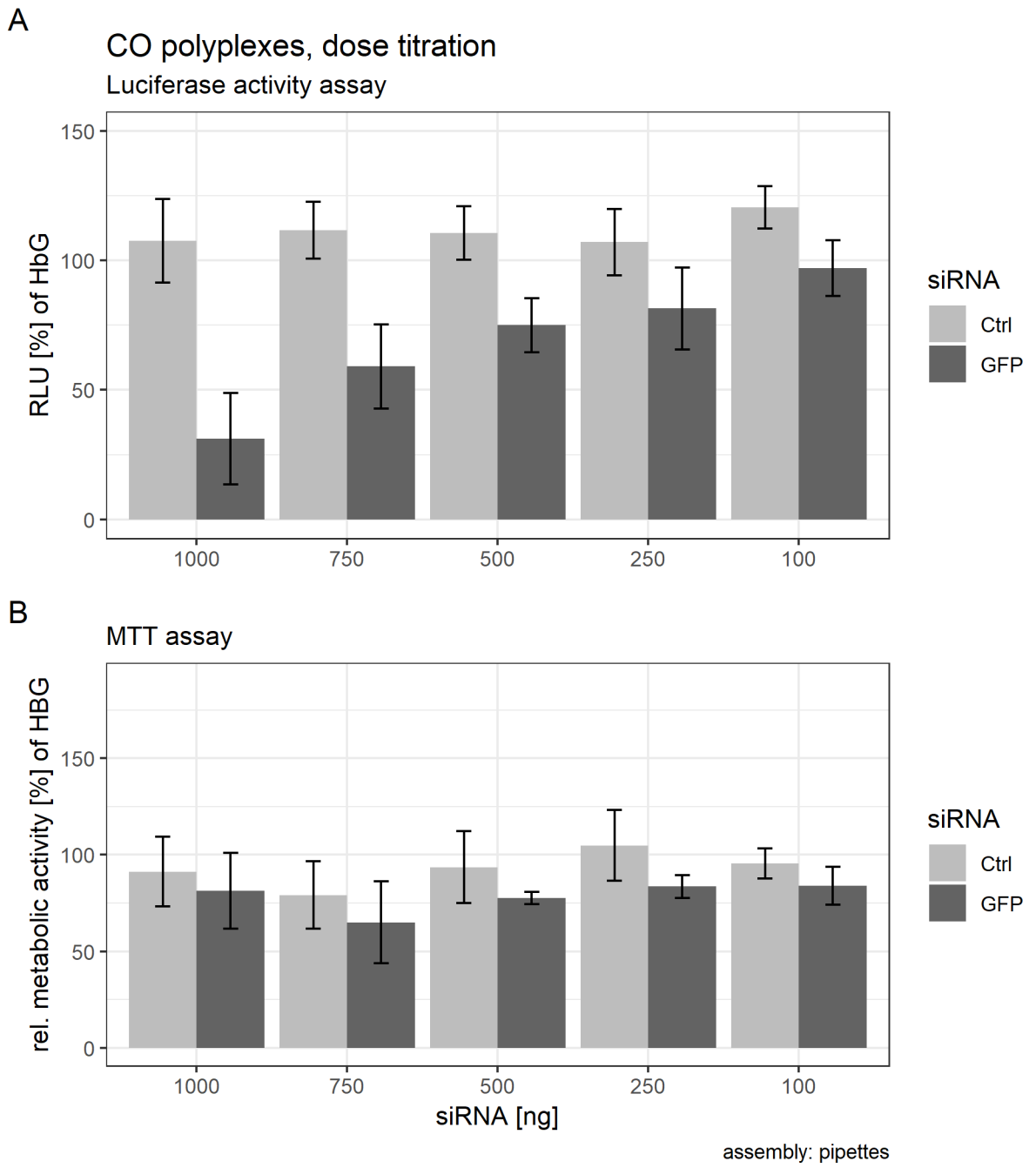

Figure 21: Dose titration assay.
siRNA dose (ng/well) is set in relation to luciferase or metabolic activity. A total of 500 ng was used in all other cell experiments. All polyplexes were prepared using pipettes. (A) Luciferase enzyme activity is measured in relative light units (RLU) and is shown relative to values of buffer treated cells. (B) Metabolic activity is shown relative to buffer treated cells. Colors indicate the type of siRNA used: Light color: control siRNA, saturated color: siGFP siRNA. Error bars correspond to 95% confidence intervals. N = 5.

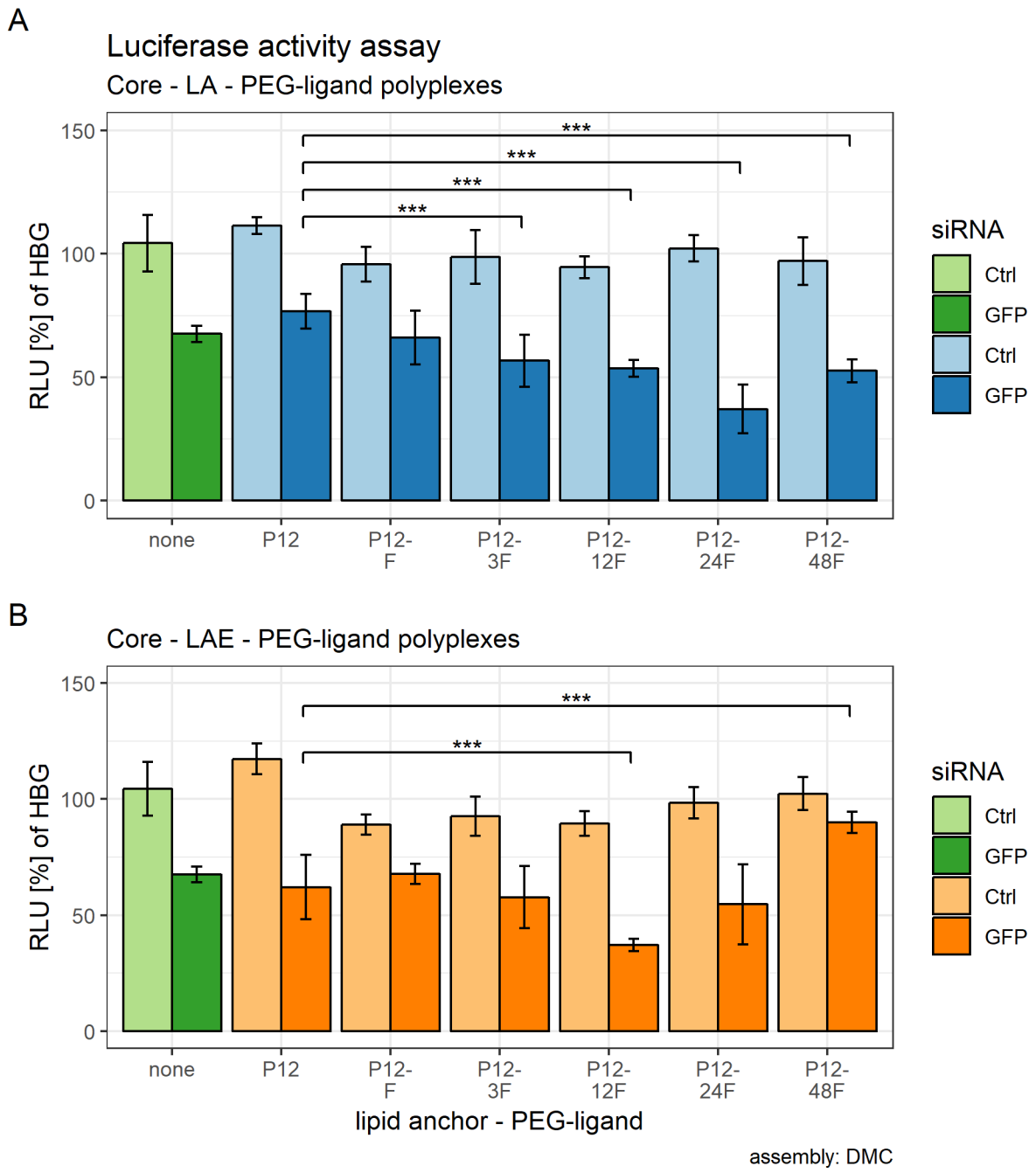

Figure 22: Luciferase activity assay of core (*CO* + siRNA) – lipid anchor – PEG-ligand polyplexes. Luciferase enzyme activity was measured in relative light units (RLU) and is shown relative to values of buffer treated cells. Colors indicate the type of siRNA used: light color: control siRNA, saturated color: siGFPLuc siRNA. Lipid anchor – PEG-ligand key: "none" (green bars): core polyplex formulation alone; used for all subsequent modifications with 20 mol % lipid anchors and lipid anchor – PEG-ligands. P12: core polyplex with unmodified lipid anchor. P12-xxF: PEG12 from the lipid anchor + PEGxx from the PEG-ligand, F: Folate. Detailed PEG-ligand description in **Figure 1A**. (A) Polyplexes with *LA* (blue bars). (B) Polyplexes with *LAE* (orange bars). Assembly: completely inside the double meander channel (DMC). Statistics: tips of horizontal lines indicate compared samples. Comparison: two-sided student's t-test with HOLM correction. N = 5. Key: NS, not significant at $\alpha = 0.05$; ***: $\alpha < 0.001$. Error bars correspond to 95% confidence intervals.

Table 15: Results of post hoc tests of core (*CO* + siRNA) – lipid anchor – PEG-ligand polyplexes.

Sample	p value	p value (corrected: HOLM)	Cohen's d
Comparison: Sample to core – *LA* formulation			
Core – *LA*: P12-F	0.018	0.142	1.45
Core – *LA*: *P12-3F*	**< 0.001**	**< 0.001**	**2.79**
Core – *LA*: *P12-12F*	**< 0.001**	**< 0.001**	**5.21**
Core – *LA*: *P12-24F*	**< 0.001**	**< 0.001**	**5.72**
Core – *LA*: *P12-48F*	**< 0.001**	**< 0.001**	**5.00**
Comparison: Sample to core – *LAE* formulation			
Core – *LAE*: P12-F	0.316	1.000	0.69
Core – *LAE*: *P12-3F*	0.452	1.000	0.39
Core – *LAE*: *P12-12F*	**< 0.001**	**< 0.001**	**3.09**
Core – *LAE*: *P12-24F*	0.199	0.996	0.58
Core – *LAE*: *P12-48F*	**< 0.001**	**< 0.001**	**3.36**
Comparison: Core – *LA* – PEG-ligand vs. core – *LAE* – PEG-ligand			
Core – *LA*	0.030	0.213	1.66
Core – *LA*: P12-F	0.702	1.000	0.25
Core – *LA*: *P12-3F*	0.861	1.000	0.12
Core – *LA*: *P12-12F*	**< 0.001**	**< 0.001**	**6.72**
Core – *LA*: *P12-24F*	0.040	0.237	1.55
Core – *LA*: *P12-48F*	**< 0.001**	**< 0.001**	**10.1**

Note: Two-sided student's t-test with and without HOLM correction. Cohen's d: effect size. Magnitude: <0.2: negligible. <0.5: small. <0.8: medium. <1.20: large. >1.20: very large. Bold values are significant at $\alpha < 0.05$. Core: core polyplex with siGFP and *CO*; *LA*/*LAE*: lipid anchor oligomers; Core – *LA*: no PEG-ligand: P12-xxF, number of PEGx from lipid anchor + PEG-ligand; F: folic acid.

3.2.4. Characterization of *CON* – PEG-ligand polyplexes

CON oligomers, in contrast to *CO* oligomers, feature an additional azidolysine N-terminally (**Figure 24A**). Consequently, PEG-ligands can be coupled covalently to *CON* containing core polyplexes. Generally, azide-bearing core oligomers were modified with PEG-ligands 45min after polyplex formation (**Figure 24B**) because coupling PEG-ligands to core oligomers before polyplex formation hampers siRNA compaction (Morys et al., 2017). This method has already been established by Klein et al. (Klein et al., 2018) and was used here to validate results generated with core polyplexes that had PEG-ligands attached by lipid anchors.

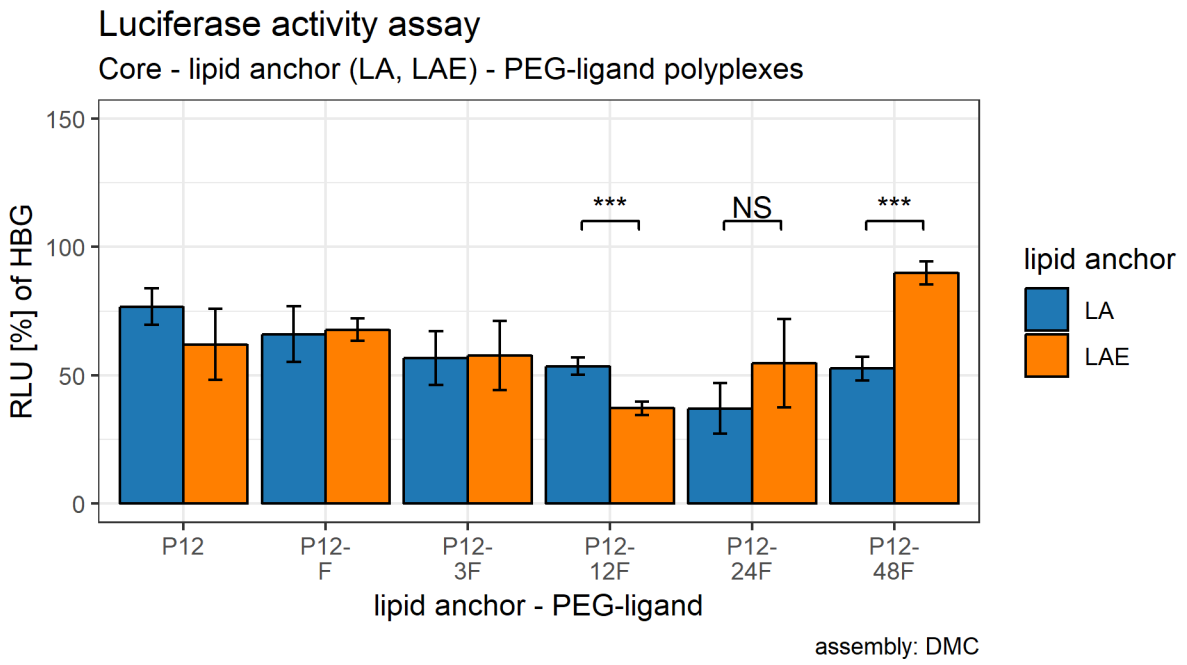

Figure 23: Luciferase activity assay of core (*CO* + siRNA) – lipid anchor – PEG-ligand polyplexes. All polyplexes were prepared using the double meander channel (DMC). Luciferase enzyme activity is measured in relative light units (RLU) and is shown relative to values of buffer treated cells. siGFP siRNA was used in all samples. Core polyplexes with 20 mol % lipid anchors and lipid anchor – PEG-ligands were used. PEG-ligand Formulation key: P12: core polyplex with unmodified lipid anchor. P12-xxF: the total amount of ethylene oxide repetitions (*LA*/*LAE* + PEG-ligand), F: Folate. Detailed PEG-ligand description in **Figure 1A**. Color key: Blue bars: polyplexes with *LA*, orange bars: polyplexes with *LAE*. Statistics: Tips of horizontal lines indicate compared samples. Samples were compared with a two-sided student's t-test with HOLM correction. N = 5. Key: NS, not significant at $\alpha = 0.05$; ***: $\alpha < 0.001$. Error bars correspond to 95% confidence intervals.

Increasing PEG-ligand length and molar amounts promotes aggregation.

I covalently bound PEG-ligands to *CON* core polyplexes prepared as described in (Klein et al., 2018) and depicted here in **Figure 1A** and **Figure 24A**. In brief, *CON* oligomers and siRNA were mixed manually and incubated for 45 min. Afterward, PEG-ligands were added and the azide-alkyne click reaction was allowed to complete for 4 h. Results from these covalently modified polyplexes were used to confirm results generated with the lipid anchor containing system. The main difference between both formulations is the mode of incorporation of target PEG-ligands. On the one hand, *CO*-based core polyplexes need lipid anchor oligomers for the non-covalent attachment of PEG-ligands. PEG-ligands are coupled covalently to lipid anchor oligomers before the polyplex formulation process. On the other hand, *CON* based core polyplexes feature azides that enable the covalent integration of the PEG-ligand into core polyplexes after core polyplex formulation.

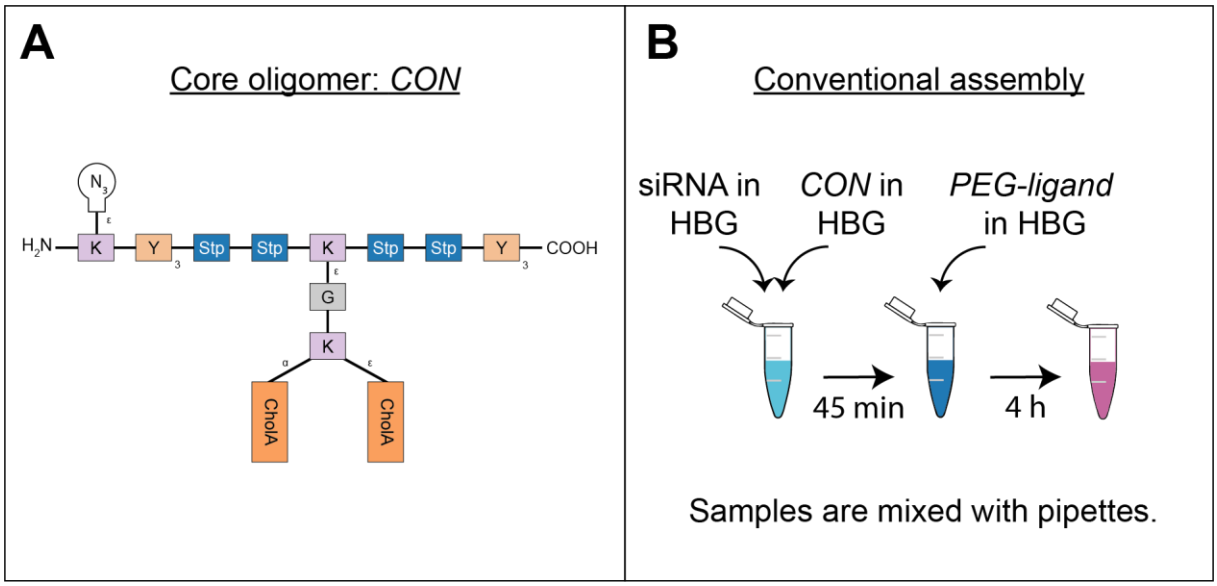

Figure 24: Sequence-defined oligomers and their corresponding nanoparticle production methods.
(A) Core oligomer featuring an azide (*CON*): PEG-ligands were coupled to *CON* after polyplex formation. Building blocks represent natural amino acids (E = glutamic acid, G = glycine, H = histidine, K = lysine, Y = tyrosine), synthetic building blocks (Stp = succinyl tetraethylene pentamine, PEG = polyethylene glycol), fatty acids (CholA = cholanic acid), and moieties for bio-orthogonal click chemistry (N3 = azide, DBCO = dibenzocyclooctyne). (B) The manual production method for *CON* – PEG-ligand polyplexes.

Additionally, I increased PEG-ligand concentrations to investigate their influence on particle size as well. I found that core polyplexes modified with 25 mol % PEG-ligand were all in the same size range (d_H ~ 120 nm, **Figure 25A**) and PDI (~ 0.15, **Figure 25B**), except for formulations with *P48F* (d_H = 136 nm, PDI = 0.20). These results were comparable to *CO*-based core – lipid anchor polyplexes with 20 mol % PEG-ligands (**Figure 11A** and **11B**), except with *LAE*, which showed a substantial increase in size and PDI with *P48F*. Increasing PEG-ligand concentration up to 100 mol % did not substantially alter size and PDI of polyplexes with F (d_H = 122 nm, PDI = 0.16), *P3F* (d_H = 115 nm, PDI = 0.14), and *P12F* (d_H = 135 nm, PDI = 0.11), but had a large effect on size and PDI of *P24F* (d_H = 1,817 nm, PDI = 0.62) and *P48F* (d_H = 8,393 nm, PDI = 0.67) containing particles which basically showed aggregation when functionalized with more than 25 mol % PEG-ligands.

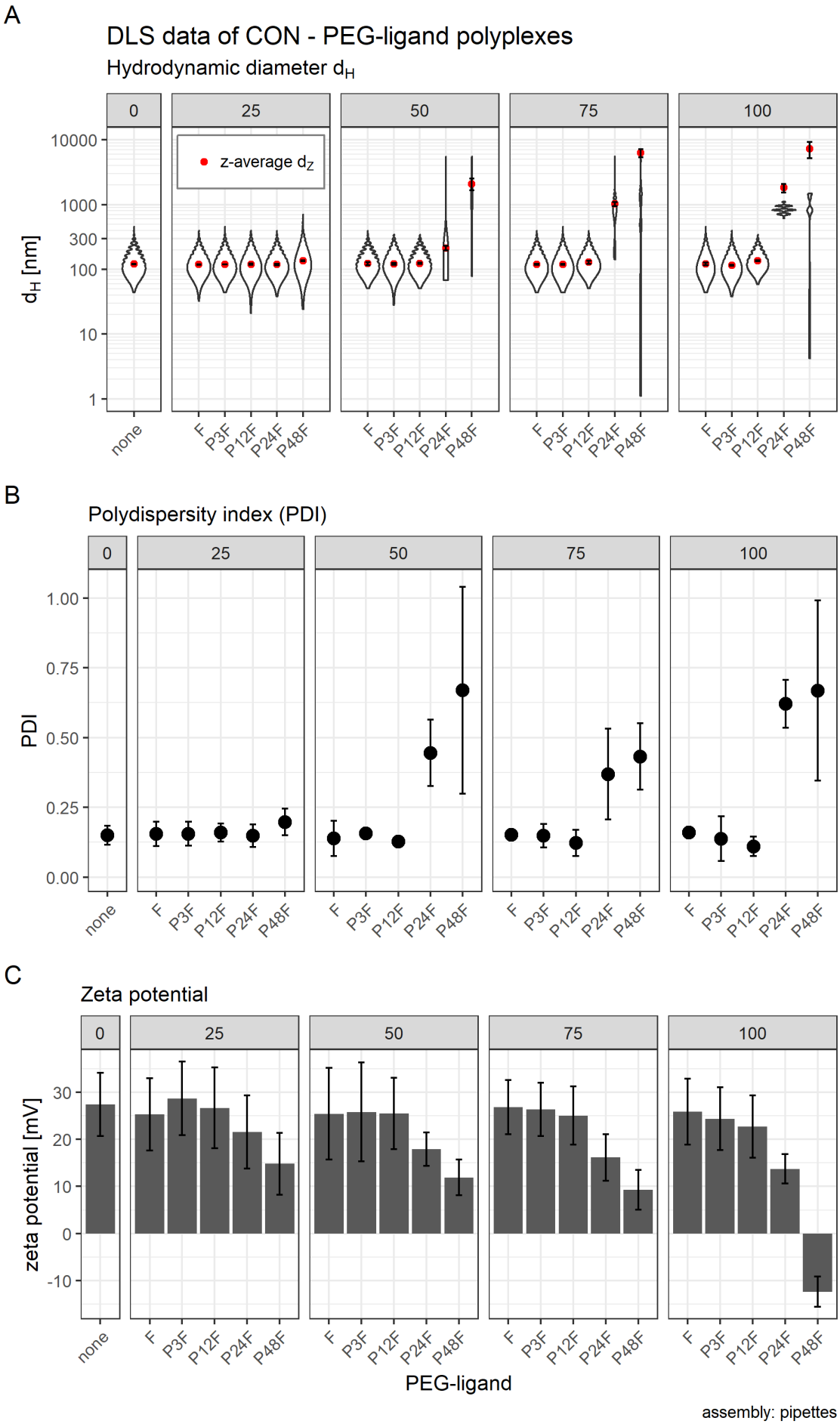
A
DLS data of CON - PEG-ligand polyplexes
Hydrodynamic diameter d_H
0
25
50
75
100
z-average d_Z
d_H [nm]
10000
1000
300
100
10
1
none
F
P3F
P12F
P24F
P48F
B
Polydispersity index (PDI)
PDI
1.00
0.75
0.50
0.25
0.00
C
Zeta potential
zeta potential [mV]
30
20
10
0
-10
PEG-ligand
assembly: pipettes

Figure 25: Hydrodynamic diameter (d_H), PDI, and zeta potential of core (*CON* + siRNA) and core – PEG-ligand polyplexes.
Subfigures are divided into five panels. Numbers indicate the amount of PEG-ligand used in mol % relative to n_{CON}. Formulation key: "core polyplex": unmodified *CON* – siGFP polyplex. Px: PEGx, F: folate. Detailed oligomer description in **Figure 1A** (PEG-ligands) and **Figure 24A** (*CON*). Assembly: conventionally with pipettes. (A) Hydrodynamic diameter (d_H) and mean z-average (red dots) with respective intensity distribution depicted as violin plot (extension in x-direction corresponds to the percentage of the total intensity measured at the specific size depicted on the y-axis). (B) Polydispersity index (PDI). (C) Zeta potential measured in HBG pH 7.4. Statistics: (A) and (B) Error bars correspond to 95% confidence intervals. (C) Error bars correspond to mean zeta deviations. N =3.

3.2.5. Transfection of *CON* – PEG-ligand polyplexes

The optimal PEG-ligand length is PEG12 or PEG24.

The influence of molar amount and PEG length of PEG-ligands on luciferase activity was estimated using a multifactorial two-way ANOVA. siCtrl polyplexes were included in addition to siGFP polyplexes to detect apparent toxicity and to attribute it to either PEG length, molar amount, or both. Significant terms suggest an influence of the tested variable (PEG length and molar amount) on transfection efficiency. A significant interaction term indicates that both variables influence each other. Main effect of PEG length for siGFP: $F(4, 90) = 3.71$, $p < 0.008$, $\omega^2 = 0.32$, main effect of molar amount used with siGFP: $F(1, 90) = 24.96$, $p < 0.001$, $\omega^2 = 0.36$, interaction effect between PEG length and molar amounts with siGFP: $F(4, 90) = 4.15$, $p = 0.004$, $\omega^2 = 0.04$.

The ANOVA with siCtrl polyplexes yielded the following results: Main effect of PEG length for siCtrl: $F(4, 90) = 4.37$, $p < 0.003$, $\omega^2 = 0.23$, main effect of molar amount used with siCtrl: $F(1, 90) = 2.48$, $p = 0.119$, $\omega^2 = 0.20$, and the interaction effect of PEG length with molar amount with siCtrl: $F(4, 90) = 13.52$, $p < 0.001$, $\omega^2 = 0.19$.

Post hoc tests were used to quantify the influence of separate PEG-ligands on luciferase knockdown in comparison to the core polyplex formulation (**Table 16** and **Table 17**). Cells treated with conventionally prepared *CON* polyplexes with siGFP showed a non-significant decrease in RLUs compared to polyplexes with siCtrl. Incubating polyplexes for 4 h with targeting PEG-ligands of various lengths decreased luciferase activity significantly compared to core formulation without PEG-ligands (**Table 16**). Increasing PEG-ligand concentration up to 100 mol % (relative to n_{CON}) increased the effect of siGFP as well, but toxicity and aggregation tendency increased simultaneously (**Figure 25** and **Figure 26B**).

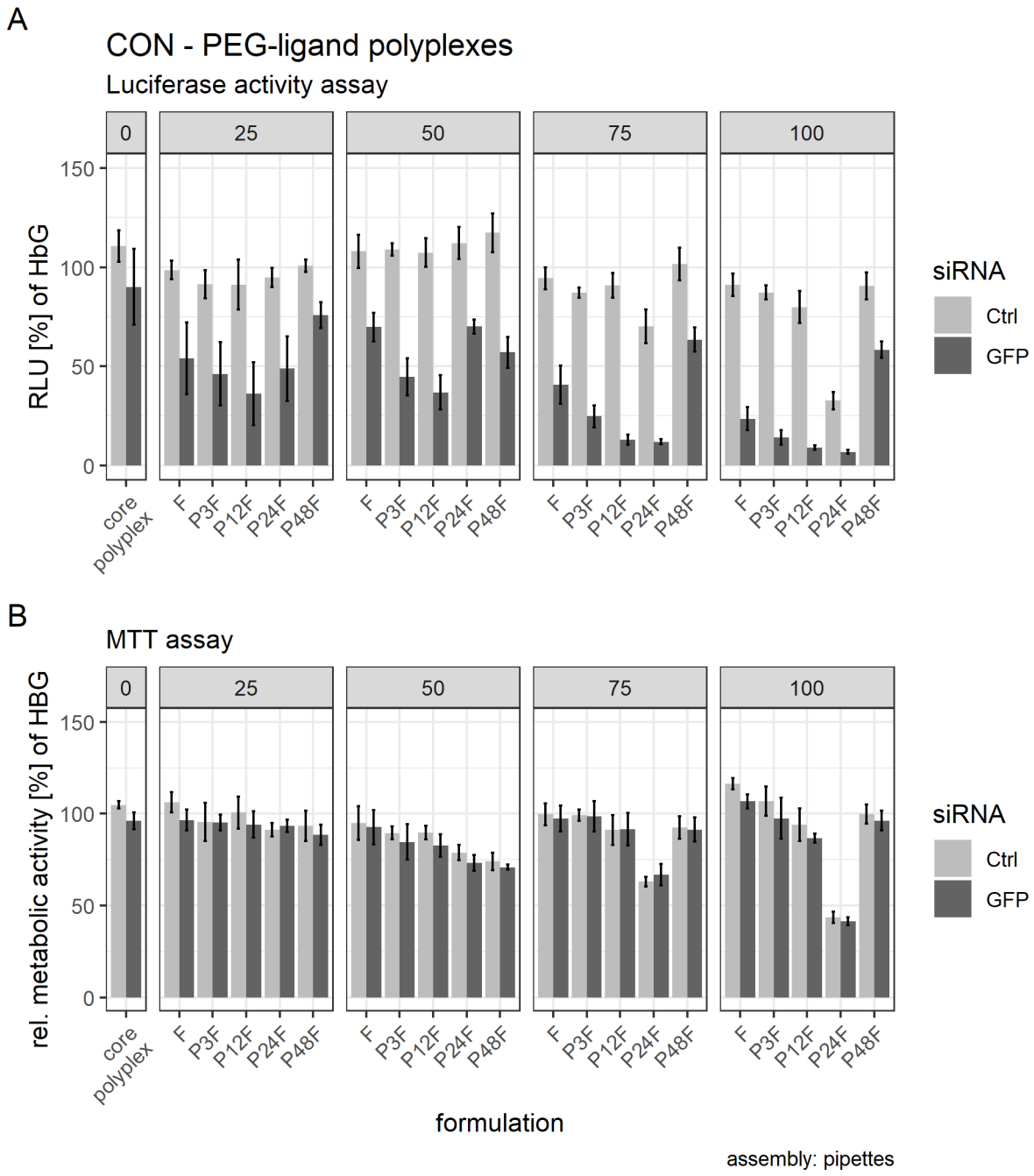

Figure 26: Luciferase activity assay and MTT assay of core (*CON* + siRNA) – PEG-ligand polyplexes.
Polyplexes were prepared conventionally. Colors indicate the type of siRNA used: light color: control siRNA, saturated color: siGFPLuc siRNA. "core polyplex" depicts particle properties of the naked core polyplex formulation used for all subsequent modifications. Panel's key: x mol % PEG-ligands relative to n_{CON}. Formulation key: Px: PEGx, F: Folate. Detailed oligomer description in **Figure 1A** (PEG-ligands) and **Figure 24A** (*CON*). Assembly: conventionally with pipettes (**Figure 24B**). (A) Luciferase assay. Luciferase enzyme activity is measured in relative light units (RLU) and shown relative to values of buffer treated cells. (B) MTT assay. Values are shown relative to values of buffer treated cells. Statistics: error bars correspond to 95% confidence intervals. N = 5.

Table 16: Results of post hoc tests between core (siGFP + *CON*) polyplex formulations with and without PEG-ligands.

mol%	PEG-ligand (siGFP + *CON* polyplex)	p value	p value (corrected: HOLM)	Cohen's d
25	***F***	**< 0.001**	**< 0.001**	**2.39**
	P3F	**< 0.001**	**< 0.001**	**3.08**
	P12F	**< 0.001**	**< 0.001**	**3.80**
	P24F	**< 0.001**	**< 0.001**	**2.88**
	P48F	**0.006**	**0.006**	**1.24**
50	***F***	**< 0.001**	**< 0.001**	**1.37**
	P3F	**< 0.001**	**< 0.001**	**3.74**
	P12F	**< 0.001**	**< 0.001**	**4.44**
	P24F	**< 0.001**	**< 0.001**	**1.80**
	P48F	**< 0.001**	**< 0.001**	**2.80**
75	***F***	**< 0.001**	**< 0.001**	**4.04**
	P3F	**< 0.001**	**< 0.001**	**5.75**
	P12F	**< 0.001**	**< 0.001**	**7.01**
	P24F	**< 0.001**	**< 0.001**	**7.15**
	P48F	**< 0.001**	**< 0.001**	**2.33**
100	***F***	**< 0.001**	**< 0.001**	**5.83**
	P3F	**< 0.001**	**< 0.001**	**6.84**
	P12F	**< 0.001**	**< 0.001**	**7.42**
	P24F	**< 0.001**	**< 0.001**	**7.62**
	P48F	**< 0.001**	**< 0.001**	**2.84**

Note: Two-sided student's t-test with and without HOLM correction. Cohen's d: effect size. Magnitude: <0.2: negligible. <0.5: small. <0.8: medium. <1.20: large. >1.20: very large. Bold values are significant at $\alpha < 0.05$. PEG-ligands are covalently bound to core polyplexes with siGFP and *CON*. Mol %: $n_{PEG\text{-}ligand}$:n_{CON}; Px: PEGx; F: folic acid.

There was, however, a "sweet spot" for the positive influence of PEG-ligand length and molar amount. Increasing the number of PEG repetitions per PEG-ligand decreased RLUs up to *P12F* when 25 mol % PEG-ligand was added. Longer PEG-ligands were not as powerful (**Figure 26A**, panel 25 mol %). Gradually increasing total PEG-ligand amount relative to free azides increased efficacy but lead to aggregation (**Figure 25**) with associated toxicity (**Figure 26B**, *P24F*) and loss of function (**Figure 26A**, *P48F*) for some polyplexes with >50 mol % PEG-ligands as well. PEG-ligands with less than 24 PEG units did not exhibit aggregation or toxicity independent from the amount used.

Producing *CON* – PEG-ligand polyplexes completely inside the DMC yielded similar results to conventionally produced polyplexes. **Figure 27A** shows the transfection results from the luciferase activity assay, and **Figure 27B** shows results from the MTT assay.

Table 17: Results of post hoc tests between core (siCtrl + *CON*) polyplex formulations with and without PEG-ligands.

mol%	PEG-ligand (siCtrl + *CON* polyplex)	p value	p value (corrected: HOLM)	Cohen's d
25	***F***	**< 0.001**	**0.007**	**2.33**
	P3F	**< 0.001**	**< 0.001**	**3.18**
	P12F	**< 0.001**	**< 0.001**	**2.30**
	P24F	**< 0.001**	**< 0.001**	**3.02**
	P48F	**0.006**	**0.039**	**2.08**
50	*F*	0.433	1.000	0.42
	P3F	0.627	1.000	0.36
	P12F	0.329	1.000	0.57
	P24F	0.686	1.000	0.22
	P48F	0.064	0.319	0.93
75	***F***	**< 0.001**	**< 0.001**	**2.97**
	P3F	**< 0.001**	**< 0.001**	**4.99**
	P12F	**< 0.001**	**< 0.001**	**3.49**
	P24F	**< 0.001**	**< 0.001**	**6.10**
	P48F	0.012	0.074	1.39
100	***F***	**< 0.001**	**< 0.001**	**3.52**
	P3F	**< 0.001**	**< 0.001**	**4.75**
	P12F	**< 0.001**	**< 0.001**	**4.82**
	P24F	**< 0.001**	**< 0.001**	**15.01**
	P48F	**< 0.001**	**< 0.001**	**3.40**

Note: Two-sided student's t-test with and without HOLM correction. Cohen's d: effect size. Magnitude: <0.2: negligible. <0.5: small. <0.8: medium. <1.20: large. >1.20: very large. Bold values are significant at $\alpha < 0.05$. PEG-ligands are covalently bound to core polyplexes with siCtrl and *CON*. Mol %: $n_{PEG\text{-}ligand} : n_{CON}$; Px: PEGx; F: folic acid.

.

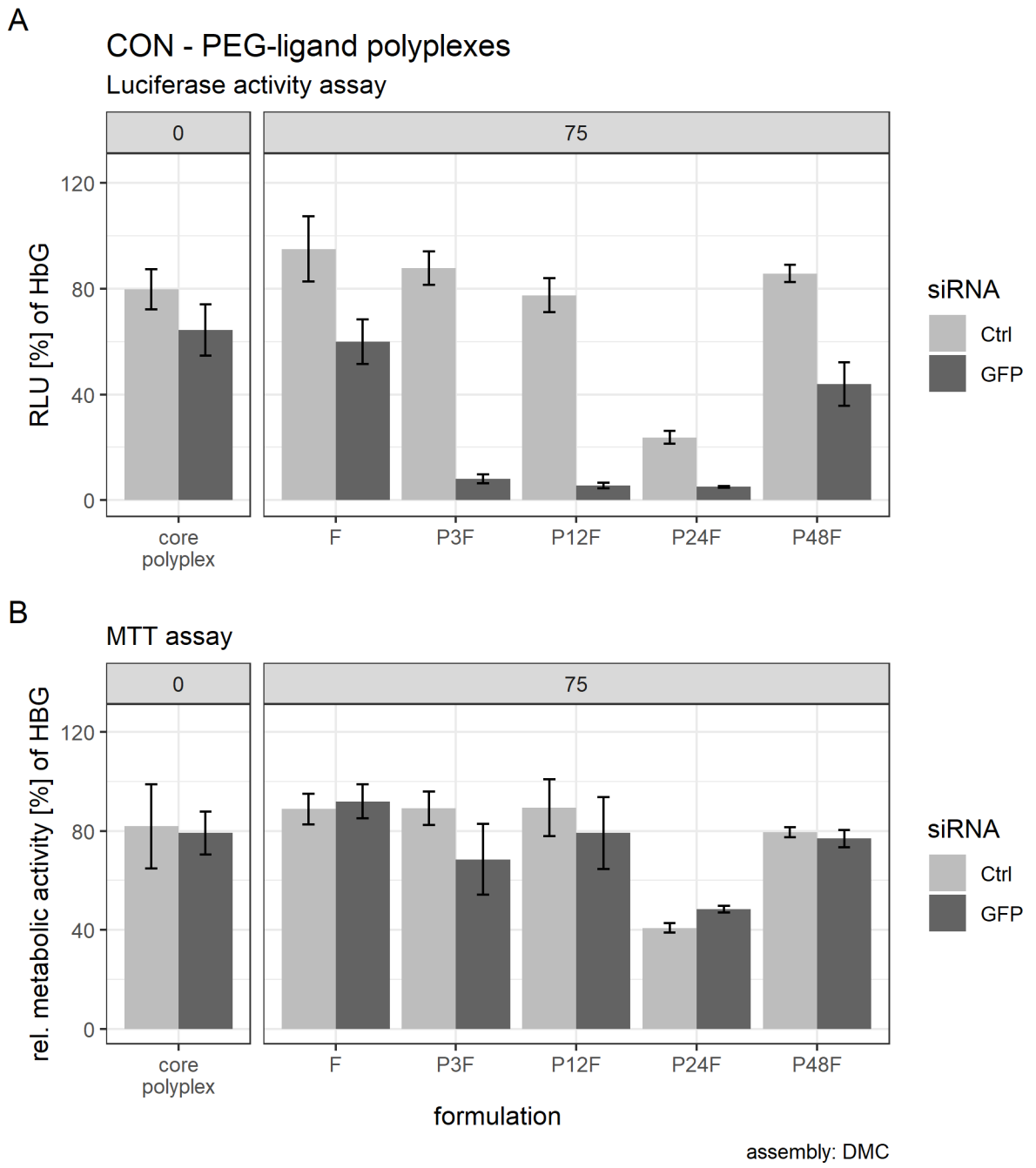

Figure 27: Luciferase activity assay and MTT assay of core (*CON* + siRNA) – PEG-ligand polyplexes.
Polyplexes were prepared in the double meander channel (DMC). Colors indicate the type of siRNA used: Light color: control siRNA, saturated color: siGFP siRNA. "core polyplex" depicts particle properties of the naked core polyplex formulation used for all subsequent modifications. Panel's key: x mol % PEG-ligands relative to n_{CON}. Formulation key: PxxF: the total amount of ethylene oxide repetitions from the PEG-ligands, F: Folate. Detailed oligomer description in **Figure 1A** (PEG-ligands) and **Figure 24A** (*CON*). (A) Luciferase assay. Luciferase enzyme activity is measured in relative light units (RLU) and shown relative to values of buffer treated cells. (B) MTT assay. Values are shown relative to values of buffer treated cells. Statistics: Error bars correspond to 95% confidence intervals. N = 5.

4. Discussion

4.1. Controlling nanoparticle formulation: a low-budget prototype for the automation of a microfluidic platform

Adapted from Loy et al. (Loy et al., 2021).

A detailed description of the automated nanoparticle production system, its hardware, and its software is provided. The control module is inexpensive, and its parts are readily available. The feeding module integrates syringe pumps as commonly applied in microfluidic systems such as in Liu et al. (PHD 2000, Harvard Apparatus) (Liu et al., 2015), Debus et al. (Aladdin, World precision Instruments) (Debus, Beck-Broichsitter & Kissel, 2012), Lim et al. (model unspecified, Harvard Apparatus) (Lim et al., 2014), Karnik et al. (SP220I, World Precision Instruments and PHD 22/2000, Harvard Apparatus) (Karnik et al., 2008), and Belliveau et al. (KD200, KD Scientific) (Belliveau et al., 2012). The schematics of the collection module are published together with this paper on GitHub (Loy, 2020a), enabling the replication of this module in any workshop. Additionally, building the collection module with additive fabrication methods, e.g., 3-D printing, might also be feasible.

The software that controls the feeding and the collection module enhances the functionality of any formulation module. With a specific, customized main module for each individual experiment, reproducibility is increased since every production cycle follows the same commands. Additionally, logs of each experiment are available to document the intended execution of the program. With each main module tailored to the specific needs of any experiment, repeating an experiment is done by simply executing the program again. Additional benefits of employing the software to control the feeding module are the ramping and purging functionalities that reduce the waste of educts to a minimum. These functionalities are cumbersome at best to program into each pump manually, but readily available in our software. The ramping functions ensure that all educts reach the mixing zone at the same time and the purging functions enable the user to choose the least expensive reagent to purge the product from the channel after the experiment.

Although volumes and flow rates of each experiment can be taken from its log, the components and concentrations must still be recorded manually. I have demonstrated the importance of detailed experiment descriptions with polyplexes prepared manually from two components. Changing the volume ratios of the educts and the mixing order varied the hydrodynamic diameter and PDI of the resulting polyplexes from 52.5 ± 9.7 nm to 141.0 ± 3.2 nm and

0.249 ± 0.144 to 0.109 ± 0.030, respectively. The effect of volume ratios on particle sizes is probably due to turbulences of varying intensity, which usually promote faster mixing of the educts. This effect is especially important during the polyplex complexation process since charge neutralization occurs in around 50 ms (Braun et al., 2005).

Additionally, I demonstrated that some formulations might be impossible to be produced with pipettes and require a formulation module – especially formulations from three or more components seem to benefit from the increased control of a microfluidic setup. Krzysztoń et al., for example, improved the efficiency of their mNALP (monomolecular nucleic acid/lipid particles) formulation by microfluidic mixing on the same hydrodynamic flow-focusing chip without our device (Krzysztoń et al., 2017). I have prepared three component polyplexes manually and automatically. Polyplexes prepared by rapid pipetting showed hydrodynamic diameters and PDIs in suboptimal ranges.

With the automated nanoparticle production system, polyplexes with d_Z = 114.7 ± 1.5 nm and PDI = 0.137 ± 0.045 could be produced. This finding and the application of the automated nanoparticle production system enabled the establishment of structure – function relationships from three component polyplexes (cf. section 3.2 A microfluidic approach for sequential assembly of siRNA polyplexes with a defined structure-activity relationship).

Sizes and PDIs in a desired range, however, do not automatically guarantee superior biological activity of target nanoparticles *in vitro* or *in vivo*. On the one hand, nanoparticles produced with controlled methods might show improved formulation characteristics and equal (but not better) biological activity. Members from our lab, for example, demonstrated the reproducible production of polyplexes from pDNA and LPEI (linear polyethylene imine) with an up-scaled micro-mixer. Compared with manually formulated polyplexes, both formulations showed comparable biological activity *in vitro* (Kasper et al., 2011). On the other hand, formulations with larger PDIs and sizes might show apparently better transfection efficiencies *in vitro*. This is usually due to large particles literally “dropping” on the cells fixed to the bottom of the cell culture flask. A formulation with these properties, however, might fail *in vivo*.

All in all, the application of this versatile software enables the creation and automated execution of a sophisticated program consisting of many individual steps in order to increase control over the formulation process of nanoparticles and foster reproducibility, which will be most relevant for pharmaceutical production.

The next step on the course to automation is the integration of a fraction collector. The device developed here was designed to work with any standard well plate to realize product collection and separation. It is independent of the previously mentioned setup, which makes it suitable for a wide range of applications. It can be integrated into the target automated process, but it can also be used to gather products produced manually. Overall, it is a versatile addition to any product formulation setup relieving the user of additional manual labor.

A well-known disadvantage of microfluidic systems is the scalability problem (Whitesides, 2006). Due to the utilization of fluid phenomena – for example, laminar flow – which are only present under certain conditions, the throughput of one microfluidic chip cannot be escalated indefinitely (Squires & Quake, 2005). The obvious solution to employ parallelization is a valid suggestion, but product output does only scale linearly in relation to dedicated resources at the current development stage of the system due to the many individual steps involved in setting up the device. However, a possible solution is already designed in the system. Since the setup is modular, any part of it can easily be replaced by a more efficient one (Chiu et al., 2017).

Placing the complete system into a laminar flow cabinet is a next obvious step for pharmaceutical applications. In the described work, nanoparticles were formulated outside of the cabinet and subsequently transferred inside for *in vitro* transfections of cells. With the complete system inside the cabinet, direct application of the product to the target cells could be achieved, which would decrease the influences of external factors and human interactions even further.

4.2. A microfluidic approach for sequential assembly of siRNA polyplexes with a defined structure-activity relationship

Adapted from Loy et al. (Loy et al., 2019).

I have shown that the controlled production of simple two-component polyplexes is feasible and that it can be extended to generate more sophisticated products. It depends on the aim of the experiment, which method is most suitable. Conventional bulk mixing with pipettes is best chosen when polyplexes must be prepared quickly, and high control over mixing parameters is not an issue. It is problematic, however, if bulk mixing is the default method for preparing polyplexes since size and polydispersity are heavily dependent on the concentration of its components and their respective volumes. T-junctions are best for continuously preparing larger volumes of polyplex solutions with some control over mixing speed. Since the mixing is turbulent and flows are fast, mixing vastly different volumes can be challenging. Moreover, the high mixing speed required would limit the further automated processing of prepared polyplexes, if the next step involved pressure-sensitive components. Microfluidics excels in producing polyplexes with a high degree of control over external mixing parameters and additional reactants, which is reflected in polydispersity indices around 0.1 for these polyplexes. Increasing throughput to T-junction levels, however, would entail parallelization of the whole set-up, which is only feasible when prototyping and sample preparation can be automated.

To demonstrate the advantages of this approach, I have produced multi-component polyplexes from their single components in one continuous experiment, which would have been impossible with bulk mixing or at a T-junction.

Morphology of core-lipid anchor polyplexes was shown with TEM and FRET experiments. TEM pictures revealed fibrous structures for samples containing only *LA* or *LAE* alone, with or without PEG-ligands. These structures, however, were not visible when core-lipid anchor polyplexes were examined. Moreover, FRET experiments showed a strong signal for labeled core (*CO* + siRNA-Cy5)-lipid anchor (Atto488) polyplexes that could not be observed in mixtures containing only siRNA-Cy5 and lipid anchor-Atto488 without *CO*. Taken together, both results indicate the successful integration of lipid anchor oligomers into core structures.

The investigation of size, PDI, and zeta potential of core-lipid anchor and core – lipid anchor – PEG-ligand polyplexes showed matching results. Mean hydrodynamic diameter (d_H) and mean PDI increased with increasing PEG-ligand length while zeta potential was gradually reduced. Zeta potential reduction could also be one reason for particles with longer PEG chains forming

aggregates since electrostatic repulsion was diminished. Similarly, polyplexes that had their PEG-ligands directly coupled to *CON* showed an increase in PDI and d_H with PEG24 and PEG48 containing PEG-ligands, specifically with PEG-ligand content > 25 mol %.

There is evidence that the integration of PEG chains into electrostatically formed nanoparticles decreases its stability (Morys et al., 2017). On the one hand, this could be a critical problem if the polyplex disintegrates before it delivers its payload. On the other hand, it has been shown that increased stability has the potential to inhibit delivery as well if the polyplex does not release its payload once inside the target cell (Schaffer et al., 2000; Leong & Grigsby, 2010). Therefore, a balance needs to be found between both extremes. Here, core – lipid anchor polyplexes and core polyplexes alone produced similar results, both when treated with poly-anions in an ethidium bromide (EtBr) displacement assay with up to five IU/ml heparin and when siRNA compaction and retention is tested with a gel shift assay with or without incubation in 90% serum at 37 °C. These findings suggest an unaltered stability profile of core-lipid anchor particles compared to its naked core polyplex formulation. Even the addition of PEG-ligands to core-lipid anchor polyplexes did not alter serum gel shift results exceedingly until the formulation had been incubated for 24 h at 37 °C.

Biological activity of core – lipid anchor – PEG-ligand particles was investigated by silencing luciferase protein expression in KB cells *in vitro*. From previous studies, I anticipated that changing the PEG-ligand on the polyplexes would have the most significant impact on luciferase activity. The results of the ANOVA confirmed our hypothesis. Additionally, the results revealed a barely significant influence of the lipid anchors used. The small effect can be explained by the function of the lipid anchor: since lipid anchors are designed to facilitate association with the core polyplex only, their effect pales in comparison to PEG-ligands, which are specially designed to enhance uptake. However, lipid anchors apparently influence the effect of PEG length in PEG-ligands by shifting the most efficient spacer from PEG12 for *LA* (*LA*: *P12-12F*) to PEG24 for *LAE* (*LAE*: *P12-24F*) containing polyplexes. Additionally, the tendency for aggregation seems to be increased with *LAE*. One could speculate whether the small, non-significant reduction in mean zeta potential serves and suffices as a trigger for aggregation. Nevertheless, the additional glutamic acids (E) in the structure of *LAE* make the purification of the compound easier, which might be the decisive argument for the integration of glutamic acids. The biological activity of polyplexes containing 20 mol % lipid anchor – PEG-ligands is comparable to polyplexes from *CON* + siRNA with 25 or 50 mol % covalently bound PEG-ligands without lipid anchors.

The predictive value of the lipid anchor containing systems has been assessed with the system published by Klein et al. (Klein et al., 2018). Here, 25 mol % PEG-ligands were covalently coupled to conventionally prepared polyplexes from *CON* and siRNA. Subsequently, KB cells were transfected. Indeed, the silencing pattern visible with core – lipid anchor polyplexes was reproduced, and the hinted-on problems with longer PEG chains – aggregations, toxicity – were also visible when PEG-ligand concentration was increased. The most striking resemblance between both systems is the U-shaped pattern when looking at the luciferase activity relative to PEG ligand length. I speculate that at least two effects influence the efficacy of the formulation, and their interplay leads to the observed pattern.

First, if the distance between core oligomer and folic acid is too short, effective interaction between folic acid and its receptor will be hampered, effectively decreasing the efficacy of formulations with short PEG chains. It has also been suggested that folate receptors need to be crosslinked to facilitate uptake of nanoparticles (Mayor, Rothberg & Maxfield, 1994). Second, polyplexes usually lose their internal stability with increasing PEG length. This could be the reason behind the decrease in transfection efficacy with polyplexes with longer PEG chains.

All in all, the results of this study suggest that lipid anchors could serve as a tool to investigate structure-activity relationships on a wide variety of core polyplexes, especially when core oligomers lack functionalities for covalently binding additional structures.

Application of microfluidic devices for various tasks (Whitesides, 2006) and especially for producing delivery systems (Liu et al., 2017) usually improves the quality of products. For example, Abstiens & Goepferich (Abstiens & Goepferich, 2019) demonstrated that the continuous production of core-lipid anchor nanoparticles from PLGA and PLA-PEG with microfluidics leads to increased control over the production process which in turn generates nanoparticles with decreased size and polydispersity. Automated production of pDNA PEI polyplexes in T-junctions has been shown by Kasper et al. (Kasper et al., 2011) in our lab. Continuous or batch-wise production of PEI pDNA polyplexes with active mixing by surface acoustic waves (SAWs) has been demonstrated by Westerhausen et al. (Westerhausen et al., 2016) and Schnitzler et al. (Schnitzler et al., 2019). The decrease in size and polydispersity is most impressive in lipid nanoparticle formulations with siRNA (Chen et al., 2012; Krzysztoń et al., 2017). They all show that increasing mixing speeds decrease size and polydispersity. I show that similar improvements can be gained with a passive micromixer and sophisticated sequence-defined oligomers and that multi-component polyplexes can easily be prepared automatically from their starting materials.

These core – lipid anchor – PEG-ligand polyplexes were used to investigate the influence of PEG length on *in vitro* efficacy and to see if using lipid anchors had a predictive value for formulations with covalently bound PEG-ligands without lipid anchors. Luciferase assays revealed the influence of PEG length and PEG-ligand concentration on transfection efficiency. It has already been shown by Klein et al. (Klein et al., 2018) that their shortest PEG-ligand (*P24F*) in combination with *CON* was most efficient in their study and that increasing PEG-ligand concentration increased efficiency. Additionally, they demonstrated that even if polyplexes with longer PEG-FolA ligands (*P48F, P72F*) had bound to FolA receptors, uptake is strongly decreased. They did not show, however, how PEG-ligands with shorter PEG chains compete. I strengthen the results generated by Klein et al. by showing that there is indeed a strong association between PEG length and transfection efficiency with peak performance with PEG12 and PEG24 containing polyplexes. These two are also statistically different from the core-*LA* ($p < 0.001$) or core-*LAE* ($p < 0.001$) formulation alone. In this work, however, lipid anchor oligomers with an additional PEG12 chain were used, raising the total number of PEG monomer repetitions in *LA*: *P12-24F* containing polyplexes to 36. All in all, our results suggest that using lipid anchors for investigating PEG-ligand performance is a valid way to screen core polyplex PEG-ligand combinations before synthesizing new structures.

These results also suggest that transfection efficiency does not only depend on the PEG-ligand alone but its chemical environment as well since changing *LA* to *LAE* did significantly increase the silencing efficiency of the *P12F* PEG-ligand (**Figure 26**, $p < 0.001$). It did also increase the silencing efficiency of the *P24F* PEG-ligand on *LA* against *LAE*, albeit not significantly ($p = 0.237$). I also observed that increasing PEG length and PEG-ligand concentration increased aggregation disposition and decreased efficacy. This is in line with results from Abstiens, Gregoritza & Goepferich (Abstiens, Gregoritza & Goepferich, 2018) who argue that increasing PEG-ligand length and PEG-ligand concentration lead to clustering of nanoparticles and a higher probability for PEG-ligand entanglement and shrouding and therefore decreased efficacy.

The microfluidic system presented here has been designed for producing multi-component siRNA polyplexes from its starting materials. During the development process, two modules have been excessively tested: The first one to produce core polyplexes, the other one for the attachment of lipid anchors and PEG-ligands. Further development should focus on the implementation of additional modules for different tasks, for example, for producing pDNA polyplexes. Additionally, producing polyplexes without the help of organic solvents, which

possibly alters the kinetically controlled assembly process, which needs mixing speeds in the order of 50 ms (Braun et al., 2005) to yield small particles, could facilitate the integration of this method into acetone intolerant applications. One solution could be the utilization of surface acoustic waves (SAWs) (Westerhausen et al., 2016) to avoid the usage of organic solvents. In the end, there could be a small set of modules researchers could choose from according to the desired properties of their particles. Furthermore, these modules should be integrated into a system that can automatically select from different starting materials and distribute polyplexes produced under controlled conditions to various containers. This approach would have the advantage of enabling faster production of various samples in a controlled manner while producing less waste in a shorter period of time in comparison to conventionally produced polyplexes. The advantage of high throughput production of many different formulations, albeit with a completely different system, has already been shown by Wang et al. (Wang et al., 2010).

The PEG-ligands presented here are successful in facilitating transfection when their density on the surface of the nanoparticle is large enough. Research by, for example, Lee et al. (Lee et al., 2012), Antony (Antony, 1992) and Mayor, Rothberg & Maxfield (Mayor, Rothberg & Maxfield, 1994), show that folic acid receptors might require a certain number and distance of folic acid PEG-ligands to interact with their respective nanoparticles successfully. Therefore, this system could be employed to test various multi-folate receptors on various optimized core structures to finally get an optimized product with ideal PEG-ligands for the target cell type.

5. Summary

Humankind is still far away from the degree of control over devices at the nanoscale envisioned by Feynman in 1959 (Feynman, 1959). Nevertheless, countless individual steps have led to enormous collective progress. The physicians' toolbox is now filled with several viral and non-viral vectors enabling the management, sometimes even cure, of hitherto untreatable conditions. Especially in the area of hereditary diseases caused by single or defined mutations, prognoses have improved distinctly. In the vast and diverse area of tumor therapy, however, curing is still the exception over managing a chronic disease. Since tumors originate from host cells due to a series of random and unfavorable mutations, they are hard to distinguish from healthy cells, and they are unique in every patient. Therefore, patients suffering from cancer require personalized treatments tailored to their individual disease. One therapeutic option could be the delivery of nucleic acids complexed with cationic oligomers (so-called polyplexes). Since the negative charge of a nucleic acid is only dependent on its length and independent of its sequence, the payload of the polyplexes can easily be interchanged according to the individual needs of the patient. This approach has the potential for tailored treatments, and the spontaneous polyplex formation implies that the formulation for the patient can theoretically be prepared on the bedside with lab on a chip devices. These devices would combine the essential parameters for reproducible polyplex formulation: control and automation. Therefore, the aim of the first part of this thesis was the development of an automated system to produce multi-component polyplexes in a controlled fashion. In the second part, the formulation of multi-component polyplexes with the automated microfluidic system described in the first part was demonstrated. Moreover, the high degree of control over the formulation process was utilized to investigate structure – function relationships: the influence of the PEG length of the ligand on the transfection efficiency of the polyplex.

To meet the first aim of the thesis, I demonstrated that polyplex properties are critically dependent on the respective production parameters: educt concentrations, solvent composition, and mode of mixing. Therefore, I applied microfluidic channels that increase control over the formulation process by shifting the mixing process from a turbulent to a laminar flow regime. The educts feeding rate into the channels was controlled by syringe pumps. Additionally, a fraction collector was designed and built-in order to enable automated product collection. The complete system was controlled by custom developed software written in python running on a headless raspberry pi. The first program controlled the syringe pumps and enabled the execution of complex pumping operations, for example, to allow the fast and lossless pumping of reactants

to the mixing zone by a ramping function. The second program controlled the fraction collector. It was independent of the first program enabling the application of the collector to completely automated and manual processes alike. The complete system was built from modules that enabled the seamless replacement of any part by a module more suited to the task at hand. Moreover, the modular structure and the fact that most microfluidic platforms utilize syringe pumps enables the interchangeability of modules between systems. Especially the control software of the pump has the potential to enhance the capabilities of many already published microfluidic platforms.

To meet the second aim of the thesis, I demonstrated that the controlled, continuous formulation of polyplexes from two and three components is advantageous. The subsequent anchoring of DBCO-PEGx-folic acid (PEG-ligands) coupled to lipid anchors on core polyplexes enabled me to investigate the influence of PEG length on transfection efficiency, eliminating the need to alter siRNA complexing oligomers synthetically. I found that core (*CO* + siGFP) – lipid anchor – PEG-ligand polyplexes with 12 + 12 to 12 + 24 EO repetitions had the largest silencing effect on luciferase activity in KB cells. PEG-ligands with 12 + 48 EOs, however, were prone to forming aggregates. These results were validated on a previously published system that binds PEG-ligands covalently. I confirmed that the optimal number of EO repetitions in PEG-ligands was 24. PEG-ligands with less than 24 EO repetitions are advantageous at PEG-ligand concentrations >50 mol % (relative to n_{core} oligomer) because formulations containing ≥50 mol % PEG-ligands with ≥24 EO repetitions tended to form aggregates.

To meet the third aim of the thesis, I published my first author publications under the creative commons license CC BY 4.0 in open access journals. This choice made these publications publicly accessible and enables the simple re-utilization of the data, figures, and code. Moreover, all data I used are published alongside the respective publication in a publicly accessible repository on Figshare (Loy, 2020b). The code applied for generating the respective figures from the data was published on Figshare as well. This practice increases confirmability of my results and fosters reproducibility of my work. Additionally, I published the code for controlling the feeding and the collection module on my public repository on GitHub (Loy, 2020a).

6. Appendix

6.1. Abbreviations

Table 18: Abbreviations

Abbreviation	Explanation
AAV	Adeno-associated vector
ACN	Acetonitrile
ADA	Adenosine deaminase
Aha1	siRNA targeting activator of heat shock 90kDa protein ATPase homolog 1
AIDS	Acquired immune deficiency syndrome
ALD	Adrenoleukodystrophy
AMD	Age-related macular degeneration
ATP	Adenosine triphosphate
Boc	tert-Butoxycarbonyl protecting group
BPEI	Branched polyethylenimine
CAR	Chimeric antigen receptor
CAS	CRISPR associated genes
CC BY	Creative commons attribution copyright license
CDG	Chronic granulomatous disease
CholA	Cholanic acid
CMV	Cytomegalovirus
CNT	carbon nanotubes
CO	Core oligomer; id: 991
CoA	Coenzyme A
CON	Core oligomer (azide bearing); id: 1106
CPN	calcium phosphate nanoparticles
CRISPR	Clustered Regularly Interspaced Short Palindromic Repeats
Ctrl	Control siRNA
Cy5	Cyanine 5, dye
DBCO	Dibenzocyclooctyne
DCM	Dichloromethane
Dde	N-(1-(4,4-dimethyl-2,6-dioxocyclohexylidene)ethyl)
DEAE	Diethylaminoethyl
d_H	Hydrodynamic diameter
DIPEA	N,N-Diisopropylethylamine (Hünig's base)
DMD	Duchenne muscular dystrophy
DMF	Dimethylformamide
DMSO	Dimethyl sulfoxide
DNA	Deoxyribonucleic acid
dsDNA	Doube stranded deoxyribonucleic acid
DTT	Dithiothreitol (Cleland's reagent)
d_Z	Hydrodynamic diameter, based on the z-average
EDTA	Ethylenediamine
Em	Emission wavelength
EMA	European Medicines Agency
EO	Ethylene oxide

Abbreviation	Explanation
EtBr	Ethidium bromide
EtOH	Ethanol
Ex	Excitation wavelength
FDA	Food and Drug Administration
Fmoc	Fluorenylmethyloxycarbonyl protecting group
FolA	Folic acid
GFP	green fluorescent protein
GPIO	General-purpose input/output
HAART	Highly active antiretroviral therapy
hATTR	Hereditary transthyretin amyloidosis
HBG	HEPES-buffered glucose
HBS	HEPES-buffered saline
HEPES	4-(2-hydroxyethyl)-1-piperazineethanesulfonic acid
HNSCC	Head and neck squamous cell carcinoma
HOBt	Hydroxybenzotriazole
HoFH	Homozygous familial hypercholesterolemia
HPLC	High-performance liquid chromatography
HSCT	Hematopoietic stem cell transplantation
kb	Kilo bases
KCl	Potassium chloride
kDa	Kilo Dalton
KH_2PO_4	Potassium dihydrogen phosphate
LA	Lipid anchor oligomer
LAE	Lipid anchor oligomer (glutamic acid bearing)
LAR	Luciferase assay reagent
LDH	layered double hydrixides
LPEI	Linear polyethylenimine
LPLD	Lipoprotein lipase deficiency
MALDI	Matrix-assisted laser desorption/ionization
MeOH	Methanol
$MgCl_2$	Magnesium chloride
miRNA	Micro ribonucleic acid
MIT	Massachusetts Institute of Technology
MOF	Metal-organic framework
mRNA	Messenger ribonucleic acid
MSN	Mesoporous silica nanoparticles
MTBE	Methyl *tert*-butyl ether
MTT	3-(4,5-dimethylthiazol-2-yl)-2,5-diphenyltetrazolium bromide
MW	Molecular weight
N/P	(Protonatable) nitrogen to phosphates ratio
Na_2HPO_4	Disodium phosphate
NaCl	Sodium chloride
NaOH	Sodium hydroxide
nm	Nanometer
NMP	N-Methyl-2-pyrrolidone
OTC	Ornithine transcarbamylase

Abbreviation	Explanation
p.a.	Pro analysi
PAMAM	Polyamidoamine
PBS	Phosphate-buffered saline
PCR	Polymerase Chain Reaction
PDI	Polydispersity index
PDMS	Polydimethylsiloxane
pDNA	Plasmid DANN
PEG	Polyethylene glycol
PEI	Polyethylenimine
pH	The scale used to specify the acidity or basicity of a water-based solution
Ph. Eur.	Pharmacopoeia Europaea
pKa	Acid dissociation constant
PMO	Phosphorodiamidate morpholino oligomer
PP	Polypropylene
PRINT	Particle replication in nonwetting templates
PTFE	Polytetrafluoroethylene
puriss.	Purissimum
PxxF	PEG 0/3/12/24/48 EO repetitions FolA
PyBOP	Benzotriazol-1-yl-oxytripyrrolidinophosphonium hexafluorophosphate
RISC	RNA induced silencing complex
RNA	Ribonucleic acid
RNAi	RNA interference
RPE65	Retinal pigment epithelium gene
RPMI	Roswell Park Memorial Institute cell culture medium
RT	Room temperature
SCID	Severe combined immunodeficiency
SELEX	Systematic evolution of ligands by exponential enrichment
siRNA	Small interfering RNA
SMA	Spinal muscular atrophy
SMN	Survival motor neuron
SPION	Superparamagnetic iron oxide nanoparticles
SPSS	Solid-phase supported synthesis
ssDNA	Single-stranded deoxyribonucleic acid
STOTDA	N″-succinyl-4,7,10-trioxa- 1,13-tridecanediamine
Stp	Succinyl tetraethylene pentamine
TALE	Transcription activator-like effectors
TBE	Tris/Borate/EDTA
TIS	Triisopropyl silane
TRIS	Tris(hydroxymethyl)-aminomethan
TTR	Transthyretin
VEGF	Vascular endothelial growth factor
VOD	Veno-occlusive disease
ZFP	Zinc-finger protein

6.2. Analytical data

Adapted from Loy et al. (Loy et al., 2019).

6.2.1. Core oligomers

Both core oligomers (*CO* and *CON*) have been published by Klein et al. (Klein et al., 2016, 2018), and accordant analytical data can be found there.

6.2.1.1. *CO* (id: 991)

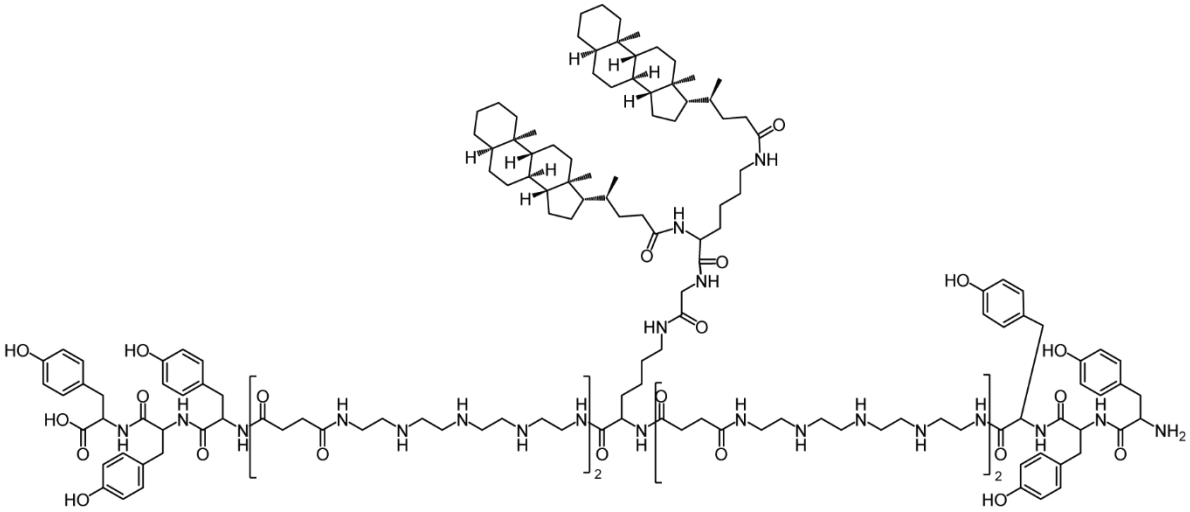

Figure 28: Chemical structure of *CO*.
Calculated molecular weight: 3081.07 Da.

6.2.1.2. *CON* (id: 1106)

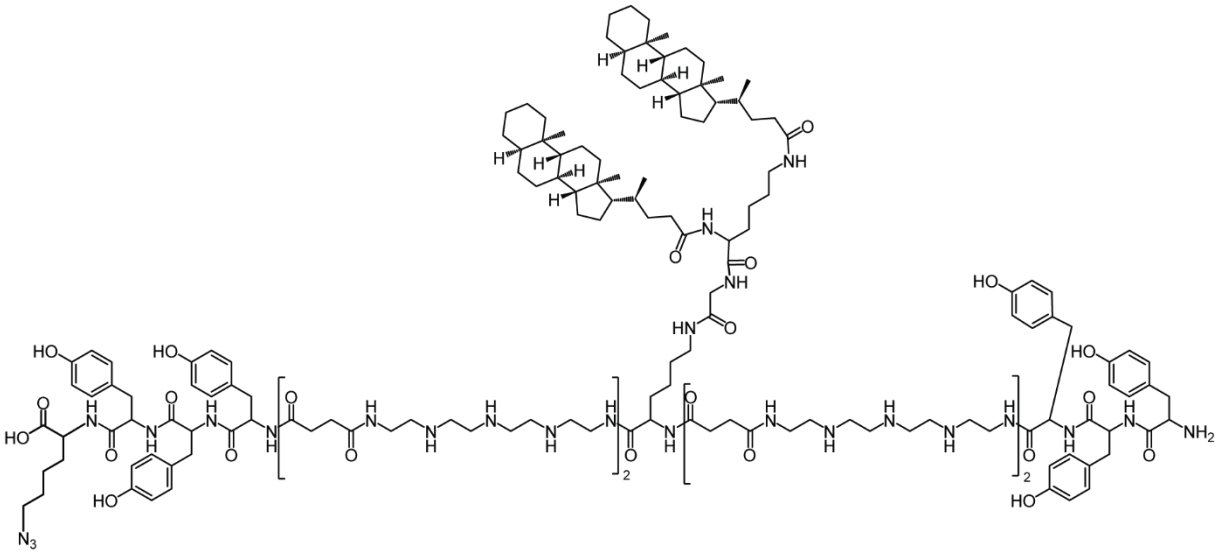

Figure 29: Chemical structure of *CON*.
Calculated molecular weight: 3235.24 Da.

6.2.2. Lipid anchors

6.2.2.1. *LA / LPO* (id: 1203)

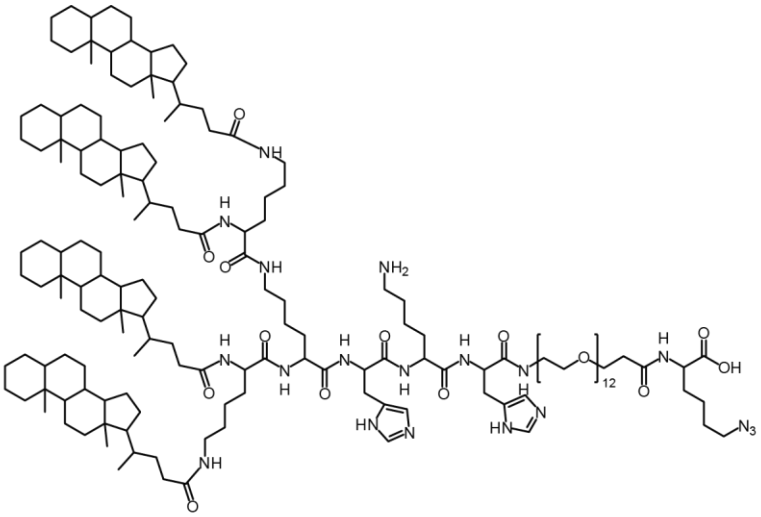

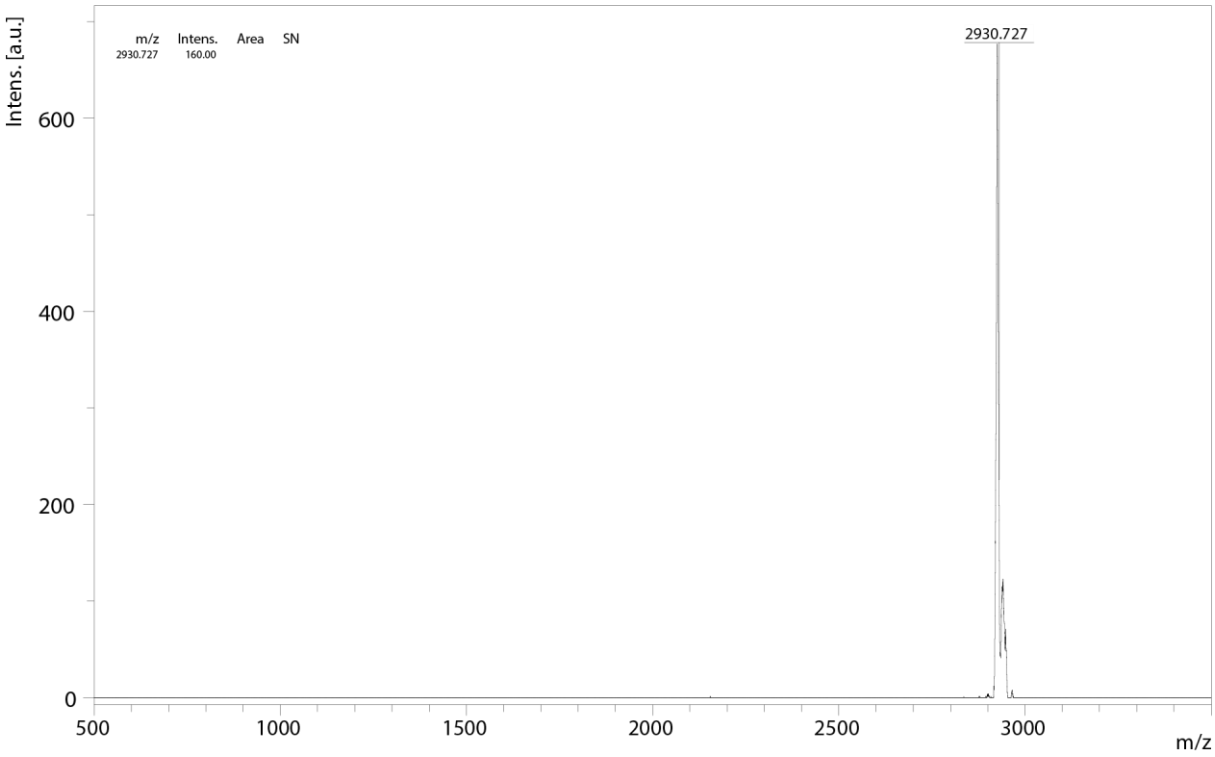

Figure 30: Chemical structure and MALDI mass spectrum of *LA* / *LPO*.
Measured in positive mode. Calculated molecular weight: 2929.16 Da. Mass found: 2930.73 Da.

6.2.2.2. *LAE / LPOE* (id: 1223)

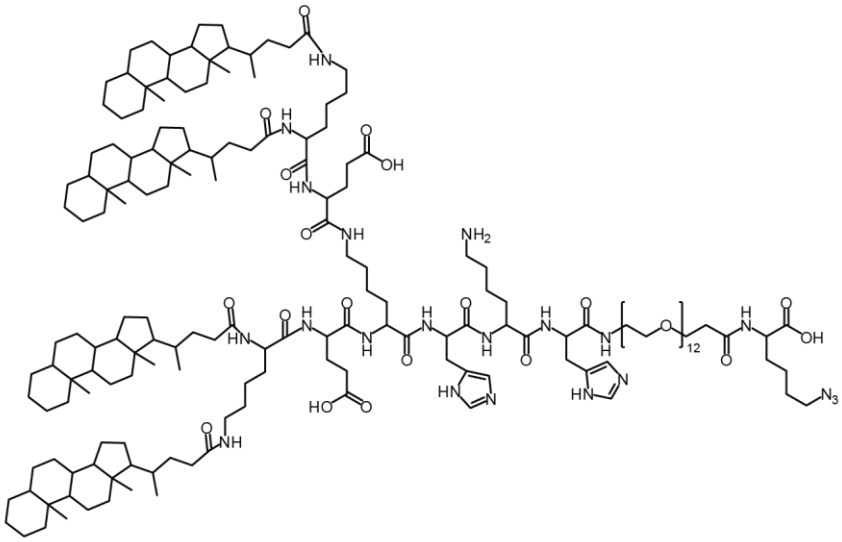

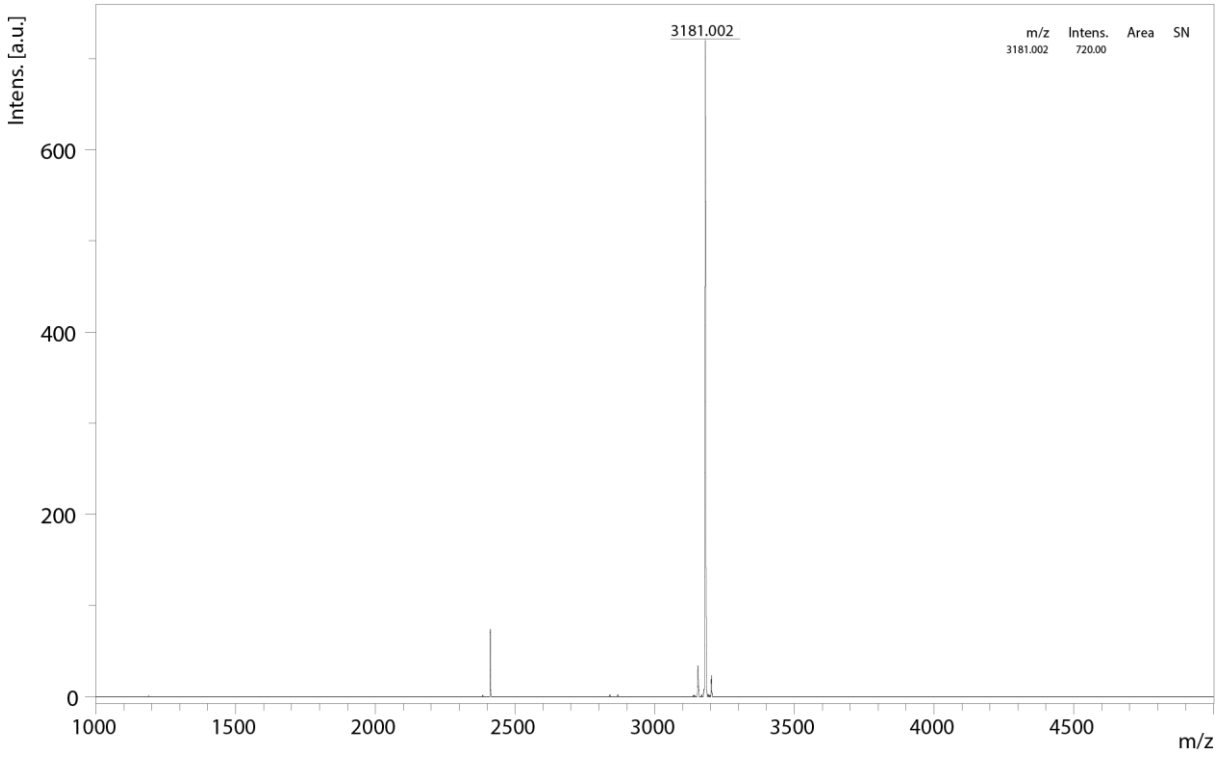

Figure 31: Chemical structure and MALDI mass spectrum of *LAE / LPOE*.
Measured in positive mode. Calculated molecular weight: 3187.39 Da. Mass found: 3181.00 Da.

6.2.3. PEG-ligands

PEG-ligand oligomers *DP24F* and *DP48F* have been published by Klein et al. (Klein et al., 2018), and accordant analytical data can be found there.

6.2.3.1. *DF* (id: 1323)

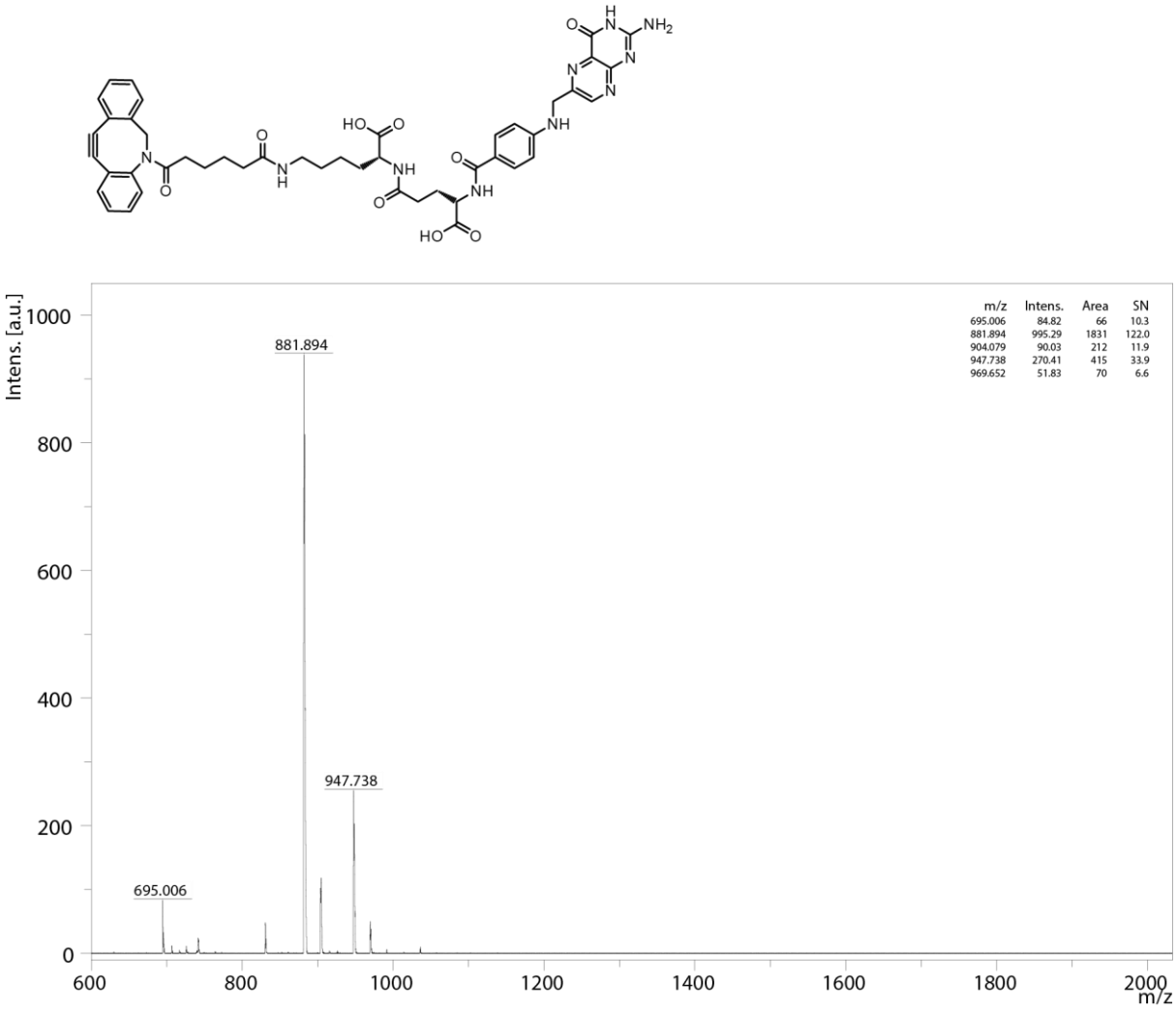

Figure 32: Chemical structure and MALDI mass spectrum of *DF*.
Measured in positive mode. Calculated molecular weight: 884.95 Da. Mass found: 881.89 Da.

6.2.3.2. *DP3F* (id: 1324)

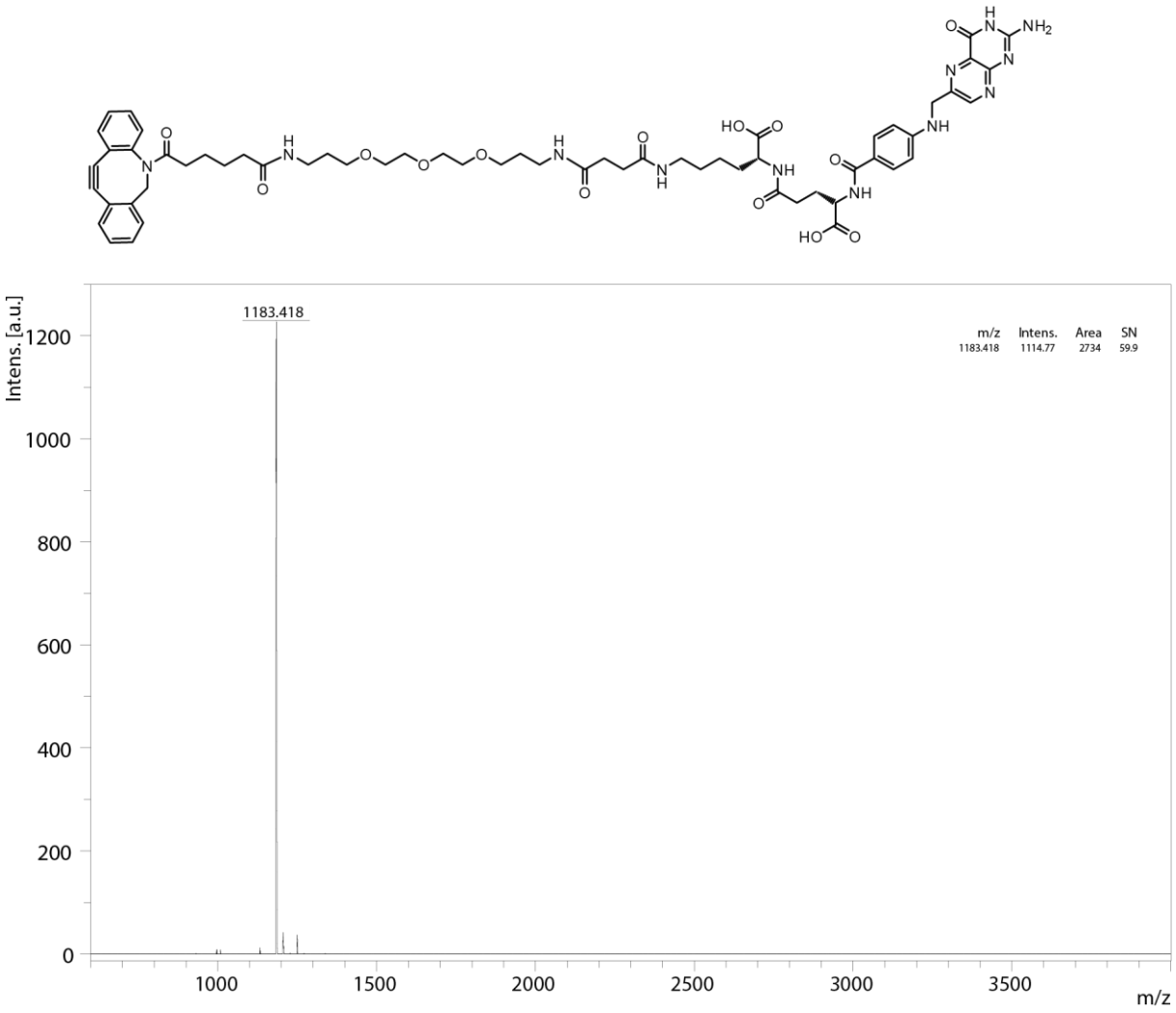

Figure 33: Chemical structure and MALDI mass spectrum of *DP3F*.
Measured in positive mode. Calculated molecular weight: 1187.32 Da. Mass found: 1183.42 Da.

6.2.3.3. *DP12F* (id: 1325)

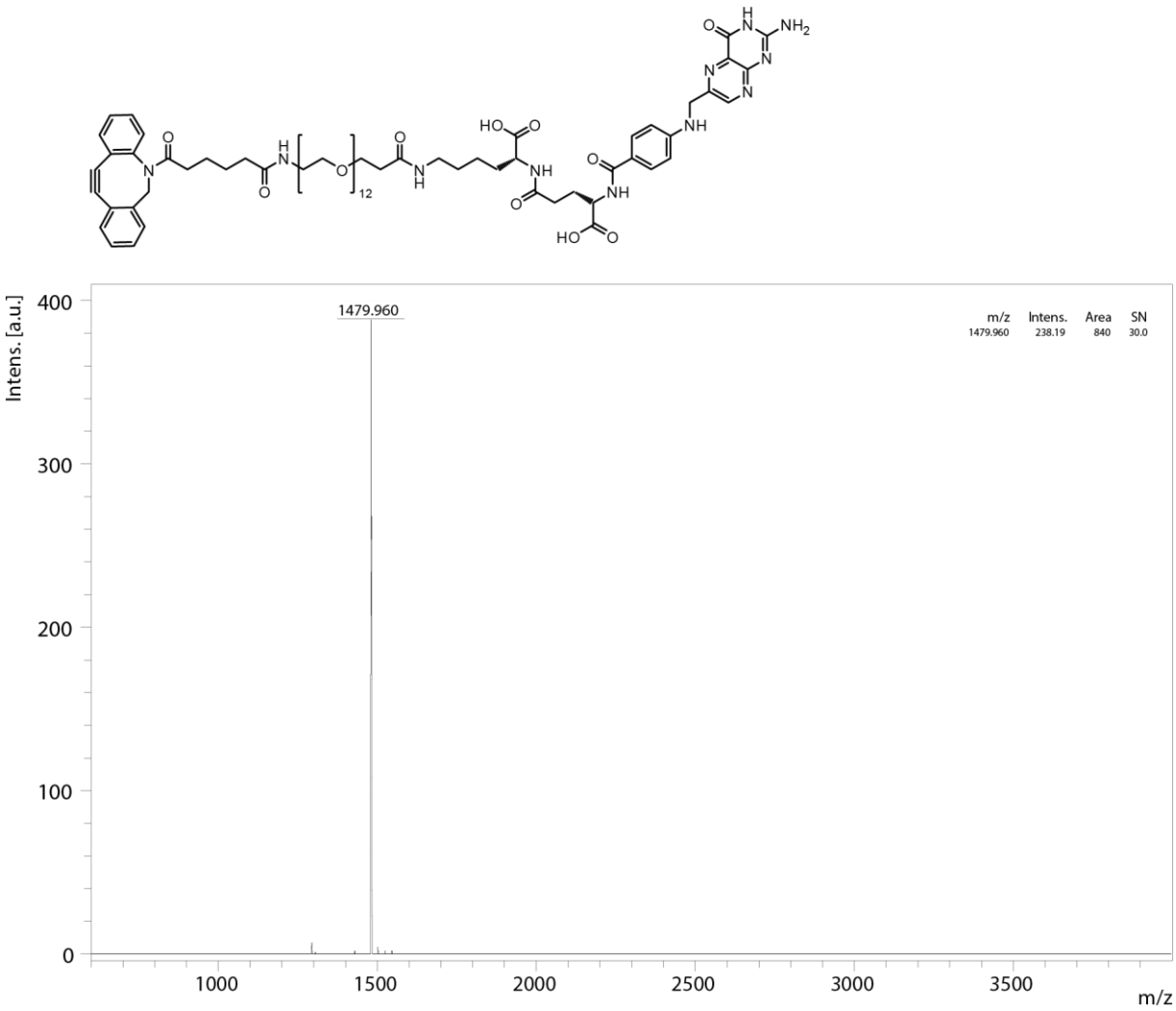

Figure 34: Chemical structure and MALDI mass spectrum of *DP12F*.
Measured in positive mode. Calculated molecular weight: 1484.67 Da. Mass found: 1479.96 Da.

6.2.3.4. *DP24F* (id: 1139)

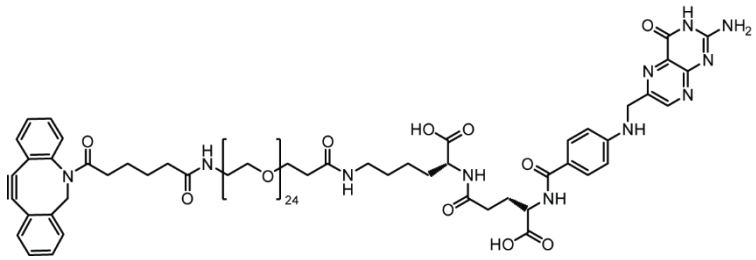

Figure 35: Chemical structure of *DP24F*.
Calculated molecular weight: 2013.30 Da.

6.2.3.5. *DP48F* (id: 1140)

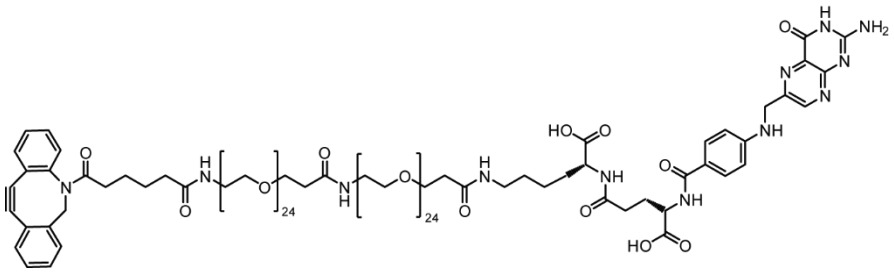

Figure 36: Chemical structure *DP48F*.
Calculated molecular weight: 3141.65 Da.

6.3. Feeding module: software

Adapted from Loy et al. (Loy et al., 2021).

The software for controlling the syringe pumps consists of seven modules: ‘channels.py’, ‘syringes.py’, ‘Module_pumps.py’, ‘setup.py’, ‘ramping_class.py’, ‘mixing_class.py’, and ‘main.py’. The UML class diagram showing the structure of the software and indicating the relations between all classes is shown in **Figure 37**.

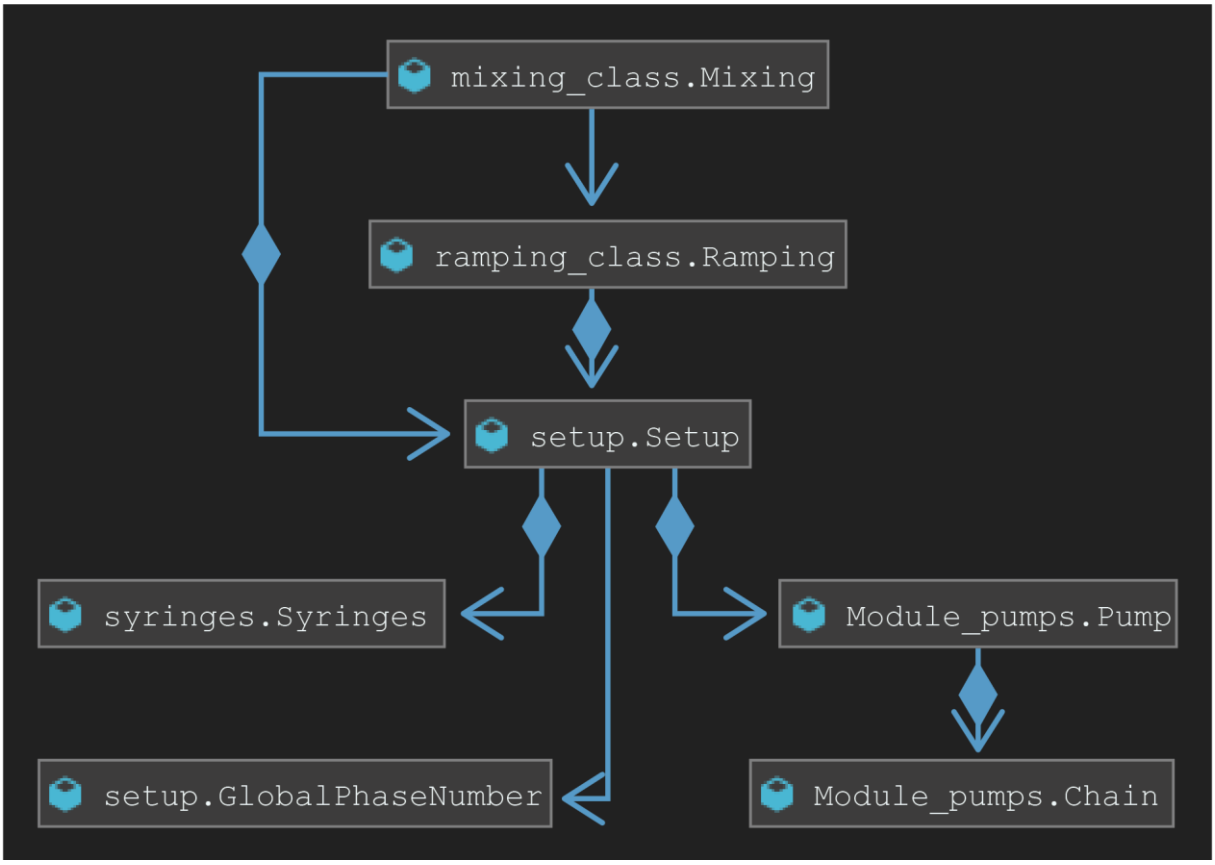

Figure 37: UML class diagram of the control software of the syringe pumps.
Each box represents a class. The name of the class is compounded from the module’s name, and the class’s name separated by a dot. Each box lists all functions from the respective class. An arrow indicates that one class can access the other. A diamond indicates dependence: for example, class ‘Pump’ cannot exist without class ‘Chain’.

The workflow of this program is straightforward (**Figure 38**). First, either the module ‘main.py’ for manual parameter input or the module ‘main_[…]_automated.py’ for automated parameter input needs to be customized to the specific experiment. Second, the user executes the program (**Figure 38**, first orange box), and the software will either ask for parameter input during runtime (manual approach, orange boxes in **Figure 38**) or execute the program automatically (automated approach). The following paragraphs describe the functions of each module.

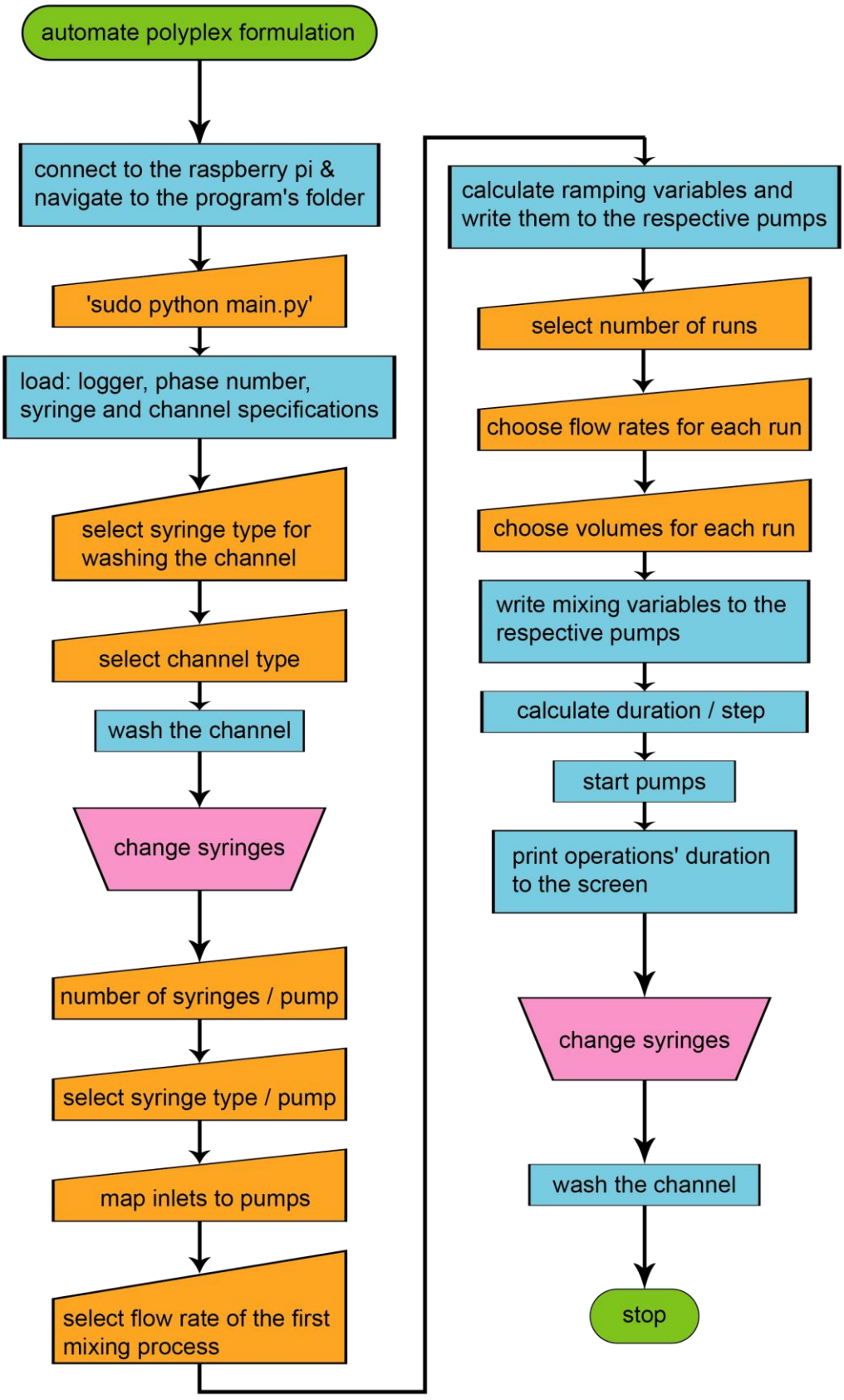

Figure 38: Flowchart describing the automation process of polyplex formulations.
Green ellipses signify the beginning and end of the process. Blue rectangles denote a process executed by the program or by the user. Orange non-symmetrical parallelograms denote user input. Pink symmetrical parallelograms indicate manual operations.

6.3.1. Module: channels.py

The module ‘channels.py’ holds the class ‘Channel()’ that reads the specifications of any channel from a *.txt file and stores them in variables. This approach guarantees the accuracy of the specifications’ data and makes adding or adjusting values a matter of changing a simple text file. The file needs to be stored in the same folder as the module. A set of regular expressions is used to extract the relevant information from the file enabling the simple implementation of additional channel designs to the program. The text files for the single or double meander channel can serve as templates for custom specification files. It is important to transfer the names of the variables from the template file to the new specifications file when new channels are added since the regular expressions recognizes the variable names and write their value to the respective variables of the program. An excerpt from the ‘_set_from_spec_file()’ function with an example of a regular expression is shown in **Code 1**.

Additionally, the class defines the functions to calculate the volume of any section of the target channel from the variables.

```
def _set_from_spec_file(self, filename):
    """ This function opens the file specified in filename. If/elif
    statements are used to detect keywords. If a keyword is detected, regex
    is used to extract the desired information. The information is stored
    in variables defined in __init__.
    """

    with open(filename, "r") as file:  # file is closed automatically when
                                       scope is exited.
        for line in file:
            if "inlets_number" in line:
                digit = [float(s.replace(",", ".")) for s in line.split()
                         if re.findall(r'\d+\.*\d*', s)]
                self.inlets_number = digit[0]
[…]
```

Code 1: Excerpt from the ‘_set_from_spec_file()’ function.
Lines 108 – 119 from the module ‘channels.py’. The function opens the file specified in filename and searches for keywords in every line (here: ‘inlets_number’). When a keyword is detected, the desired information is extracted using regular expressions and it is stored in the target variable (here: the number of inlets of the channel is extracted and stored in ‘self.inlets_number’).

6.3.2. Module: syringes.py

The module ‘syringes.py’ holds the class ‘Syringes()’ and maps each syringe to its inner diameter inside a dictionary. In order to enable the implementation of additional syringes, it defines the function ‘import_syringes()’ to add specifications of new syringes to the program. Additionally, new syringes can be added permanently to the program by customizing the

dictionary in the ‘syringes.py’ module which maps the name of the syringes to their diameter in mm.

6.3.3. Module: Module_pumps.py

The module ‘Module_pumps.py’ holds two classes and the logging function ‘start_logging()’. **Code 2** shows the last lines of the logging function. In this excerpt, two separate loggers for the pumps and the collector are instantiated. The function of the loggers is assured by writing “started” to the screen and the log file. The logger writes all events with their respective timestamp to a *.txt file and saves the file in the folder ‘logs’. When used for the first time, this folder is created in the same directory as the module ‘Module_pumps.py’. Additionally, the module contains the class ‘Chain(serial.Serial)’ which enables the initialization of the serial connection to the syringe pumps, and the class ‘Pump()’ which defines all functions to control the basic parameters of each pump, for example, functions for setting the pumping rate or the volume to be dispensed. If a pump with a different command structure is to be used, all commands in this module which are sent to the pump must be adjusted. First, the dictionary holding the units for rates and volumes (self.units_dict) must be updated. Second, all occurrences of ‘self.serialcon.write()’ must be reviewed to find deviations from the required syntax.

```
[…]
# Define loggers which represent areas in the application:
logger_pump = logging.getLogger('pump')
logger_collector = logging.getLogger('collector')
# Confirm the function of the loggers by printing "started" to the console
# and to the log file.
logger_pump.info("started")
logger_collector.info("started")
return logger_pump, logger_collector
```

Code 2: Excerpt from the initialization of the logger function.
Lines 47 – 54 from the module ‘Module_pumps.py’. The appearance of ‘logger_pump‘ and ‘logger_collector’ at any point in the code will write the string between the brackets to the log file (always) and to the screen (except the argument ‘.debug’ is given).

6.3.4. Module: setup.py

The module ‘setup.py’ holds two classes and the ‘countdown()’ function. The countdown function prints the remaining time of the current operation to the screen. The code of the function is shown in **Code 3**. The function takes two inputs: the time of the operation in seconds and the name of the operation. The output is the remaining time in minutes together with the name of the operation, e.g., ”operation: 10:22”.

```
def countdown(t, name):
    """ This function takes two inputs: t in seconds (float or int) and any
    string as name. The time is converted to minutes and seconds and every
    second the name and the time (dd:dd) is printed to the screen
    effectively counting down to zero.
    """
    t = round(t)
    while t >= 0:
        mins, secs = divmod(t, 60)
        timeformat = '{:02d}:{:02d}'.format(mins, secs)
        print("{}: {}".format(name, timeformat), end= '\r')
        time.sleep(1)
        t -= 1
    print("\n")
```

Code 3: countdown() function.
Lines 7 – 20 from the module 'setup.py'. Inputs are t in seconds and any string for a name. When the function is executed, the name is printed next to the remaining time in minutes + seconds (name: 10:22). The function terminates when the time reaches 00:00.

The first class in the 'setup.py' module is called 'GlobalPhaseNumber()' which defines the functions that control the global phase numbers. This number is used to serialize events on the syringe pumps. It contains two classmethods that are used independently of the current scope of any function to assign numbers to individual steps. This class ensures sequence consistency over all steps. The class is shown in **Code 4**.

```
class GlobalPhaseNumber(object):
    """ This class holds two classmethods to control the phase number.
    'next' increases the phase number by +1, while 'reset' resets it to 0.
    This class is used to assign a phase number to every event, creating a
    defined sequence of steps.
    """
    curr_phn = 1

    @classmethod
    def next(cls):
        cls.curr_phn += 1
        return cls.curr_phn - 1

    @classmethod
    def reset(cls):
        cls.curr_phn = 0
```

Code 4: 'GlobalPhaseNumber()' class.
Lines 22 – 36 from the module 'setup.py'. This class holds two classmethods to control the phase number. 'next' increases the phase number by +1, while 'reset' resets it to 0. This class is used to assign a phase number to every event, creating a defined sequence of steps.

The second class in the 'setup.py' module is called 'Setup()'. It combines the functions and variables from 'syringes.py', 'channels.py', and 'Module_pumps.py' to enable the connection to the pumps and to select the utilized channel and syringes. Connection to each pump is

established with functions from the 'Module_pumps.py' module, and the status of each pump is printed to the screen during instantiation of this class (**Code 5**). The washing function from this module is used to prepare the channel for the intended experiment. This function is based on two assumptions: all active pumps are used for washing and that the same type of syringes is connected to all inlets of the channel. Subsequently, the channel is washed with twice its volume and with the combined flowrates equaling the maximal flow rate defined in the variable 'self.max_flowrate' from the class 'Setup()'. The countdown function (**Code 3**) is used to print the washing sequence's remaining time to the screen.

```
class Setup(object):
    """ This class holds all functions and variables related to the setup
     of the micro mixer. Upon instantiation, it creates an instance of the
     Chain class from 'Module_pumps.py' and from the Syringes Class from
     the module 'syringes.py'. Afterwards, each pump is contacted and
     their status (active / inactive) is stored in a variable.
     The functions in this class are used to select the utilized channel
     and syringes and to wash the setup.
     """
    def __init__(self, pumps):
[…]
        self.max_flowrate = 1500  # ul/h
[…]
        # get the information which pumps are active
        try:
            self.LA120 = p.Pump(self.chain, str(sorted(pumps)[0]),
                                str(pumps[sorted(pumps)[0]]))
            self.pumps_active["LA120"] = True
            self.dict_pump_instances["LA120"] = self.LA120

        except p.PumpError:
            p.logger_pump.info("{} is not responding at address
                               {}.".format(sorted(pumps)[0],
                               pumps[sorted(pumps)[0]]))
[…]
```

Code 5: Excerpt from the 'Setup()' class.
Lines 39 – 47, 54, and 57 – 64 from the module 'setup.py'. Upon instantiation of the class, the '__init__()' function is called automatically. Here, the variable 'self.max_flowrate' is set to 1500, and the connection to the pump LA120 is established. If the pump LA120 were offline, the logger would print 'LA120 is not responding at address 01' to the screen and to the log file.

The exact configuration of the setup, for example, the mapping of inlets to pumps, is provided to the program by the user. To avoid unnecessary errors, the program checks each input for plausibility before it is committed to a variable. Simple checks verify the format of the input, for example, flow rates and volumes must be numbers, while more elaborate checks safeguard the integrity of the device by ensuring that the maximum total flow rate or the maximum volume of a syringe are not exceeded. **Code 6**, for example, shows the routine for checking if the

number of inlets connected to each syringe pump does not exceed the number of syringes each pump can hold.

```
def check_connections(self):
    """Checks if the number of syringes matches the number of inlets."""
    check_LA120 = sum(1 for x in self.dict_inlets_pumps.values() if
                      x == "LA120")
[…]
    if check_LA120 > self.pump_max_syr["LA120"]:
        print("""Pump LA120 cannot hold {} syringes.
              Please repeat the selection process.""".format(check_LA120))
        self.tubing_connections()
[…]
```

Code 6: Excerpt from the 'check_connections()' function.
Lines 207 – 223 from the module 'ramping_class.py'. The function counts the occurrences of the name of the pump (e.g., "LA120") in the dictionary 'dict_inlets_pumps'. This dictionary maps the inlets of the channel to the pumps as specified by the user. If a pump is mapped to more inlets than it has channels, a message is printed to the screen, and the mapping process is repeated.

Another way to avoid unnecessary errors is the confirmation of selections. The logging function described in **Code 2** confirms every selection by simultaneously printing it to the screen and writing it to the log file. A typical line of code that confirms the selection of a flow rate is shown in **Code 7**. If the automated approach is chosen, only the result of the function is printed. If the manual approach is chosen, then the call to the 'rate()' function from the 'mixing_class.py' module prints a question to the screen depending on the number of runs selected previously (e.g., 'What is the flow rate for run 2 for pump LA120?') and the program waits for the input of the user. The input is converted to a floating-point number (float), if possible, and the selection is confirmed by printing it to the screen (e.g., 'Run 2: LA120's rate is 500').

```
def rate(self, pumps_active, **kwargs):
    """ This function asks the user to provide rates for each run. The
    rates' unit is selected once for all subsequent runs on this pump.
    Alternatively, the rates and the respective unit can be passed directly
    to the function via the kwargs. The names of the arguments should be
    <name_of_pump>_rate for rates and <name_of_pump>_unit for units. Rates
    must be stored in a list. All active pumps must be used.
    Example: LA120_rates = [120,140,160], LA160_rates = [1200, 1400, 1600],
    LA120_unit = 'ul/h', LA160_unit = 'ul/h'.
    """
[…]
    print("What is the flow rate for run {} for pump
          {}?".format(i+1, sorted(pumps_active)[0]))
          rate = input("> ").replace(",", ".")
          try:
              self.rates_LA120.append(float(rate))
              p.logger_pump.info("Run {}: {}'s rate is {}.".format(i+1,
                                 sorted(pumps_active)[0],
                                 self.rates_LA120[-1]))
          except ValueError:
              print("Please choose a number.")
              return self.rate(pumps_active)
[…]
```

Code 7: Excerpt from the 'rate()' function.
Lines 152 – 359 from the module 'mixing_class.py'. Every time the user assigns a flow rate to a pump the function 'rate()' is called. If the automated approach is chosen, the function gets its parameters via the **kwargs. If the manual approach is chosen, the function asks the user for the respective flow rates and units for each pump. In both cases, the input is validated and stored in a separate list for each pump, e.g., 'rates_LA120' and the result is printed to the screen and the log.

After the setup of the device and the washing of the channel have been completed, the ramping and the mixing process must be defined.

6.3.5. Module: ramping_class.py

The module 'ramping_class.py' holds two classes. The class 'Ramping()' defines all functions related to bringing the reactants to the mixing zone at the intended point in time. First, it reads the parameters from the 'Setup()' class. The program assumes that the channel type is not changed after it has been washed, but the syringes can be replaced. Second, functions from the class are used to calculate volumes and rates for the respective pumps and write the ramping sequence (default: ten steps) to the pumps. The rate at which the reactants reach the mixing zone is also the first rate at which the 'mixing_class.py' module mixes reactants. When all information about the upcoming mixing process has been gathered, the ramping protocol is executed to bring all reactants to the mixing zone at the same time. This approach prevents waste of reactants and the formation of unwanted side products due to unintended mixing ratios. Moreover, this approach minimizes the displacement of reactants pumped with relatively small flow rates from the mixing zone by reactants pumped with relatively higher flow rates.

To this end, the flow rate of the first mixing opera tion is taken as the target flow rate for each pump, and a ten-step descending, or ascending sequence of flow rates and respective volumes is calculated. The direction of the ramping sequence is dependent on the magnitude of the target flow rate relative to the mean flow rate of all flow rates. If the target flow rate of a pump is lower than the mean flow rate, the ramping sequence will be descending and vice versa for target flow rates above the mean. This approach minimizes the displacement of reactants due to pressure gradients. The implementation of the calculation in the program is shown in **Code 8**.

```
def ramping_calc(self):
    """This function calculates the flow rate and volume of each step
    and stores them in a list"""

    for key in self.dict_rates_pumps.keys():
        if "LA120" in key:  # surrogate test: is pump LA120 being used?
            # Decides if ramping to the final flow rate (FR) is done from a
            # higher or lower FR

            if self.dict_rates_pumps[key] > self.total_flowrate /
            sum(self.pump_configuration_n.values()):
                self.rates_LA120.append(self.total_flowrate * 0.25)

                while len(self.rates_LA120) < self.steps:
                    self.rates_LA120.append(round(self.rates_LA120[-1]
                    + (self.dict_rates_pumps[key]
                    - self.rates_LA120[0])/9, 3))
            else:
                if self.dict_rates_pumps[key] <= self.total_flowrate /
                sum(self.pump_configuration_n.values()):
                    self.rates_LA120.append(self.mean_flowrate * 2
                    - self.dict_rates_pumps[key])

                    while len(self.rates_LA120) < self.steps:
                        self.rates_LA120.append(round(self.rates_LA120[-1]
                        + (self.dict_rates_pumps[key]
                        - self.rates_LA120[0])/9, 3))

            p.logger_pump.debug("Ramping rates LA120: {}".format(
                                ",".join(str(x) for x in self.rates_LA120))
                                )
[…]
```

Code 8: Excerpt from the 'ramping_calc()' function.
Lines 418 – 435 from the module 'ramping_class.py'. In this excerpt, the calculation of the flow rates for the pump LA120's ramping process is shown. 'dict_rates_pumps' holds the first flow rate of the mixing process mapped to the respective pump. This dictionary is used to decide if a ramping sequence must be calculated for this pump (i.e., if the pump is active). The next if-clause decides if the target flow rate of the pump LA120 is lower or higher than the mean flow rate of all active pumps. The while-clause nested inside the if-clause calculates the respective sequence of flowrates and stores them in the list 'rates_LA120'. At the end of this function, the sequence of rates is written to the log file without printing it to the screen by the logger function.

The class ‘EmptyClass()’ is used to illustrate that the named arguments ‘LA120’. ‘LA122’, and ‘LA160’ in the function ‘writing()’ from the ‘Ramping()’ class expect an instance of the respective pump from the class ‘Pump()’ from the module ‘Module_pumps.py’. If the default ‘EmptyClass()’ is passed to the named argument, an error message detailing the problem is printed to the screen when the function is called.

The mixing operations will start seamlessly when the ramping process has finished. The countdown printed to the screen will follow the individual steps and inform the user when to start gathering the product from the outlet and when to discard the product (e.g., because of the overlap volume between mixing operations).

6.3.6. Module: mixing_class.py

The module ‘mixing_class.py’ holds the class ‘Mixing()’ which defines the functions to write the mixing protocol to the pumps. It also has the capability to purge the product from the mixing zone after the last mixing step was executed in order to reduce the waste of educts. To be precise, the program expects the number of separate mixing operations and their parameters, how much total overlap volume between fraction will be given, and the number of pumps which will purge the channel.

The overlap volume is chosen once by the user. The program calculates the relative overlap volume for each pump, depending on the volume the pump is pumping relative to the total volume. The calculated volumes are then inserted between all mixing operations to avoid cross-contamination of consecutive products. An excerpt of this function can be inspected in **Code 9**.

The ‘end_process()’ function defines the pumps designated to purging the channel. When the mixing protocol has completed, a fraction of the last formulation remains in the channel section from the mixing zone to the outlet. In order to gather this product as well, the channel needs to be purged. Therefore, I advise to purge the channel after the last run. The purging function calculates the required flow rate, volume, and time for each pump, and appends them to the respective lists holding the values for each pump.

In theory, the program can store an almost unlimited number of steps. However, the internal memory of our pumps is limited to 41 steps or phases (e.g., combinations from flow rates and volumes). Although, usually, the volume of the syringes is the limiting factor for the length of the program.

```
def overlap_calc(self, overlap=None):
    """ This function asks for the overlap between runs and stores them
    in the variable 'self.overlap'. A sensible value is 8 µl. Afterwards,
    it adds volumes and rates in between runs in self.rates_LAxxx und
    self.vol_LAxxx.
    Alternatively, the overlap volume can be passed to the function via
    the kwargs. The name of the argument must be 'overlap'. For example:
    overlap = 8
    """
[…]
    # calculate relative overlap for each pump
    def _relative_overlap_calc(rates_list):
        """
        This function takes the list of the rates from one pump as
        parameter and calculates the relative overlap volume for each pump.
        """
        for j in range(0, len(rates_list)):
            # calculate total flow rate
            flowrate = 0
            if self.rates_LA120:
                flowrate += self.rates_LA120[j] *
                            self.pump_configuration_n["LA120"]
[…]
    # checks, if self.rates_LA120 exists, calculates the necessary
    # overlaps and inserts them into the pump volume's list.
    # Additionally, the name of the overlap is inserted into the
    # variable self.name which is used to inform the user with the
    # countdown function.
    if self.rates_LA120:
        _relative_overlap_calc(self.rates_LA120)
        for i in range(len(self.overlap_LA120)):
            self.name.insert(i*2, "overlap {}".format(i))
        del self.name[0]
[…]
     # insert relative overlap into each self.volume
     for i in range(0, len(self.volumes_LA120)):
         self.volumes_LA120.insert(i*2, self.overlap_LA120[i])
     if self.volumes_LA120:
         # removes first item in the list. Overlap is only necessary
         # between runs.
         del self.volumes_LA120[0]

[…]
    # insert overlap flow rate (rate of the next run) into each self.rate
    for i in range(0, len(self.rates_LA120)):
        self.rates_LA120.insert(i*2, self.rates_LA120[i*2])
        # *2 because with each iteration of the loop the
        # length of rates.LA120 grows
```

Code 9: Excerpt from the 'overlap_calc()' function.
Lines 462 – 579 from the module 'mixing_class.py'. For brevity reasons, only the code for pump LA120 is shown. This function consists of four parts. First, the relative overlap for each pump is calculated. Second, the string 'overlap' and its number is inserted into the list holding the names of all operations. The names in the list are used for the 'countdown()' function. Third, and fourth, the respective overlap volume and flowrate is inserted in the respective lists. The contents of self.rates_LA120 and self.volumes_LA120 are subsequently written to the respective pump by another function and the list 'self.name' is used to inform the user about the name of the current pumping operation.

6.3.7. Modules: main[…].py

The module ‘main.py’ holds the sequence of functions from all the modules above to execute the mixing protocol. It can be customized in order to fit any mixing regime by altering the sequence of functions and their respective arguments.

Arguments to the respective functions can be provided in two ways: either manually during execution of the ‘main.py’ module or automatically by passing the variables directly to the respective functions via the ‘**kwargs’ arguments inside the ‘main.py’ module.

The advantage of the manual approach is the increased flexibility during the experiment since variables can be changed on the fly and the ease of use since no python code must be customized. However, the disadvantage of this approach is the increased time consumption during the experiment due to the many user inputs required. A ‘main.py’ module for the manual approach can be inspected in **Code 10**.

The advantage of the automated approach is the ability to automated complete experiments without requiring a single user input during execution. However, some python knowledge is essential to leverage the full potential of this approach. Two modules – one for the single meander channel and one for the double meander channel – showcasing the potential of the automated approach are available on GitHub as well: ‘main_single_meander_automated.py’ and ‘main_double_meander_automated.py’ (Loy, 2020a).

```
import ramping_class as r_c
import mixing_class as m_c
import setup
# -- Program: --
# Usage: E.g., Formulation of core nanoparticles from two or more
# components.
# All relevant parameters are asked from the user during program execution.

# ------------------------------------------------------------------------
# -- Initialize the pumps and prepare the channel --

# Define Name and address of all pumps:
pumps = {"LA120": "01", "LA122": "02", "LA160": "03"}

# instantiate global phase number
phase_number = setup.GlobalPhaseNumber()

# test which pumps are active, select the channel and the syringes,
# wash the channel
pumps_setup = setup.Setup(pumps)
pumps_setup.select_syringe_washing()
pumps_setup.select_channel()
pumps_setup.washing()

# -- ramp your educts to the mixing zone --
ramping = r_c.Ramping(pumps_setup.channel_used)
ramping.syringes_number(pumps_setup.pumps_active)
ramping.syringes_type(pumps_setup.dict_pump_instances,
pumps_setup.pumps_active)
ramping.tubing_connections()
ramping.first_rate()
ramping.calc_mean_flowrate(pumps_setup.channel)
ramping.ramping_calc()
ramping.writing(phase_number,
                LA120=pumps_setup.dict_pump_instances["LA120"],
                LA122=pumps_setup.dict_pump_instances["LA122"],
                LA160=pumps_setup.dict_pump_instances["LA160"])

# -- mixing: formulate your products --
mixing = m_c.Mixing(ramping_instance=ramping)
mixing.number_of_runs()
mixing.rate(pumps_setup.pumps_active)
mixing.volume(pumps_setup.pumps_active)
mixing.overlap_calc()
mixing.end_process(pumps_setup.channel,
                   pumps_setup.pumps_active)
mixing.writing(pumps_setup.dict_pump_instances,
               pumps_setup.pumps_active,
               phase_number)
mixing.mixing(pumps_setup.channel_used,
              setup.countdown,
              pumps_setup.dict_pump_instances,
              pumps_setup.channel,
              pumps_setup.pumps_active,
              pumps,
              ramping_time=ramping.ramping_time,
              dict_rate_pumps=ramping.dict_rates_pumps)

# -- washing --
pumps_setup.select_syringe_washing()
pumps_setup.select_channel()
pumps_setup.washing()
```

Code 10: 'main.py' module.
Lines 1 – 55 from the 'main.py' module. The first three lines import all the other modules to enable access to their functions. Subsequently, the code for setting up the machine ('pumps_setup.*'), ramping the educts to the mixing zone ('ramping.*'), and producing the formulation ('mixing.*') is executed. In the end, another washing step is appended. A flow chart of this module is shown in **Figure 38**.

6.4. Collection module: software

Adapted from Loy et al. (Loy et al., 2021).

The control program for the fraction collector consists of three modules, 'initialize.py', 'move.py' and 'main.py'. 'initialize.py' and 'move.py' contain the code to initialize the fraction collector and to move the dispenser head around. 'main.py' imports both aforementioned modules and executes a customizable sequence of their functions according to the needs of the user. **Figure 39** shows an UML class diagram to illustrate the dependencies between the classes of the modules. A complete list of all classes and functions of the two modules can be found on GitHub (Loy, 2020a).

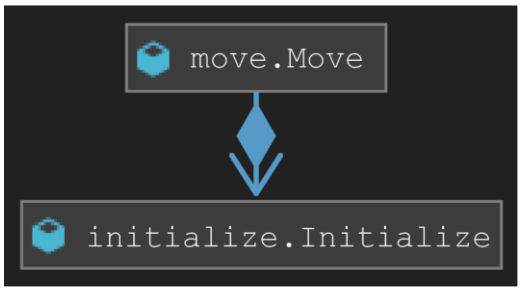

Figure 39: UML class diagram of the control software of the fraction collector.
Each box represents a class. The name of the class is compounded from the name of the module, and the name of the class separated by a dot. An arrow indicates that one class has access to the functions of the other class. The diamond indicates dependence: class 'Move' cannot exist without class 'Initialize'.

The workflow of this program is straightforward (**Figure 40**). First, the module 'main.py' needs to be customized to drive the dispenser head to the desired wells at the intended time. Second, the user executes the program (**Figure 40** orange box), and the software will follow the instructions (**Figure 40**, blue boxes 2 - 5).

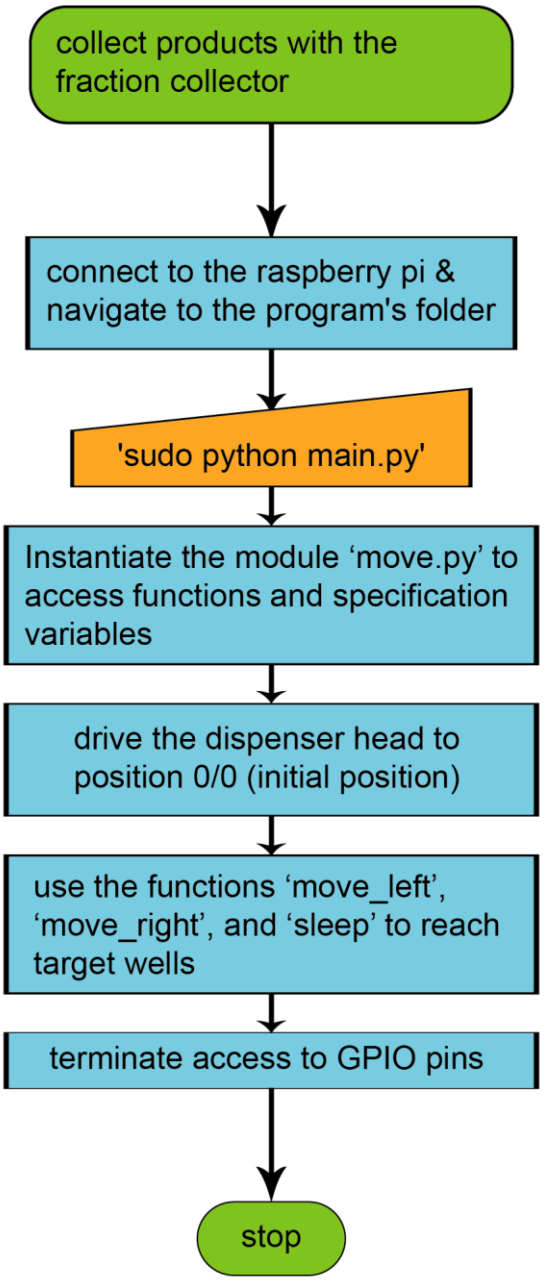

Figure 40: Flowchart describing the workflow of the fraction collector.
Green ellipses signify the start and beginning of the process. Blue rectangles denote a process executed by the program or by the user. Orange non-symmetrical parallelograms denote user input. User input is possible either during run time or automated before execution.

6.4.1. Module: initialize.py

The class ‘Initialize()’ from the module ‘initialize.py’ has three main functions. It maps the GPIO pins to the stepper motors and end switches, it defines the patterns to turn the stepper in the desired direction, and it holds the functions to enable the end switches. Whenever the program is executed, this class must be instantiated first because it lays the groundwork for the subsequent modules. The assignment of the GPIO pins and the definition of the step pattern to turn the motor left or right is shown in **Code 11**.

```
class Initialize(object):
    """ This class initializes the fraction collector. It maps the raspi's
    GPIO pins to the steppers' coils and to the end switches. It defines
    the patterns to turn the steppers in a specific direction and it holds
    the functions to enable the end switches.
    """
    def __init__(self):
        # callable variables used in this Method
[…]
        self.mask_dl = []  # pattern to turn the stepper left
        self.mask_dr = []  # pattern to turn the stepper right
        # map pins to a stepper and its end switch
        self.pins_stepper1 = {"A": 18, "B": 23, "C": 24, "D": 25,
                              "stop_1": 27}
        self.pins_stepper2 = {"A": 5, "B": 6, "C": 13, "D": 26,
                              "stop_2": 17}
[…]
        # define pattern for each step of the steppers
        patterns = [[1, 0, 1, 0], [1, 0, 0, 1], [0, 1, 0, 1], [0, 1, 1, 0]]
        # turn stepper in direction "left"
        self.mask_dl = patterns[0:4]
        # turn stepper in direction "right"
        self.mask_dr = list(reversed(patterns[0:4]))
```

Code 11: Excerpt from the 'Initialize()' class.
Lines 7 – 20 and 63 – 68 from the 'initialize.py' module. Upon instantiation of this class, the pins of stepper motor 1 and stepper motor 2 are stored in 'self.pins_stepper1' and 'self.pins_stepper2' and the pattern that drives the stepper motors left or right is generated and stored in 'self.mask_dl' and 'self.mask_dr'.

6.4.2. Module: move.py

The class 'Move()' from the module 'move.py' holds all parameters related to moving the dispenser head around: defined speeds, the maximum number of steps in x and y direction, and the number of steps between wells of the default 96 well plate. Functions for reaching the starting position and moving the dispenser head left or right are defined in this class as well. As depicted in the UML class diagram (**Figure 39**), it must create an instance of the class 'Initialize()' to access its functions. Important variables for the physical integrity of the collector are shown in **Code 12**.

The variable 'speeds' is a dictionary mapping strings – i.e., names given to certain speeds – to numbers defining the turning rate of the stepper motors. Functions moving a stepper motor in a particular direction use these numbers to determine the time in seconds to wait until the next step is taken (i.e., electrical current is directed to the next coil).

The variable 'maximum_steps_stepper1' or 'maximum_steps_stepper2' defines the boundaries for the target stepper. The program counts the steps a stepper takes in the global variable 'step_counter_stepper_1' and 'step_counter_stepper_2', and it will stop the execution of the

program if the value stored in this variable exceeds the maximum number of steps or if it falls below zero. The variables ‘steps_stepper_1’ and ‘steps_stepper_2’ hold lists of empirically found distances between wells of – in this case – 96 well plates. Since the distance between wells cannot be covered exactly with full steps, variations of the number of steps between wells were introduced to account for this inaccuracy. If a different container (e.g., a 24 well plate) were to be used with this collector, these two variables would have to be adjusted accordingly.

```
class Move(object):
    """
    Holds all the commands and attributes to move both steppers.
    Move_initial and move_initial2 move both steppers to position 0/0 on
    the x/y grids coordinate system. move_left means that the stepper
    is turning left. The carriage, however, is moving right due to the
    positioning of the steppers. Same is true for move_right.
    """
    def __init__(self):
        # initialize components and wiring
        # step counter to know the exact position of the dispenser head
        global step_counter_stepper_1
        global step_counter_stepper_2
        # speeds: 0.3 sec is very slow -> no stepping errors
        # 0.002 sec is possible without errors
        self.speeds = {"s100": 0.005, "s75": 0.01, "s50": 0.025,
                       "s25":0.05, "s0": 0.1}
        # Instantiate the class 'Initialize' from 'initialize.py' to enable
        # access to its functions and to set up the mapping of the GPIO
        # pins to the steppers and end switches.
        self.system = ini.Initialize()
        step_counter_stepper_1 = 0
        self.maximum_steps_stepper_1 = 260
        step_counter_stepper_2 = 0
        self.maximum_steps_stepper_2 = 340
        self.total_sub_steps = len(self.system.mask_dl)
        # steps for a 96 well plate.
        self.steps_stepper_1 = [43, 28, 27, 27, 28, 27, 28, 28]
        # steps from positions zero to wells A - H.
        self.steps_stepper_2 = [35, 28, 27, 27, 28, 27, 28, 27,
                                27, 28, 27, 28]  # steps from pos. 0 to
                                                 # wells 12 - 1.
[…]
```

Code 12: Excerpt from the ‘Move()’ class.
Lines 8 – 34 from the ‘move.py’ module. This class holds all commands and attributes related to moving the dispenser head around. As soon as the class is instantiated, an instance of the class ‘Initialize()’ from the module ‘initialize.py’ is created in order to access GPIO pin mappings and functions to control end switches. The ‘step_counter_stepper_1 or 2’ is used in combination with ‘maximum_steps_stepper_1 or 2’ to ensure that the dispenser head is only moved inside the boundaries of the collector.

6.4.3. Module: main.py

The module ‘main.py’ utilizes the classes and functions from the other two modules. It must always start with an instance of ‘Move()’ from ‘move.py.’ to enable access to the functions moving the dispenser head around and defining the utilized GPIO pins. Subsequently, the

'move_initial()' function must be called to move the dispenser head to its initial position. Afterwards, any sequence of 'move_left()' and 'move_right()' commands can be programmed. The program counts the number of steps taken and will abort if its predefined maximum number of steps is reached. The function 'sleep()' from the 'time' module can be used to pause the dispenser head at any position. The program should be terminated with a call to 'GPIO.cleanup()' to reset the GPIO assignment. The structure of the 'main.py' module described in the flow chart (**Figure 40**) is shown in **Code 13**.

```
import RPi.GPIO as GPIO
import move
from time import *

# Instantiate the class 'Move' from the module 'move.py' to enable access
to functions and variables.
commands = move.Move()

# Move the dispenser head to its initial position x/y = 0/0.
commands.move_initial(commands.speeds["s25"], commands.speeds["s0"])
commands.move_initial2(commands.speeds["s25"], commands.speeds["s0"])

# program: serve wells from a 96 well plate: A1-> A12 -> B12 -> B1
# go to well A1
commands.move_left(2, sum(commands.steps_stepper_2) - 16,
commands.speeds["s50"])  # -16: drives to far.
commands.move_right(1, commands.steps_stepper_1[0], commands.speeds["s50"])

# wait 3s (i.e. the time to collect your sample)
sleep(3)

# for-clause. Iterates over the elements of the list 'steps_stepper_2'
# and drives the target steps to the right (A1 -> A12)
for i in list(reversed(commands.steps_stepper_2))[:-1]:
    commands.move_right(2, i, commands.speeds["s50"])
    sleep(3)

# drives stepper 1 target steps to the right (A12 -> B12)
commands.move_right(1, commands.steps_stepper_1[1], commands.speeds["s50"])
sleep(3)

# drives stepper 2 target steps to the left (B12 -> B1)
for i in commands.steps_stepper_2[1:]:
    commands.move_left(2, i, commands.speeds["s50"])
    sleep(3)

# removes access to and any voltage from the GPIO pins.
GPIO.cleanup()
```

Code 13: The 'main.py' module of the fraction collector.
Lines 1 – 35 from the 'main.py' module. The first three lines import all necessary modules to enable access to their functions. Subsequently, the code for setting up the machine ('move.Move()') and moving the dispenser head to its initial position ('move_initial()') is executed. The following lines drive the dispenser head from its initial position to the following 24 wells: A1 -> A12 -> B12 -> B1 with a pause of 3 s at each well. In the end, access to GPIO pins is terminated ('GPIO.cleanup()').

This code drives the dispenser head to its initial position and subsequently dispenses products in the first 24 wells of a 96 well plate following the pattern A1 -> A12 -> B12 -> B1. The dispenser head pauses at each well for three seconds. A video documenting the execution of this code can be found on GitHub (Loy, 2020a).

7. References

Aagaard L, Rossi JJ. 2007. RNAi therapeutics: Principles, prospects and challenges. *Advanced Drug Delivery Reviews* 59:75–86. DOI: 10.1016/j.addr.2007.03.005.

Abstiens K, Goepferich AM. 2019. Microfluidic manufacturing improves polydispersity of multicomponent polymeric nanoparticles. *Journal of Drug Delivery Science and Technology* 49:433–439. DOI: S1773224718312681.

Abstiens K, Gregoritza M, Goepferich AM. 2018. Ligand density and linker length are critical factors for multivalent nanoparticle–receptor interactions. *ACS Applied Materials & Interfaces*:acsami.8b18843. DOI: 10.1021/acsami.8b18843.

Ahlmann-Eltze C. 2017. ggsignif: Significance Brackets for "ggplot2."

Aiuti A, Roncarolo MG, Naldini L. 2017. Gene therapy for ADA-SCID, the first marketing approval of an ex vivo gene therapy in Europe: paving the road for the next generation of advanced therapy medicinal products. *EMBO Molecular Medicine* 9:737–740. DOI: 10.15252/emmm.201707573.

Akinc A, Thomas M, Klibanov AM, Langer R. 2005. Exploring polyethylenimine-mediated DNA transfection and the proton sponge hypothesis. *The Journal of Gene Medicine* 7:657–663. DOI: 10.1002/jgm.696.

Allen TM. 2004. Drug Delivery Systems: Entering the Mainstream. *Science* 303:1818–1822. DOI: 10.1126/science.1095833.

Allen TM, Cullis PR. 2013. Liposomal drug delivery systems: From concept to clinical applications. *Advanced Drug Delivery Reviews* 65:36–48. DOI: 10.1016/j.addr.2012.09.037.

Ameri H. 2018. Prospect of retinal gene therapy following commercialization of voretigene neparvovec-rzyl for retinal dystrophy mediated by RPE65 mutation. *Journal of Current Ophthalmology* 30:1–2. DOI: 10.1016/j.joco.2018.01.006.

Amgen. 2015.FDA Approves IMLYGIC™ (Talimogene Laherparepvec) As First Oncolytic Viral Therapy In The US. *Available at https://www.amgen.com/media/news-releases/2015/10/fda-approves-imlygic-talimogene-laherparepvec-as-first-oncolytic-viral-therapy-in-the-us/* (accessed October 19, 2019).

Anchordoquy TJ, Koe GS. 2000. Physical Stability of Nonviral Plasmid-Based Therapeutics. *Journal of Pharmaceutical Sciences* 89:289–296. DOI: 10.1002/(SICI)1520-6017(200003)89:3<289::AID-JPS1>3.0.CO;2-N.

Andersen G. 2016.XY Table. *Available at https://www.thingiverse.com/thing:18678* (accessed January 18, 2020).

Antony AC. 1992. The biological chemistry of folate receptors. *Blood* 79:2807–2820. DOI: 10.1177/1059840511426747.

Bainbridge JWB, Mehat MS, Sundaram V, Robbie SJ, Barker SE, Ripamonti C, Georgiadis A, Mowat FM, Beattie SG, Gardner PJ, Feathers KL, Luong VA, Yzer S, Balaggan K, Viswanathan A, De Ravel TJL, Casteels I, Holder GE, Tyler N, Fitzke FW, Weleber RG, Nardini M, Moore AT, Thompson DA, Petersen-Jones SM, Michaelides M, Van Den Born LI, Stockman A, Smith AJ, Rubin G, Ali RR. 2015. Long-term effect of gene therapy on Leber's congenital amaurosis. *New England Journal of Medicine* 372:1887–

1897. DOI: 10.1056/NEJMoa1414221.

Bainbridge JWB, Smith AJ, Barker SS, Robbie S, Henderson R, Balaggan K, Viswanathan A, Holder GE, Stockman A, Tyler N, Petersen-Jones S, Bhattacharya SS, Thrasher AJ, Fitzke FW, Carter BJ, Rubin GS, Moore AT, Ali RR. 2008. Effect of Gene Therapy on Visual Function in Leber's Congenital Amaurosis. *New England Journal of Medicine* 358:2231–2239. DOI: 10.1056/NEJMoa0802268.

Baum C, Kustikova O, Modlich U, Li Z, Fehse B. 2006. Mutagenesis and oncogenesis by chromosomal insertion of gene transfer vectors. *Human Gene Therapy* 17:253–263. DOI: 10.1089/hum.2006.17.253.

Behr JP. 1993. Synthetic gene-transfer vectors. *Accounts of Chemical Research* 26:274–278. DOI: 10.1021/ar00029a008.

Behr J-P. 1997. The proton sponge: a trick to enter cells the viruses did not exploit. *CHIMIA International Journal for Chemistry* 2:34–36.

Belliveau NM, Huft J, Lin PJ, Chen S, Leung AK, Leaver TJ, Wild AW, Lee JB, Taylor RJ, Tam YK, Hansen CL, Cullis PR. 2012. Microfluidic Synthesis of Highly Potent Limit-size Lipid Nanoparticles for In Vivo Delivery of siRNA. *Molecular Therapy - Nucleic Acids* 1:e37. DOI: 10.1038/mtna.2012.28.

Benjaminsen R V, Mattebjerg MA, Henriksen JR, Moghimi SM, Andresen TL. 2013. The Possible "Proton Sponge " Effect of Polyethylenimine (PEI) Does Not Include Change in Lysosomal pH. *Molecular Therapy* 21:149–157. DOI: 10.1038/mt.2012.185.

Bessis N, GarciaCozar FJ, Boissier M-C. 2004. Immune responses to gene therapy vectors: influence on vector function and effector mechanisms. *Gene Therapy* 11:S10–S17. DOI: 10.1038/sj.gt.3302364.

Blaese RM, Culver KW, Miller AD, Carter CS, Fleisher T, Clerici M, Shearer G, Chang L, Chiang Y, Tolstoshev P, Greenblatt JJ, Rosenberg SA, Klein H, Berger M, Mullen CA, Ramsey WJ, Muul L, Morgan RA, Anderson WF. 1995. T Lymphocyte-Directed Gene Therapy for ADA- SCID: Initial Trial Results After 4 Years. *Science* 270:475–480. DOI: 10.1126/science.270.5235.475.

Bloomfield VA. 1997. DNA condensation by multivalent cations. *Biopolymers* 44:269–282. DOI: 10.1002/(SICI)1097-0282(1997)44:3<269::AID-BIP6>3.0.CO;2-T.

Bobo D, Robinson KJ, Islam J, Thurecht KJ, Corrie SR. 2016. Nanoparticle-Based Medicines: A Review of FDA-Approved Materials and Clinical Trials to Date. *Pharmaceutical Research* 33:2373–2387. DOI: 10.1007/s11095-016-1958-5.

Boisseau P, Kiparissides C, Pavesio A, Saxl O. 2005. *Vision Paper and a Basis for a Strategic Research Agenda for NanoMedicine*. DOI: 10.1016/1350-4789(94)90277-1.

Boletta A, Benigni A, Lutz J, Remuzzi G, Soria MR, Monaco L. 1997. Nonviral Gene Delivery to the Rat Kidney with Polyethylenimine. *Human Gene Therapy* 8:1243–1251. DOI: 10.1089/hum.1997.8.10-1243.

Bommareddy PK, Patel A, Hossain S, Kaufman HL. 2017. Talimogene Laherparepvec (T-VEC) and Other Oncolytic Viruses for the Treatment of Melanoma. *American Journal of Clinical Dermatology* 18:1–15. DOI: 10.1007/s40257-016-0238-9.

Bouard D, Alazard-Dany N, Cosset FL. 2009. Viral vectors: From virology to transgene expression. *British Journal of Pharmacology* 157:153–165. DOI: 10.1038/bjp.2008.349.

Boussif O, Lezoualc'h F, Zanta MA, Mergny MD, Scherman D, Demeneix B, Behr JP. 1995. A versatile vector for gene and oligonucleotide transfer into cells in culture and in vivo: polyethylenimine. *Proceedings of the National Academy of Sciences* 92:7297–7301. DOI: 10.1073/pnas.92.16.7297.

Braun CS, Fisher MT, Tomalia DA, Koe GS, Koe JG, Middaugh CR. 2005. A stopped-flow kinetic study of the assembly of nonviral gene delivery complexes. *Biophysical Journal* 88:4146–4158. DOI: 10.1529/biophysj.104.055202.

Buxbaum JN. 2018. Oligonucleotide Drugs for Transthyretin Amyloidosis. *New England Journal of Medicine* 379:82–85. DOI: 10.1056/NEJMe1805499.

Cartier N, Hacein-Bey-Abina S, Bartholomae CC, Veres G, Schmidt M, Kutschera I, Vidaud M, Abel U, Dal-Cortivo L, Caccavelli L, Mahlaoui N, Kiermer V, Mittelstaedt D, Bellesme C, Lahlou N, Lefrere F, Blanche S, Audit M, Payen E, Leboulch P, L'Homme B, Bougneres P, Von Kalle C, Fischer A, Cavazzana-Calvo M, Aubourg P. 2009. Hematopoietic Stem Cell Gene Therapy with a Lentiviral Vector in X-Linked Adrenoleukodystrophy. *Science* 326:818–823. DOI: 10.1126/science.1171242.

Cengizeroglu A. 2012. Targeted RNAi and pDNA based therapy for gastrointestinal tumors Targeted RNAi and pDNA based therapy for gastrointestinal tumors. *Dissertation, LMU München: Fakultät für Chemie und Pharmazie.*

Chan H-K, Kwok PCL. 2011. Production methods for nanodrug particles using the bottom-up approach. *Advanced Drug Delivery Reviews* 63:406–416. DOI: 10.1016/j.addr.2011.03.011.

Chen D, Love KT, Chen Y, Eltoukhy AA, Kastrup C, Sahay G, Jeon A, Dong Y, Whitehead KA, Anderson DG. 2012. Rapid discovery of potent siRNA-containing lipid nanoparticles enabled by controlled microfluidic formulation. *Journal of the American Chemical Society* 134:6948–6951. DOI: 10.1021/ja301621z.

Chen Y, Zhou H, Wang Y, Li W, Chen J, Lin Q, Yu C. 2013. Substrate hydrolysis triggered formation of fluorescent gold nanoclusters-a new platform for the sensing of enzyme activity. *Chemical Communications* 49:9821–9823. DOI: 10.1039/c3cc45494k.

Chiu DT, DeMello AJ, Di Carlo D, Doyle PS, Hansen C, Maceiczyk RM, Wootton RCR. 2017. Small but Perfectly Formed? Successes, Challenges, and Opportunities for Microfluidics in the Chemical and Biological Sciences. *Chem* 2:201–223. DOI: 10.1016/j.chempr.2017.01.009.

Cideciyan A V., Jacobson SG, Beltran WA, Sumaroka A, Swider M, Iwabe S, Roman AJ, Olivares MB, Schwartz SB, Komáromy AM, Hauswirth WW, Aguirre GD. 2013. Human retinal gene therapy for Leber congenital amaurosis shows advancing retinal degeneration despite enduring visual improvement. *Proceedings of the National Academy of Sciences of the United States of America* 110:517–525. DOI: 10.1073/pnas.1218933110.

Clegg RM. 1996. Fluorescence Resonance Energy Transfer. *Fluorescence Imaging Spectroscopy and Microscopy*. DOI: 10.1016/0958-1669(95)80016-6.

Crichton M. 2008. *Prey*. Harper.

Crooke RM, Graham MJ, Lemonidis KM, Whipple CP, Koo S, Perera RJ. 2005. An apolipoprotein B antisense oligonucleotide lowers LDL cholesterol in hyperlipidemic mice without causing hepatic steatosis. *Journal of Lipid Research* 46:872–884. DOI:

10.1194/jlr.M400492-JLR200.

Croston B. 2019.raspberry-gpio-python. *Available at https://sourceforge.net/projects/raspberry-gpio-python/* (accessed January 18, 2020).

Darrow JJ. 2019. Luxturna: FDA documents reveal the value of a costly gene therapy. *Drug Discovery Today* 24:949–954. DOI: 10.1016/j.drudis.2019.01.019.

Debus H, Beck-Broichsitter M, Kissel T. 2012. Optimized preparation of pDNA/poly(ethylene imine) polyplexes using a microfluidic system. *Lab on a Chip* 12:2498. DOI: 10.1039/c2lc40176b.

Dinauer MC, Li LL, Björgvinsdóttir H, Ding C, Pech N. 1999. Long-term correction of phagocyte NADPH oxidase activity retroviral- mediated gene transfer in murine X-linked chronic granulomatous disease. *Blood* 94:914–922.

Dohmen C, Edinger D, Fröhlich T, Schreiner L, Lächelt U, Troiber C, Rädler J, Hadwiger P, Vornlocher HP, Wagner E. 2012a. Nanosized multifunctional polyplexes for receptor-mediated SiRNA delivery. *ACS Nano* 6:5198–5208. DOI: 10.1021/nn300960m.

Dohmen C, Fröhlich T, Lächelt U, Röhl I, Vornlocher H-P, Hadwiger P, Wagner E. 2012b. Defined Folate-PEG-siRNA Conjugates for Receptor-specific Gene Silencing. *Molecular Therapy - Nucleic Acids* 1:e7. DOI: 10.1038/mtna.2011.10.

Dong Y, Siegwart DJ, Anderson DG. 2019. Strategies, design, and chemistry in siRNA delivery systems. *Advanced Drug Delivery Reviews* 144:133–147. DOI: 10.1016/j.addr.2019.05.004.

Drexler KE. 2007. *Engines of Creation 2.0: The Coming Era of Nanotechnology - Updated and Expanded*.

Duggan ST, Keating GM. 2011. Pegylated Liposomal Doxorubicin. *Drugs* 71:2531–2558. DOI: 10.2165/11207510-000000000-00000.

EMA. 1999.Vitravene. *Available at https://www.ema.europa.eu/en/medicines/human/EPAR/vitravene* (accessed October 21, 2019).

EMA. 2006.Macugen. *Available at https://www.ema.europa.eu/en/medicines/human/EPAR/macugen* (accessed October 24, 2019).

EMA. 2012.European Medicines Agency recommends first gene therapy for approval. *Available at https://www.ema.europa.eu/en/news/european-medicines-agency-recommends-first-gene-therapy-approval* (accessed October 19, 2019).

EMA. 2016.Strimvelis: autologous CD34+ enriched cell fraction that contains CD34+ cells transduced with retroviral vector that encodes for the human ADA cDNA sequence. *Available at https://www.ema.europa.eu/en/documents/smop-initial/chmp-summary-opinion-strimvelis_en.pdf* (accessed October 19, 2019).

EMA. 2019a. Zynteglo.

EMA. 2019b.Waylivra. *Available at https://www.ema.europa.eu/en/medicines/human/EPAR/waylivra* (accessed October 24, 2019).

Emily Whitehead Foundation. 2017.Celebrating 5 Years Cancer Free! *Available at*

https://emilywhiteheadfoundation.org/news/celebrating-5-years-cancer-free/ (accessed October 17, 2019).

Erbacher P, Roche AC, Monsigny M, Midoux P. 1996. Putative Role of Chloroquine in Gene Transfer into a Human Hepatoma Cell Line by DNA/Lactosylated Polylysine Complexes. *Experimental Cell Research* 225:186–194. DOI: 10.1006/excr.1996.0169.

Eshhar Z, Bach N, Fitzer-Attas CJ, Grosse G, Lustgarten J, Waks T, Schindler DG. 1996. The T-body approach: potential for cancer immunotherapy. *Springer Seminars in Immunopathology* 18:199–209. DOI: 10.1007/BF00820666.

Farber FE, Melnick JL, Butel JS. 1975. Optimal conditions for uptake of exogenous DNA by chinese hamster lung cells deficient in hypoxanthine-guanine phosphoribosyltransferase. *Biochimica et Biophysica Acta (BBA) - Nucleic Acids and Protein Synthesis* 390:298–311. DOI: 10.1016/0005-2787(75)90350-0.

FDA. 2016a.FDA grants accelerated approval to first drug for Duchenne muscular dystrophy. *Available at https://www.fda.gov/news-events/press-announcements/fda-grants-accelerated-approval-first-drug-duchenne-muscular-dystrophy?source=govdelivery* (accessed October 24, 2019).

FDA. 2016b.FDA approves first treatment for rare disease in patients who receive stem cell transplant from blood or bone marrow. *Available at https://www.fda.gov/news-events/press-announcements/fda-approves-first-treatment-rare-disease-patients-who-receive-stem-cell-transplant-blood-or-bone* (accessed October 24, 2019).

FDA. 2016c.FDA approves first drug for spinal muscular atrophy. *Available at https://www.fda.gov/news-events/press-announcements/fda-approves-first-drug-spinal-muscular-atrophy* (accessed October 24, 2019).

FDA. 2017a.FDA briefing document: Oncologic Drugs Advisory Committee meeting; BLA 125646; Tisagenlecleucel, Novartis Pharmaceuticals Corporation. *Available at https://www.fda.gov/downloads/AdvisoryCommittees/CommitteesMeetingMaterials/Drugs/OncologicDrugsAdvisoryCommittee/UCM566166.pdf*

FDA. 2017b.FDA approval brings first gene therapy to the United States. *Available at https://wayback.archive-it.org/7993/20180726035813/https://www.fda.gov/NewsEvents/Newsroom/PressAnnouncements/ucm574058.htm* (accessed October 19, 2019).

FDA. 2017c.FDA approves CAR-T cell therapy to treat adults with certain types of large B-cell lymphoma. *Available at https://www.fda.gov/news-events/press-announcements/fda-approves-car-t-cell-therapy-treat-adults-certain-types-large-b-cell-lymphoma* (accessed October 20, 2019).

FDA. 2017d.FDA approves novel gene therapy to treat patients with a rare form of inherited vision loss. *Available at https://www.fda.gov/news-events/press-announcements/fda-approves-novel-gene-therapy-treat-patients-rare-form-inherited-vision-loss* (accessed October 20, 2019).

FDA. 2019.FDA approves innovative gene therapy to treat pediatric patients with spinal muscular atrophy, a rare disease and leading genetic cause of infant mortality. *Available at https://www.fda.gov/news-events/press-announcements/fda-approves-innovative-gene-therapy-treat-pediatric-patients-spinal-muscular-atrophy-rare-disease* (accessed October 20, 2019).

Felgner PL, Barenholz Y, Behr JP, Cheng SH, Cullis P, Huang L, Jessee JA, Seymour L, Szoka F, Thierry AR, Wagner E, Wu G. 1997. Nomenclature for Synthetic Gene Delivery Systems. *Human Gene Therapy* 8:511–512. DOI: 10.1089/hum.1997.8.5-511.

Ferrari G, Rossini S, Giavazzi R, Maggioni D, Nobili N, Soldati M, Ungers G, Mavilio F, Gilboa E, Bordignon C. 1991. An in vivo model of somatic cell gene therapy for human severe combined immunodeficiency. *Science* 251:1363 LP – 1366. DOI: 10.1126/science.1848369.

Feynman RP. 1959. Plenty of Room at the Bottom. In: *APS annual meeting*.

Fire A, Xu S, Montgomery MK, Kostas SA, Driver SE, Mello CC. 1998. Potent and specific genetic interference by double-stranded RNA in Caenorhabditis elegans. *Nature* 391:806–811. DOI: 10.1038/35888.

Fong Y. 2015. Oncolytic Treatment for Cancer Recommended for Approval. *Molecular Therapy* 23:1131. DOI: 10.1038/mt.2015.94.

Förster T. 1948. Zwischenmolekulare Energiewanderung und Fluoreszenz (Intermolecular energy migration and fluorescence, Translated by Knox RS). *Ann. Phys.* DOI: 10.1002/andp.19484370105.

Freund R, Lächelt U, Gruber T, Rühle B, Wuttke S. 2018. Multifunctional Efficiency: Extending the Concept of Atom Economy to Functional Nanomaterials. *ACS Nano* 12:2094–2105. DOI: 10.1021/acsnano.8b00932.

Fröhlich T, Edinger D, Kläger R, Troiber C, Salcher E, Badgujar N, Martin I, Schaffert D, Cengizeroglu A, Hadwiger P, Vornlocher HP, Wagner E. 2012. Structure-activity relationships of siRNA carriers based on sequence-defined oligo (ethane amino) amides. *Journal of Controlled Release* 160:532–541. DOI: 10.1016/j.jconrel.2012.03.018.

Furukawa H, Cordova KE, O'Keeffe M, Yaghi OM. 2013. The Chemistry and Applications of Metal-Organic Frameworks. *Science* 341:1230444–1230444. DOI: 10.1126/science.1230444.

Gansbacher B. 2003. Report of a second serious adverse event in a clinical trial of gene therapy for X-linked severe combined immune deficiency (X-SCID). *The Journal of Gene Medicine* 5:261–262. DOI: 10.1002/jgm.390.

Gaudet D, de Wal J, Tremblay K, Déry S, van Deventer S, Freidig A, Brisson D, Méthot J. 2010. Review of the clinical development of alipogene tiparvovec gene therapy for lipoprotein lipase deficiency. *Atherosclerosis Supplements* 11:55–60. DOI: 10.1016/j.atherosclerosissup.2010.03.004.

Gene therapy's next installment. 2019. *Nature Biotechnology* 37:697–697. DOI: 10.1038/s41587-019-0194-z.

Giblett E, Anderson J, Cohen F, Pollara B, Meuwissen H. 1972. Adenosine-deaminase deficiency in two patients with severely impaired cellular immunity. *The Lancet* 300:1067–1069. DOI: 10.1016/S0140-6736(72)92345-8.

Ginn SL, Alexander IE, Edelstein ML, Abedi MR, Wixon J. 2013. Gene therapy clinical trials worldwide to 2012 - an update. *The Journal of Gene Medicine* 15:65–77. DOI: 10.1002/jgm.2698.

Ginn SL, Amaya AK, Alexander IE, Edelstein M, Abedi MR. 2018. Gene therapy clinical trials worldwide to 2017: An update. *Journal of Gene Medicine* 20:1–16. DOI:

10.1002/jgm.3015.

Godbey WT, Wu KK, Mikos AG. 1999. Size matters: Molecular weight affects the efficiency of poly(ethylenimine) as a gene delivery vehicle. *Journal of Biomedical Materials Research* 45:268–275. DOI: 10.1002/(SICI)1097-4636(19990605)45:3<268::AID-JBM15>3.0.CO;2-Q.

Grez M, Reichenbach J, Schwäble J, Seger R, Dinauer MC, Thrasher AJ. 2011. Gene therapy of chronic granulomatous disease: The engraftment dilemma. *Molecular Therapy* 19:28–35. DOI: 10.1038/mt.2010.232.

Grigsby CL, Ho Y-P, Lin C, Engbersen JFJ, Leong KW. 2013. Microfluidic Preparation of Polymer-Nucleic Acid Nanocomplexes Improves Nonviral Gene Transfer. *Scientific Reports* 3:3155. DOI: 10.1038/srep03155.

Grosjean P, Ibanez F. 2018. pastecs: Package for Analysis of Space-Time Ecological Series.

Guo J, Xin H. 2006. Chinese Gene Therapy: Splicing Out the West? *Science* 314:1232–1235. DOI: 10.1126/science.314.5803.1232.

Hacein-Bey-Abina S. 2003. LMO2-Associated Clonal T Cell Proliferation in Two Patients after Gene Therapy for SCID-X1. *Science* 302:415–419. DOI: 10.1126/science.1088547.

Hacein-Bey-Abina S, Von Kalle C, Schmidt M, Le Deist F, Wulffraat N, McIntyre E, Radford I, Villeval JL, Fraser CC, Cavazzana-Calvo M, Fischer A. 2003. A serious adverse event after successful gene therapy for X-linked severe combined immunodeficiency [1]. *New England Journal of Medicine* 348:255–256. DOI: 10.1056/NEJM200301163480314.

Haensler J, Szoka FC. 1993. Polyamidoamine cascade polymers mediate efficient transfection of cells in culture. *Bioconjugate Chemistry* 4:372–379. DOI: 10.1021/bc00023a012.

Hair P, Cameron F, McKeage K. 2013. Mipomersen Sodium: First Global Approval. *Drugs* 73:487–493. DOI: 10.1007/s40265-013-0042-2.

Hall A, Lächelt U, Bartek J, Wagner E, Moghimi SM. 2017. Polyplex Evolution: Understanding Biology, Optimizing Performance. *Molecular Therapy* 25:1476–1490. DOI: 10.1016/j.ymthe.2017.01.024.

Harrington KJ, Puzanov I, Hecht JR, Hodi FS, Szabo Z, Murugappan S, Kaufman HL. 2015. Clinical development of talimogene laherparepvec (T-VEC): a modified herpes simplex virus type-1–derived oncolytic immunotherapy. *Expert Review of Anticancer Therapy* 15:1389–1403. DOI: 10.1586/14737140.2015.1115725.

Havens MA, Hastings ML. 2016. Splice-switching antisense oligonucleotides as therapeutic drugs. *Nucleic Acids Research* 44:6549–6563. DOI: 10.1093/nar/gkw533.

He S, Arscott PG, Bloomfield VA. 2000. Condensation of DNA by multivalent cations: Experimental studies of condensation kinetics. *Biopolymers* 53:329–341. DOI: 10.1002/(SICI)1097-0282(20000405)53:4<329::AID-BIP5>3.0.CO;2-6.

Ho YP, Grigsby CL, Zhao F, Leong KW. 2011. Tuning physical properties of nanocomplexes through microfluidics-assisted confinement. *Nano Letters* 11:2178–2182. DOI: 10.1021/nl200862n.

Horcajada P, Chalati T, Serre C, Gillet B, Sebrie C, Baati T, Eubank JF, Heurtaux D, Clayette P, Kreuz C, Chang J-S, Hwang YK, Marsaud V, Bories P-N, Cynober L, Gil S, Férey G,

Couvreur P, Gref R. 2010. Porous metal–organic-framework nanoscale carriers as a potential platform for drug delivery and imaging. *Nature Materials* 9:172–178. DOI: 10.1038/nmat2608.

Hoy SM. 2018. Patisiran: First Global Approval. *Drugs* 78:1625–1631. DOI: 10.1007/s40265-018-0983-6.

Hu CMJ, Zhang L, Aryal S, Cheung C, Fang RH, Zhang L. 2011. Erythrocyte membrane-camouflaged polymeric nanoparticles as a biomimetic delivery platform. *Proceedings of the National Academy of Sciences of the United States of America* 108:10980–10985. DOI: 10.1073/pnas.1106634108.

Ibraheem D, Elaissari A, Fessi H. 2014. Gene therapy and DNA delivery systems. *International Journal of Pharmaceutics* 459:70–83. DOI: 10.1016/j.ijpharm.2013.11.041.

Irving BA, Weiss A. 1991. The cytoplasmic domain of the T cell receptor ζ chain is sufficient to couple to receptor-associated signal transduction pathways. *Cell* 64:891–901. DOI: 10.1016/0092-8674(91)90314-O.

Itaka K, Harada A, Yamasaki Y, Nakamura K, Kawaguchi H, Kataoka K. 2004. In situ single cell observation by fluorescence resonance energy transfer reveals fast intra-cytoplasmic delivery and easy release of plasmid DNA complexed with linear polyethylenimine. *The Journal of Gene Medicine* 6:76–84. DOI: 10.1002/jgm.470.

Jang J, Oh JH. 2004. A top-down approach to fullerene fabrication using a polymer nanoparticle precursor. *Advanced Materials* 16:1650–1653. DOI: 10.1002/adma.200400032.

Johnson S, Buessing M, O'Connell T, Pitluck S, Ciulla TA. 2019. Cost-effectiveness of Voretigene Neparvovec-rzyl vs Standard Care for RPE65 -Mediated Inherited Retinal Disease. *JAMA Ophthalmology* 02186:1115–1123. DOI: 10.1001/jamaophthalmol.2019.2512.

Kabanov A V., Kabanov VA. 1995. DNA Complexes with Polycations for the Delivery of Genetic Material into Cells. *Bioconjugate Chemistry* 6:7–20. DOI: 10.1021/bc00031a002.

Kalos M, Levine BL, Porter DL, Katz S, Grupp SA, Bagg A, June CH. 2011. T Cells with Chimeric Antigen Receptors Have Potent Antitumor Effects and Can Establish Memory in Patients with Advanced Leukemia. *Science Translational Medicine* 3:95ra73-95ra73. DOI: 10.1126/scitranslmed.3002842.

Karnik R, Gu F, Basto P, Cannizzaro C, Dean L, Kyei-Manu W, Langer R, Farokhzad OC. 2008. Microfluidic Platform for Controlled Synthesis of Polymeric Nanoparticles. *Nano Letters* 8:2906–2912. DOI: 10.1021/nl801736q.

Kasper JC, Schaffert D, Ogris M, Wagner E, Friess W. 2011. The establishment of an up-scaled micro-mixer method allows the standardized and reproducible preparation of well-defined plasmid/LPEI polyplexes. *European journal of pharmaceutics and biopharmaceutics : official journal of Arbeitsgemeinschaft für Pharmazeutische Verfahrenstechnik e.V* 77:182–5. DOI: 10.1016/j.ejpb.2010.11.012.

Kawabata K, Takakura Y, Hashida M. 1995. The Fate of Plasmid DNA After Intravenous Injection in Mice: Involvement of Scavenger Receptors in Its Hepatic Uptake. *Pharmaceutical Research: An Official Journal of the American Association of*

Pharmaceutical Scientists 12:825–830. DOI: 10.1023/A:1016248701505.

Kay MA, Glorioso JC, Naldini L. 2001. Viral vectors for gene therapy: the art of turning infectious agents into vehicles of therapeutics. *Nature Medicine* 7:33–40. DOI: 10.1038/83324.

Keam SJ. 2018. Inotersen: First Global Approval. *Drugs* 78:1371–1376. DOI: 10.1007/s40265-018-0968-5.

Klein PM, Kern S, Lee D-J, Schmaus J, Höhn M, Gorges J, Kazmaier U, Wagner E. 2018. Folate receptor-directed orthogonal click-functionalization of siRNA lipopolyplexes for tumor cell killing in vivo. *Biomaterials* 178:630–642. DOI: 10.1016/j.biomaterials.2018.03.031.

Klein PM, Reinhard S, Lee D-J, Müller K, Ponader D, Hartmann L, Wagner E. 2016. Precise redox-sensitive cleavage sites for improved bioactivity of siRNA lipopolyplexes. *Nanoscale* 8:18098–18104. DOI: 10.1039/C6NR05767E.

Koh CG, Kang X, Xie Y, Fei Z, Guan J, Yu B, Zhang X, Lee LJ. 2009. Delivery of Polyethylenimine/DNA Complexes Assembled in a Microfluidics Device. *Molecular Pharmaceutics* 6:1333–1342. DOI: 10.1021/mp900016q.

Koontz D. 2003. *Watchers*. Berkeley.

Koontz D. 2017. *The Silent Corner: A Novel of Suspense (Jane Hawk)*. Bantam.

Krzysztoń R, Salem B, Lee DJ, Schwake G, Wagner E, Rädler JO. 2017. Microfluidic self-assembly of folate-targeted monomolecular siRNA-lipid nanoparticles. *Nanoscale* 9:7442–7453. DOI: 10.1039/C7NR01593C.

Kuhn J, Klein PM, Al Danaf N, Nordin JZ, Reinhard S, Loy DM, Höhn M, El Andaloussi S, Lamb DC, Wagner E, Aoki Y, Lehto T, Lächelt U. 2019. Supramolecular Assembly of Aminoethylene-Lipopeptide PMO Conjugates into RNA Splice-Switching Nanomicelles. *Advanced Functional Materials* 29:1906432. DOI: 10.1002/adfm.201906432.

Kulkarni JA, Cullis PR, van der Meel R. 2018. Lipid Nanoparticles Enabling Gene Therapies: From Concepts to Clinical Utility. *Nucleic Acid Therapeutics* 28:146–157. DOI: 10.1089/nat.2018.0721.

Lächelt U, Wagner E. 2015. Nucleic Acid Therapeutics Using Polyplexes: A Journey of 50 Years (and Beyond). *Chemical Reviews* 115:11043–11078. DOI: 10.1021/cr5006793.

Lee H, Lytton-Jean AKR, Chen Y, Love KT, Park AI, Karagiannis ED, Sehgal A, Querbes W, Zurenko CS, Jayaraman M, Peng CG, Charisse K, Borodovsky A, Manoharan M, Donahoe JS, Truelove J, Nahrendorf M, Langer R, Anderson DG. 2012. Molecularly self-assembled nucleic acid nanoparticles for targeted in vivo siRNA delivery. *Nature Nanotechnology* 7:389–393. DOI: 10.1038/nnano.2012.73.

Lee, Park, Whitesides. 2003. Solvent compatibility of poly (dimethylsiloxane)-based microfluidic devices. *Analytical Chemistry-Washington Dc-* 75:6544–6554. DOI: 10.1021/ac0346712.

Lee CY, Wang WT, Liu CC, Fu LM. 2016. Passive mixers in microfluidic systems: A review. *Chemical Engineering Journal* 288:146–160. DOI: 10.1016/j.cej.2015.10.122.

Lehrman S. 1999. Virus treatment questioned after gene therapy death. *Nature* 401:517–518.

Leong KW, Grigsby CL. 2010. Balancing protection and release of DNA: tools to address a bottleneck of non-viral gene delivery. *Journal of the Royal Society Interface* 7:S67–S82. DOI: 10.1098/rsif.2009.0260.

Li W, Szoka FC. 2007. Lipid-based nanoparticles for nucleic acid delivery. *Pharmaceutical Research* 24:438–449. DOI: 10.1007/s11095-006-9180-5.

Liechti C. 2017. pySerial.

Lim KR, Maruyama R, Yokota T. 2017. Eteplirsen in the treatment of Duchenne muscular dystrophy. *Drug Design, Development and Therapy* Volume11:533–545. DOI: 10.2147/DDDT.S97635.

Lim J-M, Swami A, Gilson LM, Chopra S, Choi S, Wu J, Langer R, Karnik R, Farokhzad OC. 2014. Ultra-High Throughput Synthesis of Nanoparticles with Homogeneous Size Distribution Using a Coaxial Turbulent Jet Mixer. *ACS Nano* 8:6056–6065. DOI: 10.1021/nn501371n.

Liu D, Cito S, Zhang Y, Wang C-F, Sikanen TM, Santos HA. 2015. A Versatile and Robust Microfluidic Platform Toward High Throughput Synthesis of Homogeneous Nanoparticles with Tunable Properties. *Advanced Materials* 27:2298–2304. DOI: 10.1002/adma.201405408.

Liu D, Zhang H, Fontana F, Hirvonen J, Santos HA. 2017. Microfluidic-Assisted Fabrication of Carriers for Controlled Drug Delivery. *Lab Chip* 17:1856–1883. DOI: 10.1039/C7LC00242D.

Locke FL, Ghobadi A, Jacobson CA, Miklos DB, Lekakis LJ, Oluwole OO, Lin Y, Braunschweig I, Hill BT, Timmerman JM, Deol A, Reagan PM, Stiff P, Flinn IW, Farooq U, Goy A, McSweeney PA, Munoz J, Siddiqi T, Chavez JC, Herrera AF, Bartlett NL, Wiezorek JS, Navale L, Xue A, Jiang Y, Bot A, Rossi JM, Kim JJ, Go WY, Neelapu SS. 2019. Long-term safety and activity of axicabtagene ciloleucel in refractory large B-cell lymphoma (ZUMA-1): a single-arm, multicentre, phase 1–2 trial. *The Lancet Oncology* 20:31–42. DOI: 10.1016/S1470-2045(18)30864-7.

Loy DM. 2020a.Dominik Loy on GitHub. *Available at https://github.com/Dominikmloy* (accessed November 7, 2020).

Loy DM. 2020b.Dominik Loy on Figshare. *Available at https://figshare.com/authors/Dominik_Loy/6569300* (accessed December 6, 2020).

Loy DM, Klein PM, Krzysztoń R, Lächelt U, Rädler JO, Wagner E. 2019. A microfluidic approach for sequential assembly of siRNA polyplexes with a defined structure-activity relationship. *PeerJ Materials Science* 1:e1. DOI: 10.7717/peerj-matsci.1.

Loy DM, Krzysztoń R, Lächelt U, Rädler JO, Wagner E. 2021. Controlling Nanoparticle Formulation: A Low-Budget Prototype for the Automation of a Microfluidic Platform. *Processes* 9:129. DOI: 10.3390/pr9010129.

Lüdecke D. 2019. sjstats: Statistical Functions for Regression Models. DOI: 10.5281/zenodo.1284472.

Luo D, Saltzman WM. 2000. Synthetic DNA delivery systems. *Nature Biotechnology* 18:33–37. DOI: 10.1038/71889.

Maguire AM, High KA, Auricchio A, Wright JF, Pierce EA, Testa F, Mingozzi F, Bennicelli JL, Ying G, Rossi S, Fulton A, Marshall KA, Banfi S, Chung DC, Morgan JI, Hauck B,

Zelenaia O, Zhu X, Raffini L, Coppieters F, De Baere E, Shindler KS, Volpe NJ, Surace EM, Acerra C, Lyubarsky A, Redmond TM, Stone E, Sun J, McDonnell JW, Leroy BP, Simonelli F, Bennett J. 2009. Age-dependent effects of RPE65 gene therapy for Leber's congenital amaurosis: a phase 1 dose-escalation trial. *The Lancet* 374:1597–1605. DOI: 10.1016/S0140-6736(09)61836-5.

Maguire AM, Simonelli F, Pierce EA, Pugh EN, Mingozzi F, Bennicelli J, Banfi S, Marshall KA, Testa F, Surace EM, Rossi S, Lyubarsky A, Arruda VR, Konkle B, Stone E, Sun J, Jacobs J, Dell'Osso L, Hertle R, Ma J, Redmond TM, Zhu X, Hauck B, Zelenaia O, Shindler KS, Maguire MG, Wright JF, Volpe NJ, McDonnell JW, Auricchio A, High KA, Bennett J. 2008. Safety and Efficacy of Gene Transfer for Leber's Congenital Amaurosis. *New England Journal of Medicine* 358:2240–2248. DOI: 10.1056/NEJMoa0802315.

Maher J, Brentjens RJ, Gunset G, Rivière I, Sadelain M. 2002. Human T-lymphocyte cytotoxicity and proliferation directed by a single chimeric TCRζ /CD28 receptor. *Nature Biotechnology* 20:70–75. DOI: 10.1038/nbt0102-70.

Mahto A. 2018. splitstackshape: Stack and Reshape Datasets After Splitting Concatenated Values.

Malik P. 2016. Gene Therapy for Hemoglobinopathies: Tremendous Successes and Remaining Caveats. *Molecular Therapy* 24:668–670. DOI: 10.1038/mt.2016.57.

Manzur AY, Kinali M, Muntoni F. 2008. Update on the management of Duchenne muscular dystrophy. *Archives of Disease in Childhood* 93:986–990. DOI: 10.1136/adc.2007.118141.

Maude SL, Laetsch TW, Buechner J, Rives S, Boyer M, Bittencourt H, Bader P, Verneris MR, Stefanski HE, Myers GD, Qayed M, De Moerloose B, Hiramatsu H, Schlis K, Davis KL, Martin PL, Nemecek ER, Yanik GA, Peters C, Baruchel A, Boissel N, Mechinaud F, Balduzzi A, Krueger J, June CH, Levine BL, Wood P, Taran T, Leung M, Mueller KT, Zhang Y, Sen K, Lebwohl D, Pulsipher MA, Grupp SA. 2018. Tisagenlecleucel in Children and Young Adults with B-Cell Lymphoblastic Leukemia. *New England Journal of Medicine* 378:439–448. DOI: 10.1056/NEJMoa1709866.

Mayor S, Rothberg KG, Maxfield FR. 1994. Sequestration of GPI-anchored proteins in caveolae triggered by cross-linking. *Science (New York, N.Y.)* 264:1948–1951. DOI: 10.1126/science.7516582.

McCutchan JH, Pagano JS. 1968. Enhancement of the Infectivity of Simian Virus 40 Deoxyribonucleic Acid With Diethylaminoethyl-Dextran. *JNCI: Journal of the National Cancer Institute* 41:351–357. DOI: 10.1093/jnci/41.2.351.

Mendell JR, Al-Zaidy S, Shell R, Arnold WD, Rodino-Klapac LR, Prior TW, Lowes L, Alfano L, Berry K, Church K, Kissel JT, Nagendran S, L'Italien J, Sproule DM, Wells C, Cardenas JA, Heitzer MD, Kaspar A, Corcoran S, Braun L, Likhite S, Miranda C, Meyer K, Foust KD, Burghes AHM, Kaspar BK. 2017. Single-dose gene-replacement therapy for spinal muscular atrophy. *New England Journal of Medicine* 377:1713–1722. DOI: 10.1056/NEJMoa1706198.

Merrifield RB. 1963. Solid Phase Peptide Synthesis. I. The Synthesis of a Tetrapeptide. *Journal of the American Chemical Society* 85:2149–2154. DOI: 10.1021/ja00897a025.

Miyoshi H, Smith KA, Mosier DE, Verma IM, Torbett BE. 1999. Transduction of Human

CD34 + Cells That Mediate Long-Term Engraftment of NOD/SCID Mice by HIV Vectors. *Science* 283:682–686. DOI: 10.1126/science.283.5402.682.

Morys S, Krhac Levacic A, Urnauer S, Kempter S, Kern S, Rädler J, Spitzweg C, Lächelt U, Wagner E. 2017. Influence of Defined Hydrophilic Blocks within Oligoaminoamide Copolymers: Compaction versus Shielding of pDNA Nanoparticles. *Polymers* 9:142. DOI: 10.3390/polym9040142.

Naldini L, Blömer U, Gallay P, Ory D, Mulligan R, Gage FH, Verma IM, Trono D. 1996. In vivo gene delivery and stable transduction of nondividing cells by a lentiviral vector. *Science* 272:263–267. DOI: 10.1126/science.272.5259.263.

Naz S, Shamoon M, Wang R, Zhang L, Zhou J, Chen J. 2019. Advances in therapeutic implications of inorganic drug delivery nano-platforms for cancer. *International Journal of Molecular Sciences* 20:1–17. DOI: 10.3390/ijms20040965.

Neelapu SS, Locke FL, Bartlett NL, Lekakis LJ, Miklos DB, Jacobson CA, Braunschweig I, Oluwole OO, Siddiqi T, Lin Y, Timmerman JM, Stiff PJ, Friedberg JW, Flinn IW, Goy A, Hill BT, Smith MR, Deol A, Farooq U, McSweeney P, Munoz J, Avivi I, Castro JE, Westin JR, Chavez JC, Ghobadi A, Komanduri K V., Levy R, Jacobsen ED, Witzig TE, Reagan P, Bot A, Rossi J, Navale L, Jiang Y, Aycock J, Elias M, Chang D, Wiezorek J, Go WY. 2017. Axicabtagene Ciloleucel CAR T-Cell Therapy in Refractory Large B-Cell Lymphoma. *New England Journal of Medicine* 377:2531–2544. DOI: 10.1056/NEJMoa1707447.

Neu M, Fischer D, Kissel T. 2005. Recent advances in rational gene transfer vector design based on poly(ethylene imine) and its derivatives. *The Journal of Gene Medicine* 7:992–1009. DOI: 10.1002/jgm.773.

Neuwirth E. 2014. RColorBrewer: ColorBrewer Palettes.

Ng EWM, Shima DT, Calias P, Cunningham ET, Guyer DR, Adamis AP. 2006. Pegaptanib, a targeted anti-VEGF aptamer for ocular vascular disease. *Nature Reviews Drug Discovery* 5:123–132. DOI: 10.1038/nrd1955.

Niemietz C, Chandhok G, Schmidt H. 2015. Therapeutic Oligonucleotides Targeting Liver Disease: TTR Amyloidosis. *Molecules* 20:17944–17975. DOI: 10.3390/molecules201017944.

Ott MG, Schmidt M, Schwarzwaelder K, Stein S, Siler U, Koehl U, Glimm H, Kühlcke K, Schilz A, Kunkel H, Naundorf S, Brinkmann A, Deichmann A, Fischer M, Ball C, Pilz I, Dunbar C, Du Y, Jenkins NA, Copeland NG, Lüthi U, Hassan M, Thrasher AJ, Hoelzer D, von Kalle C, Seger R, Grez M. 2006. Correction of X-linked chronic granulomatous disease by gene therapy, augmented by insertional activation of MDS1-EVI1, PRDM16 or SETBP1. *Nature Medicine* 12:401–409. DOI: 10.1038/nm1393.

Ou Z, Muthukumar M. 2006. Entropy and enthalpy of polyelectrolyte complexation: Langevin dynamics simulations. *The Journal of Chemical Physics* 124:154902. DOI: 10.1063/1.2178803.

Pack DW, Hoffman AS, Pun S, Stayton PS. 2005. Design and development of polymers for gene delivery. *Nature Reviews Drug Discovery* 4:581–593. DOI: 10.1038/nrd1775.

Paik J, Duggan S. 2019. Volanesorsen: First Global Approval. *Drugs*. DOI: 10.1007/s40265-019-01168-z.

Pearson S, Jia H, Kandachi K. 2004. China approves first gene therapy. *Nature Biotechnology* 22:3–4. DOI: 10.1038/nbt0104-3.

Peer D, Lieberman J. 2011. Special delivery: targeted therapy with small RNAs. *Gene Therapy* 18:1127–1133. DOI: 10.1038/gt.2011.56.

PeerJ. 2019.PeerJ. *Available at https://peerj.com/blog/post/115284881832/peerj-celebrates-first-chemistry-publications-peerj-chemistry-open-science-ecr-award/* (accessed December 6, 2020).

Pescador R, Capuzzi L, Mantovani M, Fulgenzi A, Ferrero ME. 2013. Defibrotide: Properties and clinical use of an old/new drug. *Vascular Pharmacology* 59:1–10. DOI: 10.1016/j.vph.2013.05.001.

Plank C, Mechtler K, Szoka FC, Wagner E. 1996. Activation of the complement system by synthetic DNA complexes: a potential barrier for intravenous gene delivery. *Human gene therapy* 7:1437–1446. DOI: 10.1089/hum.1996.7.12-1437.

Porter DL, Levine BL, Kalos M, Bagg A, June CH. 2011. Chimeric Antigen Receptor–Modified T Cells in Chronic Lymphoid Leukemia. *New England Journal of Medicine* 365:725–733. DOI: 10.1056/NEJMoa1103849.

R Core Team. 2018. R: a language and environment for statistical computing.

Reinhard S, Zhang W, Wagner E. 2017. Optimized solid-phase assisted synthesis of oleic acid-containing siRNA nanocarriers. *ChemMedChem*. DOI: 10.1002/cmdc.201700350.

Rejman J, Oberle V, Zuhorn IS, Hoekstra D. 2004. Size-dependent internalization of particles via the pathways of clathrin- and caveolae-mediated endocytosis. *Biochemical Journal* 377:159–169. DOI: 10.1042/bj20031253.

Roehr B. 1998. Fomivirsen approved for CMV retinitis. *Journal of the International Association of Physicians in AIDS Care* 4:14.

Rolland JP, Maynor BW, Euliss LE, Exner AE, Denison GM, DeSimone JM. 2005. Direct fabrication and harvesting of monodisperse, shape-specific nanobiomaterials. *Journal of the American Chemical Society* 127:10096–10100. DOI: 10.1021/ja051977c.

Romeo C, Amiot M, Seed B. 1992. Sequence requirements for induction of cytolysis by the T cell antigen Fc receptor ζ chain. *Cell* 68:889–897. DOI: 10.1016/0092-8674(92)90032-8.

Rosenberg SA, Aebersold P, Cornetta K, Kasid A, Morgan RA, Moen R, Karson EM, Lotze MT, Yang JC, Topalian SL, Merino MJ, Culver K, Miller AD, Blaese RM, Anderson WF. 1990. Gene Transfer into Humans — Immunotherapy of Patients with Advanced Melanoma, Using Tumor-Infiltrating Lymphocytes Modified by Retroviral Gene Transduction. *New England Journal of Medicine* 323:570–578. DOI: 10.1056/NEJM199008303230904.

Van Rossum G, Drake Jr FL. 2009. *Python 3 Reference Manual*. CA: CreateSpace.

RStudio Team. 2018. RStudio: integrated development for R.

Ruckman J, Green LS, Beeson J, Waugh S, Gillette WL, Henninger DD, Claesson-Welsh L, Janjic N. 1998. 2′-Fluoropyrimidine RNA-based Aptamers to the 165-Amino Acid Form of Vascular Endothelial Growth Factor (VEGF 165). *Journal of Biological Chemistry* 273:20556–20567. DOI: 10.1074/jbc.273.32.20556.

Sadelain M, Brentjens R, Rivière I. 2009. The promise and potential pitfalls of chimeric

antigen receptors. *Current Opinion in Immunology* 21:215–223. DOI: 10.1016/j.coi.2009.02.009.

Scaiewicz V, Sorin V, Fellig Y, Birman T, Mizrahi A, Galula J, Abu-lail R, Shneider T, Ohana P, Buscail L, Hochberg A, Czerniak A. 2010. Use of H19 Gene Regulatory Sequences in DNA-Based Therapy for Pancreatic Cancer. *Journal of Oncology* 2010:1–10. DOI: 10.1155/2010/178174.

Schaffer D V., Fidelman NA, Dan N, Lauffenburger DA. 2000. Vector unpacking as a potential barrier for receptor-mediated polyplex gene delivery. *Biotechnology and Bioengineering* 67:598–606. DOI: 10.1002/(SICI)1097-0290(20000305)67:5<598::AID-BIT10>3.0.CO;2-G.

Schaffert D, Badgujar N, Wagner E. 2011. Novel Fmoc-polyamino acids for solid-phase synthesis of defined polyamidoamines. *Organic Letters* 13:1586–1589. DOI: 10.1021/ol200381z.

Schaffert D, Troiber C, Salcher EE, Fröhlich T, Martin I, Badgujar N, Dohmen C, Edinger D, Kläger R, Maiwald G, Farkasova K, Seeber S, Jahn-Hofmann K, Hadwiger P, Wagner E. 2011. Solid-phase synthesis of sequence-defined T-, i-, and U-shape polymers for pDNA and siRNA delivery. *Angewandte Chemie (International ed. in English)* 50:8986–9. DOI: 10.1002/anie.201102165.

Schiffelers RM, Blenke EO, Mastrobattista E. 2019. Oligonucleotides. In: Crommelin DJA, Sindelar RD, Meibohm B eds. *Pharmaceutical Biotechnology*. Cham: Springer International Publishing, 305–322. DOI: 10.1007/978-3-030-00710-2_15.

Schindelin J, Arganda-Carreras I, Frise E, Kaynig V, Longair M, Pietzsch T, Preibisch S, Rueden C, Saalfeld S, Schmid B, Tinevez J-Y, White DJ, Hartenstein V, Eliceiri K, Tomancak P, Cardona A. 2012. Fiji: an open-source platform for biological-image analysis. *Nature Methods* 9:676.

Schnitzler LG, Junger S, Loy DM, Wagner E, Wixforth A, Hörner A, Lächelt U, Westerhausen C. 2019. Size tunable nanoparticle formation employing droplet fusion by acoustic streaming applied to polyplexes. *Journal of Physics D: Applied Physics* 52:244002. DOI: 10.1088/1361-6463/ab131f.

Scholz C, Kos P, Wagner E. 2014. Comb-like oligoaminoethane carriers: Change in topology improves pDNA delivery. *Bioconjugate Chemistry* 25:251–261. DOI: 10.1021/bc400392y.

Seemann R, Brinkmann M, Pfohl T, Herminghaus S. 2012. Droplet based microfluidics. *Rep. Prog. Phys. Rep. Prog. Phys* 75:16601–41. DOI: 10.1088/0034-4885/75/1/016601.

Seib FP, Jones AT, Duncan R. 2007. Comparison of the endocytic properties of linear and branched PEIs, and cationic PAMAM dendrimers in B16f10 melanoma cells. *Journal of Controlled Release* 117:291–300. DOI: 10.1016/j.jconrel.2006.10.020.

Sinn PL, Sauter SL, McCray PB. 2005. Gene Therapy Progress and Prospects: Development of improved lentiviral and retroviral vectors – design, biosafety, and production. *Gene Therapy* 12:1089–1098. DOI: 10.1038/sj.gt.3302570.

Sletten EM, Bertozzi CR. 2011. From mechanism to mouse: A tale of two bioorthogonal reactions. *Accounts of Chemical Research* 44:666–676. DOI: 10.1021/ar200148z.

de Smet MD, Meenken C, van den Horn GJ. 1999. Fomivirsen – a phosphorothioate

oligonucleotide for the treatment of CMV retinitis. *Ocular Immunology and Inflammation* 7:189–198. DOI: 10.1076/ocii.7.3.189.4007.

Sokolova V, Epple M. 2008. Inorganic Nanoparticles as Carriers of Nucleic Acids into Cells. *Angewandte Chemie International Edition* 47:1382–1395. DOI: 10.1002/anie.200703039.

Squires TM, Quake SR. 2005. Microfluidics: Fluid physics at the nanoliter scale. *Reviews of Modern Physics* 77:977–1026. DOI: 10.1103/RevModPhys.77.977.

Stein CA, Castanotto D. 2017. FDA-Approved Oligonucleotide Therapies in 2017. *Molecular Therapy* 25:1069–1075. DOI: 10.1016/j.ymthe.2017.03.023.

Sun W, Mao S, Shi Y, Li LC, Fang L. 2011. Nanonization of itraconazole by high pressure homogenization: Stabilizer optimization and effect of particle size on oral absorption. *Journal of Pharmaceutical Sciences* 100:3365–3373. DOI: 10.1002/jps.22587.

Sykes EA, Chen J, Zheng G, Chan WCW. 2014. Investigating the impact of nanoparticle size on active and passive tumor targeting efficiency. *ACS Nano* 8:5696–5706. DOI: 10.1021/nn500299p.

Tanaka R, Ueoka I, Takaki Y, Kataoka K, Saito S. 1983. High molecular weight linear polyethylenimine and poly(N-methylethylenimine). *Macromolecules* 16:849–853. DOI: 10.1021/ma00240a003.

Thomas CE, Ehrhardt A, Kay MA. 2003. Progress and problems with the use of viral vectors for gene therapy. *Nature Reviews Genetics* 4:346–358. DOI: 10.1038/nrg1066.

Torchiano M. 2018. effsize: Efficient Effect Size Computation. DOI: 10.5281/zenodo.1480624.

Troiber C, Edinger D, Kos P, Schreiner L, Kläger R, Herrmann A, Wagner E. 2013a. Stabilizing effect of tyrosine trimers on pDNA and siRNA polyplexes. *Biomaterials* 34:1624–1633. DOI: 10.1016/j.biomaterials.2012.11.021.

Troiber C, Kasper JC, Milani S, Scheible M, Martin I, Schaubhut F, Küchler S, Rädler J, Simmel FC, Friess W, Wagner E. 2013b. Comparison of four different particle sizing methods for siRNA polyplex characterization. *European Journal of Pharmaceutics and Biopharmaceutics* 84:255–264. DOI: 10.1016/j.ejpb.2012.08.014.

Valencia PM, Farokhzad OC, Karnik R, Langer R. 2012. Microfluidic technologies for accelerating the clinical translation of nanoparticles. *Nature Nanotechnology* 7:623–629. DOI: 10.1038/nnano.2012.168.

Waehler R, Russell SJ, Curiel DT. 2007. Engineering targeted viral vectors for gene therapy. *Nature Reviews Genetics* 8:573–587. DOI: 10.1038/nrg2141.

Wang J, Chen W, Sun J, Liu C, Yin Q, Zhang L, Xianyu Y, Shi X, Hu G, Jiang X. 2014a. A microfluidic tubing method and its application for controlled synthesis of polymeric nanoparticles. *Lab Chip* 14:1673–1677. DOI: 10.1039/C4LC00080C.

Wang M, Glass ZA, Xu Q. 2016. Non-viral delivery of genome-editing nucleases for gene therapy. *Gene Therapy*:1–30. DOI: 10.1038/gt.2016.72.

Wang X, Gobbo P, Suchy M, Workentin MS, Hudson RHE. 2014b. Peptide-decorated gold nanoparticles via strain-promoted azide-alkyne cycloaddition and post assembly deprotection. *RSC Advances* 4:43087–43091. DOI: 10.1039/c4ra07574a.

Wang H, Liu K, Chen KJ, Lu Y, Wang S, Lin WY, Guo F, Kamei KI, Chen YC, Ohashi M, Wang M, Garcia MAA, Zhao XZ, Shen CKF, Tseng HR. 2010. A rapid pathway toward a superb gene delivery system: Programming structural and functional diversity into a supramolecular nanoparticle library. *ACS Nano* 4:6235–6243. DOI: 10.1021/nn101908e.

Warner E. 2017.Goodbye Glybera! The World's First Gene Therapy will be Withdrawn. *Available at https://www.labiotech.eu/medical/uniqure-glybera-marketing-withdrawn/* (accessed October 30, 2019).

Westerhausen C, Schnitzler L, Wendel D, Krzysztoń R, Lächelt U, Wagner E, Rädler J, Wixforth A. 2016. Controllable Acoustic Mixing of Fluids in Microchannels for the Fabrication of Therapeutic Nanoparticles. *Micromachines* 7:150. DOI: 10.3390/mi7090150.

Whitesides GM. 2006. The origins and the future of microfluidics. *Nature* 442:368–373. DOI: 10.1038/nature05058.

Wickham H. 2016. *ggplot2: Elegant Graphics for Data Analysis*. Springer-Verlag New York.

Wickham H. 2017. tidyverse: Easily Install and Load the "Tidyverse."

Wickham H. 2018. stringr: Simple, Consistent Wrappers for Common String Operations.

Wickham H, Bryan J. 2018. readxl: Read Excel Files.

Wilson RW, Bloomfield VA. 1979. Counterion-induced condensation of deoxyribonucleic acid. A light-scattering study. *Biochemistry* 18:2192–2196. DOI: 10.1021/bi00578a009.

Wu Y, Fei Z, Lee LJ, Wyslouzil BE. 2010. Coaxial electrohydrodynamic spraying of plasmid DNA/polyethylenimine (PEI) polyplexes for enhanced nonviral gene delivery. *Biotechnology and Bioengineering* 105:834–841. DOI: 10.1002/bit.22583.

Yamamoto A, Kormann M, Rosenecker J, Rudolph C. 2009. Current prospects for mRNA gene delivery. *European Journal of Pharmaceutics and Biopharmaceutics* 71:484–489. DOI: 10.1016/j.ejpb.2008.09.016.

Yin H, Kanasty RL, Eltoukhy AA, Vegas AJ, Dorkin JR, Anderson DG. 2014. Non-viral vectors for gene-based therapy. *Nature Reviews Genetics* 15:541–555. DOI: 10.1038/nrg3763.

Ylä-Herttuala S. 2012. Endgame: Glybera Finally Recommended for Approval as the First Gene Therapy Drug in the European Union. *Molecular Therapy* 20:1831–1832. DOI: 10.1038/mt.2012.194.

Ylä-Herttuala S. 2016. ADA-SCID Gene Therapy Endorsed By European Medicines Agency For Marketing Authorization. *Molecular Therapy* 24:1013–1014. DOI: 10.1038/mt.2016.98.

Yu M, Wu J, Shi J, Farokhzad OC. 2016. Nanotechnology for protein delivery: Overview and perspectives. *Journal of Controlled Release* 240:24–37. DOI: 10.1016/j.jconrel.2015.10.012.

Zabner J. 1997. Cationic lipids used in gene transfer. *Advanced Drug Delivery Reviews* 27:17–28. DOI: 10.1016/S0169-409X(97)00019-7.

Zelphati O, Nguyen C, Ferrari M, Felgner J, Tsai Y, Felgner PL. 1998. Stable and monodisperse lipoplex formulations for gene delivery. *Gene Therapy* 5:1272–1282. DOI: 10.1038/sj.gt.3300707.

Zhu QL, Xu Q. 2014. Metal-organic framework composites. *Chemical Society Reviews* 43:5468–5512. DOI: 10.1039/c3cs60472a.

Zimmermann GR, Wick CL, Shields TP, Jenison RD, Pardi A. 2000. Molecular interactions and metal binding in the theophylline-binding core of an RNA aptamer. *RNA* 6:S1355838200000169. DOI: 10.1017/S1355838200000169.

8. Publications

8.1. Original articles

Loy, Dominik M.*, Rafał Krzysztoń, Ulrich Lächelt, Joachim O. Rädler, and Ernst Wagner. "Controlling Nanoparticle Formulation: A Low-Budget Prototype for the Automation of a Microfluidic Platform." *Processes*. 2021; 9(1):129. doi.org/10.3390/pr9010129. (* indicates corresponding authorship)

Wang, Yanfang, Jie Luo, Ines Truebenbach, Sören Reinhard, Philipp Michael Klein, Miriam Höhn, Sarah Kern, Stephan Morys, **Dominik M. Loy**, Ernst Wagner, and Wei Zhang. 2020. "Double Click-Functionalized siRNA Polyplexes for Gene Silencing in Epidermal Growth Factor Receptor-Positive Tumor Cells." *ACS Biomaterials Science & Engineering* 6 (2): 1074–89. https://doi.org/10.1021/acsbiomaterials.9b01904.

Loy, Dominik M*, Philipp M Klein, Rafał Krzysztoń, Ulrich Lächelt, Joachim O Rädler, and Ernst Wagner*. 2019. "A Microfluidic Approach for Sequential Assembly of siRNA Polyplexes with a Defined Structure-Activity Relationship." *PeerJ Materials Science* 1 (October): e1. https://doi.org/10.7717/peerj-matsci.1.
(* indicates corresponding authorship)

Kuhn, Jasmin, Philipp M. Klein, Nader Al Danaf, Joel Z. Nordin, Sören Reinhard, **Dominik M. Loy**, Miriam Höhn, Samir El Andaloussi, Don C. Lamb, Ernst Wagner, Yoshitsugu Aoki, Taavi Lehto, and Ulrich Lächelt. 2019. "Supramolecular Assembly of Aminoethylene-Lipopeptide PMO Conjugates into RNA Splice-Switching Nanomicelles." *Advanced Functional Materials* 29 (48): 1906432. https://doi.org/10.1002/adfm.201906432.

Schnitzler, Lukas Gabriel, Stefanie Junger, **Dominik M. Loy**, Ernst Wagner, Achim Wixforth, Andreas Hörner, Ulrich Lächelt, and Christoph Westerhausen. 2019. "Size Tunable Nanoparticle Formation Employing Droplet Fusion by Acoustic Streaming Applied to Polyplexes." *Journal of Physics D: Applied Physics* 52 (24): 244002. https://doi.org/10.1088/1361-6463/ab131f.

Truebenbach, Ines, Sarah Kern, **Dominik M. Loy**, Miriam Höhn, Jan Gorges, Uli Kazmaier, and Ernst Wagner. 2019. "Combination Chemotherapy of L1210 Tumors in Mice with Pretubulysin and Methotrexate Lipo-Oligomer Nanoparticles." *Molecular Pharmaceutics* 16 (6): 2405–17. https://doi.org/10.1021/acs.molpharmaceut.9b00038.

Luo, Jie, Miriam Höhn, Sören Reinhard, **Dominik M. Loy**, Philipp Michael Klein, and Ernst Wagner. 2019. "IL4-Receptor-Targeted Dual Antitumoral Apoptotic Peptide – siRNA Conjugate Lipoplexes." *Advanced Functional Materials* 1900697 (April): 1900697. https://doi.org/10.1002/adfm.201900697.

Westerhausen, Christoph, Lukas Schnitzler, **Dominik Wendel**, Rafał Krzysztoń, Ulrich Lächelt, Ernst Wagner, Joachim Rädler, and Achim Wixforth. 2016. "Controllable Acoustic Mixing of Fluids in Microchannels for the Fabrication of Therapeutic Nanoparticles." *Micromachines* 7 (9): 150. https://doi.org/10.3390/mi7090150.

8.2. Meeting abstracts and poster presentations

Wendel, Dominik, U. Lächelt, R. Krzysztoń, R. Berger, J. Rädler, and E. Wagner. "Formulation of multi-component Polyplexes for siRNA delivery." Design and Control of Nanosystems. CeNS/SFB1032 Workshop, Venice, Italy. (September 2017)

Wendel, Dominik, R. Krzysztoń, C. Westerhausen, U. Lächelt, J. Rädler, A. Wixforth, and E. Wagner. "Mixing of polyplexes for gene therapy by acoustic streaming." International Symposium on NanoBiotechnology, California NanoSystems Institute UCLA, Los Angeles, USA. (February 2016)

8.3. Honors

2019 **Open Science Early Career Researcher Award**, PeerJ Chemistry, for the publication Loy et al. 2019, "A Microfluidic Approach for Sequential Assembly of siRNA Polyplexes with a Defined Structure-Activity Relationship." in *PeerJ Materials Science* (PeerJ, 2019).

9. Acknowledgments

This Ph.D. was a period of my life marked by many arduous as well as fascinating and enjoyable moments. I want to thank the people who walked this path with me and supported me throughout this experience. You rock!

First of all, I thank Prof. Ernst Wagner for giving me the opportunity to work on this multifaceted project in his lab. I enjoyed the freedom to choose the direction of my projects almost independently. I benefited greatly from your overview of the current literature and guidance, and I learned a lot under your supervision.

I thank Dr. Ulrich Lächelt for his guidance, many fruitful discussions about my projects, his many excellent suggestions, and his time he spent reading and commenting on my drafts. I really enjoyed working with you, and I am happy I could share some of my enthusiasm with you: for statistics, single-board computers, programming, and starting a family.

I thank my external collaborators, as well. Prof. Wixforth, Dr. Chris Westerhausen, and Lukas Schnitzler from the Universität Augsburg introduced me to microfluidic mixing and supported me in setting up my own micromixer. Your expertise in dealing with surface acoustic waves is enormous!
Prof. Rädler, Dr. Rafal Krzysztoń, Ricarda Berger, and Susi Kempter from the physics department of the LMU were always there to help me with problems related to physics, leaky channels, FACS experiments, and TEM measurements. I had a great time working with you; I really enjoyed visiting you at your lab!

I thank the indispensable people from our lab: Wolfgang for his time we spend indulging in everything technical and teaching me equipment maintenance and essential methods, Ursula for her generous support in keeping things stocked and organized and her delicious cakes, of course. Miriam for her support in cell culture, Markus for all the fun we had together, it was really schön dich zu sehen! Last but not least, Olga for handling all the paperwork.

I thank my lab mates Dr. Yanfang Wang and Jie Luo, for our successful collaboration on your projects. It was a pleasure to be included in your work and to support you in bringing your projects to fruition.

I thank Gines for many enjoyable breaks during the daily routine. Without you, I would not have been able to follow the many entangled veins of gossip surrounding our lab, royals, or

topfmodels. You were also a treasure trove for Nobels, conferences, science in general, the English language, and especially pointing out asinine behavior with amiable words.

I thank Jasmin for brightening my days with her many talents. You always made sure that there was enough delicious food, and no one had to stay hangry. Thank you for carving time out of your insane workload for listening, venting and laughing about all things important, especially gym memberships (sauna), publishing (ACS nano for sure), diets (is butter a carb?), our remaining time here (endless), and our mental health (we are all mad here).

I thank all my colleagues from the AK Wagner; I really enjoyed our time together! Especially Anna-Lina for her immense kindness, Johannes who was the only person with a refined taste in music and books in this lab, PK for many enlightening conversation about cryptos, self-employment, or polyplexes, Sören and Basti for great times offline on the soccer pitch and online defending the ancients, Stephan for his support during my first years, Sarah for always spreading joy, and last but not least Dr. Kesselhoff for her tartness and inspiring fear with her snarky remarks.

I thank Philipp Schröder for his endless patience with my countless questions about statistics and R in particular, his willingness to discuss science in general with me, and his support in writing this thesis.

I thank Thomas Unterlinner for his help in getting me started with the raspberry pi and the fraction collector in particular. Your support was invaluable!

I thank Adrian Loy for reading code written by an absolute beginner (i.e., me), taking the time to improve it and introducing me to the finer concepts of programming and python in particular.

I thank my band Last Argument for taking my mind of the lab work from time to time and for your patience with my rants about science in general and my work in particular. I am always looking forward to our monthly practice sessions and other joined activities!

I thank my parents and my siblings for always backing me up regardless of the paths I chose. Thank you for all the encouragement, the never-ending support, the time, and the trust during every phase of my life. You are perfect.

I am especially thanking Martina for her love and continuous support throughout all the ups and downs of this Ph.D. – I could not have done it without you! Your trust in my abilities and your never-ending support – e.g., listening to presentations at 1 am in the morning, or sacrificing shared time when deadlines were looming – were invaluable for me. I really appreciate all the

time and effort you put in reading my drafts, listening to my stories and presentations, encouraging me to keep going, criticizing me, putting up with my rants and foul moods, and showing me that there is a life outside of academia. I love you.

Thank you, Ronja, for showing me every day that no matter how much more there is to be done, their importance pales in relation to you just being there, looking at me with your great, blue eyes.